



**HAL**  
open science

# Développement et intégration d'un récupérateur d'énergie thermique à base de bilames thermiques et de matériaux piézoélectriques

Jihane Boughaleb

► **To cite this version:**

Jihane Boughaleb. Développement et intégration d'un récupérateur d'énergie thermique à base de bilames thermiques et de matériaux piézoélectriques. Thermique [physics.class-ph]. Université de Lyon, 2016. Français. NNT: 2016LYSEI114 . tel-01920841v1

**HAL Id: tel-01920841**

**<https://theses.hal.science/tel-01920841v1>**

Submitted on 13 Nov 2018 (v1), last revised 11 Jan 2019 (v2)

**HAL** is a multi-disciplinary open access archive for the deposit and dissemination of scientific research documents, whether they are published or not. The documents may come from teaching and research institutions in France or abroad, or from public or private research centers.

L'archive ouverte pluridisciplinaire **HAL**, est destinée au dépôt et à la diffusion de documents scientifiques de niveau recherche, publiés ou non, émanant des établissements d'enseignement et de recherche français ou étrangers, des laboratoires publics ou privés.



N°d'ordre NNT : 2016LYSEI114

**THESE de DOCTORAT DE L'UNIVERSITE DE LYON**  
Opérée au sein de  
**Laboratoire de recherche: Laboratoire de Génie électrique et de  
ferroélectricité (LGEF)**  
**Entreprise : STMicroelectronics (Crolles 2)**

**Ecole Doctorale N° ED160**  
**Electronique, Electrotechnique et Automatique**

**Spécialité/ discipline de doctorat** : Génie Electrique

Soutenue publiquement le 09/11/2016, par :

**Jihane BOUGHALEB**

---

**Développement et intégration d'un récupérateur  
d'énergie thermique à base de bilames  
thermiques et de matériaux piézoélectriques**

---

Devant le jury composé de :

LIANG, Zhiyong GUIFFARD, Benoit	Professeur des universités Professeur des universités	FLORIDA STATE UNIVERSITY IETR	Rapporteur Rapporteur
ROUVIERE, Emmanuelle KANDA, Masae	Chef de service SERE Maitre de conférences	CEA Liten CHUBU UNIVERSITY	Examinatrice Examinatrice
GUYOMAR, Daniel COTTINET, Pierre-Jean	Professeur des universités Maitre de conférences	INSA de Lyon INSA de Lyon	Directeur de thèse Co-directeur de thèse
SKOTNICKI, Thomas MONFRAY, Stéphane QUENARD, Sébastien	Directeur Docteur Ingénieur Ingénieur	STMicroelectronics STMicroelectronics CEA Liten	Invité Invité Invité



## Département FEDORA – INSA Lyon - Ecoles Doctorales – Quinquennal 2016-2020

SIGLE	ECOLE DOCTORALE	NOM ET COORDONNEES DU RESPONSABLE
<b>CHIMIE</b>	<b>CHIMIE DE LYON</b> <a href="http://www.edchimie-lyon.fr">http://www.edchimie-lyon.fr</a>  Sec : Renée EL MELHEM Bat Blaise Pascal 3 <sup>e</sup> etage <a href="mailto:secretariat@edchimie-lyon.fr">secretariat@edchimie-lyon.fr</a> Insa : R. GOURDON	<b>M. Stéphane DANIELE</b> Institut de Recherches sur la Catalyse et l'Environnement de Lyon IRCELYON-UMR 5256 Équipe CDFA 2 avenue Albert Einstein 69626 Villeurbanne cedex <a href="mailto:directeur@edchimie-lyon.fr">directeur@edchimie-lyon.fr</a>
<b>E.E.A.</b>	<b>ELECTRONIQUE, ELECTROTECHNIQUE, AUTOMATIQUE</b> <a href="http://edeea.ec-lyon.fr">http://edeea.ec-lyon.fr</a>  Sec : M.C. HAVGOUDOUKIAN <a href="mailto:Ecole-Doctorale.eea@ec-lyon.fr">Ecole-Doctorale.eea@ec-lyon.fr</a>	<b>M. Gérard SCORLETTI</b> Ecole Centrale de Lyon 36 avenue Guy de Collongue 69134 ECULLY Tél : 04.72.18 60.97 Fax : 04 78 43 37 17 <a href="mailto:Gerard.scorletti@ec-lyon.fr">Gerard.scorletti@ec-lyon.fr</a>
<b>E2M2</b>	<b>EVOLUTION, ECOSYSTEME, MICROBIOLOGIE, MODELISATION</b> <a href="http://e2m2.universite-lyon.fr">http://e2m2.universite-lyon.fr</a>  Sec : Sylvie ROBERJOT Bât Atrium - UCB Lyon 1 04.72.44.83.62 Insa : H. CHARLES <a href="mailto:secretariat.e2m2@univ-lyon1.fr">secretariat.e2m2@univ-lyon1.fr</a>	<b>M. Fabrice CORDEY</b> CNRS UMR 5276 Lab. de géologie de Lyon Université Claude Bernard Lyon 1 Bât Géode 2 rue Raphaël Dubois 69622 VILLEURBANNE Cédex Tél : 06.07.53.89.13 <a href="mailto:cordey@univ-lyon1.fr">cordey@univ-lyon1.fr</a>
<b>EDISS</b>	<b>INTERDISCIPLINAIRE SCIENCES-SANTE</b> <a href="http://www.ediss-lyon.fr">http://www.ediss-lyon.fr</a>  Sec : Sylvie ROBERJOT Bât Atrium - UCB Lyon 1 04.72.44.83.62 Insa : M. LAGARDE <a href="mailto:secretariat.ediss@univ-lyon1.fr">secretariat.ediss@univ-lyon1.fr</a>	<b>Mme Emmanuelle CANET-SOULAS</b> INSERM U1060, CarMeN lab, Univ. Lyon 1 Bâtiment IMBL 11 avenue Jean Capelle INSA de Lyon 696621 Villeurbanne Tél : 04.72.68.49.09 Fax :04 72 68 49 16 <a href="mailto:Emmanuelle.canet@univ-lyon1.fr">Emmanuelle.canet@univ-lyon1.fr</a>
<b>INFOMATHS</b>	<b>INFORMATIQUE ET MATHEMATIQUES</b> <a href="http://infomaths.univ-lyon1.fr">http://infomaths.univ-lyon1.fr</a>  Sec :Renée EL MELHEM Bat Blaise Pascal 3 <sup>e</sup> etage <a href="mailto:infomaths@univ-lyon1.fr">infomaths@univ-lyon1.fr</a>	<b>Mme Sylvie CALABRETTO</b> LIRIS – INSA de Lyon Bat Blaise Pascal 7 avenue Jean Capelle 69622 VILLEURBANNE Cedex Tél : 04.72. 43. 80. 46 Fax 04 72 43 16 87 <a href="mailto:Sylvie.calabretto@insa-lyon.fr">Sylvie.calabretto@insa-lyon.fr</a>
<b>Matériaux</b>	<b>MATERIAUX DE LYON</b> <a href="http://ed34.universite-lyon.fr">http://ed34.universite-lyon.fr</a>  Sec : M. LABOUNE PM : 71.70 –Fax : 87.12 Bat. Direction <a href="mailto:Ed.materiaux@insa-lyon.fr">Ed.materiaux@insa-lyon.fr</a>	<b>M. Jean-Yves BUFFIERE</b> INSA de Lyon MATEIS Bâtiment Saint Exupéry 7 avenue Jean Capelle 69621 VILLEURBANNE Cedex Tél : 04.72.43 71.70 Fax 04 72 43 85 28 <a href="mailto:jean-yves.buffiere@insa-lyon.fr">jean-yves.buffiere@insa-lyon.fr</a>
<b>MEGA</b>	<b>MECANIQUE,ENERGETIQUE,GENIE CIVIL,ACOUSTIQUE</b> <a href="http://mega.universite-lyon.fr">http://mega.universite-lyon.fr</a>  Sec : M. LABOUNE PM : 71.70 –Fax : 87.12 Bat. Direction <a href="mailto:mega@insa-lyon.fr">mega@insa-lyon.fr</a>	<b>M. Philippe BOISSE</b> INSA de Lyon Laboratoire LAMCOS Bâtiment Jacquard 25 bis avenue Jean Capelle 69621 VILLEURBANNE Cedex Tél : 04.72 .43.71.70 Fax : 04 72 43 72 37 <a href="mailto:Philippe.boisse@insa-lyon.fr">Philippe.boisse@insa-lyon.fr</a>
<b>ScSo</b>	<b>ScSo*</b> <a href="http://recherche.univ-lyon2.fr/scso/">http://recherche.univ-lyon2.fr/scso/</a>  Sec : Viviane POLSINELLI Brigitte DUBOIS Insa : J.Y. TOUSSAINT Tél : 04 78 69 72 76 <a href="mailto:viviane.polsinelli@univ-lyon2.fr">viviane.polsinelli@univ-lyon2.fr</a>	<b>M. Christian MONTES</b> Université Lyon 2 86 rue Pasteur 69365 LYON Cedex 07 <a href="mailto:Christian.montes@univ-lyon2.fr">Christian.montes@univ-lyon2.fr</a>

\*ScSo : Histoire, Géographie, Aménagement, Urbanisme, Archéologie, Science politique, Sociologie, Anthropologie



# Contents

<b>Chapter 1</b> .....	1
<b>I. Motivation: Wireless sensor network development</b> .....	2
1. Body Sensor Networks .....	4
2. Smart cities .....	5
<b>II. Potential power sources for WSN applications</b> .....	6
1. Vibrational energy harvesting methods .....	7
2. Thermal energy harvesting methods .....	8
3. Photovoltaic energy harvesting .....	11
<b>III. Thermal energy harvesting: Thermoelectric and HEATec devices</b> .....	11
1. Thermoelectric energy harvesters .....	11
1.1. Working principle .....	11
1.2. State of the art of seebeck energy harvesters .....	14
2. Coupled piezoelectric and bimetal heat engine used in Heatec Project .....	21
2.1. Presentation of the HEATec project .....	21
2.2. Presentation of the device studied in this thesis .....	24
2.2.1. Thermo-mechanical conversion by bimetallic strip heat engine .....	25
2.2.2. Electromechanical conversion by piezoelectric membrane .....	28
<b>III. Objective of this thesis</b> .....	31
<b>IV. References</b> .....	32

<b>Chapter 2</b> .....	36
<b>I. Introduction</b> .....	37
<b>II. State of the art of thermal energy harvesters modeling</b> .....	38
<b>III. Thermal study in steady state conditions</b> .....	41
1. Modeling .....	41
1.1. Simplification of the modeling.....	41
1.2. Analytical model.....	42
1.3. Finite element model .....	44
2. Results and discussions .....	45
2.1. Matrix analysis using the FEM .....	45
2.2. Thermal optimization and design improvement.....	46
2.3. Electrical optimization thanks to thermal improvements .....	48
3. Scaling the devices after their thermal improvements .....	49
<b>IV. Dynamic modeling of the harvester taking into account the bimetal</b> .....	54
1. Purpose of the study .....	54
2. Dynamic modeling.....	55
2.1. Model analysis with the bimetal at its lower position.....	56
2.2. Model analysis with the bimetal in its upper position .....	56
2.3. Estimation of the model parameters: contact resistances and switched capacitances of the bimetal .....	57
3. Dynamic model application .....	58
3.1. Range of hot source functioning temperatures of a bimetal having a certain hysteresis once mounted in the harvester .....	58
3.2. Calculation of the intrinsic snap-up and -down temperatures $T_s$ and $T_{sb}$ of a bimetal mounted in the harvester as a function of the desired minimum hot source temperature $T_{hotmin}$ .....	58
3.3. Calculation of bimetal's maximal snapping frequency.....	59
4. Model experimental validation and interpretation .....	59
4.1. Study of bimetal's hot source operation windows as a function of their hysteresis and of the hot source temperatures .....	59
4.2. Simulations using bimetal's with the same snapping temperature and different thermal hystereses .....	61
4.3. Simulations with different snapping temperatures and a fixed thermal hysteresis.....	62
4.4. Electrical output power as a function of the bimetal's thermal hystereses .....	63
4.5. Analyses of the bimetal snapping temperature shift when it is put alone on a hot plate and once mounted in the harvester .....	64
<b>V. Conclusion</b> .....	64

<b>VI. References</b> .....	65
<b>Chapter 3</b> .....	68
<b>I. Introduction</b> .....	69
<b>II. Piezoelectric materials selection</b> .....	70
1. Types of piezoelectric materials .....	70
1.1. Naturally piezoelectric crystals .....	70
1.2. Synthetic piezoelectric ceramics .....	70
1.3. Synthetic piezocrystals .....	71
1.4. Piezopolymers .....	71
1.5. Piezocomposites .....	72
1.6. Comparison of the piezoelectric materials .....	72
2. Impact of the piezoelectric materials properties on the output power .....	73
2.1. Elastic compliance $s_{11}$ .....	73
2.2. Piezoelectric strain constant $d_{31}$ and piezoelectric stress coefficient $g_{31}$ .....	74
2.3. Electromechanical coupling coefficient $k_{31}$ .....	75
2.4. Factor of merit FOM: .....	75
3. Comparison of piezoelectric materials properties .....	76
<b>III. Device architectures improvements</b> .....	76
1. Electrical power output calculation .....	76
2. Substrate material .....	78
3. Contact of the bimetal with the cold surface .....	80
4. Decreasing the device and bimetal dimensions .....	81
5. Positioning of the piezoelectric membrane .....	83
6. Test of piezoelectric membrane from different manufactures .....	85
7. Study of bimetals of higher thermal hysteresis and dimensions .....	88
8. Improved device efficiency .....	94
<b>IV. Device lifetime and aging</b> .....	95
1. Bimetals lifetime .....	95
2. Piezoelectric membranes lifetime .....	97
2.1. Thermal degradation .....	97
2.2. Mechanical degradation .....	98
<b>V. Conclusion</b> .....	102

<b>VI. References</b> .....	102
<b>Chapter 4</b> .....	104
<b>I. Introduction</b> .....	104
<b>II. Energy harvesting using piezoelectric bimetals</b> .....	105
1. Piezoelectric composite deposition on bimetals.....	105
1.1. Preparation and deposition of the piezoelectric paint on bimetals.....	106
1.2. Piezoelectric paint characterization.....	110
2. Piezoelectric thin films deposition on bimetals .....	112
2.1. Experimental procedure .....	112
2.2. Characterization of the piezoelectric bimetals .....	115
<b>III. Thermal and mechanical energy harvesting</b> .....	123
1. Available vibration sources .....	123
2. Dual energy harvester design rules .....	124
3. Numerical modeling.....	128
<b>IV. Conclusion</b> .....	131
<b>V. References</b> .....	131
<b>Chapter 5</b> .....	133
<b>I. Introduction</b> .....	133
<b>II. Device electromechanical modeling</b> .....	134
1. General model of Kinetic energy harvesters .....	134
2. Modeling of piezoelectric energy harvesters .....	136
2.1. Mechanical modeling .....	136
2.2. Electrical modeling .....	138
3. SPICE modelling of the harvester .....	139
<b>III. Power management</b> .....	144
1. Review of the different power management technologies .....	144

1.1. Energy conversion steps .....	144
1.2. Power management circuits state of the art .....	144
<b>2. Power management simulation.....</b>	<b>151</b>
2.1. First modules using a rectifier and a storage capacitor .....	151
2.2. Power management results using discrete element PMC.....	153
2.3. Power management simulation using Integrated interface circuits .....	153
<b>IV. Wireless sensor node demonstrations.....</b>	<b>154</b>
<b>V. Conclusion.....</b>	<b>160</b>
<b>VI. References.....</b>	<b>161</b>
<b><i>General Conclusion.....</i></b>	<b>165</b>

## Chapter 1

# Introduction: Context and application of power scavenging technologies

<i>Chapter 1</i> .....	1
I. Motivation: Wireless sensor network development .....	2
1. Body Sensor Networks .....	4
2. Smart cities .....	5
II. Potential power sources for WSN applications .....	6
1. Vibrational energy harvesting methods .....	7
2. Thermal energy harvesting methods .....	8
3. Photovoltaic energy harvesting .....	11
III. Thermal energy harvesting: Thermoelectric and HEATec devices .....	11
1. Thermoelectric energy harvesters .....	11
1.1. Working principle .....	11
1.2. State of the art of seebeck energy harvesters .....	14
2. Coupled piezoelectric and bimetal heat engine used in Heatec Project .....	21
2.1. Presentation of the HEATec project .....	21
2.2. Presentation of the device studied in this thesis .....	24
2.2.1. Thermo-mechanical conversion by bimetallic strip heat engine .....	25
2.2.2. Electromechanical conversion by piezoelectric membrane .....	28
III. Objective of this thesis .....	31
IV. References .....	32

## I. Motivation: Wireless sensor network development

The concept of energy harvesting designates the process of using ambient energy source to generate usable electrical energy. This concept is not new and has known a great development during the last half of the twentieth century with the generation of electricity based on similar conversion techniques. We are all familiar with their large-scale deployment such as electrical and thermal power generation for buildings power requirements as well as solar panels and wind turbines. Contrary to these power generation devices, energy harvesting systems are only intended to power small and autonomous electronic devices more specifically wireless sensor nodes (WSN) that have the ability to monitor their surrounding environment.

The development of these systems has been enabled by the reduction of the size and the power consumption of electronic components. Usually, the most common power source for wireless sensor nodes are batteries. Batteries combine good energy density with a range of commercially available sizes and have the advantage of supplying their energy at the voltage levels required by modern electronics [1]. However, many drawbacks are related to their use; as sensor networks increase in number, replacement of depleted batteries is time-consuming and wasteful. Also a battery that is large enough to last the life of a sensor node would dominate the overall size of the WSN which is not practical. Otherwise, the lifetime of the sensor node would be determined by the battery's lifetime and not determined by the failure of the other electrical components. Additionally, the batteries' chemistry often involves toxic materials and presents disposal issues. Consequently, researchers started looking for new green and unlimited energy sources to power autonomous WSN to overcome the economic and environmental limitations related to the batteries use [2].

The ultimate objective of WSN is to develop networks composed of hundreds of self-sufficient sensor nodes in order to replace long transmission distances with small-price and low-power wireless systems, leading to the emergence of intelligent environments [3]. In a Wireless Sensor Network (WSN), devices are able to interface with physical sensing hardware, to perform some treatment on sampled data and to wirelessly communicate the information by means of radio transceivers to other devices in order to monitor spatially distributed data about their environment [4]. A typical wireless sensor node architecture is given in Fig. 1. It is composed of an energy harvester for the sensor node supply and power autonomy, a power management circuit to rectify the output energy of the energy harvester and to power electronic subsystems (such as sensors or microcontrollers). An energy storage element is also needed to temporarily store the harvested energy and to play the role of a buffer, a microcontroller with various sensors depending on the targeted application, and finally communication peripherals to transmit data toward a reception node.

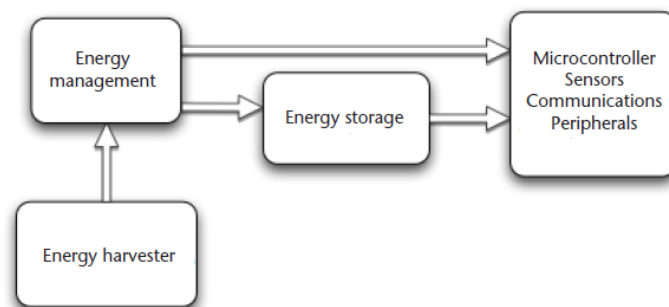


*Fig. 1. General block diagram of an energy harvesting sensor node [5].*

Communication in wireless sensor networks is generally performed with a low data rate and short transmission range (comprised between 10m and 100m). For applications like home security and automation, sub-GHz networks offer substantive benefits over the most powerful protocols such as Wi-Fi and Bluetooth. A discussion of the different communication protocols used for Internet of Things applications is presented in Chapter 5. Also, In a WSN, data can be transmitted using either synchronous or asynchronous communication modes. Choosing an operation mode depends on the needs of the targeted application and on the available energy. In asynchronous operation, sensor nodes' wake-up period is not synchronized so that whenever a transmitter has a data packet to deliver, it detects when its targeted receiver is ready for reception and then it carries out packet delivery. This allows to send data as soon as enough energy is available. Otherwise the microcontroller is switched off between two measurements and no synchronization between the different nodes of a network occurs. In such a mode of working, very low energy is needed for each cycle and the system can work with only few microwatts. At the opposite, in synchronous operation mode, all the nodes in a neighborhood have the same time of wake-up period and they run a synchronization procedure by exchanging data periodically. This means that each node can communicate with another node and that the microcontroller only sleeps between two measurements and is not switched off as in the case of asynchronous operation. This leads to a higher power consumption that cannot be lower than  $10\mu\text{W}$  [6-7]. For WSN supplied by energy harvesters, as the amount of harvested power has an order of magnitude of few to tenth of microwatts, asynchronous operation mode is preferred [6]. Fig. 2 shows a WSN in synchronous and in asynchronous modes.

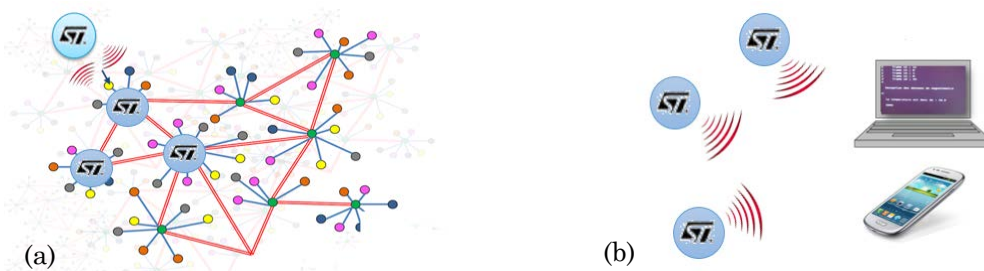


**Fig. 2.** WSN in (a). Synchronous and (b). Asynchronous operation modes.

Due to the development of WSN and because of the drawbacks related to batteries, energy harvesting technologies have attracted much attention during the last decades provided that there is sufficient exploitable environmental energy available (such as light, vibrations, temperature difference...). Even if ambient energy harvesters produce only low levels of power, they provide enough energy to supply sensor nodes thanks to the improvements aimed at decreasing the consumptions of electronic circuits: typical power levels of a WSN can be in the range of a few microwatts up to a few dozen microwatts [5-8-9]. This trend is clearly presented by Beeby in [5] as he shows an increase in both the number of published papers on energy harvesting sensor networks and the percentage of papers on sensor networks that feature energy harvesting (Fig. 3).

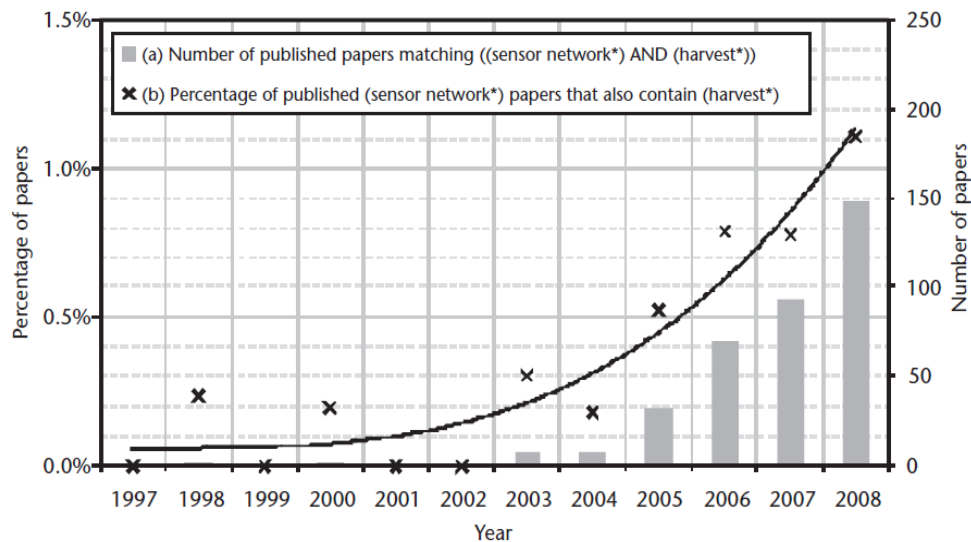


**Fig. 3.** Increase in research in energy harvesting technologies and WSN developments [5].

WSN can potentially be used in a wide range of applications and many scientists have focused their research work on their applications [2-8]. Such networks provide superior quality data than a single sensor node and promise to provide a significant positive impact on many parts of human life such as more effective use of resources, good understanding of human behavior and an increased safety and security. Some of the various applications of WSN are developed hereafter.

### 1. Body Sensor Networks

Body sensor networks are a new and fast-growing multidisciplinary research area that have known an important development these last decades with the increased development of energy harvesting technologies and WSN [10-11]. In the medical field, implantable and wearable medical devices can be used for both short-term and long-term health treatments. As an example, we can imagine that hospital patients are equipped with WSN monitoring the patient's vital signs and detecting their exact location. In that case, no constant supervision of patients is necessary and they can move more freely. If an accident happens, the sensors can directly alert the closest doctors or hospital workers and give them the information about the patient location and condition [8]. Another kind of applications concerns chronically-ill patients that can have a better quality of life and life expectancy if certain biological signs can continually be monitored and controlled. As an example, continually monitoring blood pressure in patients with hypertension may significantly increase medication compliance [12], early stages of heart disease can be revealed by real time processing of electrocardiograph [13] and closed loop control of insulin administration for diabetic patients may significantly reduce the risk of hypoglycemia [14]. The finality of such devices is to keep surgery and medical costs to a minimum. However, to do so, it is particularly important to eliminate both maintenance and power sources replacements [15]. The combination of low power requirements and the need to eliminate maintenance makes BSN an attractive application for energy harvesting.

## 2. Smart cities

The application of Internet of Things to an urban context is of a particular interest as it can lead to an optimized management of public affairs. Such an urban IoT system is called the “Smart City” concept and can bring a number of benefits in the management and optimization of traditional public services. In [16], the author deals with this concept and gives an overview of the most important services that may be enabled by an urban IoT. A first practical implementation and demonstration was realized in “Padova Smart City” [16]. Some of these services are presented hereafter.

### - *Structural health of buildings:*

To properly maintain the historical buildings in the cities but not only, monitoring the state of each buildings and the identification of areas subject to external agents impacts should be realized. To do so, the urban IoT can be of a great help as it may provide information about buildings structural integrity by means of vibrations and deformations sensors to monitor the buildings stress, atmospheric agent sensors to monitor pollution levels and even temperature or humidity sensors to characterize the environment around the building [17]. Such sensors deployment can reduce the costs of the periodic structural testing and can allow targeted restoration actions operated by humans. That way, urban IoT will contribute to the cities historical heritage preservation.

### - *Waste management*

Waste management is becoming a real issue in most of the modern cities because of the cost of the service and the storage of garbage in the landfills. To decrease some economic and ecological savings [18], the use of intelligent waste containers can be of a great help. Thanks to such containers, it is possible to detect the level of the load and to optimize the collector’s trucks route.

### - *Air quality*

Because of the global climate warming, the European Union adopted a 20-20-20 Renewable energy directive setting climate change reduction goals for the next decade. More information about this directive can be found in [19]. It calls for a 20% reduction in gas emission by 2020 compared with 1990 and a 20% in the use of renewable energy by 2020 [16]. To do so, urban IoT can be very useful as it may allow the air quality monitoring in different places [20].

### - *Traffic congestion*

Urban IoT can also allow traffic monitoring congestion in cities. Not only modern vehicles are equipped with GPS but also roads can be equipped with air quality sensors and acoustic sensors for noise detection. This can lead to a more disciplined traffic if the information of the traffic is made available to the citizens.

### - *City energy consumption*

Urban IoT can also provide information to monitor the energy consumption of cities by enabling a detailed view of the energy consumptions of various services, for example public transportations and lightening, traffic lights, control cameras.... This goes in the direction of the decisions of the European Union for energy efficient management and waste reduction.

Other than medical applications and urban IoT, potential uses of WSN include military tracking, security, animal tracking or forest fire detection [2,8].

## II. Potential power sources for WSN applications

As previously exposed, WSN have plenty of applications in many environmental and industrial monitoring systems. For this reason, researchers have focused their attention on energy harvesting technologies to power WSN. The principle of energy harvesting systems is to use ambient and environmental power sources and to convert it into electrical energy by means of various transduction techniques and systems.

Literature on energy harvesting technologies shows a large spectrum of generators demonstrating their capability to supply wireless sensor nodes. In the next part of this chapter, we sum up the different groups of energy harvesters according to the nature of energy they scavenge. Numerous works have focused of these different energy harvesting technologies and provide more details on it [3,5,9,22]. Fig. 4 shows some applications of energy harvesting devices and WSN applications and Fig. 5 presents a schematic explaining of the architecture of a WSN with both the energy harvester and the battery.



**Fig. 4.** Some applications of energy harvesting devices and Wireless Sensors Networks [21].

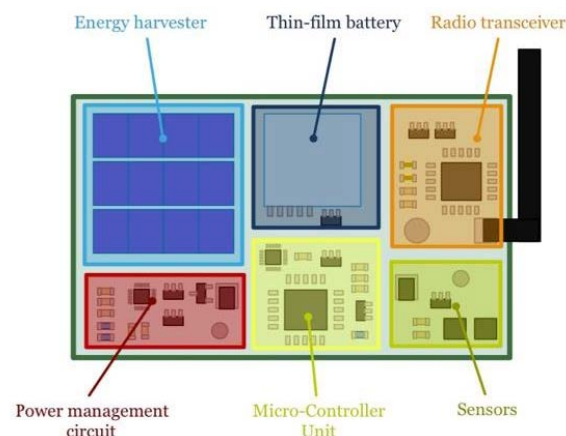


**Fig. 5.** Simplified schematic explaining the architecture of a Wireless Sensing Node [21].

The power consumption of a sensor node has been estimated by many researchers, the corresponding power values are comprised between 1 and  $20\mu\text{W}$  [10]. To power these WSN, energy can be harvested from the ambient using vibrational/mechanical energy, thermal energy

or light energy. Table 1 sums up the output power that may be obtained from environmental sources when using optimized devices built with the currently available transducer technology [23].

Source	Source power	Harvested power
<b>Ambient light</b>		
<i>Indoor</i>	0.1mW/cm <sup>2</sup>	10μW/cm <sup>2</sup>
<i>Outdoor</i>	100mW/cm <sup>2</sup>	10mW/cm <sup>2</sup>
<b>Vibrations and mechanical energy</b>		
<i>Human</i>	1m/s <sup>2</sup> at 50Hz	4μW/cm <sup>2</sup>
<i>Industrial</i>	10m/s <sup>2</sup> at 1kHz	100μW/cm <sup>2</sup>
<b>Thermal energy</b>		
<i>Human</i>	20mW/cm <sup>2</sup>	30μW/cm <sup>2</sup>
<i>Industrial</i>	100mW/cm <sup>2</sup>	1-10mW/cm <sup>2</sup>

**Table 1.** Comparison of various energy sources available in the environment [23].

## 1. Vibrational energy harvesting methods

Vibrations is an abundant energy source in our environment, especially in industrial environments. Conversion of mechanical vibrations into electrical energy is one of the most studied techniques of energy harvesting and it is one of the fields that knew the broadest diversification in terms of transduction technologies. The common point between all vibrations energy harvesters is that all of them work on the principle of the resonant vibrations of an oscillator caused by the inertia of a seismic mass [10]. Common methods for harvesting vibrations include:

- Piezoelectric transduction: this transduction is realized by means of piezoelectric materials that have the property of generating electrical charges when mechanical strains is applied on it. Consequently, when an oscillating load is placed on a structure with piezoelectric materials, an AC power source is generated [24].
- Electrostatic transduction: it generally consists of two conducting plates separated by a dielectric (forming a capacitor) which move relatively to one another. As the plates move, the energy stored in the capacitor changes thus providing the mechanism of mechanical to electrical energy conversion [25].
- Electromagnetic transduction: this conversion process results from the relative motion of an electrical conductor in a magnetic field. The conductor is wound in a coil to make an inductor and the relative motion between the coil and the magnetic field causes a current to flow in the coil [26].

Fig. 6 presents a schematic representation of these three kinds of vibrations energy harvesters.

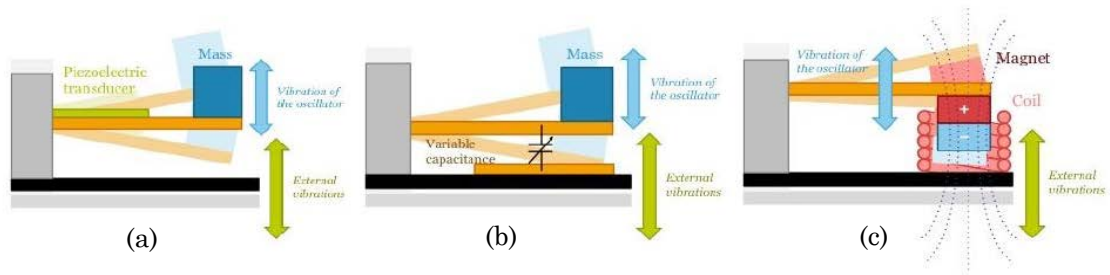


**Fig. 6.** Vibration energy harvesters based on different transduction mechanisms, (a). Piezoelectric, (b). Capacitive, (c). Electromagnetic.

Williams and Yates [27] have worked on such kinetic energy harvesters and developed an equivalent single degree of freedom model of it (this model is developed in more details in chapter 5). It allows to obtain the maximum theoretical energy from a vibration based energy harvester whatever is the transduction mechanism or its geometry. Thanks to this work, the authors showed that the output power is maximized by matching the resonance frequency of the oscillator to the frequency of the environmental oscillations and also by increasing the quality factor of the system. However, the main drawback of using energy harvesters with high-Q linear oscillators is a narrowing of the frequency bandwidth of the generators which restricts access to the energy associated to frequencies other than the resonant frequency. Some researchers thus are orientating their researches toward designing piezoelectric energy harvesters with large bandwidths, for example by using an array of oscillators working at different frequencies [28] or using bistable oscillators [29].

Roundy in his thesis established a comparison of the maximum energy density of the three different vibration energy harvesters based on Williams and Yates model [23]; He also compared the pros and cons of each conversion mechanism (table 2).

	Maximum energy density	Advantages	Disadvantages
<b>Piezoelectric</b>	17 mJ/cm <sup>3</sup>	- No separate voltage source is needed - Voltages of 2 to 10V - Highest energy density	- Microfabrication processes are not compatible with standard CMOS processes and piezoelectric thin films have poor coupling
<b>Electrostatic</b>	4mJ/cm <sup>3</sup>	- Easier to integrate with electronics and microsystems - Voltages of 2 to 10V	- Separate voltage source is needed
<b>Electromagnetic</b>	4mJ/cm <sup>3</sup>	- No separate voltage source is needed	- Maximum voltages of 0.1V - Difficult to integrate with electronics and microsystems

**Table 2.** Comparison of the three kinetic energy harvesters' properties [3].

In addition to this study, Mitcheson in [10] reported a comparison between these different transduction mechanisms efficiencies and showed that electromagnetic systems have an efficiency of 1% whereas the electrostatic generators have an efficiency of 20% and more than 30% for piezoelectric energy converters.

## 2. Thermal energy harvesting methods

Like mechanical energy and vibrations, heat is one of the most abundant energies in the environment which makes it be a viable energy source to power WSN. Any temperature difference existing between two locations results in a flow of heat from the hot side toward the cold side in

an attempt to establish a thermal equilibrium. Many transduction mechanisms can be used to convert that thermal energy into electricity. When spatial thermal gradients exist, thermoelectric devices are generally used. Otherwise, when thermal fluctuations occur, pyroelectric materials are preferred.

For thermal energy harvesting, there exist a maximal efficiency depending of the external temperatures only. Carnot gave a simple expression of this maximal theoretical efficiency without making any assumption of the type of working medium. This efficiency only depends of the cold source's and hot source's temperatures. The expression of the Carnot efficiency is given in equation 1 where  $T_C$  is the cold source's temperature and  $T_H$  the hot source's temperature.

$$\eta_{carnot} = 1 - \frac{T_C}{T_H} \quad (1)$$

Modern thermoelectric converters are made of semiconductors that offer higher conversion efficiency and larger power output than metals. A typical thermoelectric generator is made of a number of thermocouples connected electrically in series and thermally in parallel, sandwiched between a bottom chip and a top chip. A thermocouple junction consists of an n-type and a p-type semiconductor thermoelement connected electrically in series and a typical thermoelectric generator is a matrix constructed by repeating this basic building block. When a temperature difference occurs between the thermocouple junctions, an output voltage is generated through the Seebeck effect [30].

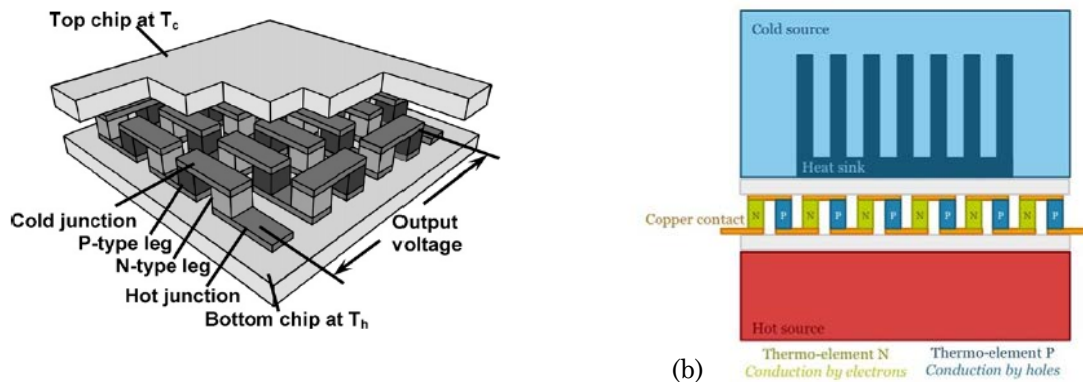


**Fig. 7.** (a). Schematic representation of a thermoelectric generator [29], (b). Representation of a thermoelectric generator with a heat sink.

Thermoelectric modules are the main modules used to convert thermal spatial gradients into electricity and it is now possible to find commercial thermoelectric devices generating from microwatts to several milliwatts of electric power like Micropelt thermoelectric generators [31]. To improve these device performances, materials properties and device geometry are key parameters to study [5]. To reach a maximum output power using a thermoelectric energy harvester (THE), its internal thermal impedance must match the thermal impedance of the heat sink used to evacuate heat from the generator [32]. However, the possibility of harvesting thermal energy is limited in the case of thermoelectric micro-generators as the temperature difference across the chip is very low as TEH are composed of many thermocouples made of semiconductors having good electrical but also thermal properties. Thus, it is compulsory to use a heat sink to generate electricity from a temperature difference even for macroscale devices. Theoretical efficiency of these devices generally reaches 14% of the Carnot limit for a hot source at 30°C. As a

thermal energy harvester is studied in this thesis, more details about thermoelectric generators working principle and properties will be given later in this chapter.

Leonov in [33] developed a thermoelectric generator and integrated it on human clothes. It generated a power in the range of 5–0,5 mW at ambient temperatures of 15°C–27°C, respectively. Fig. 8 presents the evolution of the harvested power in such conditions as a function of the ambient air temperature and the situation of the person wearing the shirt. Despite some applications at ambient temperatures adapted to human body applications, technologies of thermoelectric generators are generally developed to harvest heat at higher temperatures around 100°C which is more adapted to industrial environments. In such environments where the use of bulky heat sinks is not problematic, thermal energy harvesters can generate up to 10mW/cm<sup>2</sup> which is largely enough to power WSN.

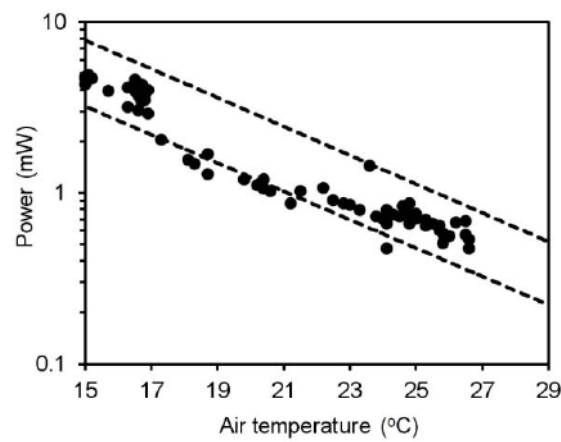


**Fig. 8.** Power generated by the TEH hidden in a shirt at different ambient temperatures and activities (points). For comparison, two dashed lines illustrate power in a TEH of electroencephalography shirt with metal plates located beyond the external surface of a shirt: on a walking person (top) and standing/sitting person (bottom) [32].

Contrary to thermoelectric generators, pyroelectric generators do not need a temperature spatial gradient but temporal temperature changes [34] to generate electricity. The pyroelectric effect is the property of some dielectric materials with polar point symmetry to exhibit an electrical polarization when temperature varies. A temporal change in the material's temperature generates a variation in the induced charge producing thus a pyroelectric current. Usually, the pyroelectric effect is mainly used for pyroelectric infrared temperature detectors but some researchers already realized pyroelectric energy harvesters [34-37]. Sebald in his papers first demonstrated that a pyroelectric device may reach an efficiency up to 50% of Carnot efficiency, then, he estimated the amount of power that can be expected from natural time variations of temperature of a wearable device as the pyroelectric material was fixed on a piece of fabric of a coat. He showed that power peaks up to 0,2mW.cm<sup>-3</sup> were reached and a mean power of 0,1μW.cm<sup>-3</sup> was determined within 24h testing. Yet the advantages of pyroelectric materials are counterbalanced by the need for temperature variations, which is the main difficulty to overcome with such generators. Natural temperature variations are quite unusual in practical cases, whereas it is easy to find temperature gradients. However, it is possible to transform temperature spatial gradients into temperature time variations or to find temperature variations on portable devices going from inside to outside several times per day as it was the case for the experiment presented before.

### 3. Photovoltaic energy harvesting

Ambient light energy harvesting is also a solution to power WSN as there exist mature technologies able to convert incoming photons into electricity and based on photovoltaic cells. A solar cell is made of p-n type semi-conductor materials. The P-doped material and N-doped material are positioned such that they form a p-n diode junction close to the top surface of the solar cell, as shown in Figure 7. When the solar cell is exposed to photonic radiations, an electric voltage is developed between the p-type and n-type materials. A single solar cell has an open-circuit voltage of about 0.6 V but can easily be placed in series with other cells to get almost any desired voltage and in parallel with other cells to increase the current [1,5].

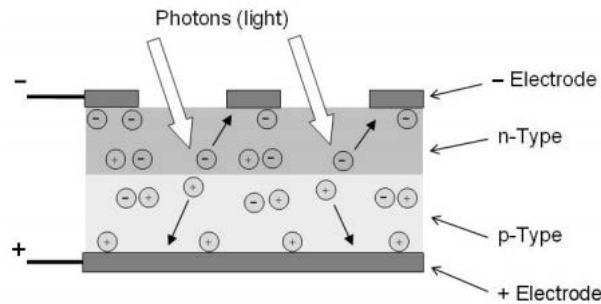


Fig. 8. Solar cell for photovoltaic energy harvesting [1].

For photovoltaic energy harvesting, we distinguish indoor from outdoor illuminations as the amounts of harvested energy are different, given the difference of incident irradiance between these two cases [9]. Outdoors, the sun can provide around 100mW/cm<sup>2</sup> of optical power, a cloudy day may provide 10 mW/cm<sup>2</sup>, whereas indoors, the incident optical power is of 0.1mW/cm<sup>2</sup> (table 1). Typical solar cells have an efficiency values in the range of 5% to 20% under standard conditions. The power density available from solar cells operating outdoors can exceed that available with other sources of energy but the value is much less for indoor operation. Nevertheless, even indoor light energy harvesting can provide sufficient power densities for low power technologies such as WSN.

## III. Thermal energy harvesting: Thermoelectric and HEATec devices

### 1. Thermoelectric energy harvesters

Thermoelectricity is the most used technology to convert heat into electricity. In this part, an overview of thermoelectric generators is given and then a benchmark of a thermoelectric generator developed by Micropelt is exposed.

#### 1.1. Working principle

Thermoelectricity describes the coupling between heat and electricity in solids and can be summarized by three thermoelectric effects: Seebeck effect, Peltier effect and Thomson effect. Based on these effects, thermoelectric devices have been developed and employed for power generation, refrigeration and temperature sensing. The three thermoelectric effect are summarized in Figure 9.

Seebeck effect corresponds to a voltage generation by the temperature difference across a junction of two materials. Equation 2 describes this phenomenon where  $\Delta T = T_H - T_C$  and  $\alpha_{ab}$  is referred to as the seebeck coefficient.

$$V = \alpha_{ab}\Delta T \quad (2)$$

Peltier effect corresponds to heat absorption or rejection at a junction of two materials due to an electrical current flowing through it. Equation 3 gives the amount of heat removed per unit time from one junction to another where  $I$  is the electrical current in the circuit and  $\pi_{ab}$  is referred to as Peltier effect.

$$\dot{Q} = \pi_{ab} \cdot I \quad (3)$$

Thomson effect: at the opposite of both Seebeck and Peltier effects that can only occur in systems where at least two different materials are used, Thomson effect corresponds to heat absorption or dissipation by a material when subject to temperature difference and electrical current. The total heat absorption or rejection is given by equation 4 where  $\beta$  corresponds to Thomson coefficient.

$$\dot{Q} = \beta I \Delta T \quad (4)$$

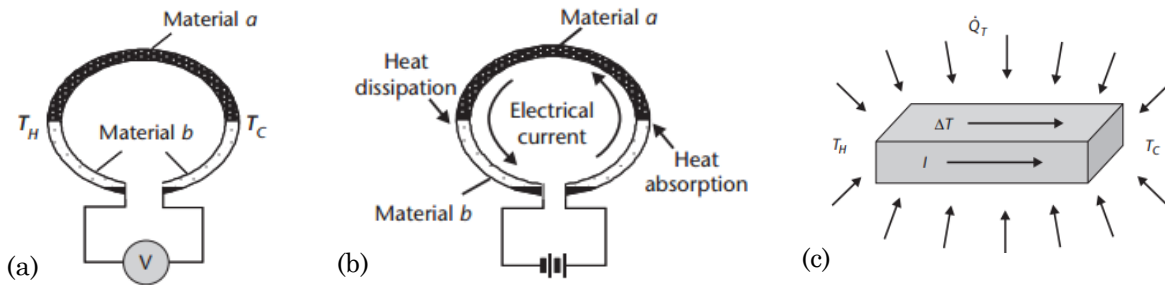


**Fig. 9.** (a). The Seebeck effect, (b). The Peltier effect, (c). The Thomson effect [5].

From these three thermoelectric effects, only the Seebeck effect is appropriate to harvest thermal energy. This is the reason why we will only focus on this effect hereafter.

Modern thermoelectric converters are fabricated using semiconductors that offer higher conversion efficiency and larger power output than metal alloys. The core element of a thermoelectric energy harvester is a thermopile corresponding to a large number of thermocouples placed between a hot and a cold place and connected thermally in parallel and electrically in series. A thermocouple consists of an n-type and p-type semiconductor thermoelement connected usually using either copper or aluminum. The structure in Figure 10 is the basic block of these thermal generators. Besides the thermopile, the generator includes a radiator for efficient dissipation of heat.

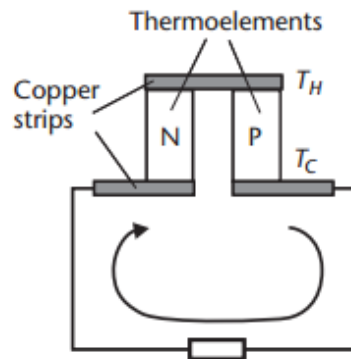


**Fig. 10.** Schematic representation of a thermoelement.

The principal factor that dictates the performance of a thermoelectric generator is the material's thermoelectric figure of merit,  $zT$ . By common convention, the thermoelectric figure of merit of a single material is denoted as  $zT$  (lower case  $z$ ), whereas the effective thermoelectric figure of merit of a thermoelectric couple, module, or generator system is denoted as  $ZT$  (upper case  $Z$ ). The higher the  $ZT$  of the materials used in a thermoelectric generator, the higher potential electrical power and conversion efficiency may be achieved in an energy harvester. For a given operation temperature and thermoelectric material, the figure of merit,  $ZT$ , is defined in equation 5.

$$zT = \frac{\alpha^2 \sigma}{\lambda} T \quad (5)$$

Where  $\alpha$  is the seebeck coefficient,  $\sigma$  is the electrical conductivity,  $\lambda$  the thermal conductivity and  $T$  the absolute temperature in kelvin.

The effective thermoelectric figure of merit of two materials used in a thermoelectric module can be defined as follows in equation 6.

$$ZT = \frac{(\alpha_p - \alpha_n)^2}{\sqrt{\lambda_p \rho_p} + \sqrt{\lambda_n \rho_n}} T \quad (6)$$

Where the subscripts  $n$  and  $p$  denote the properties of the  $n$ - and  $p$ -type materials, respectively and  $\rho$  is the material electrical resistivity. This equation gives important criterions for the selection of materials for thermoelectric applications: a thermoelectric material should have a large seebeck coefficient to produce high voltage, a large electrical conductivity to minimize joule heating and a low thermal conductivity to retain the heat at the hot junction and maintain the thermal gradient across the device. However, an increase of  $\sigma$  is accompanied by a decrease of  $\alpha$  and an increase of  $\lambda$ . Consequently, obtaining a maximum  $ZT$  requires a compromise between these three quantities and the optimization is achieved for heavily doped semiconductors [5]. Figure 11 presents the evolution of  $ZT$  with temperature for some thermoelectric materials. This figure shows that most of the thermoelectric materials have a  $ZT$  around unity. The maximum value of  $ZT$  for  $\text{Bi}_2\text{Te}_3$  is obtained around 300K which makes it a good candidate for applications at room temperature. At the opposite,  $\text{PbTe}$  and  $\text{SiGe}$  have a maximum  $ZT$  at temperature around 650K and 1000K respectively which make them suitable for medium and high temperatures respectively. Figure 12 shows that bismuth telluride has the highest Carnot efficiency in comparison with other materials at ambient temperatures (around 300K) and until 200°C.

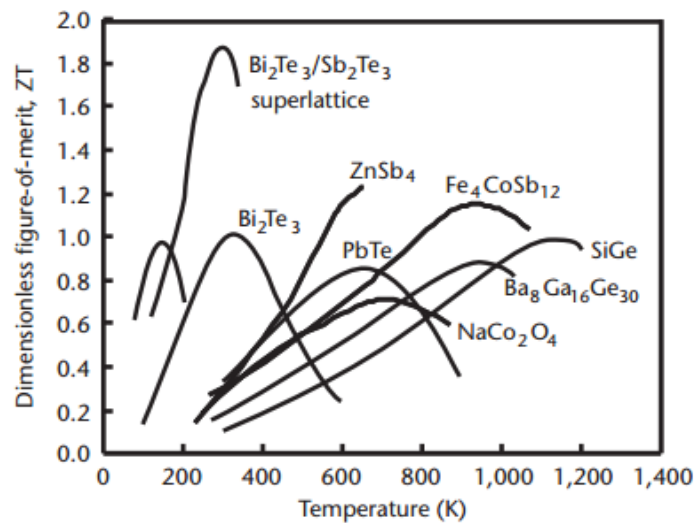
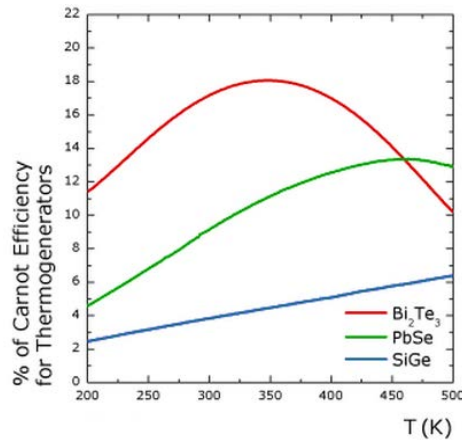


Fig. 11. Dimensionless figure of merit for some thermoelectric materials [5].

The efficiencies of thermoelectric generators have remained low for the past 50 years as commercial converters currently operate at an efficiency of less than 6%. ZT is the main factor that limits the conversion efficiency of these devices and the search for high ZT materials is the key challenge in thermoelectric research. The design of a thermoelectric generator include not only the selection of the appropriate materials but also the formation of high quality electrical and thermal contacts and the optimization of the device geometry. More details on these last optimization steps can be found in [1,5,9].



**Fig. 12.** Percentage of Carnot efficiency of different materials in function of temperature.

In the next part, we benchmark a thermoelectric module from Micropelt and made of that material.

## 1.2. State of the art of seebeck energy harvesters

This thesis is dealing with a thermal energy harvester developed by STMicroelectronics based on bimetallic strip heat engines and piezoelectric membranes. Before presenting the HEATec project and the energy harvester itself, we will first present the thermal and electrical properties of a thermoelectric energy harvester developed by Micropelt. The goal of this part, is to experimentally extract the properties of one of the energy harvesters developed by this company and to access to some data that are not available in the device datasheet. The final purpose is to compare the thermoelectric properties with those of the HEATec thermal energy harvester.

Micropelt is a German company developing a new generation of thermoelectric thin film devices in order to satisfy the design demands on a micrometer scale. To do so, microelectronic thin film technology and manufacturing methods are employed to realize these devices. The thermoelectric elements in Micropelt thermogenerator consist of n-type and p-type semiconductor materials, which are separately produced on two different wafers. The wafers are then sawed and finally the n-part and the p-part are bonded together to create a thermoelectric generator.

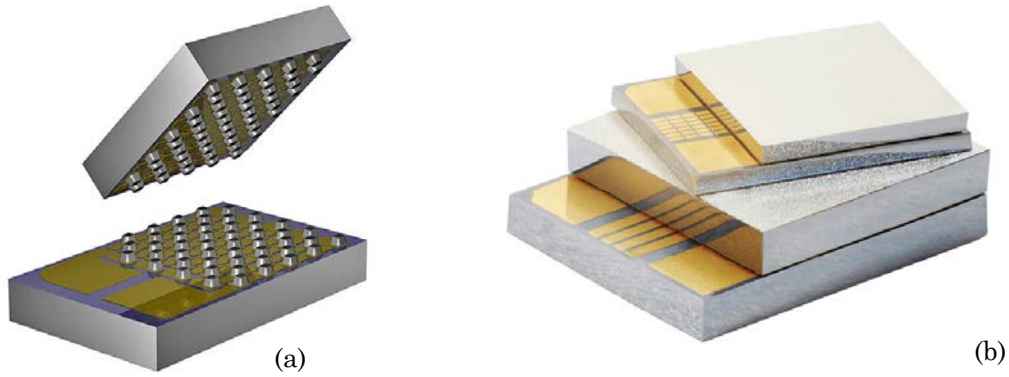


**Fig. 13.** (a). View of the internal architecture of a thermoelectric energy harvester developed by Micropelt, (b). Thermoelectric thin film energy harvesters developed by Micropelt [38].

The manufacturing process used to fabricate these generators uses microelectronic techniques. Standard silicon wafers with silicon dioxide are used as a substrate. The thermoelectric  $\text{Bi}_2\text{Te}_3$ -materials are deposited via sputtering. Finally, n-wafers and p-wafers are structured by dry etching.

Wafers are sawn into single n- and p-type dies. Finally, the n-part and p-part are soldered together to realize a Micropelt thermoelectric energy harvester (TEH).

The voltage (U) generated by a thermogenerator is directly proportional to the number of leg pairs (N), to the temperature difference ( $\Delta T$ ) between top and bottom sides of the generator and to the Seebeck coefficient ( $\alpha$ ). Equation 7 gives the obtained output voltage of a thermoelectric energy harvester V.

$$V = \alpha \cdot \Delta T \cdot N \quad (7)$$

With the technology developed by Micropelt, it is possible to have more than 100 legs per millimeter square as shown in Figure 14. For these devices, the material bismuth-telluride has a thickness of 40  $\mu\text{m}$ . Figure 15 gives the dimensions of the thermoelectric generator MPG-D751 used here. The miniaturized dimensions of this generator makes it ideal for ultra-compact equipment. Due to its 540 thermoelectric leg pairs, the MPG-D751 outputs an open circuit voltage of 110 mV/K, which enable extremely efficient voltage converter solutions (DC-Booster) and operation at very low temperature differences even at 5 degrees Celsius [39]. The TEH has a thermal resistance of 18K/W and an electrical resistance of 250 Ohms.

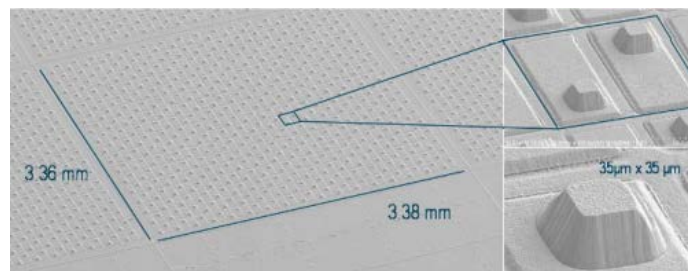


**Fig. 14.** Thermoelectric microstructure and number of legs available per millimeter square in the thin films thermoelectric generators developed by Micropelt [39].

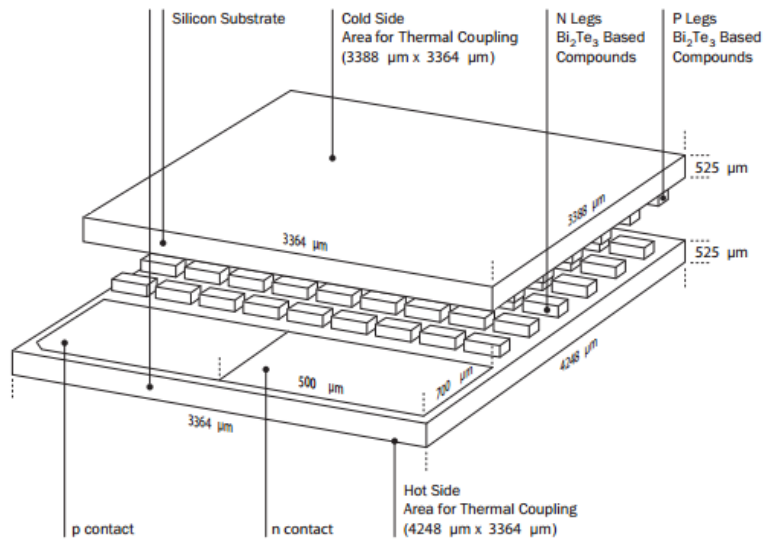


**Fig. 15.** Dimensions of the thermoelectric generator MPG-D751 [39].

This thermoelectric generator have been integrated to a thermogenerator in package the TE-Core 7 [40]. This module converts locally available wasted heat and delivers an output voltage of 2.4V because the TE-Core 7 integrates a power management circuit and an energy storage system (a buffer capacitor). This module is shown in Figure 16.



**Fig. 16.** (a). Composition of the thermoelectric energy harvesting module TE-Core from Micropelt, (b). TE-Core 7 with a heat sink.

Figure 17 shows a detailed view of the TE-Core 7 presented in Figure 16 and the position of the thermoelectric generator MPG-D751 in the package module.

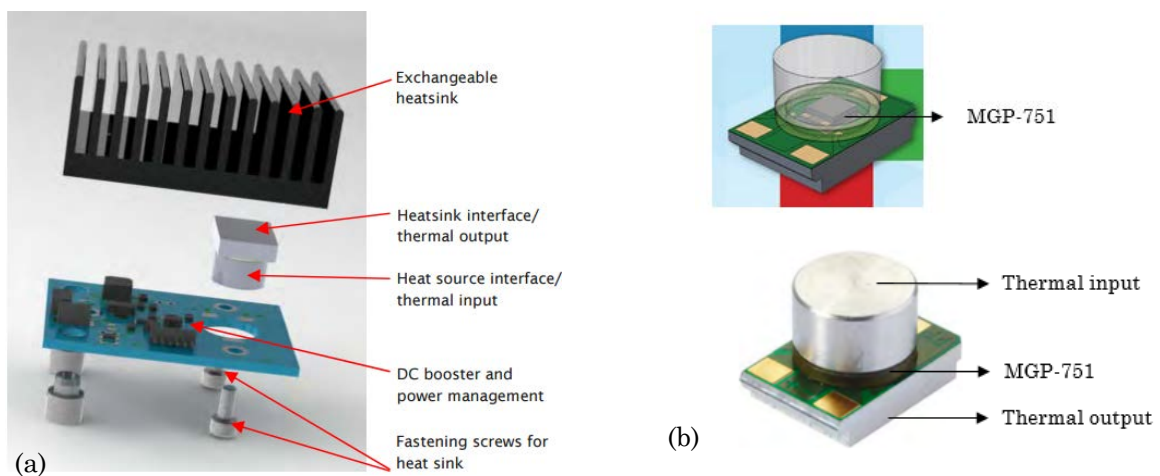


**Fig. 17.** (a). TE-Core exploded view, (b). Position of the MGP-751 in the thermoelectric harvesting module.

In order to be able to compare the performances of HEATec modules and the devices developed by Micropelt, we benchmarked the TE-Core7. To do so, we have characterized thermally and electrically the TE-Core7 with a heat sink to compare the measures with the data available in the datasheet. Then, the same measurement is realized without the heat sink and a comparison of the module with and without the heat sink are confronted. Finally, the thermoelectric module with its both thermal input and output parts is extracted from the electronic board and its thermal properties are measured. In fact, to compare our coupled piezoelectric and bimetal energy harvester with thermoelectric energy harvesters, it is compulsory to have no heat sink and no board. The reasons behind this will be explained further in this part.

*Thermal and electrical characterization of the thermoelectric generator of the TE-Core7 module with a heat sink*

For this characterization step, the power management circuit implemented in the TE-Core7 is not used in order to measure the open circuit voltage across the thermoelectric generators. A heat sink (ref: Sk 422-33) is disposed over the thermoelectric module as shown in Fig. 16.b. Then, for hot source temperatures going from 40°C and up to 100°C, the thermoelectric open-circuit voltage and the temperature of the cold surface are measured. The measurements are realized using an oscilloscope whose reference is DSO6054A with a 1 MΩ probe. The measure of the cold surface temperature of the thermogenerator is realized using a pyrometer. The experimental setup used for the Micropelt module characterization is showed in Figure 18.

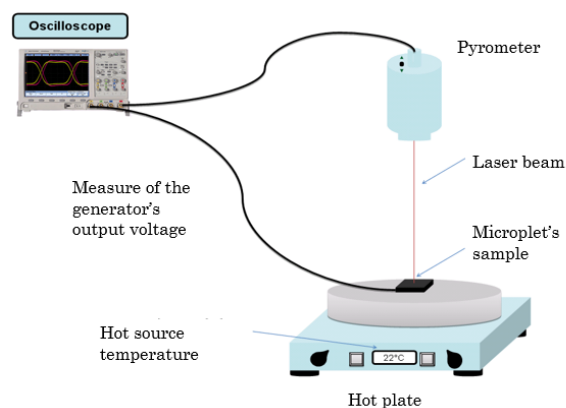


**Fig. 18.** Experimental setup used to characterize the Micropelt module TE-Core 7.

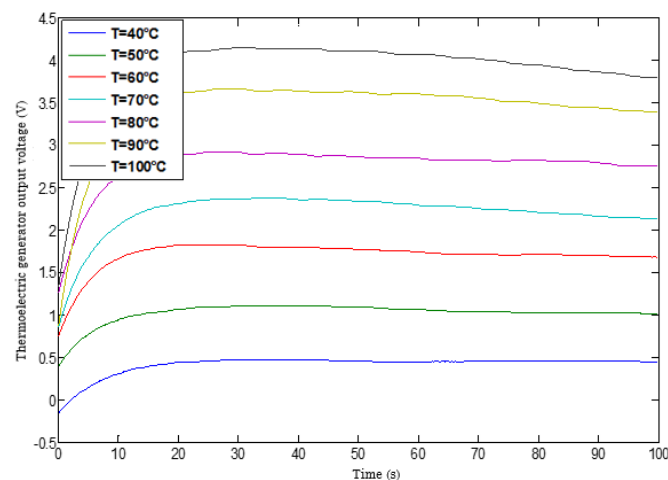


**Fig. 19.** Measurement of the thermoelectric generator output voltage in an open circuit configuration with a heat sink.

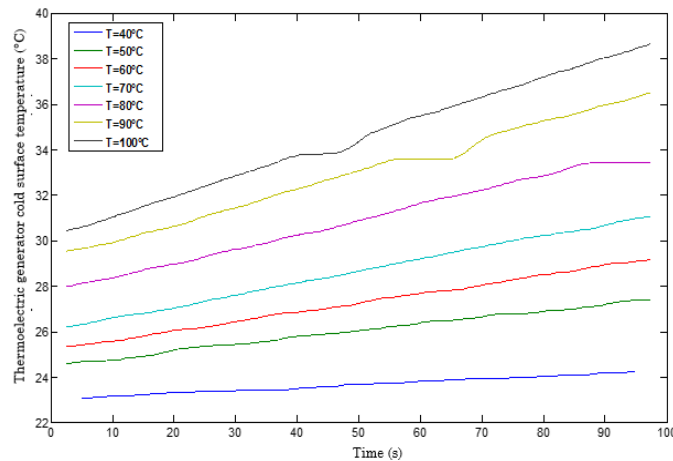


**Fig. 20.** Measurement of the cold surface temperature of the thermoelectric generator (on the heat sink).

Figures 19 and 20 respectively present the evolution of the Microplet's thermoelectric generator output voltage in open circuit and the evolution of the cold surface temperature for various temperatures (40°C - 100°C). In these figures, we observe that the heat sink allows a good keeping of the thermal gradient across the thermal energy harvester. In fact, the output voltage reaches a maximum value in the 15 seconds following the beginning of the measurement and is stabilized after that. It reaches a value of 3,8V for a hot source temperature of 100°C. The slow decrease in the maximum output voltage can be explained by the increase in the cold surface temperature as seen in figure 20. For hot source temperatures going from 40°C to 100°C, the cold surface temperature increases respectively of 1°C and 8°C.

#### *Characterization of the thermoelectric generator of the TE-Core7 module without heat sink*

To be able to compare the performances of the Microplet's thermoelectric generator with the HEATec energy harvester, it is necessary to characterize the thermoelectric generator without any heat sink. The same measurements as previously are then repeated without the heat sink (the thermoelectric generator mounted on the electronic board). The characterized system is shown in Figure 21. Figure 22 and 23 present respectively the evolution of the device output voltage in an open circuit configuration and the corresponding evolution of the cold surface temperature for hot source temperatures going from 40°C to 100°C.



**Fig. 21.** Image of the thermoelectric generator studied (mounted on the board and without the heat sink).

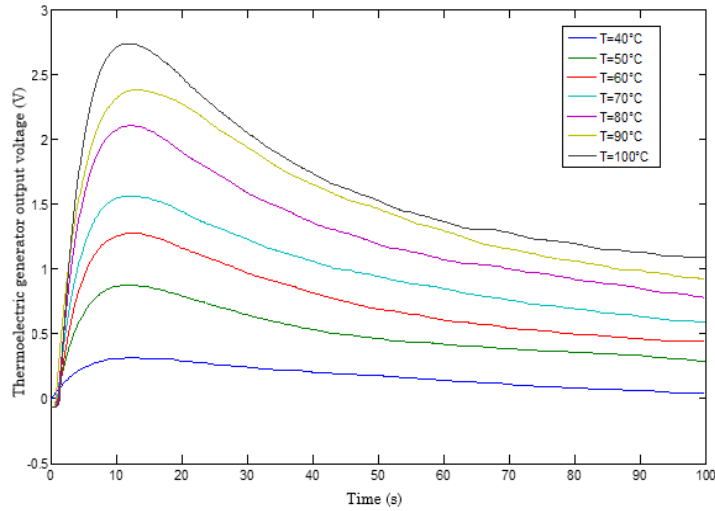


**Fig. 22.** Measurement of the thermoelectric generator output voltage in open circuit without heat sink.

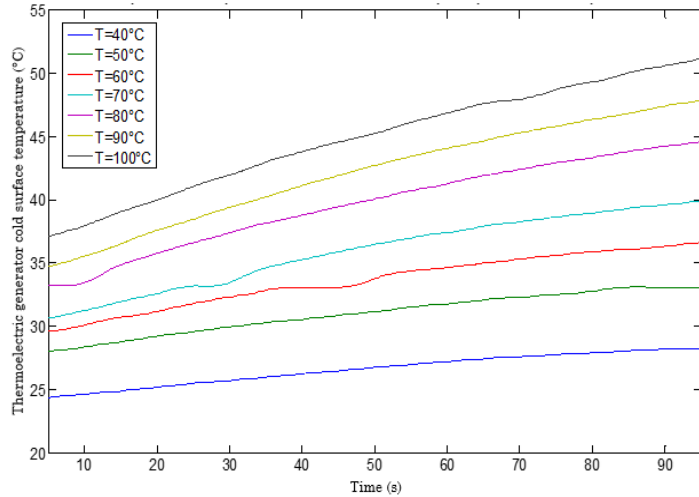


**Fig. 23.** Measurement of the cold surface temperature of the thermoelectric generator without the heat sink.

These measurements show that the heat sink used to evacuate heat has an important effect on the device performances. For hot source temperatures comprises between 40°C and 100°C, the cold surface temperature increases of 4 and 14°C respectively. The effect of such an increase of the cold surface temperature impacts the thermoelectric generator output voltage. Using exactly the same thermoelectric generator, the output voltage increases rapidly when the generator is put on a hot source, but contrary to the case with a heat sink, that voltage decreases very significantly. At a hot source temperature of 100°C, the output voltage reaches 2,7V 15 seconds after the beginning of the experiment and it stabilizes to 1,1V. With a heat sink, the output voltage stabilizes at 3,8V.

To more precisely see the impact of the heat sink on the performances of the thermoelectric generator, we measured the output power on an adapted electrical charge. The electrical resistance of the thermoelectric generator is equal to 250Ω. The output power is then measured across an electrical resistance having this same value. Figure 24 shows the output power measured across that load resistance of 250Ω when the hot source's temperature goes from 40°C to 100°C.

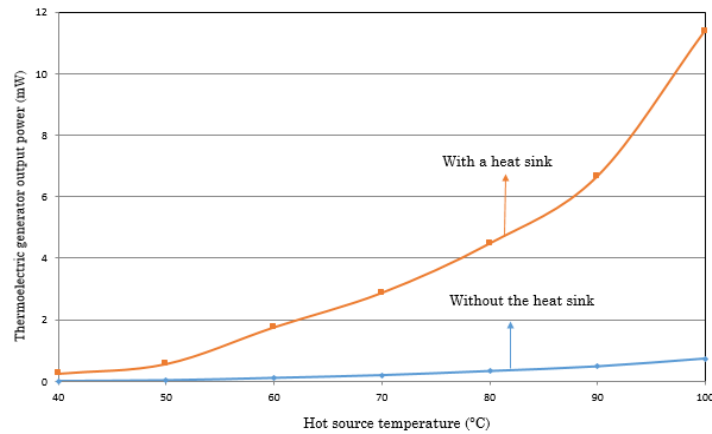


**Fig. 24.** Comparison of the output power of a thermoelectric generator with and without a heat sink.

The graph in Figure 24 shows that the output power is 15 times higher when the thermoelectric generator is used with a heat sink in comparison with the same device without any heat sink. The role of heat sink is to allow the matching of the internal TEH impedance with the impedance of the superficial exchanges. Without it, the impedance matching is no more valid leading to a non-optimized thermal gradient across the TEH.

*Thermal characterization of the thermoelectric generator of the TE-Core7 module without heat sink nor board*

The previous measurements showed that the thermal gradient is still important even without any heat sink. The reason of such a behavior may be the board on which the thermoelectric generator is mounted. To check the validity of this assumption, we extracted the TEG from the electric board and characterized it thermally. We also tried to characterize it electrically by measuring the output power and voltage but no signal was observed on the oscilloscope (a problem with the electrical contacts of the TEG have occurred during its extraction from the electrical board). Figure 17.b shows the TEG characterized on a hot source temperature going from 40°C to 100°C. Figure 25 compares the temperature difference across Micropelt's energy harvester without any heat sink but mounted on a board to the case where it is not mounted on a board and does not have a heat sink. It shows that the board has an important effect on the temperature maintain across the thermoelectric generator as it acts like a radiator: the thermal gradient across the thermoelectric generator is 5 times higher when it is mounted on a board. Figure 26 presents the experimental measures of the temperature difference across the thermoelectric generator from Micropelt and the temperature difference across the thermal energy harvester developed by STMicroelectronics (this system is presented in the next part). We observe that the thermal gradient across the HEATec energy harvester is 1,5 times higher in comparison with the Micropelt thermal energy harvester.

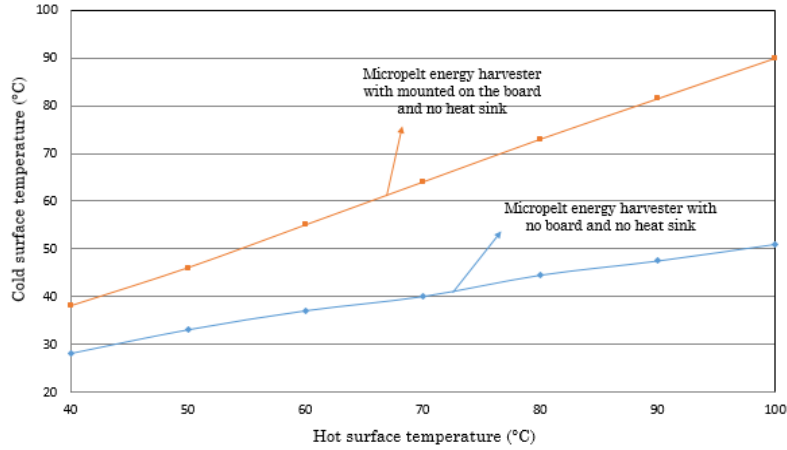


**Fig. 25.** Comparison of the thermal properties of a thermoelectric generator from Micropelt with the thermal energy harvester developed by STMicroelectronics.

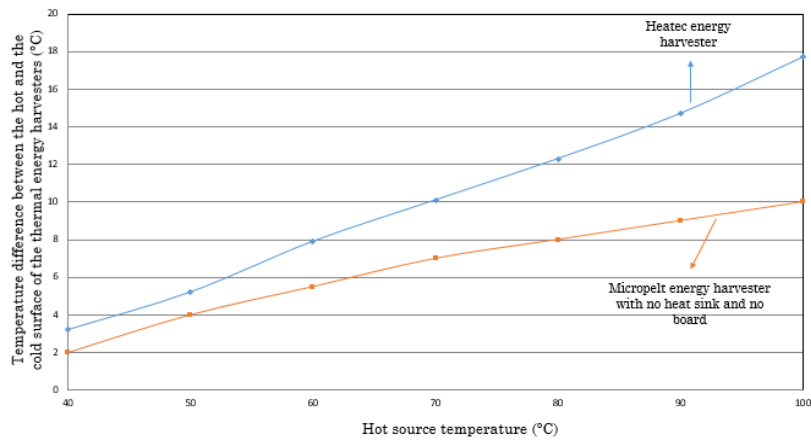


**Fig. 26.** Comparison of the thermal properties of a thermoelectric generator from Micropelt with the thermal energy harvester developed by STMicroelectronics.

From this study, HEATec thermal energy harvesters seem to have good thermal performances in comparison with the thermoelectric generators. It explains why the coupled piezoelectric and bimetallic strips heat engines can be used without any heat sink making it easy to integrate. The next part will then deal with the presentation of the HEATec project with a special focus on the macroscopic thermal energy harvester based on bimetallic strip heat engine and piezoelectric membranes.

## 2. Coupled piezoelectric and bimetal heat engine used in Heatec Project

### 2.1. Presentation of the HEATec project

STMicroelectronics have developed an alternative thermal energy harvester that offers the advantage of overcoming the main issue of thermoelectric generators (TEG). These generators are the most used and efficient thermal energy harvesters known. As previously said, they use solid-state materials exhibiting high electrical conductivities and consequently high thermal conductivities. This property makes it very difficult to maintain a significant temperature difference across the generator especially if the usage temperatures are close to ambient conditions, which leads to the use of heat sinks and thus raises the issue of congestion as it occupies the main part of the harvester [31]. Moreover, devices exploiting Seebeck's effect need

some rare and toxic materials like bismuth telluride ( $\text{Bi}_2\text{Te}_3$ ). To avoid these drawbacks, thin and flexible modules capable of harvesting heat flows and available thermal gradients, including those close to ambient temperature, without any heat sink, were developed based on the patent by Skotnicki [41].

The technology developed by STMicroelectronics is based on thermal spatial gradient energy harvesting thanks to bistable bimetals. A bimetal is composed of two metals one having a high coefficient of thermal expansion (CTE) and the other one having a low CTE. This makes them bend when subjected to temperature variations. Initially, this asymmetry of the membrane's thermal properties is not sufficient to produce a bistable behavior, but, as explained by Wittrick in the case of bimetallic shells [42], combining the membrane with another kind of asymmetry involving an antagonistic effect such as an initial curvature, makes it possible to observe the occurrence of a mechanical instability, characterized by the existence of a thermal hysteresis. When the bimetal's temperature raises and reaches the snap temperature  $T_s$ , the bimetal switches from an unstable state to a stable state, releasing part of its thermal strain energy under the form of kinetic energy. Once the bimetal has snapped, if its temperature decreases and reaches the snap-back temperature  $T_{SB}$  (with  $T_{SB} < T_s$ ), the membrane switches back to its initial state, while releasing kinetic energy. This working principle is well known and frequently used in boilers for example. Such bimetallic strip beams are used in the HEATec project to ensure the conversion of thermal energy into mechanical energy. The basic idea is to place the bimetallic strip between a hot and a cold source so as to create a constant instability of the bimetallic strip constantly switching from one source to the other one. This first transduction step is followed by another transduction in order to convert the bimetal's mechanical energy into electrical energy. To do so, piezoelectric or electrostatic transducers can be coupled to the bimetallic strips.

Up to now, two macroscopic bimetallic strip heat engines were developed by STMicroelectronics. Puscasu worked on the piezoelectric transduction to convert the bimetal's impacts on a piezoelectric transducer into electricity during his thesis [43-46]. He realized the first proof of concept of thermal energy harvesters based on bimetals and piezoelectric membranes capable of working without needing any bulky heat sink. This work was realized in collaboration with LGEF, CEA Liten and Delta Concept. For this proof of concept, the used bimetal snaps up at  $122^\circ\text{C}$  and down at  $117^\circ\text{C}$  with an area of  $6.5\text{ cm}^2$ , and a  $0.6\text{ mm}$  thickness. Figure 27 presents the developed device with its corresponding electrical signal. The bimetals used for such prototypes are made of Invar-NC4 acting as a passive layer and NC4 as an active material. Per bimetal snap, an electrical energy of  $5\mu\text{J}$  is measured which corresponds to an average power of  $1,25\mu\text{W}$  per device.

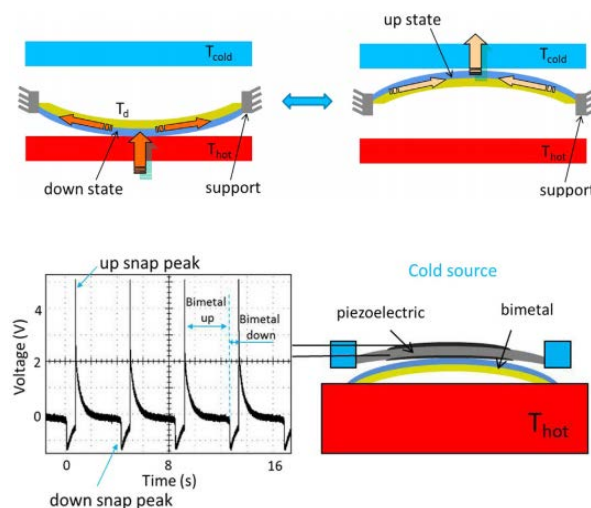


**Fig. 27.** Coupled piezoelectric and bimetallic strip heat engine working principle with the different states of the bimetal and the output electrical signal [46].

A second type of generator based on bimetallic strip heat engines coupled with an electret-based capacitive transducer was jointly developed with CEA-Leti's R&D teams and Delta-Concept (Fig. 28). In that case, the capability of generating electric energy from heat flux is not linked to the kinetic energy released by the switching bimetallic strips, but to the capacitance variations caused by the curvature reversal of the bistable membrane. The operation and performances of these electrostatic bimetallic strip heat engines are reported in [47-48]. Using Invar-B72M bimetallic strips (hysteresis temperatures of 47°C and 43°C) and FEP-based electrets (25  $\mu\text{m}$ -thick layer) having a surface potential of 500 V, these devices generate output power of around 5  $\mu\text{W}$  at 2 Hz of working frequency. Experimental demonstration of their capability to power sensing nodes was demonstrated in [48]. Until now, difficulties were encountered to operate electrostatic generators without bulky heat sink, linked to the absence of thermal optimization of this kind of device.

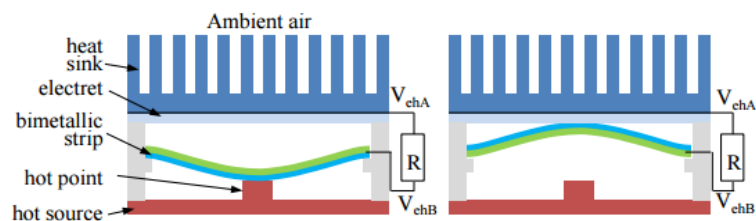


**Fig. 28.** Bimetal and electret based thermal energy harvester [47].

Based on scaling rules predicting a linear improvement of the surface density of generated power at the microscale [45-46], two parallel thesis projects were launched in order to integrate micro bimetallic strip heat engines on silicon wafers using MEMS fabrication techniques. A first approach was to process thermo-mechanically bistable piezoelectric bimorphs in order to directly transform heat into electrical energy without decreasing the overall efficiency of the energy harvester, by multiplying the number of conversion steps. This work was realized by Trioux during her PhD and involved a collaboration between the Ceramics Laboratory LC of EPFL University at Lausanne and TIMA laboratory at Grenoble [49-51]. She demonstrated the generation of electrical charges due to the thermo-mechanical instability of Al-AlN bimorph beams.

The second approach, developed through a collaboration between STMicroelectronics, G2ELab and CEA-Leti consists in directly scaling down the electrostatic bimetallic strip heat engine to the sub-millimetric scale by developing a microelectronics process fully compatible with the facilities of the 300 mm clean room of STMicroelectronics. This work was realized by Arnaud during his thesis [52-54]. Arnaud developed models based on non-linear mechanics to find the conditions under which bimetallic strips, and more generally laminated strips, become thermally bistable. These results were used to study the first-order phase transitions associated to bimetal snap and snap-back and to theoretically demonstrate the possibility to convert heat into mechanical energy using bistable bimetal. This allowed to find analytical expressions of the performances of bimetallic strip heat engines (available energy per cycle, absolute efficiency, Intrinsic Carnot efficiency, available mechanical power) as function of their physical properties and geometries and external conditions such as heat sources' temperatures or use or not of bulky heat sink. He also developed models to describe tertiary pyroelectric effect appearing when a pyroelectric/piezoelectric materials is directly deposited on a bistable bimetallic strip, performances and operation of heat engines coupled with an electret transducer, and coupling between a piezoelectric oscillator and a bimetallic strip, showing that best performances

are obtained with pyroelectric coupling. He then applied these results to design bimetallic strips at the microscale, based on Puscasu's scaling law but demonstrated that this law was invalid, mainly because the evolution of the working frequency is slower than previous (only L-scaling), that the energy produced by a single device becomes too small to be individually harvested, and that available thermal gradient in the cavity becomes very small and reduces the chances of fabricating fully integrated generator at the microscale (bimetallic strip and electro-mechanical transducer), even if it is possible to fabricate bistable structures. Despite these results, he achieved to fabricate some bistable bimetallic strips made of aluminum and silicon oxide.

## 2.2. Presentation of the device studied in this thesis

This thesis follows the first thesis realized by Puscasu on thermal energy harvesting through bistable bimetals and piezoelectric membranes. The heat engine presented here uses a shell-like bimetal made from Invar (Fe-Ni 36%) acting as the low coefficient of thermal expansion (CTE) layer and from NC4 (Fe- Ni 22%-Cr 3%) acting as the high CTE layer. Figure 29 presents the used bimetals for these harvesters. Since the bimetal converts heat into kinetic energy, it is coupled with a piezoelectric transducer turning mechanical energy into electric energy, as presented in figure 30. The energy is harvested when the bimetal snaps and hits the transducer and also when the bimetal releases the transducer as it switches back. To harvest this energy, the latter must be set in a configuration of constant instability. This temporal instability is ensured by placing the unsnapped membrane in contact with the hot source having a temperature higher than its snap temperature. This way, the membrane is heated and switches to its up-state where it comes into contact with the transducer acting as a cold source. Then, the membrane is cooled down to the temperature at which it switches back to its initial state.

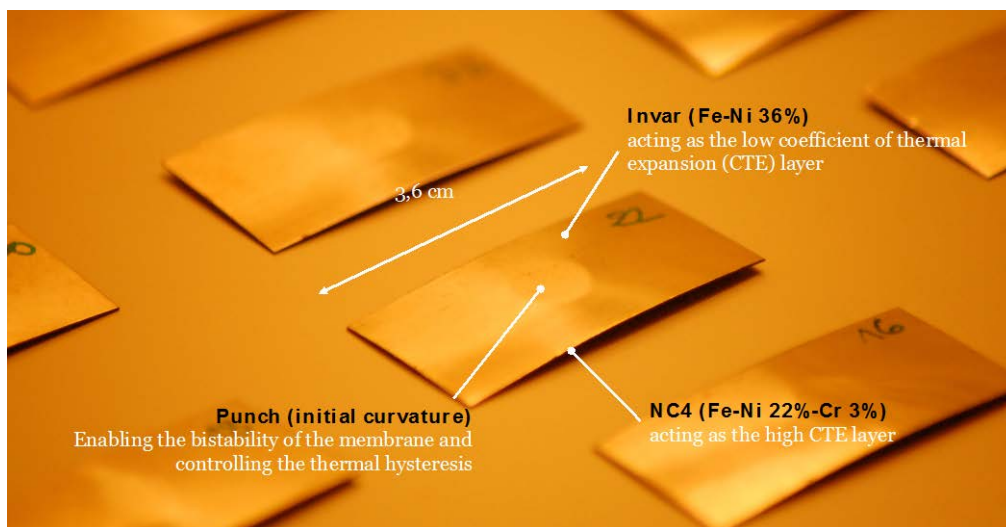


**Fig. 29.** Image of Invar-NC4 bimetallic strip fabricated by Delta Concept and used in the piezoelectric generator.

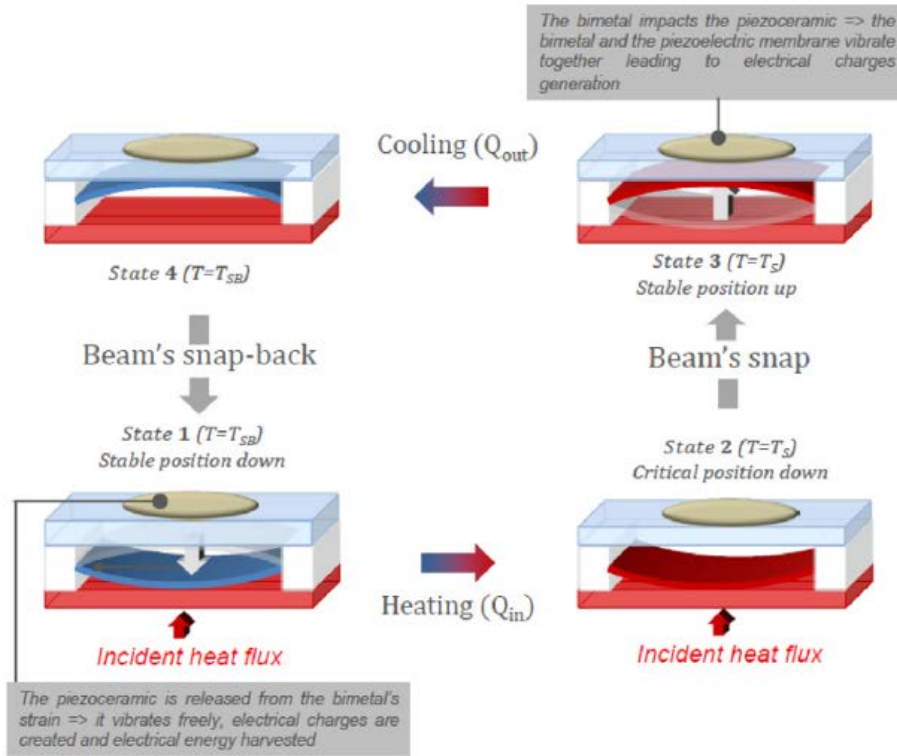


**Fig. 30.** Coupled piezoelectric and bimetal energy harvester working principle.

### 2.2.1. Thermo-mechanical conversion by bimetallic strip heat engine

To understand how it is possible to harvest energy by means of bimetals, it is first necessary to explain the origins of their thermo-mechanical bistability. To do so, we must explain what buckling is. This effect was first modeled by Euler in the case of perfectly straight beams. It corresponds to the loss of stability of a structure submitted to a compressive in plane load  $p$  which causes the bifurcation of the beam from an unstable equilibrium position to a stable one; this is accompanied by out of plane displacement. The beam is considered to have a thickness  $t$ , a length  $L$ , a Young modulus  $E$ , a cross section  $A$ , an inertial moment  $I$  and a shape  $w$ . Euler demonstrated that the action of the axial load produces a strain in the straight beam given by equation 8 and the equilibrium equation of the beam is described by equation 9.

$$p = E \cdot A \cdot \varepsilon \quad (8)$$

$$E \cdot I \cdot w_{,xx} + p \cdot w = 0 \quad (9)$$

With this equation, Euler showed that the simply-supported beam remains straight until the load  $p$  reaches the value, known as the first Euler load (equation 10), corresponding to the eigenvalue of equation 9. When the load  $p$  equals the Euler load, the beam can bend, taking the shape of a half-sine wave (equation 11). Figure 31.b shows the evolution of the compressive load  $p$  as a function of the strain  $\varepsilon$  and Figure 31.c shows the evolution of the corresponding beam's deflection and the pitchfork bifurcation of the straight beam.

$$w(x) = 0 \text{ if } p \leq E \cdot I \cdot \frac{\pi^2}{L^2} = p_{Euler} \quad (10)$$

$$w(x) = w_1 \cdot \sin\left(\frac{\pi}{L} \cdot x\right) \quad (11)$$

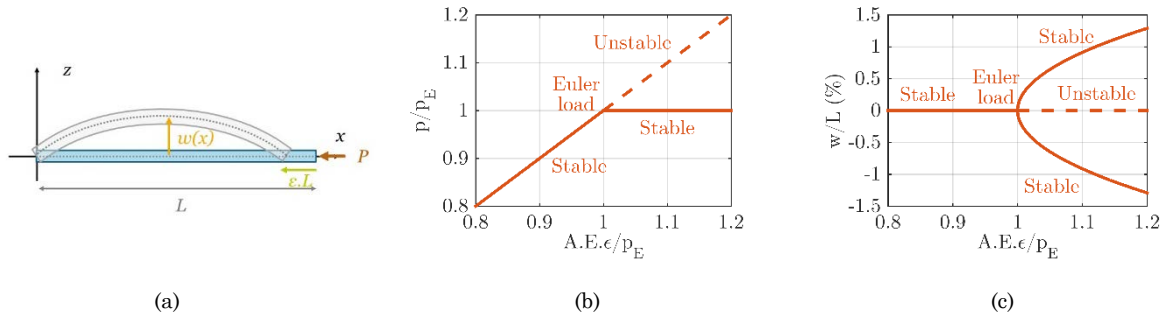


**Figure 31.** *a. Illustration of the buckling of a straight beam. b. Evolution of the compressive load  $p$  as a function of the strain  $\epsilon$ . c. Evolution of the beam's deflection and pitchfork bifurcation of the straight beam [52].*

Contrary to the behavior of perfectly straight beams and plates made of a single material following a pitchfork bifurcation when buckling, the behavior of composite or initially curved structures is different. The mechanical response of these structures to an external stress can be greatly affected by these properties, and their behavior tend to diverge from the behavior of perfectly straight and homogeneous structures. In the case of a beam with an initial curvature with an axial load, the beam curves in the direction fixed by its initial imperfection before reaching the Euler load.

The same observation is made in the case of inhomogeneous structures under the effect of spatially-homogeneous temperature variations. As the thermal expansion is not the same across the structure's thickness, a thermal moment  $M^T$  appears which behaves like an imperfection. The buckling behavior of initially-curved beams and composite structures is showed in Figure 33.

Snap-through is a form of buckling that is characterized by a sudden jump of the structure from an equilibrium position to another. Snap-through can be observed when two imperfections have antagonistic effects on the behavior of a structure. It can be a consequence of the thermal stress acting on a curved beam. Figure 32 presents a bimetallic beam made of two layers having different coefficients of thermal expansion and an initial curvature  $a_0$ . The first explanation of this type of thermal snap-through is due to Timoshenko who modeled the instability of bimetallic thermostats in [59]. In this article, he demonstrated that the curvature caused by the difference of thermal expansion of the two layers of a bimetallic beam produces a curvature  $\rho$  verifying equation 12 where  $\alpha_1$  and  $\alpha_2$  are the coefficient of thermal expansion of the two layers constituting the beam,  $t$  its thickness and  $T$  the temperature.

$$\frac{t}{\rho} = \frac{3}{2} \cdot (\alpha_2 - \alpha_1) \cdot T \quad (12)$$

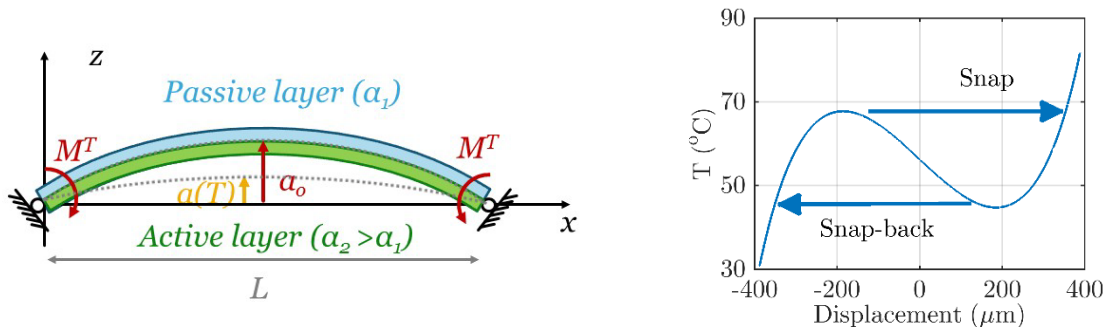


**Figure 32.** *a. Illustration of a bimetallic beam made of two layers having different coefficients of thermal expansion and an initial curvature  $a_0$ . b. Snapping behavior of the beam following Timoshenko model [52].*

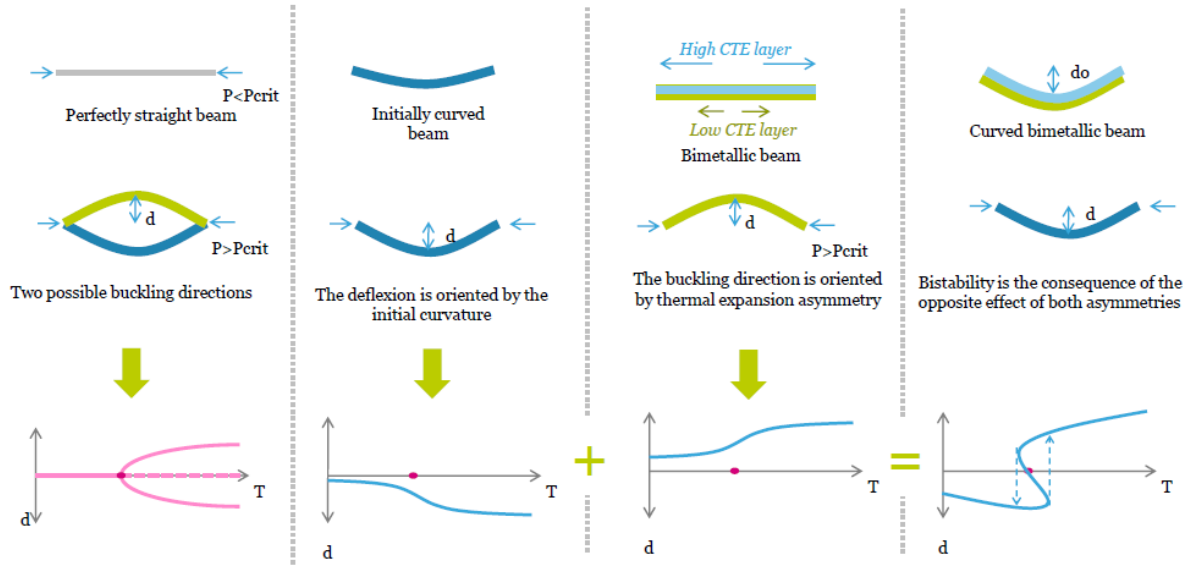
Timoshenko found that such a bimetallic beam can be bistable if its initial deflection is superior to its thickness according to equation 13. In that case, the temperatures at which the beam snaps and snaps back are given by equation 14 and 15.

$$1 - \frac{4.I}{a_o^2.A} > 0 \Leftrightarrow a_o > \frac{t}{\sqrt{3}} \quad (13)$$

$$T_S = \frac{16}{3} \cdot \frac{a_o t}{L^2 \cdot (\alpha_2 - \alpha_1)} \left( 1 + \frac{2 \cdot \sqrt{3} a_o^2}{t^2} \cdot \sqrt{\left( 1 - \frac{t^2}{3 \cdot a_o^2} \right)^3} \right) \quad (14)$$

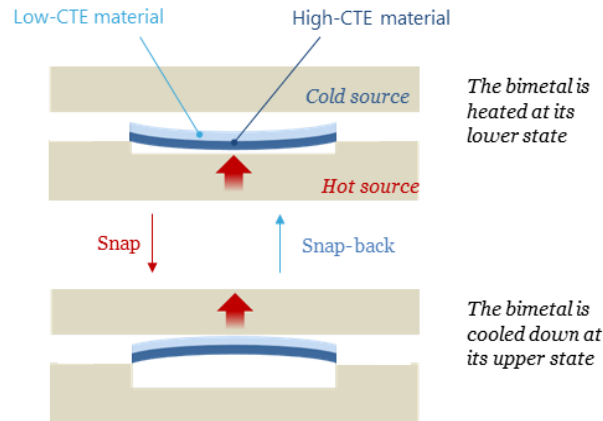
$$T_{SB} = \frac{16}{3} \cdot \frac{a_o t}{L^2 \cdot (\alpha_2 - \alpha_1)} \left( 1 - \frac{2 \cdot \sqrt{3} a_o^2}{t^2} \cdot \sqrt{\left( 1 - \frac{t^2}{3 \cdot a_o^2} \right)^3} \right) \quad (15)$$

Figure 32 shows the corresponding beam and its snapping behavior given Timoshenko's model whereas Figure 33 sums up the phenomenon of beam's buckling. It shows that two antagonistic imperfections are needed to observe a bistable behavior, a thermal asymmetry and an initial curvature.



**Figure 33.** Explanation of the Euler beam buckling.

These two imperfections are used by Delta Concept to fabricate the bistable bimetallic beams that are integrated into HEATec energy harvesters. These bimetals have an initial curvature and are made of two materials of different coefficients of thermal expansion (CTE) (Invar (Fe–Ni 36%) acting as the low CTE layer and NC4 (Fe–Ni 22%–Cr 3%) acting as the high CTE layer. The low CTE layer has a CTE as low as  $1,1 \times 10^{-6} \text{ K}^{-1}$  and the high CTE layer has CTE value as high as  $26,4 \times 10^{-6} \text{ K}^{-1}$ . Figure 34 shows the snapping actions of the bimetal in the inside air cavity of the HEATec energy harvesters.



**Figure 33.** State of the bimetal in the inside air cavity of the coupled piezoelectric and bimetal energy harvester.

Arnaud worked on the modeling of bistable bimetals and the performances of the bimetallic strip heat engines in his thesis [52]. He showed that the absolute conversion efficiency of the generator is an increasing function of the bimetal's thermal hysteresis, whereas their Carnot efficiency decreases in the same time: typically, for bimetals made of Invar and Aluminum having an hysteresis between 1°C and 10°C, the absolute thermo-mechanical efficiency is of around 0,01%, and the Carnot efficiency between 2% and 0,5%.

### 2.2.2. Electromechanical conversion by piezoelectric membrane

Piezoelectricity is the property of some crystalline materials to generate electrical charges due to the application of a mechanical stress. Conversely, if the crystal is placed in an electric field, it experiences a mechanical strain. These effects were discovered by Jacques and Pierre Curie in 1880. Although the magnitude of generated piezoelectric voltages, movements, or forces are small, piezoelectric materials have been adapted to a large range of applications: the piezoelectric effect is used in sensing applications (force or displacement sensors) whereas the inverse piezoelectric effect is used in actuation applications, such as in motors and devices that need to precisely control the positioning [55].

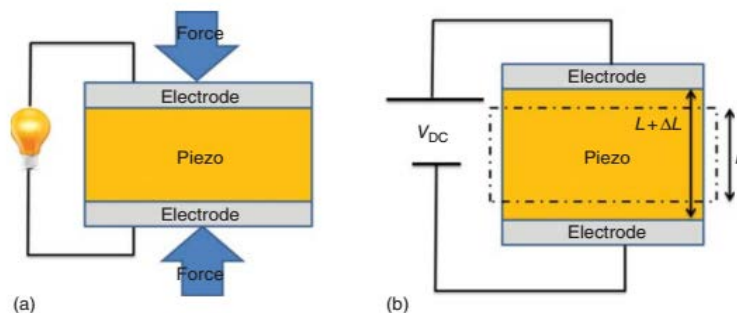


**Fig. 31.** (a). Direct and (b). Inverse piezoelectric effects [22].

Figure 31 presents the direct and the converse piezoelectric effects. Figure 31.a shows that the application of an external force to the piezoelectric material results into the apparition of an electric current flowing through the circuit. At the opposite, Figure 31.b shows the deformation experienced by a piezoelectric material when an external voltage is applied to it., Direct piezoelectric effect is the effect exploited by energy harvesting applications.

For a crystal to exhibit a piezoelectric effect, its structure must have no center of symmetry. When a stress is applied to it, a separation occurs between the positive and negative charge sites in each elementary cell leading to a net polarization at the crystal's surface. The polarization directly varies with the applied stress and is direction dependent so that compressive and tensile stresses generate electric fields and voltages of opposite polarity. Over 32 crystallographic groups, 20 are non-centrosymmetric. The piezoelectric effect is exhibited by a number of naturally occurring crystals among which quartz, tourmaline and sodium potassium tartrate [56]. Consequently, every crystal belonging to one of these groups is piezoelectric. Among these 20 classes, 10 are pyroelectric as they have an electric polarization when the temperature changes. For example, Aluminum nitride (AlN) and zinc oxide (ZnO) are pyroelectric materials. Among pyroelectric crystals, there are some whose spontaneous polarization can be modulated by an electric field. These are the ferroelectric crystals whose polar axis (the preferred direction of polarization) is mobile in the crystal lattice under the influence of an external electrical field. For those materials, it is possible to reverse the direction of remanent polarization if the applied field is sufficiently strong (called a coercive field). The perovskite family, including  $\text{BaTiO}_3$  and  $\text{Pb}(\text{Zr,Ti})\text{O}_3$ , characterizes the ferroelectric materials [57]. Figure 32 gives the different crystal classes.

An important group of piezoelectric materials are the piezoelectric ceramics among which lead zirconate titanate (PZT) is the most commonly used. Its general formula is  $\text{PbZr}_{1-x}\text{Ti}_x\text{O}_3$  and it belongs to polycrystalline ferroelectric materials with the perovskite structure. Inside a ferroelectric material, groups of dipoles with the same alignment are called Weiss domains. These domains are randomly distributed with different alignments inside the material. Consequently, the ceramic exhibits no macroscopic polarization and thus no piezoelectric effect. Such materials are polarized by applying a strong piezoelectric field leading to a rearrangement of the different Weiss domains and the material becomes ferroelectric. Figure 33 shows the arrangement of the Weiss domains of polycrystalline piezoelectric ceramics before and after poling.

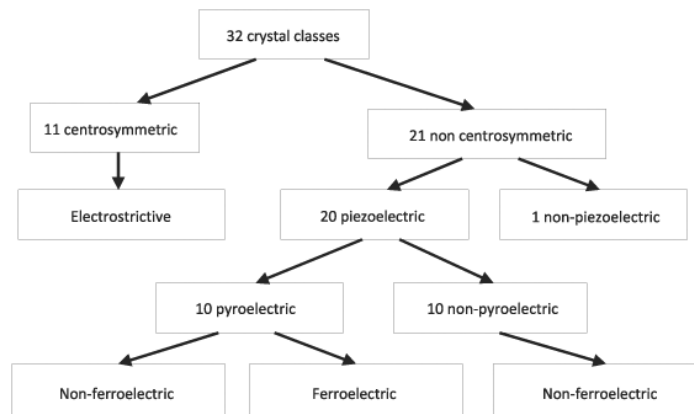


**Fig. 32.** Grouping of crystal classes according to their piezoelectric, pyroelectric, ferroelectric and electrostrictive properties [57].

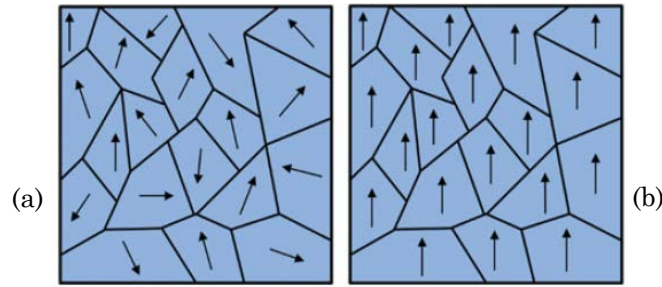


**Fig. 33.** Arrangement of the Weiss domains of polycrystalline piezoelectric ceramics (a). Before and (b). After poling [58].

Ferroelectric materials are characterized by the dependence of their properties on temperature. Above a critical temperature called the Curie point, each perovskite crystal in the fired ceramic element exhibits a simple cubic symmetry with no dipole moment. At the opposite, at temperatures below the Curie point, each crystal has tetragonal or rhombohedral symmetry and a dipole moment (Figure 34) [58]. The Crystallite structure of lead zirconate titanate above and below Curie temperature is shown in Figure 34.

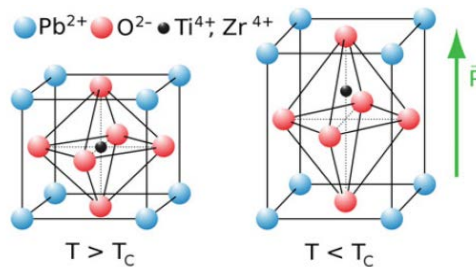


**Fig. 34.** Crystallite structure of lead zirconate titanate material above and below curie temperature  $T_c$  [55].

Another characteristic of poled ferroelectric materials is their hysteretic behavior. Figure 35 shows a typical hysteresis curve created by applying an electric field to a piezoelectric ceramic until the maximum polarization,  $P_s$ , is attained, reducing the field to zero in order to determine the remanent polarization,  $P_r$ , reversing the field to attain a negative maximum polarization and negative remanent polarization, and finally re-reversing the field to restore the positive remanent polarization.

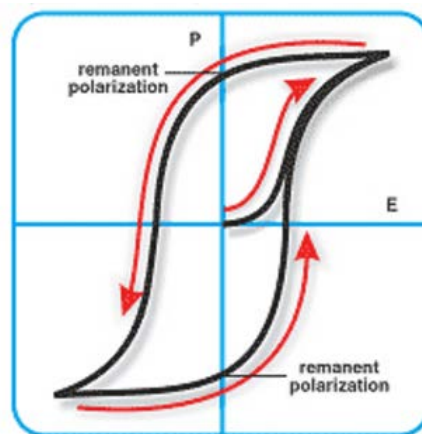


**Fig. 34.** Hysteresis curve for the polarization of a ferroelectric material [55].

A review of the different piezoelectric materials is presented in Chapter 3 and so does the constitutive equations describing the piezoelectric effect in Chapter 5.

Generally, a piezoelectric material is characterized by:

- The piezoelectric charge coefficient  $d_{ik}$  which measures the charges density per unit stress or the strain per unit electrical field. The double subscript links the electrical and mechanical quantities, the first subscript gives the direction of the electrical field associated with the voltage applied or produced whereas the second subscript gives the direction of the mechanical stress or strain.
- The piezoelectric voltage coefficient  $g_{ik}$  which is a measure of the field per unit stress or strain per unit charge density. The first subscript indicates the direction of the generated voltage and the second one indicates the direction of the force.
- The Young modulus that characterizes the stiffness of the material as it represents the ratio of stress to strain.
- The dissipation factor or loss tangent that measures the dielectric losses in the material.
- The piezoelectric coupling coefficient also named electromechanical coupling coefficient that describes the conversion of electrical energy into mechanical one or the opposite.
- The mechanical quality factor that characterizes the quality of the ceramic as a harmonic oscillator. The mechanical quality factor is inversely proportional to material's mechanical quality factor.
- The Curie point characterizes the temperature at which the crystal structure of the material changes from a piezoelectric to a non-piezoelectric state. This explains the reason why a piezoelectric material should operate below the Curie temperature.

#### IV. Objective of this thesis

This thesis manuscript is divided into five chapters starting with a state of the art of energy harvesting technologies motivations and wireless sensor nodes development and applications. The main energy harvesting technologies are briefly reviewed in this introduction with a special focus on thermal energy harvesting. In this context, a detailed benchmark of a thermoelectric generator from Micropelt is presented and the device developed by STMicroelectronics and which is studied in this thesis is exposed.

Chapter 2 presents the thermal modeling work and experiments realized on the coupled piezoelectric and bimetallic strip heat engine. The first step deals with its static thermal modeling using the analogy between thermal and electrical quantities. Then, a dynamic model taking into account the bimetal as a switched capacitance is presented. These models allow a better understanding of the thermal phenomenon occurring in the harvester and its thermal properties improvements.

Chapter 3 is devoted to the improvement of the energy harvester's design and architecture as well as its materials. The different kinds of piezoelectric materials used for energy harvesting applications are reviewed and compared to point out the most adapted ones for our application. Then, different energy harvester's architectures are proposed and studied: a complete benchmark is presented depending on the bimetals to be used, the position and the boundary condition of the piezoelectric membranes and even the size of the harvester. Finally, after comparing all the developed architectures, the most powerful one is pointed out and aging tests are realized on it.

Chapter 4 presents alternative ways to harvest heat based on bimetallic strip heat engines and piezoelectric materials. To do so, both direct deposition of piezoelectric composites and piezoelectric thin films on bimetals are investigated. The fabrication process of each of these materials is exposed as well as the experimental tests carried on the obtained samples. Moreover, a dual energy harvester realizing at the same time vibrations and thermal energies harvesting is

presented. To do so, a finite element modeling is realized to design numerous piezoelectric cantilevers to harvest the most frequent vibrations in our environment.

Chapter 5 finally deals with the integration part of the thermal energy harvester studied in this manuscript. To do so, an equivalent SPICE model of the harvester taking into account the two consecutive transductions occurring in the device is presented. Then, this model is used by CEA and STMicroelectronics designer's team to realize power management simulations of the harvester's output signal. To end this work, numerous wireless sensor nodes demonstrations are carried out using various communication protocols to validate the ability of our energy harvester to power such nodes.

The manuscript concludes with a general conclusion summarizing the results obtained and giving the perspectives.

## V. References

- [1] Knight, Chris, Joshua Davidson, and Sam Behrens. "Energy Options for Wireless Sensor Nodes". *Sensors* 8.12 (2008): 8037-8066.
- [2] Zahid Kausar, A.S.M. et al. "Energizing Wireless Sensor Networks By Energy Harvesting Systems: Scopes, Challenges And Approaches". *Renewable and Sustainable Energy Reviews* 38 (2014): 973-989.
- [3] Roundy, Shad, Paul Kenneth Wright, and Jan M Rabaey. *Energy Scavenging For Wireless Sensor Networks*. Boston: Kluwer Academic Publishers, 2004.
- [4] Culler, D., D. Estrin, and M. Srivastava. "Guest Editors' Introduction: Overview Of Sensor Networks". *Computer* 37.8 (2004): 41-49.
- [5] Beeby, Stephen and Neil White. *Energy Harvesting For Autonomous Systems*. Norwood, Mass.: Artech House, 2010.
- [6] Buhrig, Aurélien, Marc Renaudin, and Laurent Fesquet. *Optimisation De La Consommation Des Noeuds De Réseaux De Capteurs Sans Fil*. [S. l.]: [s. n.], 2008.
- [7] Kyung, Chong-Min. *Smart Sensors For Health And Environment Monitoring*. Dordrecht: Springer Netherlands, 2015.
- [8] Stojmenović, Ivan. *Handbook Of Sensor Networks*. Hoboken, NJ: Wiley, 2005.
- [9] Priya, Shashank and D. J Inman. *Energy Harvesting Technologies*. New York: Springer, 2008.
- [10] Mitcheson, P.D. et al. "Energy Harvesting From Human And Machine Motion For Wireless Electronic Devices". *Proceedings of the IEEE* 96.9 (2008): 1457-1486.
- [11] Wanless, Derek. *Securing Our Future Health*. [London]: [HM Treasury], 2002.
- [12] Flowerday, Adrian and Robert Smith. "Lessons learnt from Long-Term Chronic Condition Monitoring". Proc. 1st Int. Workshop Wearable Implantable Body Sensor Netw., Imperial College London, U.K., (2004): 48.

- [13] Needham, P. and Gamlyn, L. "Arrhythmia analysis in the community", Proc. 1st Int. Workshop Wearable Implantable Body Sensor Netw., Imperial College London, U.K., (2004): 49–50.
- [14] A. Heller, "Drug delivering integrated therapeutc systems". Proc. 2nd Int. Workshop Wearable Implantable Body Sensor Netw., Imperial College London, South Kensington, London, U.K., (2005): 6–11.
- [15] Knight, Chris, Joshua Davidson, and Sam Behrens. "Energy Options For Wireless Sensor Nodes". *Sensors* 8.12 (2008): 8037-8066.
- [16] Zanella, Andrea et al. "Internet Of Things For Smart Cities". *IEEE Internet of Things Journal* 1.1 (2014): 22-32.
- [17] Lynch, J. P. "A Summary Review Of Wireless Sensors And Sensor Networks For Structural Health Monitoring". *The Shock and Vibration Digest* 38.2 (2006): 91-128.
- [18] Nuortio, T et al. "Improved Route Planning And Scheduling Of Waste Collection And Transport". *Expert Systems with Applications* 30.2 (2006): 223-232. Web.
- [19] 4 Decision No. 406/2009/Ec of the European Parliament and of the Council of 23 April 2009 on the effort of Member States to reduce their greenhouse gas emissions to meet the Community's greenhouse gas emission reduction commitments up to 2020 [Online]. Available: <http://eur-lex.europa.eu/eli/dec/2009/406/oj>.
- [20] Al-Ali, A. R., Imran Zualkernan, and Fadi Aloul. "A Mobile GPRS-Sensors Array For Air Pollution Monitoring". *IEEE Sensors J.* 10.10 (2010): 1666-1671.
- [21] Arnaud Arthur, "Modeling and design of thermomechanical conversion systems for thermal energy harvesting applications", Université Grenoble Alpes, 2016.
- [22] Briand, Danick, Eric Yeatman, and Shad Roundy. *Micro Energy Harvesting*.
- [23] Vullers, R.J.M. et al. "Micropower Energy Harvesting". *Solid-State Electronics* 53.7 (2009): 684-693.
- [24] Guyomar, D. et al. "Toward Energy Harvesting Using Active Materials And Conversion Improvement By Nonlinear Processing". *IEEE Transactions on Ultrasonics, Ferroelectrics and Frequency Control* 52.4 (2005): 584-595.
- [25] Peano, F. and T. Tambosso. "Design And Optimization Of A MEMS Electret-Based Capacitive Energy Scavenger". *Journal of Microelectromechanical Systems* 14.3 (2005): 429-435.
- [26] Glynne-Jones, P. et al. "An Electromagnetic, Vibration-Powered Generator For Intelligent Sensor Systems". *Sensors and Actuators A: Physical* 110.1-3 (2004): 344-349.
- [27] Williams, C.B. and R.B. Yates. "Analysis Of A Micro-Electric Generator For Microsystems". *Sensors and Actuators A: Physical* 52.1-3 (1996): 8-11.
- [28] Zhu, Dibin, Michael J Tudor, and Stephen P Beeby. "Strategies For Increasing The Operating Frequency Range Of Vibration Energy Harvesters: A Review". *Measurement Science and Technology* 21.2 (2009): 022001.

- [29] Harne, R L and K W Wang. "A Review Of The Recent Research On Vibration Energy Harvesting Via Bistable Systems". *Smart Mater. Struct.* 22.2 (2013): 023001.
- [30] Wang, Ziyang et al. "Realization Of A Wearable Miniaturized Thermoelectric Generator For Human Body Applications". *Sensors and Actuators A: Physical* 156.1 (2009): 95-102.
- [31] [http://micropelt.com/downloads/datasheet\\_thermogenerator\\_package.pdf](http://micropelt.com/downloads/datasheet_thermogenerator_package.pdf).
- [31] Leonov, Vladimir, Paolo Fiorini, and Ruud J.M. Vullers. "Theory And Simulation Of A Thermally Matched Micromachined Thermopile In A Wearable Energy Harvester". *Microelectronics Journal* 42.4 (2011): 579-584.
- [33] Leonov, Vladimir. "Thermoelectric Energy Harvesting Of Human Body Heat For Wearable Sensors". *IEEE Sensors J.* 13.6 (2013): 2284-2291.
- [34] Sebald, G., E. Lefeuvre, and D. Guyomar. "Pyroelectric Energy Conversion: Optimization Principles". *IEEE Transactions on Ultrasonics, Ferroelectrics and Frequency Control* 55.3 (2008): 538-551.
- [35] Sebald, G., Guyomar, D. and Agbossou, A. On thermoelectric and pyroelectric energy harvesting. *Smart Mater. Struct.*, 18(12), (2009):125006.
- [36] Guyomar, D., Sebald, G., Lefeuvre, E. and Khodayari, A. Toward Heat Energy Harvesting using Pyroelectric Material. *Journal of Intelligent Material Systems and Structures*, 20(3) (2008): pp.265-271.
- [37] Dalola, S., Ferrari, V. and Marioli, D. Pyroelectric effect in PZT thick films for thermal energy harvesting in low-power sensors. *Procedia Engineering*, 5, (2010): 685-688.
- [38] <http://micropelt.com/technology.php>.
- [39] [http://thermalforce.de/engl/product/thermogenerator/micropelt\\_d751.pdf](http://thermalforce.de/engl/product/thermogenerator/micropelt_d751.pdf).
- [40] [http://www.micropelt.com/down/datasheet\\_te\\_core.pdf](http://www.micropelt.com/down/datasheet_te_core.pdf).
- [41] Skotnicki, T. (2009) Dispositifs de conversion d'énergie thermique en électricité, France Patent FR2951873 (A1).
- [42] Wittrick, W., Myers, D. and Blunden, W. (1953). Stability of a bimetallic disk. *The Quarterly Journal of Mechanics and Applied Mathematics*, 6(1), pp.15-31.
- [43] Puscasu Onoriu, "Dispositifs innovants pour la Récupération d'énergie thermique", Ph.D thesis, INSA de LYON, 2014.
- [44] Puscasu Onoriu et al, "An innovative heat harvesting technology (HEATec) for above Seebeck performance," in Electron Devices Meeting (IEDM), 2012 IEEE international, (2012): 12-5.
- [45] Puscasu Onoriu et al, "A disruptive technology for thermal to electrical energy conversion," in Thermal Investigations of ICs and Systems (THERMINIC), 18th International Workshop on, (2012): 1-3.
- [46] Puscasu, O., Monfray, S., Maître, C., Cottinet, P., Rapisarda, D., Savelli, G., Gaillard, F., Ricotti, G., Ancey, P., Boeuf, F., Guyomar, D. and Skotnicki, T. A disruptive technology for thermal to electrical energy conversion. *Microelectronics Journal*, 45(5), (2014): 554-558.

- [47] Boisseau, S., Despesse, G., Monfray, S., Puscasu, O. and Skotnicki, T. Semi-flexible bimetal-based thermal energy harvesters. *Smart Mater. Struct.*, 22(2), (2013): 025021.
- [48] Arnaud, A., Boisseau, S., Monfray, S., Puscasu, O., Despesse, G., Boughaleb, J., Sanchez, Y., Battegay, F., Fourel, M., Audran, S., Boeuf, F., Delamare, J., Delepierre, G., Pitone, G. and Skotnicki, T. Piezoelectric and electrostatic bimetal-based thermal energy harvesters. *J. Phys.: Conf. Ser.*, 476, (2013): 012062.
- [49] Emilie Trioux "Piezoelectric micro-generators for energy harvesting applications. Micro and nanotechnologies/Microelectronics", Université Grenoble Alpes, 2015.
- [50] Trioux, E., Monfray, S., Skotnicki, T., Basrour, S. and Muralt, P. Characterization of piezoelectric material for micro thermal harvesters. *J. Phys.: Conf. Ser.*, 557(2014):012087.
- [51] Trioux, E., Rufer, L., Monfray, S., Skotnicki, T., Muralt, P. and Basrour, S. Electrical characterization of a buckling thermal energy harvester. *J. Phys.: Conf. Ser.*, 660 (2015): 012106.
- [52] Arnaud Arthur, "Modeling and design of thermomechanical conversion systems for thermal energy harvesting applications", Université Grenoble Alpes, 2016.
- [53] Arnaud, Arthur et al. "Reduced Model For The Comprehension Of The Operation Of A Thermo-Mechanical Energy Harvester". *2015 IEEE 13th International New Circuits and Systems Conference (NEWCAS)* (2015), pp: 1-4.
- [54] Arnaud, A et al. "Thermo-Mechanical Efficiency Of The Bimetallic Strip Heat Engine At The Macro-Scale And Micro-Scale". *J. Micromech. Microeng.* 25.10 (2015): 104003.
- [55] <https://www.americanpiezo.com/knowledge-center/piezo-theory/piezoelectricity.html>.
- [56] [www.morgantechinc.com/sites/default/files/documents/chapter2\\_1.pdf](http://www.morgantechinc.com/sites/default/files/documents/chapter2_1.pdf).
- [57] Defay, E. *Integration of ferroelectric and piezoelectric thin films*. London: ISTE. (2011).
- [58] Hehn, T. and Manoli, Y. *CMOS circuits for piezoelectric energy harvesters*. Dordrecht: Springer. (2014).
- [59] Timoshenko, S. "Analysis Of Bi-Metal Thermostats". *Journal of the Optical Society of America* 11.3 (1925): 233.

## Chapter 2

# Thermal modeling and optimization of the harvester

Chapter 2 .....	36
I. Introduction .....	38
II. State of the art of thermal energy harvesters modeling .....	38
III. Thermal study in steady state conditions .....	41
1. Modeling .....	41
1.1. Simplification of the modeling .....	41
1.2. Analytical model .....	42
1.3. Finite element model .....	45
2. Results and discussions .....	46
2.1. Matrix analysis using the FEM .....	46
2.2. Thermal optimization and design improvement .....	47
2.3. Electrical optimization thanks to thermal improvements .....	49
3. Scaling the devices after their thermal improvements .....	50
IV. Dynamic modeling of the harvester taking into account the bimetal .....	55
1. Purpose of the study .....	55
2. Dynamic modeling .....	56
2.1. Model analysis with the bimetal at its lower position .....	57
2.2. Model analysis with the bimetal in its upper position .....	57
2.3. Estimation of the model parameters: contact resistances and switched capacitances of the bimetal .....	58
3. Dynamic model application .....	59
	36

3.1. Range of hot source functioning temperatures of a bimetal having a certain hysteresis once mounted in the harvester .....	59
3.2. Calculation of the intrinsic snap-up and -down temperatures $T_s$ and $T_{sb}$ of a bimetal mounted in the harvester as a function of the desired minimum hot source temperature $T_{hotmin}$ .....	59
3.3. Calculation of bimetal's maximal snapping frequency.....	60
<b>4. Model experimental validation and interpretation .....</b>	<b>60</b>
4.1. Study of bimetal's hot source operation windows as a function of their hysteresis and of the hot source temperatures .....	60
4.2. Simulations using bimetal's with the same snapping temperature and different thermal hystereses .....	62
4.3. Simulations with different snapping temperatures and a fixed thermal hysteresis.....	63
4.4. Electrical output power as a function of the bimetal's thermal hystereses .....	64
4.5. Analyses of the bimetal snapping temperature shift when it is put alone on a hot plate and once mounted in the harvester.....	65
<b>V. Conclusion .....</b>	<b>65</b>
<b>VI. References.....</b>	<b>66</b>

## I. Introduction

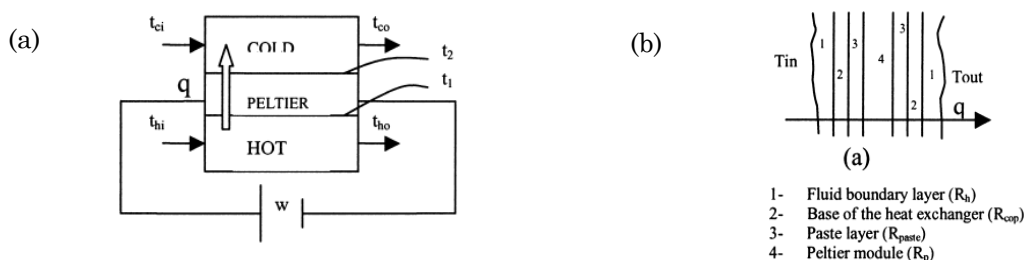
The thermal energy harvester studied in this thesis is based on a bimetallic strip heat engine and a piezoelectric membrane. Each of these components insures a part of the thermo-electrical conversion. As said previously in the introduction, the bimetal realizes the thermo-mechanical conversion step and the piezoelectric membrane transforms the bimetal's mechanical energy into electrical energy. Generally, thermal energy harvesters encounter the problem of fast thermalization in absence of heat management strategies. Some of them like thermoelectric generators based on Seebeck effect use heat sinks to evacuate heat and to maintain an important thermal gradient across the system [1]. In our case, we intend to develop a thin energy harvester able to overcome these limitations. The harvester is bound to be as thin as 6mm to be easiky integrated. To do so, a key point is to understand all the ways by which heat is transferred inside the device and to control them with the goal of keeping a sufficient thermal gradient between the hot source and the cold surface. This chapter is dedicated to the thermal study and modeling of our thermal energy harvester. The work presented hereafter will allow many devices improvements including:

- A good operation of the bimetallic strip and its cycling between the hot source and the cold surface.
- A good sustainability of the piezoelectric properties of the PZT membrane by ensuring that the temperature of the cold surface do not exceed its Curie temperature.

In this chapter, the energy harvester is first thermally modeled in steady-state conditions. Then a dynamic model of the whole system is proposed. The system's architecture is thus improved by applying the main guidelines derived from the thermal model, enabling a more efficient use of heat flowing through the device. Finally, the impact of these optimizations on the system's functioning is studied because it is expected to improve the performances of the harvester.

## II. State of the art of thermal energy harvesters modeling

The study developed in the first part of this chapter is similar to those established for thermoelectric generator. In fact, many researchers already worked on the thermal management in such devices to increase the thermal gradient across it. In [3], J. Esarte have worked on the modeling of different heat exchanges geometries to observe their impact on the temperature difference between the cold and the hot surfaces of his device ( $\Delta T$ ). Going from the general working principle of a thermoelectric generator that consists of a Peltier module sandwiched between two heat exchangers, the author pointed out that many papers have focused on the development and improvement of thermoelectric materials [4,5] but the temperature difference across the device is always supposed to be known and no studies have focused on this point to improve it. A thermal model in steady state conditions of the system is consequently proposed as shown in Fig. 1.



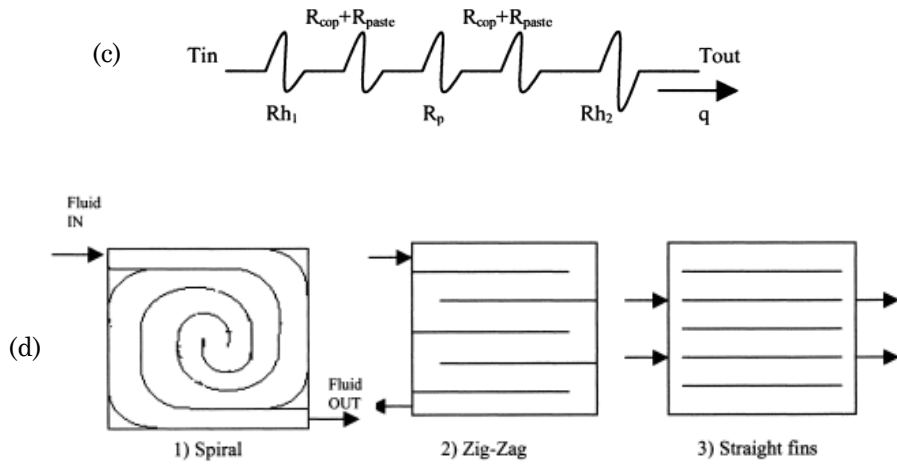


**Fig. 1.** (a) General scheme of a thermoelectric generator, (b) Heat transmission inside the device, and (c) its corresponding electric circuit [3], (d). Different heat exchanger geometries tested in [3].

The next step in that study concerned the heat exchangers geometries and their impact on the available  $\Delta T$ . Many geometrical configurations were compared to find out the one maximizing the convective heat transfer coefficient (Fig. 1.d). In fact, thermoelectric generators are composed of many thermocouples made of semiconductors having good electrical but also thermal properties, so it is compulsory to use a heat sink to generate electricity from a temperature difference.

Other studies have followed the same modeling approach to develop thermoelectric harvesters assuming that neither the temperature difference nor a constant heat flow can be considered constant. V. Leonov in [6-8] have modeled thermally a micro-machined thermopile using the electro-mechanical analogy. In his study, the author estimated the equivalent resistance of the device and compared it to the equivalent resistance of the superficial exchanges with the surrounding to find out the optimized architecture and more specifically the main guidelines for its design improvement. Fig. 2 represents the studied device and its corresponding thermal circuit where  $R_{env}$  is the sum of the thermal resistance between the hot source and the thermopile and the top of it with the heat sink. The goal of that modeling was to find out the configuration of maximum output power. The equivalent resistance of the thermopile was then matched to that of superficial environment to satisfy that condition. Moreover, thanks to that model, the author has been able to investigate the thermal behavior of low-dimensional thermopile after scaling down the initial harvester.

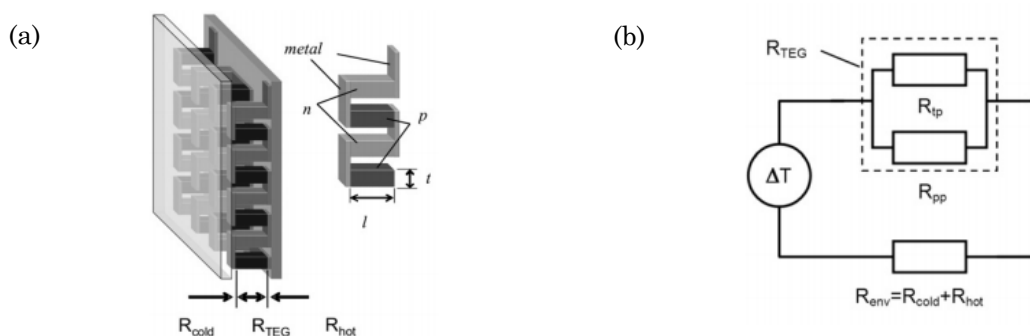


**Fig. 2.** Thermoelectric generator and its corresponding thermal circuit [6].

Z. Wang have worked in [9] on a wearable miniaturized thermoelectric generator for human body applications and health monitoring. The goal was to replace the non-rechargeable batteries by more advantageous energy harvesters in regards of their life time and their autonomy. Knowing that the temperature difference between the human body and the surroundings is not that big (around 10 to 15K) and that the thermal resistance taking into account the exchanges between the human body and the ambient air is bigger than the one corresponding the harvester only, the author have modeled the device thermally to ensure a proper operation of the TEG (thermo-electric generator).

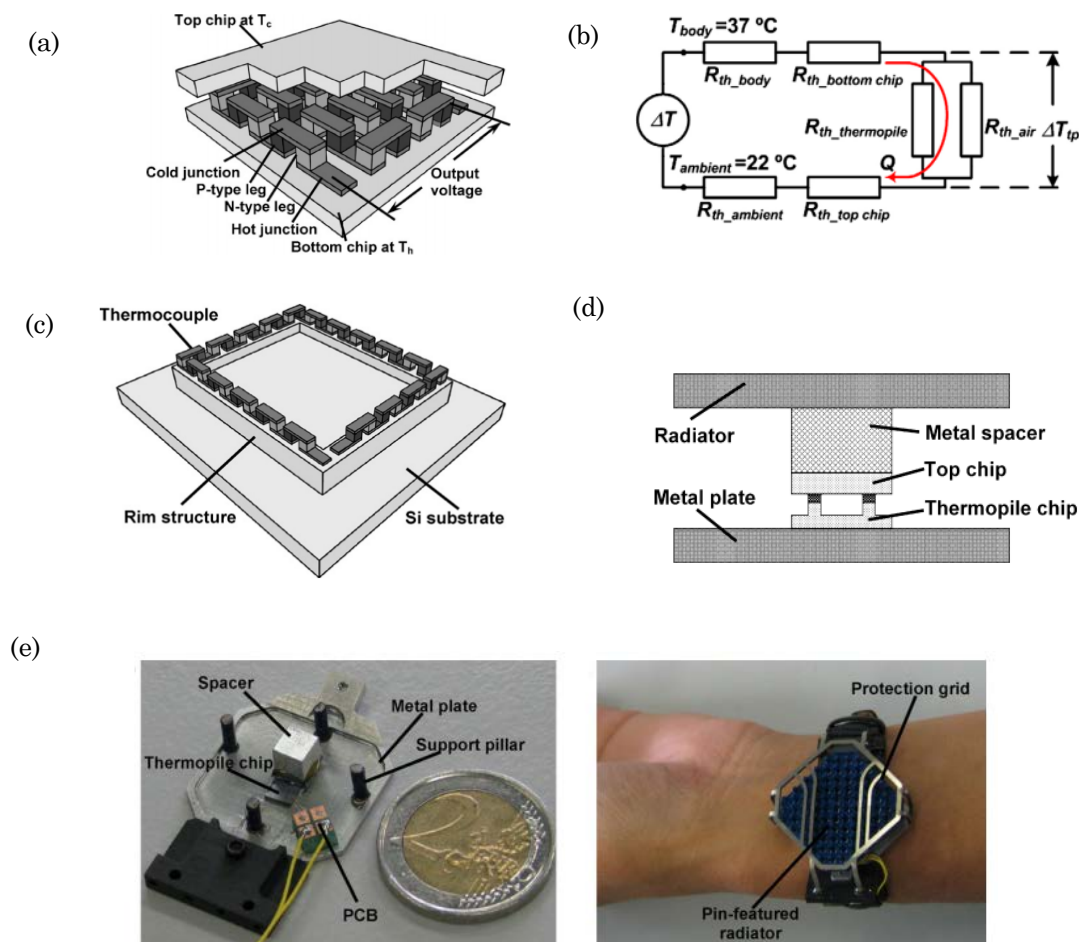


**Fig. 3.** (a) Schematic representation of a thermoelectric generator, (b) its equivalents circuit model when deployed on a human body, (c) rim structure added to the TEG to increase the air gap inside the generator, (d) schematic arrangement of the TEG and, (e) photo of the TEG being assembled and worn on a human body [9].

In this work, the author increased the equivalent thermal resistance of the TEG to make a large temperature drop occur between the cold and the hot junctions of the generator (Fig. 3.a,b). He also reduced the thermal resistances of the other constituting components of the generator through proper packaging of the TEG. To do so, a rim structure have been added to the device to increase the air gap between the top and bottom chips (Fig.3.c,d). Then, considering that in an optimized configuration the equivalent resistance of the thermocouples should match that of the air gap between the two chips as explained in [10], the number of thermocouples have been changed until this condition is satisfied. The consequence of such a work is the increase of the temperature difference across the thermopile and thus better output performances. In Fig.3.e, one can see a photo of the entire device being assembled and worn on a human body. The first

observation that can be made is that the size of the thermopile is very small in comparison with the entire system's size. This is due to the volume occupied by the radiator. To overcome this drawback in our coupled piezoelectric and bimetal heat engine, a complete thermal modeling is proposed hereafter.

### III. Thermal study in steady state conditions

#### 1. Modeling

##### 1.1. Simplification of the modeling

By studying the working properties of the device, some useful simplifications can be made for the thermal modeling. The first observation involves the effect of the bimetal on the thermal properties of the energy harvester. It can be simply understood that the bimetal behaves like a switched thermal capacitance, transferring the heat from the hot source to its cold counterpart. To measure bimetal's impact on thermal transfers inside the device, temperature mapping is realized using an infrared thermal camera (NEC G-120, NEC, Japan) on two devices, one with a working bimetal and the other one with an empty cavity. Thermal profiles are generated using cross sections of the structure as shown in Fig. 4. The experimental results displayed in Fig. 5 reveal that the oscillating bimetal does not significantly modify the temperature of the brass membrane used as a cold thermal exchanger: the temperature difference for a hot source at  $80^{\circ}\text{C}$  is about  $11^{\circ}\text{C}$  with a working bimetal and equals  $12^{\circ}\text{C}$  if no bimetal is used. These results suggest that the medium heat transfer behavior of the bimetal can be neglected in the analytical modeling and, consequently, steady-state conditions are hereafter considered for the thermal transfer.

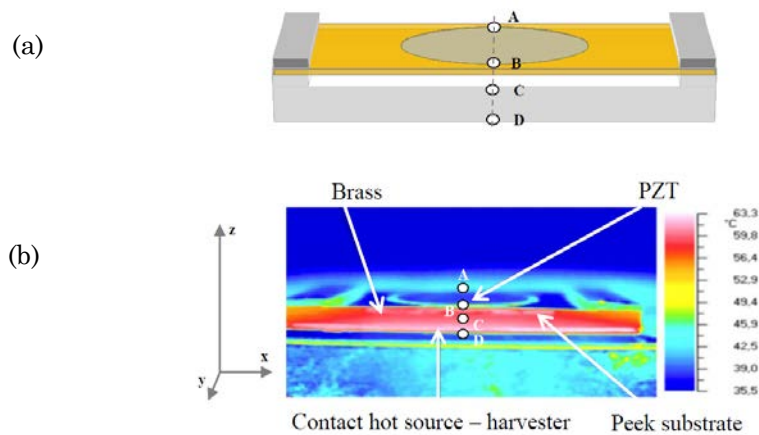


**Fig. 4.** (a) Thermal energy harvesting device on a hot plate at  $64^{\circ}\text{C}$ , and (b) its corresponding stationary temperature field obtained with an infrared thermal camera.

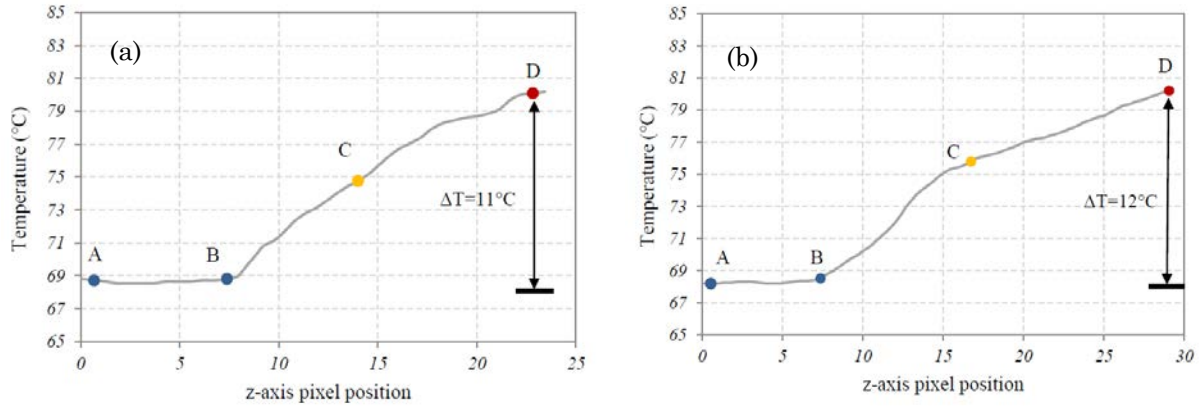


**Fig. 5.** Cross-sectional view (Fig. 4.b) of the temperature distribution with a hot plate at 80°C in steady-state conditions in (a) a device with a bimetal and (b) a device without a bimetal.

For the next section, we consider that heat is transferred only in the direction defined by the hot source and the cold source, enabling to model the device with a one-dimension system.

## 1.2. Analytical model

To thermally model the harvester, the different ways by which heat is transferred inside the device are considered. The various heat transfer modes are linearized and a lumped-element model based on the electrical-to-thermal analogy is developed. In this system, Fourier's law, which describes the conduction process taking place through solid materials and stationary fluids (air in the inside cavity), is expressed as:

$$Q = k \cdot S \cdot \frac{\Delta T}{e} \quad (1)$$

where  $Q$  is the heat flux,  $\Delta T$  is the temperature difference across the material layer,  $e$  is the thickness of the solid in the  $z$  direction,  $S$  is the surface crossed by the heat flux and  $k$  is the thermal conductivity.

Newton's law is used to describe natural convection present at the top surface of the harvester. It links the heat evacuated from the energy harvester to the temperature difference between the top layer and the ambient air ( $T_s - T_\infty$ ) by means of convection heat transfer with the coefficient  $h_c$ .

$$Q = h_c (T_s - T_\infty) \quad (2)$$

To determine whether convection takes place inside the air cavity, one evaluates the dimensionless Rayleigh number ( $R_a$ ), describing the relationship between the buoyancy (based on Archimedes' principle) and the viscosity forces in a fluid. Its calculation is done using (3) which is a function of the temperatures of the two layers on the two sides of the air cavity,  $T_1$  and  $T_2$ , the acceleration due to gravity,  $g$ , the air thermal expansion coefficient,  $\beta$ , the kinematic viscosity of air,  $\gamma$ , and its thermal diffusivity,  $\alpha$ .

$$R_a = \frac{g \cdot \beta \cdot (T_1 - T_2) \cdot L^3}{\gamma \cdot \alpha} \quad (3)$$

For a hot source temperature around 100°C, the value of  $R_a$  is equal to 1.2, which is far below the critical value of 1708 [11], signifying that the viscous forces are too large to be overcome by the buoyancy forces, and that the convection consequently is negligible.

The Stefan-Boltzmann law is used to describe the radiation process that occurs between the top layer of the harvester and the ambient air, and the one occurring in the inside air cavity. This law links the heat flux  $Q$  emitted by a body to the temperature difference of a layer at  $T_1$  and ambient air at  $T_\infty$  (considering that  $T_1 - T_\infty < 100\text{K}$  [11]), to the surface  $S$  of the emitting body and the radiative heat transfer coefficient  $h_r$ :

$$Q = h_r \cdot S \cdot (T_1 - T_\infty) \quad (4)$$

The radiative heat transfer coefficient depends strongly on the temperature. Its expression is given by the equation (5) where  $T_m$  is the mean value of  $T_1$  and  $T_2$ , and  $F$  is a correcting view factor:

$$h_r = F \cdot 4 \cdot \sigma \cdot \varepsilon \cdot T_m^3 \quad (5)$$

The view factor is the part of the radiative flux leaving a surface  $A$  toward a surface  $B$ . For the calculation of the view factor in the air enclosure where the bimetal takes place, the emissivity of brass is considered equal to 0.4 and the Teflon's emissivity equal to 0.85. The calculation of the value of the correcting view factor is given by (6a) for the radiative transfer inside the cavity and (6b) for the transfer with the ambient air.

$$F_{cavity} = 0.04 \quad (6a)$$

$$F_{ambient} = 1 \quad (6b)$$

By using the linearized equations (1) through (6), it is possible to describe an equivalent electrical model where all the thermal transfers are modeled using thermal resistances, and the temperatures are simulated by equivalent electric potentials. In this way, the simplified model of the harvester represented in Fig. 6 can be modeled as shown in Fig. 7. Given the good thermal contact between the harvester and the hot plate, the contact resistance is neglected.

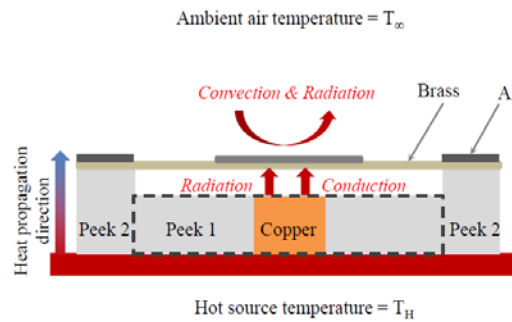


**Fig. 6.** Schematic representation of the harvester with the different heat transfer processes occurring through it.

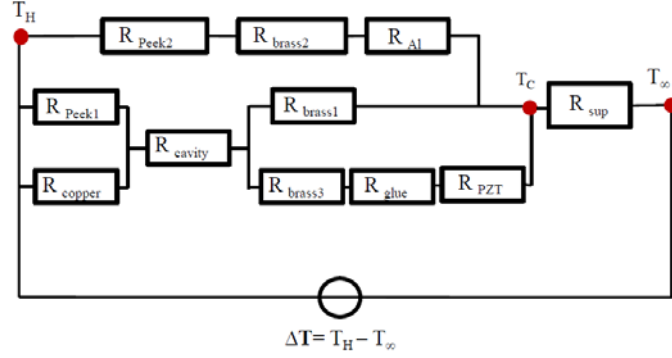


**Fig. 7.** Equivalent thermal circuit of the coupled piezoelectric-bimetal heat engine.

In this thermal circuit, all the thermal resistances correspond to conduction except for  $R_{cavity}$  (in reference to the thermal exchanges inside the air cavity) and  $R_{sup}$  (in reference to the superficial exchanges with ambient air). In  $R_{cavity}$ , two modes occur simultaneously: radiation between the top and the bottom surfaces in the rectangular air space and conduction through the stationary air.  $R_{sup}$  represents the heat transferred from the surface of the device to the colder ambient air above by convective and radiative modes.

The described analytical model is implemented and the thermal resistance values are calculated thanks to the thermal conductivities of the materials summarized in Table 1.

Material	K (W.m <sup>-1</sup> .K <sup>-1</sup> )
PEEK	0.25
Brass	121
Aluminum	237
Glue	2
PZT ceramic	25
Copper	390
Air in the cavity	0.0262

**Table 1.** Summary of the thermal conductivities of the materials.

The coefficient of convective heat exchange, used later during the thermal optimization, is initially extracted by fitting the model with the measurements performed on the non-optimized harvester, to ensure that models will describe the experimental results, as explained in [12]. The circuit in Fig. 7 can as shown in Fig. 8 be simplified by calculating the equivalent resistance of the system  $R_{eq}$ . This way, the cold temperature  $T_C$  is simply expressed in the equation (8).

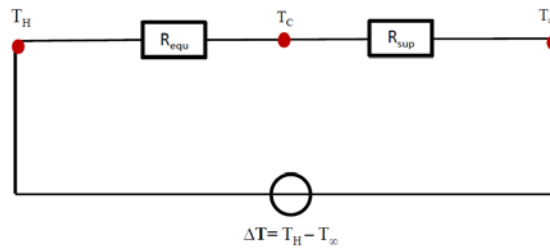


**Fig. 8.** Simplified thermal circuit of the thermal energy harvester.

$$Q = \frac{T_H - T_\infty}{R_{eq} + R_{sup}} \quad (7)$$

$$T_C = Q \cdot R_{sup} + T_\infty \quad (8)$$

The superficial exchange resistance has a value of 63K/W whereas the equivalent system resistance has a value of 19K/W.

### 1.3. Finite element model

To numerically validate the analytical approach, a finite element analysis was created using the ESI software (CFD-ACE+). All the modes of heat transfer were taken into account for this simulation and the temperature of ambient air was set to 25°C with no forced convection. Simulations were carried out for a hot source temperature varying from 40°C to 100°C, rendering it possible to obtain thermal profiles of the structure, as shown in Fig. 9.

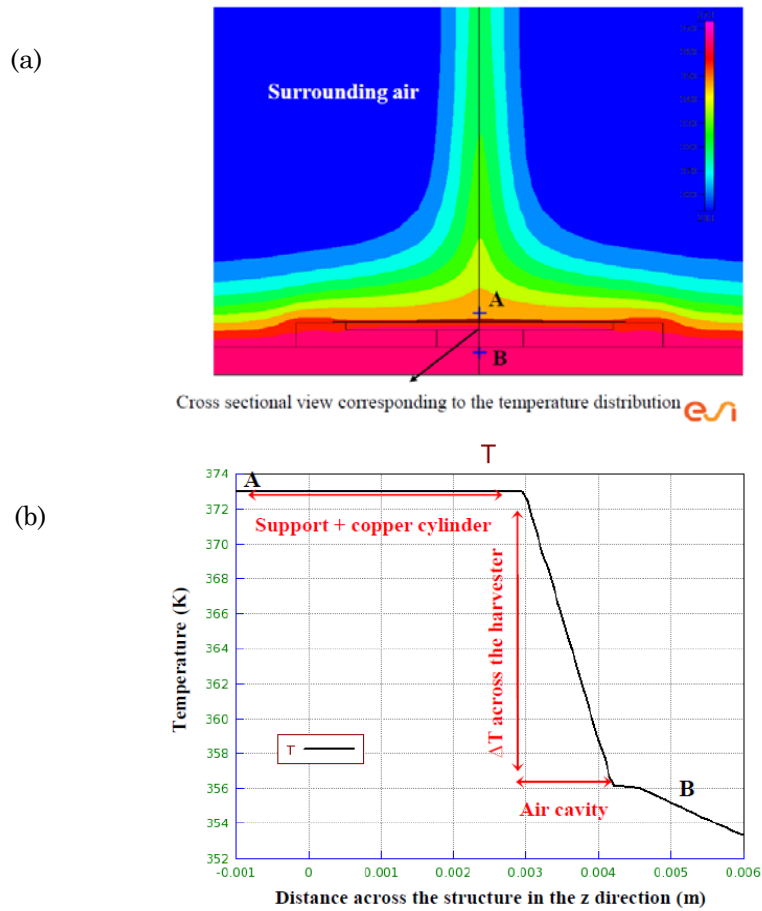


**Fig. 9.** (a) A stationary temperature field using the Finite Element Model (FEM) of the harvester on a hot source at 100°C. (b) Temperature distribution using the cross-sectional view.

The comparison between the electrical model, the FEM model and the experimental data is presented in Fig. 10 where a good agreement between each modeling technique and the experiment is observed, thus validating each approach.

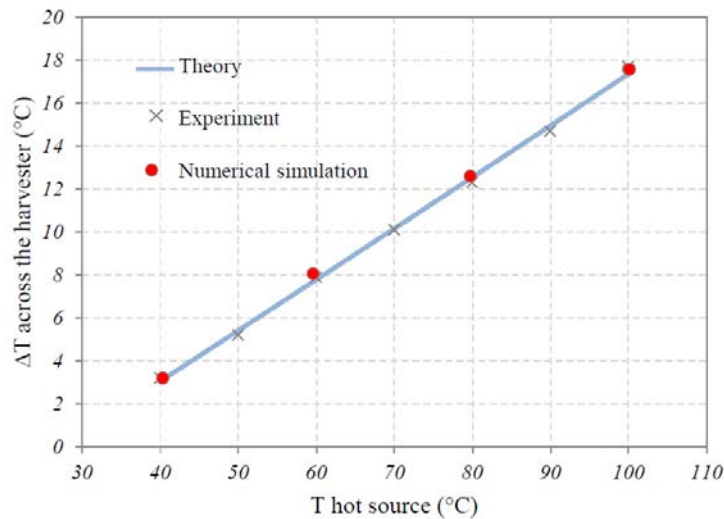


**Fig. 10.** Comparison between the theoretical, experimental and numerical temperature differences across the harvester for an ambient air temperature of 25°C.

## 2. Results and discussions

### 2.1. Matrix analysis using the FEM

The coupled piezoelectric-bimetallic strip heat engines studied here can work individually or in a matrix configuration. This latter case is useful when the level of energy needed to supply certain applications exceeds what is provided by a single cell. Consequently, the thermal behavior of matrix devices was also investigated.

Using the numerical model, simulations were realized using 3 cells with a hot source at 80°C. Fig. 11 shows the 3 modules used as well as the 3 cross-sections realized to extract the available temperature difference through each module. For the cell in the middle,  $\Delta T$  equaled 11°C whereas it reached a value of 12°C for the cell on each side. This can be explained by the fact that the cells on the sides were cooled down by more natural convection than the one in the middle due to its neighboring cells. However, the realization of matrix structures did not compromise the functionality of the devices as a high  $\Delta T$  remained for all the harvesters in the matrix.

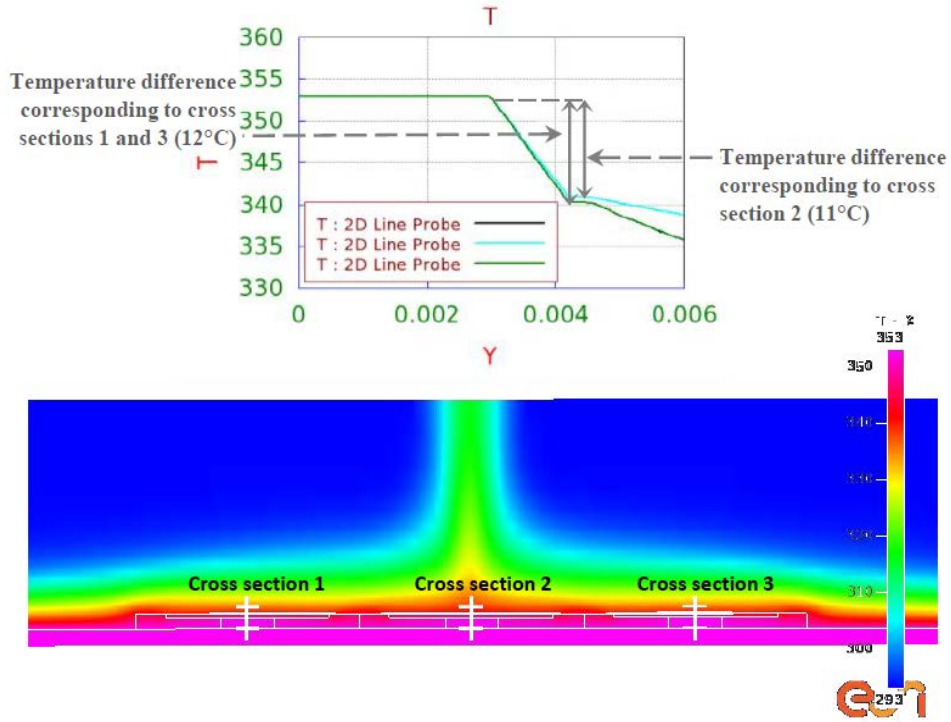


**Fig. 11** Temperature distribution using an FEM of a matrix structure with 3 cells on a hot plate at 80°C and the corresponding cross-sectional view of each of the cells.

## 2.2. Thermal optimization and design improvement

At this point, the heat transfer modes were well known and allowed a thermal optimization of the harvester. We first attempted to improve the heat transfer coefficient between the cold surface and the ambient air by increasing the thermal radiation, which is the most efficient and dominant way to evacuate heat at an interface with ambient air. The emissivity of the cold surface was increased to get closer to the emissivity of a black body thanks to a black matted paint. This first step made it possible to reduce the mean value of the superficial exchange resistance from 63K/W to 41K/W over a temperature range from 40°C to 100°C.

The next step was to improve the internal thermal resistance of the harvester. It is commonly known that the optimal configuration is a thermally matched device where both the thermal flux crossing the device and the obtained  $\Delta T$  ( $T_{\text{hot source}} - T_{\text{cold surface}}$ ) are maximized. The harvester should consequently be designed in such a way that the two thermal resistances described above are equal. This technique is widely used for the design of thermoelectric generators as shown in Stevens' studies [13] as well as those of Leonov [6] and Wang [9]. The temperature drop across the harvester is given by the equation (9).

$$\Delta T_{\text{harvester}} = \Delta T_{\text{available}} \frac{R_{eq}}{R_{eq} + R_{sup}} \quad (9)$$

where  $\Delta T_{\text{harvester}} = T_H - T_C$  and  $\Delta T_{\text{available}} = T_H - T_{\infty}$ . To match the resistance of the device  $R_{eq}$  to 41K/W, the most dominant resistances in the circuit of Fig. 7 are thus considered simplified, leading to the equivalent circuit of Fig. 12 where only the most effective resistances remain.

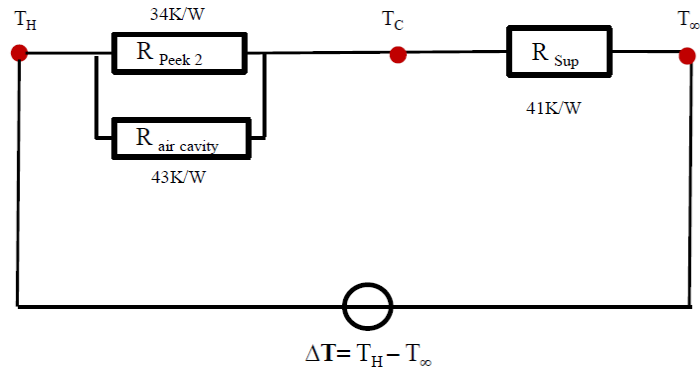


**Fig. 12.** Simplified equivalent thermal circuit of the harvester.

As a result, the thickness of the air inside the cavity increased about three times and the surface of the PEEK in the sides was divided by a factor 2. The new optimized structure is presented in Fig. 13a.b and Fig. 13a.c (for the sake clarity, no paint was applied to the harvester in this figure). The equivalent impedance of the device then presented a mean value of 40K/W over the considered temperature range from 40°C to 100°C. Fig. 13b shows a comparison and the good agreement between the theoretical model presented in Fig.7 and the experimental data of the thermally-optimized device (peek etching + black paint) measured in ambient air at 27°C. For a hot source at 100°C, a temperature difference of 36°C across the harvester was obtained, whereas a difference of only 17°C was found for the non-optimized structure. These results validated the assumption of matching only the resistances presented in Fig.12.

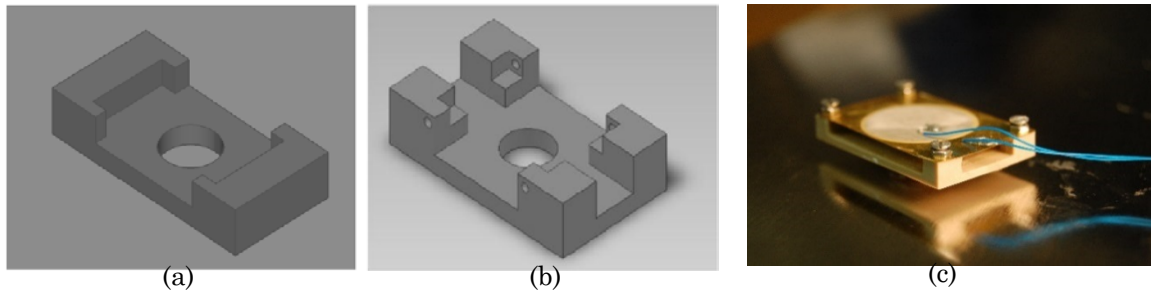


**Fig. 13a.** (a) Non-optimized PEEK substrate design. (b) Thermally optimized PEEK substrate design. (c) Thermal energy harvester after thermal improvements.

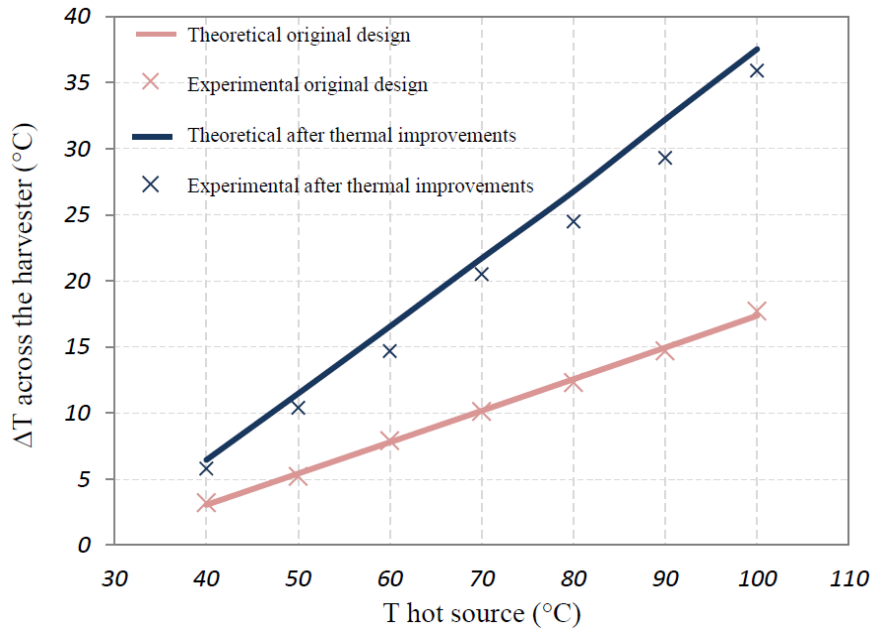


**Fig. 13b.** Thermal management improvements thanks to design optimization and black paint, and a comparison between theoretical values and experimental measurements.

### 2.3. Electrical optimization thanks to thermal improvements

These thermal improvements have a significant impact on the functioning of the device: a bimetal with a small thermal hysteresis can keep on snapping up and down at a maximum hot range temperature of  $3^{\circ}\text{C}$  in a non-optimized structure. With the new architecture, the energy can be harvested over a wider range of hot source temperatures. Experiments (Fig. 14) reveals that a  $3^{\circ}\text{C}$  hysteretic bimetal with an optimal performance at  $88^{\circ}\text{C}$  can function at hot source temperatures varying from  $83^{\circ}\text{C}$  up to  $105^{\circ}\text{C}$ . The optimized structure significantly extends the hot source working temperature range for each bimetal.

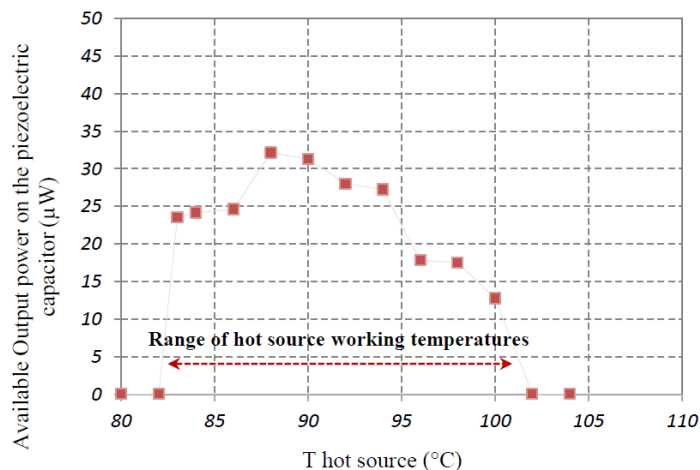


**Fig. 14.** Effect of the thermal optimization on the electrical properties of the harvester (bimetal  $67^{\circ}\text{C}$ - $70^{\circ}\text{C}$ ).

Moreover, thanks to these optimizations, we were able to use a bimetal with a larger hysteresis ( $19^{\circ}\text{C}$ ) since a bimetal with a snapping and snapping back temperature of respectively  $92^{\circ}\text{C}$  and  $73^{\circ}\text{C}$  could function from  $115^{\circ}\text{C}$  to  $137^{\circ}\text{C}$ . The snapping frequency was lower due to the high hysteresis but the device functioned in a permanent regime as shown in Fig. 15.

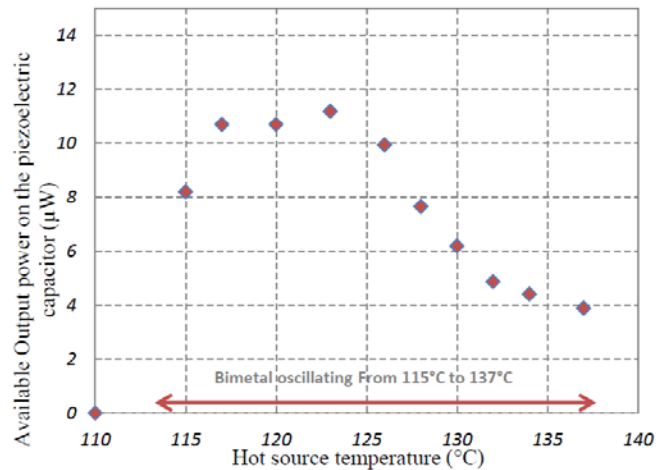


**Fig. 15.** Output signal using a high thermal hysteresis bimetal (bimetal 73°C-92°C).

### 3. Scaling the devices after their thermal improvements

Once the thermal optimization of the harvester architecture is achieved, it is possible to evaluate how downscaling of the harvester's size would change device's performances. In fact, previous studies have focused on scaling down the device dimensions [14] in order to increase the snapping frequency and thus the amount of harvested power. As a starting point, a new optimized harvester with a surface twice smaller than that of the previous harvester was designed (Fig. 16). This new design has a new air gap between the hot source and the bottom of the harvester and only the copper cylinder is in contact with the hot source. A piece of copper is added to the brass membrane of the piezoelectric transducer to improve the heat transfer from the bimetal when it snaps up (Fig. 16).

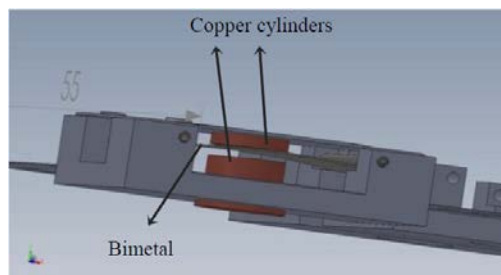


**Fig. 16.** Schematic representation of the millimetric thermal energy harvesting device.

The procedure in section 3 is used to model the new harvester structure. Fig. 17 presents a scheme of this harvester with the considered heat transfer modes and Fig. 18 shows the corresponding thermal circuit. Here again, the coefficient of convective heat exchange taking place at the cold surface is used as a fitting parameter for the analytical model with the experimental measurements ( $8 \text{ W}\cdot\text{m}^{-2}\cdot\text{K}^{-1}$ ).

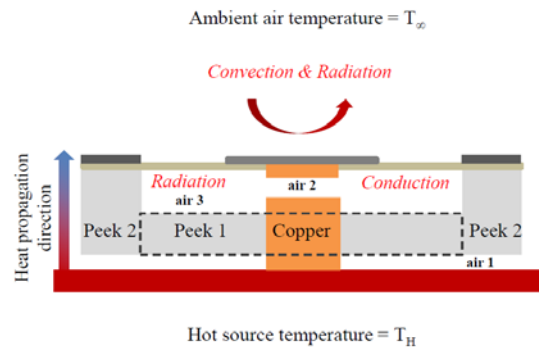


**Fig. 17.** Cross sectional view of the design-optimized energy harvesting device with the different heat transfer processes through it.

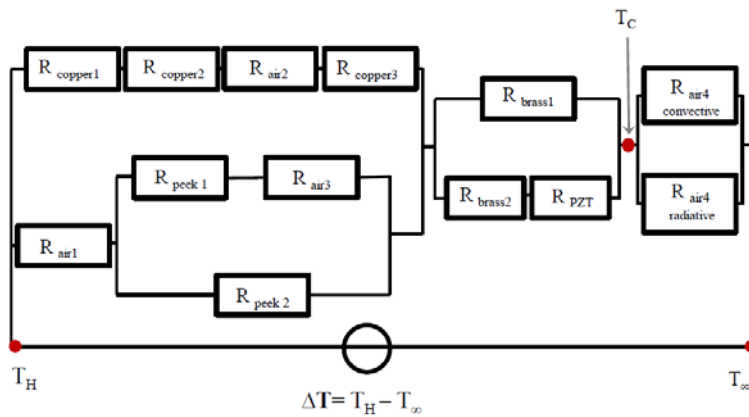


**Fig. 18.** Equivalent thermal circuit of the design-optimized harvester.

Using this analytical model, the cold surface temperatures are obtained and compared with experimental measurements as presented in Fig. 19 where a good agreement between the two data sets can be observed between 40°C and 150°C. The two thermal resistances of the harvester displayed a mean value of 200K/W.

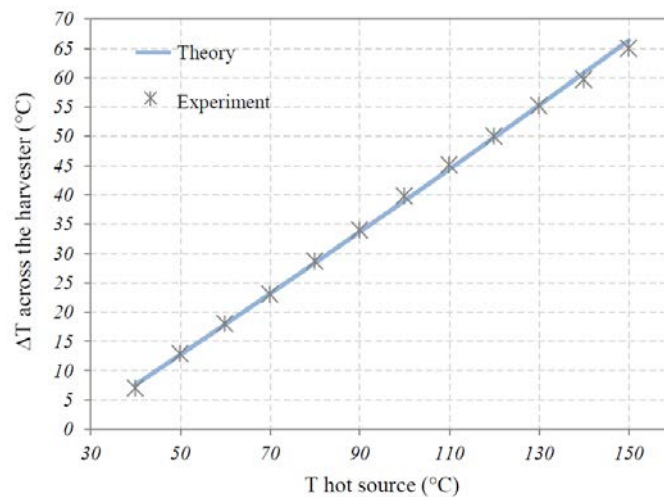


**Fig. 19.** Theoretical values of the temperature difference across the millimetric energy harvester compared with experimental measurements using a thermocouple.

Fig. 20 shows the simplified thermal equivalent circuit of the harvester by eliminating the negligible thermal resistance. In this circuit, all the thermal resistances corresponded to a conductive heat transfer except  $R_{\text{air } 4}$ , since the evaluation of the radiation effects in the air cavity has shown that it has no impact on the cold source temperature contrary to the conduction transfer. This can be explained by the low emissivity of brass and copper. Fig. 21 compares the complete and simplified models and validates the simplifying hypothesis.

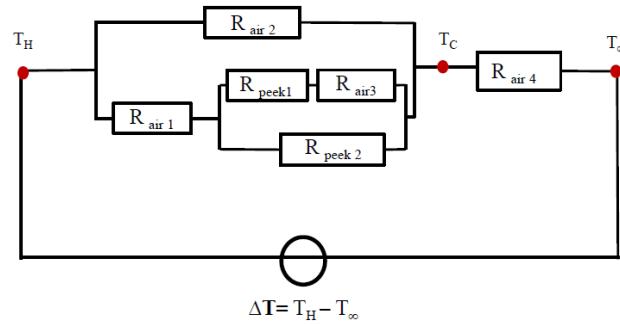


**Fig. 20.** Simplified thermal circuit of the harvester.

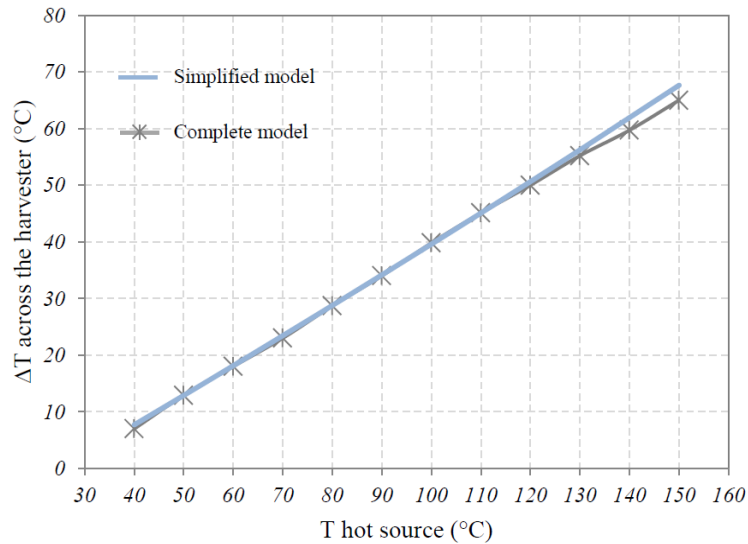


**Fig. 21.** Comparison of theoretical values and experimental measurements of the temperature difference across the harvester.

Now, using the expressions of the different thermal resistances, the device is considered to be miniaturized by a factor  $x$  (i.e., all the dimensions are divided by this factor). The evolution of the thermal resistances after applying this scaling are summarized in Table 2 where  $R'$  represents the thermal resistance once the scaling has been applied and  $R$  is the initial resistance (in the case of the thermally matched device presented before).

Conduction	Convection	Radiation
$R'_{cond} = \frac{e \cdot x}{k \cdot S} = x \cdot R_{cond}$	$R'_{conv} = \frac{x^2}{hc \cdot S} = x^2 \cdot R_{conv}$	$R'_{rad} = \frac{x^2}{hr \cdot S} = x^2 \cdot R_{rad}$

**Table 2.** Expressions of the thermal resistances after scaling down the device dimensions by a factor  $x$ .

Using these expressions, the simplified circuit becomes:

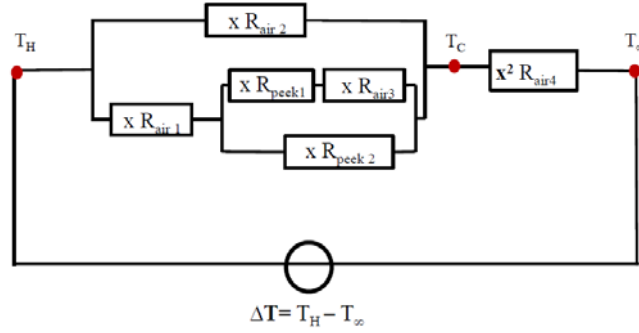


**Fig. 22.** Equivalent thermal circuit after scaling down the structure.

The calculation of the temperature difference across the harvester is then developed in equations (10 - 11):

$$T_C - T_H = \frac{x \cdot R_{eq}}{x \cdot R_{eq} + x^2 \cdot R_{air4}} (T_H - T_\infty) \quad (10)$$

$$\Delta T_{harvester} = \frac{R_{eq}}{R_{eq} + x \cdot R_{air4}} \Delta T_{available} \quad (11)$$

This expression indicates that when all the geometrical dimensions are scaled down, the available  $\Delta T$  across the harvester decreases. Figure 23, based on the equation (11), shows the evolution of the temperature difference across the harvester as a function of the hot source temperature for different scaling factors.

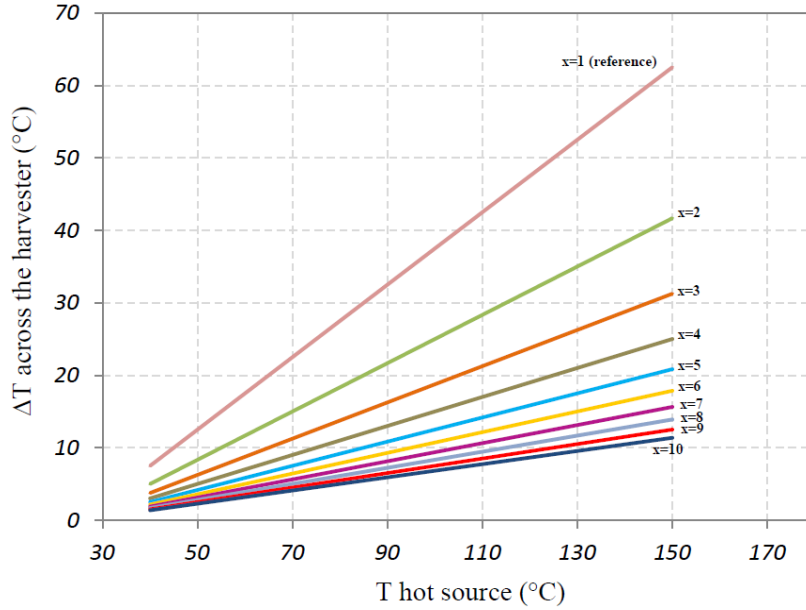


**Fig. 23.** Thermal properties and temperature differences across the harvester for different scaling factors  $x$ .

The observed evolution can be explained by two main factors. First of all, radiative and convective thermal resistances evolve in the same way (Table 2) but do not follow the same evolution compared to the conductive thermal resistance. Consequently, each time the harvester size is scaled down, the device architecture should be thermally re-optimized by matching  $R_{eq}$  and  $R_{air}$ . The second factor leading to this behavior is related to the available thermal gradient between the hot source and the surrounding air that is more significant when the device is thicker. If the device thickness is scaled down like the other dimensions, the available thermal gradient of a thermally matched harvester decreases like the available temperature difference. Numerical simulations were carried out to study the evolution of the available temperature difference between the hot source and the ambient air as a function of the scaling factor of the harvester. The hot source temperature is set at  $70^{\circ}\text{C}$  and the ambient air is at  $20^{\circ}\text{C}$ .

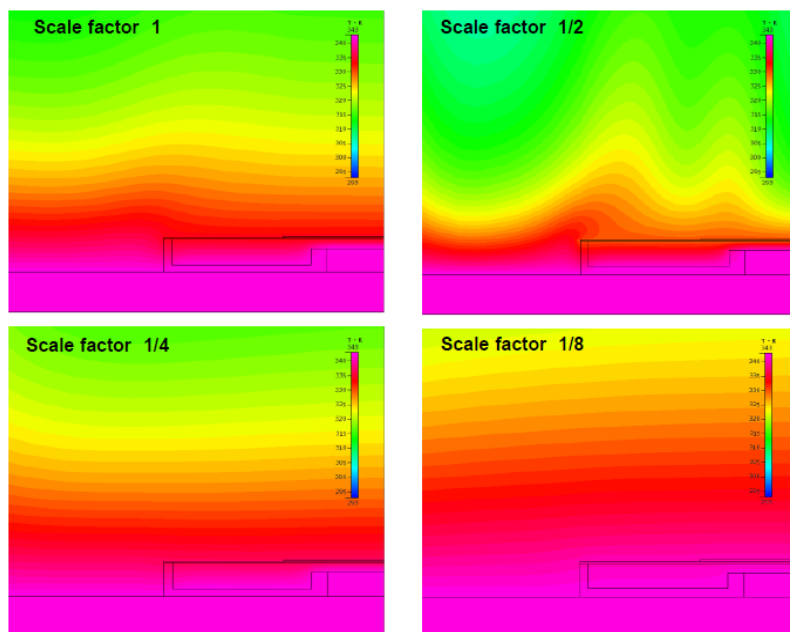


**Fig. 24.** Thermal distribution as a function of the scaling factor.

The results of Fig. 24 demonstrate this last observation: for high values of the scaling factor, the temperature difference inside the harvester decreases due to the smaller thermal gradient available. In order to efficiently scale the harvester and maintain the same temperature difference inside the device architecture one must scale all the dimensions except the thickness. For this scaling method, the evolution of the temperature inside the device is described by (12).

$$T_H - T_c = \frac{x^2 \cdot R_{eq}}{x^2 \cdot R_{eq} + x^2 \cdot R_{air\ 4}} (T_H - T_\infty) \quad (12)$$

Matching the impedance logically gives:

$$\Delta T_{harvester} = \frac{1}{2} \Delta T_{available} \quad (13)$$

This means that by scaling the surface and keeping the thickness constant, the system remains thermally matched (equation 13) and good thermal properties are maintained. This is verified experimentally in Fig. 25 for the two devices presented before with a scaling factor equal to 2.

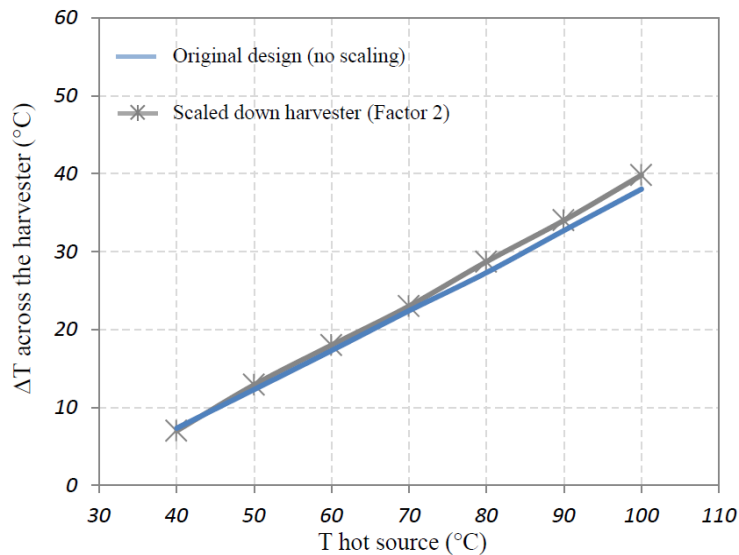


**Fig. 25.** Comparison of the experimental temperature difference across the original and miniaturized devices.

## IV. Dynamic modeling of the harvester taking into account the bimetal

### 1. Purpose of the study

Before modeling the thermal energy harvester in dynamic mode and presenting the results of this study, it is important to point out the reasons explaining this work. In fact, the bimetal used in Fig. 26 has a snap temperature of 70°C and a snap-back temperature of 67°C. Once mounted in the harvester, it starts oscillating only at a hot source temperature of 84°C and stops at 102°C. This difference is well illustrated in Fig. 26 and makes it essential to study the device in dynamic mode to take into account the bimetal acting as a shuttle between the cold and hot reservoirs especially since we observe the same behavior for any used bimetal regardless of its hysteresis.

To close the gap between the model and the experimental data of Fig. 26, the model in Fig. 7 was modified to predict the dynamic behavior of the structure with an oscillating bimetal inside it. To

reach that goal, a lumped element model inspired from the previous one was developed and can be seen below.

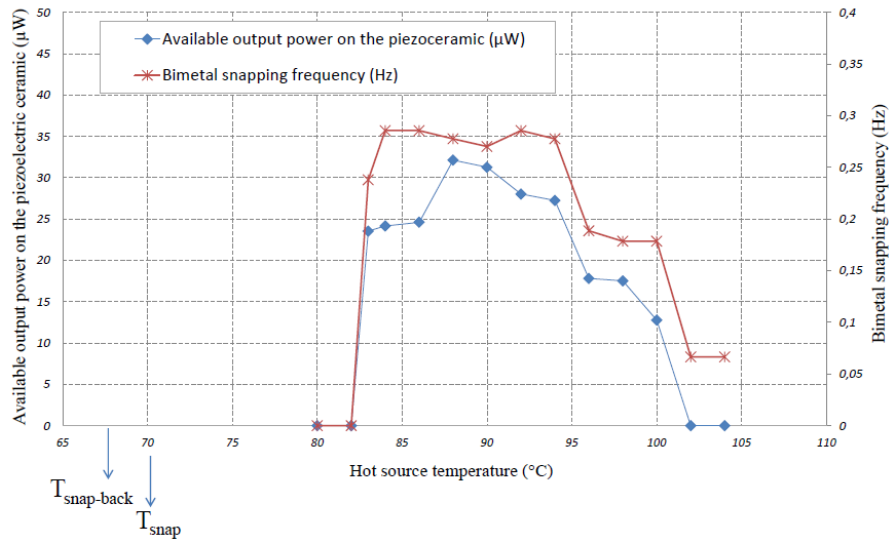


**Fig. 8.** Range of hot source functioning temperatures for a 3°C hysteretic bimetal (67°C-70°C).

## 2. Dynamic modeling

To model the whole harvester in dynamic mode, inspiration is obtained from the model in Fig. 5 under steady-state conditions and without taking into account the oscillating bimetal. In fact,  $R_{equ}$  (Fig. 8) is the same as  $R_{architecture}$  (Fig. 27) as it represents the heat flow that does not go through the bimetal, the active part of the device. Then,  $R_{superficial\ exchanges}$  (Fig. 27) is equal to  $R_{sup}$  (Fig. 8). To model the dynamical effect of the bimetal, a capacitance  $C_b$  representing the bimetal's thermal capacitance with two switches are added. These switches are used to represent the behavior of the bimetal each time it snaps up and comes in contact with the cold surface at  $T_{cold}$  or when it snaps back and comes in contact with the hot reservoir at  $T_{hot}$  [16-17]. For the dynamic model, we assume that the contact resistances represented on the dynamic circuit in Fig. 27,  $R_{heating}$  and  $R_{cooling}$ , are equal.

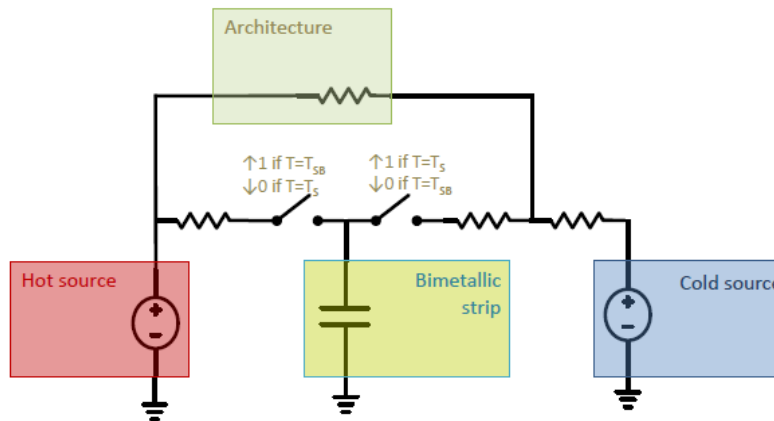


**Fig. 27.** Equivalent circuit of the harvester in dynamic mode taking into account the bimetal as a switched capacitance.

For the bimetals studied in Fig. 27, we consider the time spent in the upper position  $\Delta t_{\text{cold}}$  and the time spent in the lower position by the bimetal  $\Delta t_{\text{hot}}$  to be equal, meaning that the structure is in a thermal equilibrium. Also, we consider the snap-up and -down temperatures of the bimetal, respectively  $T_s$  and  $T_{sb}$ , to be well known since these are values given by the bimetal's manufacturer.

To study the circuit shown in Fig. 27, we separately investigate the two states of the bimetal: first the circuit when the bimetal is at its lower state, i.e., when switch 1 is closed and switch 2 opened until the bimetal's temperature reaches the snapping temperature; and then the opposite i.e., when the bimetal is cooled down by ambient air until it reaches its snap-back temperature.

### 2.1. Model analysis with the bimetal at its lower position

When the bimetal is at its lower state, switch 1 is closed and switch 2 opened. Here,  $T_b(t)$  is the instantaneous temperature of the bimetal,  $T_s$  its snap-up temperature and  $T_{sb}$  its snap-back temperature.

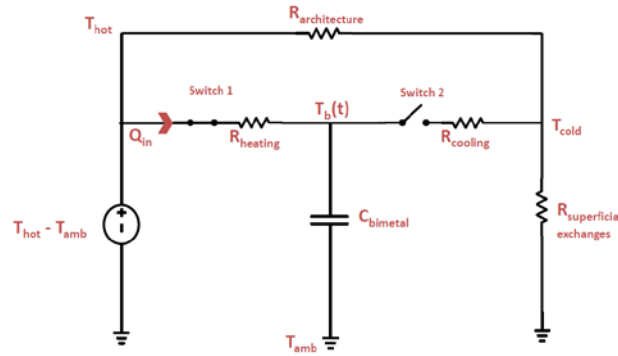


**Fig. 28.** Equivalent circuit in dynamic mode with the bimetal at its lower state.

By applying the conventional electrical laws in the circuit of Fig. 28, we obtain the expression of the thermal flux absorbed by the bimetal given by (14). We then calculate  $T_b(t)$  and obtain the bimetal's instantaneous temperature during each moment of the heating process (15). When  $T_b(t) = T_s$ ,  $\Delta t_{\text{hot}}$  is the time during which the bimetal is heated up in the lower position is given by expression (16).

$$Q_{in} = C_b \cdot \frac{dT_b}{dt} \quad (14)$$

$$T_b(t) = (T_{sb} - T_{hot}) e^{\frac{-t}{R_{heating} \cdot C_b}} + T_{hot} \quad (15)$$

$$\Delta t_{hot} = R_{heating} \cdot C_b \cdot \ln \left( \frac{T_{sb} - T_{hot}}{T_s - T_{hot}} \right) \quad (16)$$

### 2.2. Model analysis with the bimetal in its upper position

We then apply the same strategy as previously with the bimetal in its upper state, meaning that switch 1 is opened and switch 2 closed.

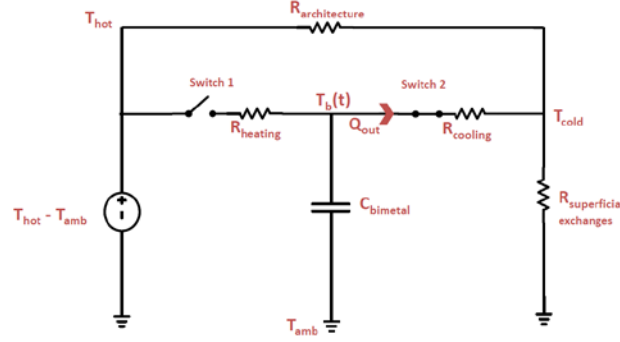


**Fig. 29.** Equivalent circuit in dynamic mode with the bimetal at its upper state.

The thermal flux evacuated by the bimetal is given by (17). In this new configuration,  $T_b(t)$  is given by (18) and finally, at the end of the cooling time, when  $T_b(t)=T_{SB}$ ,  $\Delta t_{cold}$  represents the time during which the bimetal is in its upper position, according to expression (19).

$$Q_{out} = C_b \cdot \frac{dT_b}{dt} \quad (17)$$

$$T_b(t) = (T_s - T_{cold}) e^{\frac{-t}{R_{cooling} \cdot C_b}} + T_{cold} \quad (18)$$

$$\Delta t_{cold} = R_{cooling} \cdot C_b \cdot \ln\left(\frac{T_s - T_{cold}}{T_{sb} - T_{cold}}\right) \quad (19)$$

### 2.3. Estimation of the model parameters: contact resistances and switched capacitances of the bimetal

To fully understand our model, one needs to catch the meaning of a switched capacitance. In fact, the working principle of a switched capacitance is to charge and discharge a given capacitance, here represented by the bimetal. It behaves like a resistance whose value changes with the switching frequency. Taking into account the definition of a switched capacitance, it is possible to evaluate its mean value. To do so, the first step is to estimate the value of the switched capacitance  $C_b$  expressed in  $J \cdot K^{-1}$  according to eq (20):

$$C_b = m C_m \quad (20)$$

where  $m$  is the mass of the active part of the bimetal and  $C_m$  its specific heat capacity.

The equivalent resistance of the switched capacitance is consequently expressed in  $W \cdot K^{-1}$  eq. (21):

$$R_{capacitance} = \frac{1}{C_b \cdot f_{switch}} = \frac{T_{switch}}{C_b} \quad (21)$$

where  $f_{switch}$  is the frequency with which the bimetal switches from one state to the other and  $T_{switch}$  is the switching period.

Another important parameter that we can estimate with this model is the value of the contact resistances  $R_{heating}$  and  $R_{cooling}$  represented in Fig. 28 and Fig. 29.

These contact resistances appear in the expressions of the time spent in the lower and upper positions by the bimetal as can be seen in eq. (16) and eq. (19). Consequently, to estimate the values of these resistances, we use experimental values of the time spent in the lower and upper positions, expressed respectively as  $\Delta t_{hot}$  and  $\Delta t_{cold}$ . The expression of  $R_{cooling}$  and  $R_{heating}$  can thus

be evaluated for each bimetal depending on the snapping temperature of the considered bimetal, its snap-back frequency, the time spent in the lower as well as in the upper position and finally as a function of the switched capacitance as shown in eq. (22) and eq. (23).

$$R_{cooling} = \frac{\Delta t_{cold}}{C_b \cdot \ln\left(\frac{T_s - T_{cold}}{T_{sb} - T_{cold}}\right)} \quad (22)$$

$$R_{heating} = \frac{\Delta t_{hot}}{C_b \cdot \ln\left(\frac{T_{sb} - T_{hot}}{T_s - T_{hot}}\right)} \quad (23)$$

### 3. Dynamic model application

#### 3.1. Range of hot source functioning temperatures of a bimetal having a certain hysteresis once mounted in the harvester

Knowing that each bimetal mounted in the harvester is in thermal equilibrium, so that  $\Delta t_{hot} = \Delta t_{cold}$ ,  $T_{cold} = (T_{hot} + T_{amb})/2$  and  $R_{cooling} = R_{heating}$ , we can obtain the expression of the minimum hot source temperature at which the bimetal with a snapping temperature of  $T_s$  and a snapping-back temperature of  $T_{sb}$  will start snapping once mounted in the device in eq. (24):

$$T_{hot}^{min} = \frac{2 \cdot T_s^2 - 2 \cdot T_{sb}^2 - T_s \cdot T_{amb} + T_{sb} \cdot T_{amb}}{3 \cdot (T_s - T_{sb})} \quad (24)$$

Then, to find the temperature at which the bimetal will stop snapping inside the device, one should satisfy the following condition:  $T_{cold} \geq T_{sb}$ . This leads to the maximal analytical hot source temperature at which the bimetal is bound to snap in eq. (25):

$$T_{hot}^{max} \geq 2 \cdot T_{sb} - T_{amb} \quad (25)$$

This way, by obtaining the expressions of  $T_{hot}^{min}$  and  $T_{hot}^{max}$  one can for each bimetal estimate the operation window on which it will keep on oscillating between the hot source and the cold surface according to eq. (26):

$$\text{Hot source operation window} = T_{hot}^{max} - T_{hot}^{min} \quad (26)$$

#### 3.2. Calculation of the intrinsic snap-up and -down temperatures $T_s$ and $T_{sb}$ of a bimetal mounted in the harvester as a function of the desired minimum hot source temperature $T_{hot}^{min}$

Another application of the model is the ability to design a bimetal with its own snap-up temperature  $T_s$  and snap-back temperature  $T_{sb}$  for a fixed desired  $T_{hot}^{min}$ . In fact, for some cases, if one wants a bimetal with a fixed hysteresis  $\Delta T$  to start oscillating at a certain hot source temperature, it is possible to calculate the intrinsic snap-up and snap-back temperatures of the bimetal.

Using equations (24) and (25) where  $T_{hot}^{min}$  is well known so as  $\Delta T$ , and knowing that  $T_{sb} = T_s + \Delta T$ , it is possible to calculate the snapping temperature of a certain bimetal with the previous fixed characteristics according to eq. (27):

$$T_s = \frac{3T_{hot}^{min} \cdot \Delta T - \Delta T^2 + \Delta T \cdot T_{amb}}{4\Delta T} \quad (27)$$

Then, the snapping back temperature  $T_{sb}$  is deduced thanks to the value of the bimetal hysteresis.

### 3.3. Calculation of bimetal's maximal snapping frequency

By using the model of the harvester in dynamic mode, it is possible to study the behavior of the bimetal and the evolution of its snapping frequency, snapping period and output power depending on the hot source temperature.

In fact, referring to the equations 16 and 19, the snapping period of the bimetal is equal to:

$$t_{Snap} = \Delta t_{hot} + \Delta t_{cold} \quad (28)$$

Consequently, the snapping frequency of the bimetal is given by:

$$f_{Snap} = \frac{1}{t_{Snap}} = \frac{1}{\Delta t_{hot} + \Delta t_{cold}} = \frac{1}{R_{heating} \cdot C_b \cdot \ln\left(\frac{T_{sb} - T_{hot}}{T_s - T_{hot}}\right) + R_{cooling} \cdot C_b \cdot \ln\left(\frac{T_s - T_{cold}}{T_{sb} - T_{cold}}\right)} \quad (29)$$

Then, using equation (29), we can for each bimetal mounted in the harvester with a snapping temperature  $T_s$  and a snap-back temperature  $T_{sb}$  calculate the hot source temperature for an optimized frequency. In fact, this point is characterized by an optimum in the harvested power as the duration between two snaps of the bimetal is minimized.

To obtain the hot source temperature that fulfills this condition, the frequency should satisfy the following equation:

$$\frac{\partial f_{snap}(T_{hot})}{\partial T_{hot}} = 0 \quad (30)$$

This is equivalent to solve the equation below:

$$T_{hotmax}^2 - T_{amb}^2 + 2T_{amb}T_{sb} - 2T_sT_{sb} + 2T_{amb}T_s - 2T_{amb}T_{hotmax} = 0 \quad (31)$$

The hot source temperature at which the snapping frequency of the bimetal is optimized is then given by equation (32):

$$T_{hotmax} = T_{amb} + \sqrt{2 \cdot (T_{amb} - T_s)(T_{amb} - T_{sb})} \quad (32)$$

Using these previous equations, we can simulate and analyze the behavior of the bimetal in two different cases: we can first study the case of bimetal having the same snapping temperature and different thermal hysteresis, and then the case of bimetal having the same thermal hysteresis and different snapping temperatures.

## 4. Model experimental validation and interpretation

### 4.1. Study of bimetal's hot source operation windows as a function of their hysteresis and of the hot source temperatures

An important step for each model operation is to be able to validate the results experimentally. Consequently, experimental tests are performed on a number of bimetal with different snap-up and snap-back temperatures but the same hysteresis of 3°C. Then a comparison of the experimental operation windows with the analytical ones given by equations (24) and (25) are performed. The experiments are carried out at an ambient temperature of 25°C. Consequently, to estimate  $T_{hot}^{min}$  and  $T_{hot}^{max}$ , we considered that  $T_{amb} = 25^\circ\text{C}$ . Tests are done for snap-up temperatures ranging from 50°C and up to 90°C. A comparison between the experimental data and the

analytical results is shown in Fig. 30.a.

Moreover, a study using the analytical dynamic model of the evolution of the operation window as a function of the hystereses of the bimetals is established. For this, simulations are carried out for hystereses going from 1°C up to 15°C using bimetals with a snap-up temperature of 70°C. The results of these simulations are shown in Fig. 30.b.

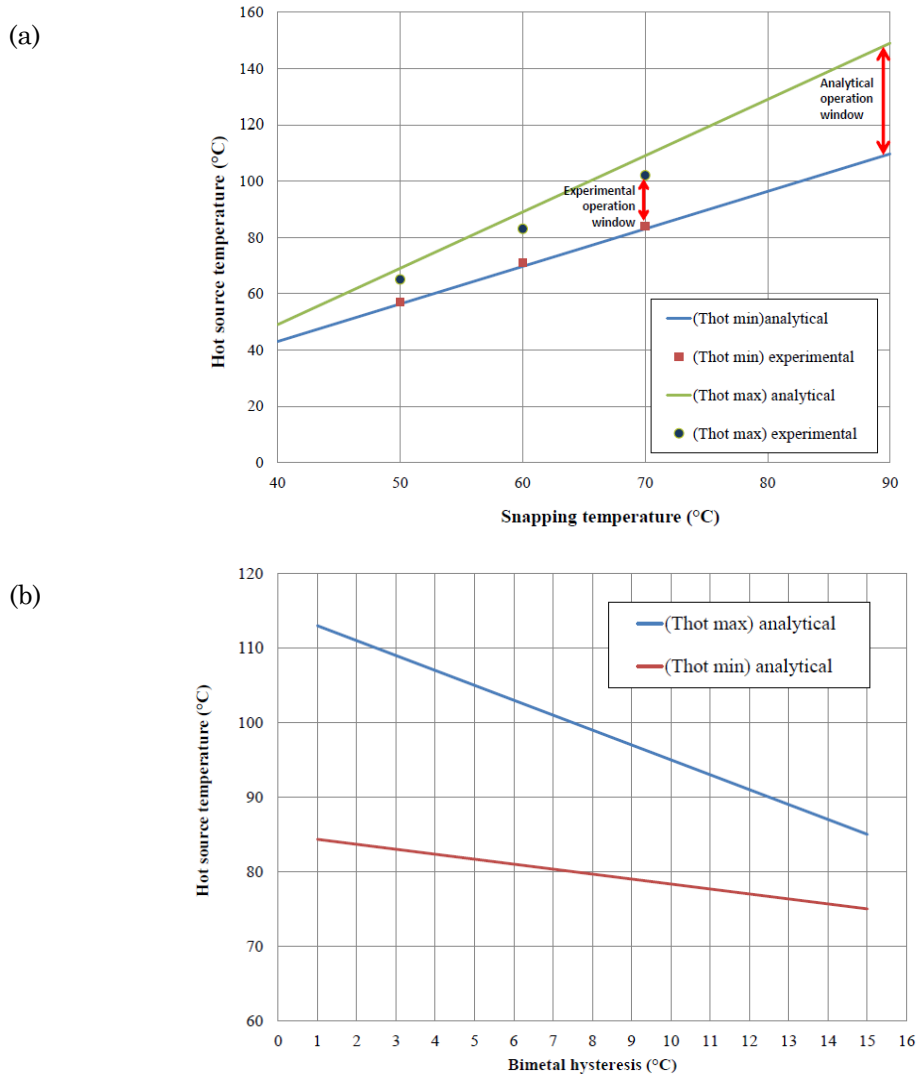


**Fig. 30.** a. Comparison of the experimental operation windows with their analytical counterparts ( $\Delta T=3^{\circ}\text{C}$  for all the bimetals), b. Simulations of the effect of the bimetal hysteresis on the hot source operation window ( $T_s=70^{\circ}\text{C}$  for all the bimetals).

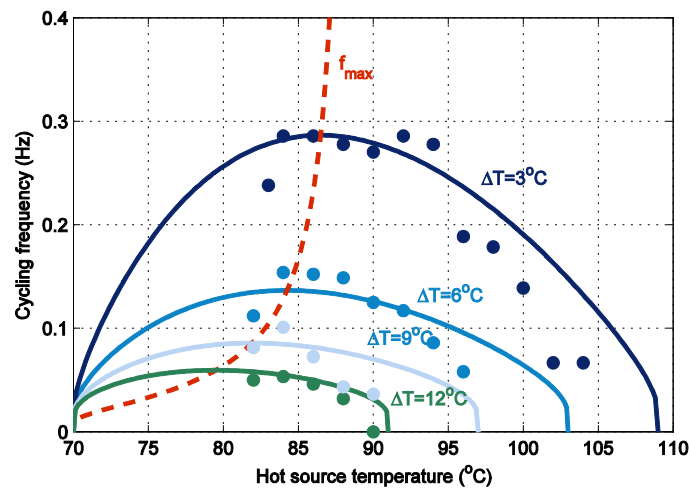
The experimental data and the analytical values given by the dynamic model are in a good agreement as shown in Fig. 30.a. In fact, the analytical operation windows are higher than the experimental ones but this can be due to the fact that, in the model,  $T_{hot}^{max}$  corresponded to the maximal temperature at which the bimetal would no longer oscillate and would be stuck at its upper position whereas experimentally, we did not achieve this temperature since the oscillating frequency of the bimetal becomes very low. This can be confirmed since the comparison of  $T_{hot}^{min}$  experimental vs analytical shows a perfect agreement while the comparison of  $T_{hot}^{max}$  analytical vs experiment shows that the analytical values are higher than the experimental ones.

Figure 30.a also makes it possible to conclude that it is better to use bimetals at higher temperatures meaning their snap-up temperatures are higher as their operation windows are more extended. Moreover, the comparison established in Fig. 30.b shows that it is more

interesting to use bimetals with the lowest hystereses if one wants the most extended operation windows. These main guidelines reveal that to obtain an extended operation window using only one device, one should prefer bimetals having high snapping temperatures and low thermal hysteresis.

#### 4.2. Simulations using bimetals with the same snapping temperature and different thermal hystereses

For this first study, we used four different types of bimetals. All of them have a fixed snap temperature of  $70^{\circ}\text{C}$  and hysteresis values ranging from 3K to 12K. For a complete study and interpretation of the results, using the previous equations, simulations of the evolution of the snapping frequency as a function of the hot source temperature are carried out. Experimental measurements are also established using the same bimetals sets and the different switching frequencies are measured over the range of hot source functioning temperatures. We observe in Fig. 31 that the experimental data show good agreement with the simulated model. This allows once again to validate the dynamic model. Furthermore, using the expression of the maximal snapping frequency thanks to equations 17 and 20, the snapping frequency evolution is plotted in that same graph Fig. 31 and the intersection of the dashed curve representing the maximal snapping frequency and each of the cycling frequencies curves gives the optimal hot source temperature at which the bimetal snapping frequency reaches a maximum.



**Fig. 31.** Snapping frequency evolution as a function of the hot source temperature ( $T_{\infty}=25^{\circ}\text{C}$ , Bimetal dimensions  $36*18*0,3\text{mm}^3$ ) experimental data (circular points) Vs analytical model (Continuous line).

Moreover, simulating the evolution of the time spent by the bimetal in the lower and then in the upper positions makes it possible to determine the point where these two times were equal. This point allows us to find the hot source temperature where the bimetal is at a thermal equilibrium. This is shown in Fig. 32.

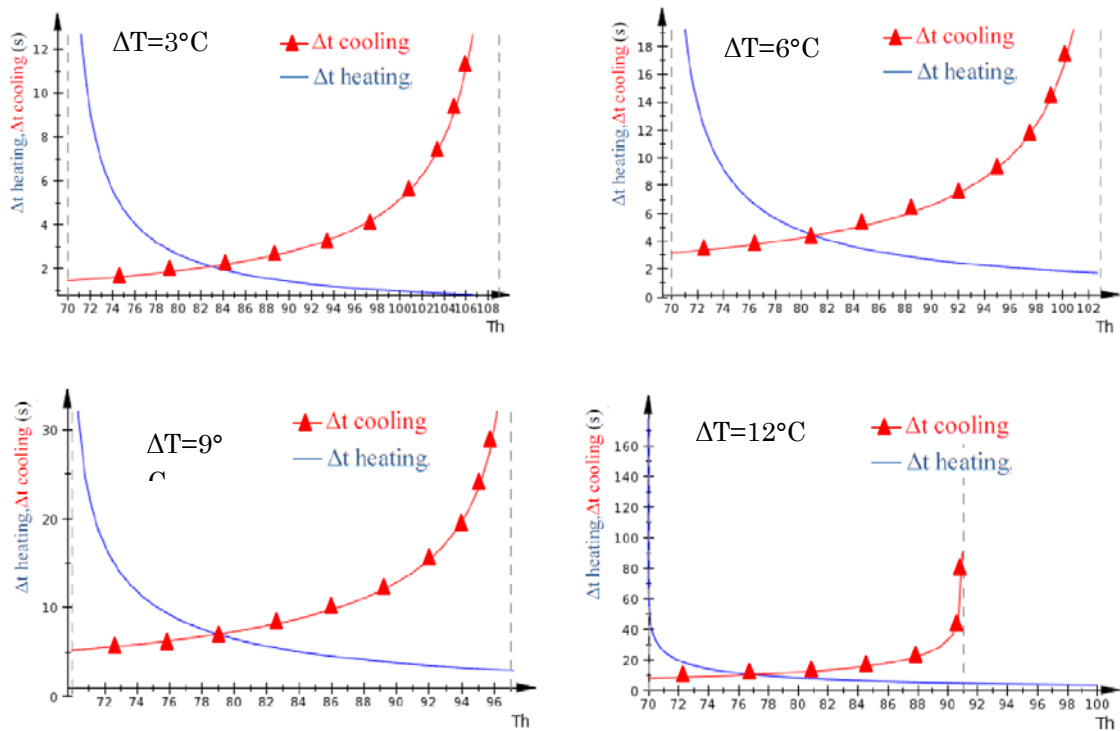


**Fig. 32.** Evolution of the cooling and heating times as a function of the hot source temperature.

First of all, according to Fig. 31, it can be stated that the lower the hysteresis of a bimetal is, the higher is its operation window. In fact, the bimetal with a hysteresis of  $3^\circ\text{C}$  shows a larger operation window than all the other hystereses. The explanation for this behavior is that the smaller the hysteresis is, the quicker the bimetal cools down and reaches its snap-back temperature in comparison with higher hystereses. Moreover, the comparison of the equilibrium temperatures of the bimetals in Fig. 32 shows that for a group of bimetals that all have the same snapping temperature but different snap-back ones, the higher the hysteresis of the bimetal is, the lower is the equilibrium temperature. In fact, the bimetal snapping at  $70^\circ\text{C}$  and with a  $15\text{K}$  hysteresis is the one with the lowest equilibrium temperature.

#### 4.3. Simulations with different snapping temperatures and a fixed thermal hysteresis

We use here the same procedure as previously described but this time we consider that all the bimetals have the same thermal hysteresis and different snapping temperatures. The studied bimetallic strips have snapping temperatures of  $70^\circ\text{C}$ ,  $80^\circ\text{C}$ ,  $90^\circ\text{C}$  and finally  $100^\circ\text{C}$ . The same simulations as those described in the last section are carried out with these bimetals and the results are summed up in Figure 33.

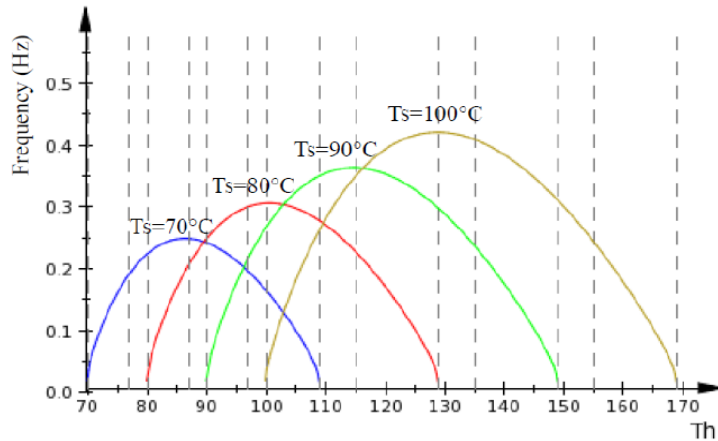


**Fig. 33.** Snapping frequency evolution as a function of the hot source temperature.

Referring to Fig. 33, we can say that even if bimetals have the same thermal hysteresis their operation window increases with the snapping temperature.

#### 4.4. Electrical output power as a function of the bimetals thermal hystereses

Using different sets of bimetals having hysteresis of 3K, 6K, 9K and 12K, experimental tests are realized to extract the available electrical output power on the piezoelectric capacitor. To do so, the first step is to have the exact snapping up and down temperatures of each bimetal. The bimetallic strips manufacturer provided us with these values summed up in Fig. 34.

Then, experimental measurements are carried out using these bimetals to measure the electrical output power on the piezoelectric capacitor. The experimental data measured when the bimetal is mounted in the harvester are shown in Fig. 35.

This graph clearly shows that the amount of electrical power decreases when the bimetal hysteresis increases; In fact, the bimetals having an hysteresis of 3K are the most powerful one. This can be explained by the fact that the 3K bimetals have quicker thermal exchanges with both the cold surface and with the hot source leading to more elevated snapping frequencies and consequently to higher amounts of electrical power.

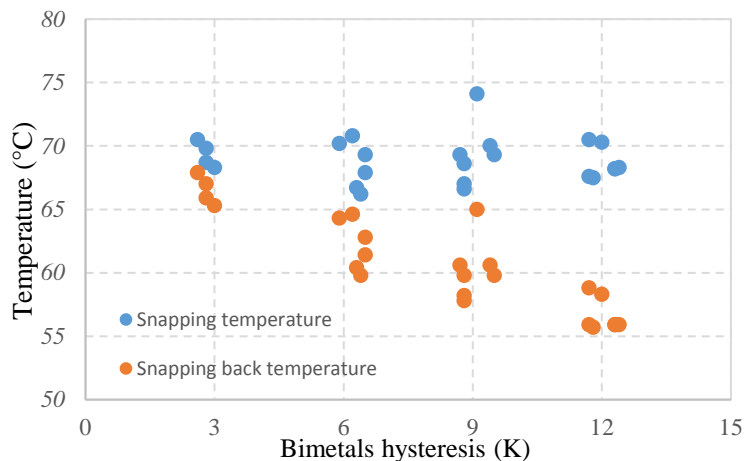


**Fig. 34.** Snapping up and down temperatures of different set of bimetals.

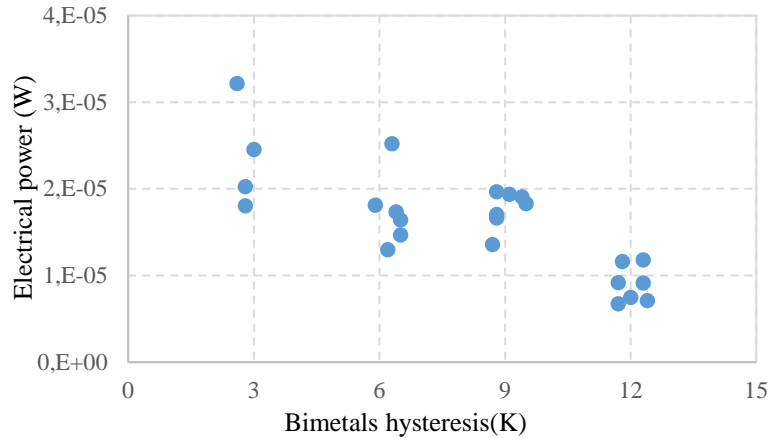


**Fig. 35.** Available electrical output power on the piezoelectric capacitor in function of the bimetal hysteresis.

#### 4.5. Analyses of the bimetal snapping temperature shift when it is put alone on a hot plate and once mounted in the harvester

The bimetals used in this work have two characteristic temperatures: the snap temperature  $T_s$  and the snap-back temperature  $T_{sb}$ . These temperatures are fixed by the fabrication process. To find these, the bimetals are put into an oven in which the temperature is uniform and the bimetals are being heated from all the sides by forced convection and not only at their middle where the hallmark is. Consequently, a difference occurs between the configuration where the bimetal is tested by the manufacturer to give the snapping temperatures and the case where only the hallmark is in direct contact with the hot source. Thus, a small shift of some degrees is observed.

Once it is mounted in the structure, the previously observed shift in the snapping temperatures is also increased for two reasons:

1. The bimetal is no more in contact with the hot plate directly but with a copper cylinder, consequently, thermal resistances are added and one should have higher hot source temperature to make the bimetal snap.
2. The bimetal is put into an air cavity inside a peek substrate. Consequently, the thermal flux from the hot source is divided into two parts: a first part goes through the peek substrate, this part is considered as losses and the only efficient thermal flux that makes the bimetal snap is the one going through the copper cylinder and lately crossing the bimetal. Consequently, higher hot source temperature are needed to make the intrinsic bimetal snapping temperature correspond to the one given by the manufacturer.

## V. Conclusion

In the first part of this chapter, the various steps of thermal analytical modeling in steady state conditions are presented. An equivalent circuit approach taking into account all the modes of heat transfer in the harvester is then proposed. This thermal model makes it possible to obtain an analytical value of the cold surface temperature in good agreement with the experimental measures over a wide range of hot source temperatures. A 2-D Finite Element Model developed by the ESI software platform also confirms the proposed model. In this investigation, the analytical model based on the electrical-to-thermal analogy allowed further improvements based

on the matching of thermal resistances. That principle is the key point of this work since it ensures that a maximum temperature difference can be maintained across the structure for any hot source temperature. An optimal design of the structure is also found: for a fixed external thermal resistance, the internal thermal impedance of the structure is matched with the external one giving consequently the main guidelines for design improvements. This approach is then validated on an optimized harvester where the experimental measurements confirm the thermal gradient maximization by a factor two.

The heat transfer inside a matrix of many cells is also studied using the finite element model developed by ESI. Given the thermal optimization performed on one individual harvester, the temperature distribution remained very close to that of a single cell when matrix structures are considered. Moreover, predictions of the thermal behavior as a function of scaling the harvester's geometrical dimensions are given based on the thermal model of a thermally matched energy harvester. Finally, in the case of a scaled-down device, ways of improvements in order to maintain good thermal properties were proposed. This work have been published in the journal *Smart materials and structures* in reference [15]

In the second part of this chapter, we established a dynamic model describing the dynamic behavior of a bimetal inside the harvester. This model assumes that bimetals behave like switched capacitances oscillating between two equilibrium states depending on the evolution of their intrinsic temperature. The analytical results given by the model are validated by the experimental data, thus confirming that the model can be a very useful tool for estimating the snapping temperatures of a bimetal once mounted in a harvester and for improving the thermal window of each bimetal introduced in a prototype. This approach gives us the main guidelines to determine what kind of bimetals and which hysteresis and snap-up temperatures must be used, depending on the use case and the desired operation window. This work has been published in the journal *Sensors and actuators* in reference [18].

## VI. References

- [1] [www.micropelt.com](http://www.micropelt.com).
- [2] Arnaud, A et al. "Thermo-Mechanical Efficiency Of The Bimetallic Strip Heat Engine At The Macro-Scale And Micro-Scale". *J. Micromech. Microeng.* 25.10 (2015): 104003.
- [3] Esarte, J., G. Min, and D.M. Rowe. "Modelling Heat Exchangers For Thermoelectric Generators". *Journal of Power Sources* 93.1-2 (2001): 72-76.
- [4] Rowe, D.M., and G. Min. "Design Theory Of Thermoelectric Modules For Electrical Power Generation". *IEE Proceedings - Science, Measurement and Technology* 143.6 (1996): 351-356.
- [5] Rowe, D.M., and Gao Min. "Evaluation Of Thermoelectric Modules For Power Generation". *Journal of Power Sources* 73.2 (1998): 193-198.
- [6] Leonov, Vladimir, Paolo Fiorini, and Ruud J.M. Vullers. "Theory And Simulation Of A Thermally Matched Micromachined Thermopile In A Wearable Energy Harvester". *Microelectronics Journal* 42.4 (2011): 579-584.
- [7] Leonov, Vladimir. "Thermoelectric Energy Harvesting Of Human Body Heat For Wearable Sensors". *IEEE Sensors J.* 13.6 (2013): 2284-2291.

- [8] Leonov, Vladimir. "Simulation of Maximum Power In The Wearable Thermoelectric Generator With A Small Thermopile". *Microsystem Technologies* 17.4 (2011): 495-504.
- [9] Wang, Ziyang et al. "Realization of A Wearable Miniaturized Thermoelectric Generator For Human Body Applications". *Sensors and Actuators A: Physical* 156.1 (2009): 95-102.
- [10] V. Leonov, P. Fiorini, "Thermal matching of a thermoelectric energy scavenger with the ambient, in: Proceedings of 5th European Conference on thermoelectrics", Odessa, Ukraine, September 10–12, (2007):129–133
- [11] Incropera, FP et al., 1996, *Fundamentals of heat and mass transfer*, 4th edition, John wiley & sons, USA.
- [12] Schalles, M et al., "Comparison of thermal modeling approaches for complex measurement equipments", *International journal of thermophysics* 35, (2014): 725-737.
- [13] Stevens, J W, "Optimal design of small  $\Delta T$  thermoelectric generation systems", *Energy conversion and management* 42, (2001): 709-720.
- [14] Puscasu, Onoriu et al, "An innovative heat harvesting technology (HEATec) for above-Seebeck performance" in *Electron Devices Meeting (IEDM), IEEE International*, (2012): 12.5.1–12.5.4.
- [15] Boughaleb, J et al. "Thermal Modeling And Optimization Of A Thermally Matched Energy Harvester". *Smart Mater. Struct.* 24.8 (2015): 085025.
- [16] Lurie, Eli, and Abraham Kribus. "Analysis Of A Microscale 'Saturation Phase-Change Internal Carnot Engine'". *Energy Conversion and Management* 51.6 (2010): 1202-1209.
- [17] McKay, Ian Salmon, and Evelyn N. Wang. "Thermal Pulse Energy Harvesting". *Energy* 57 (2013): 632-640.
- [18] Boughaleb, J. et al. "Analysis Of The Thermal Impact Of A Bimetal On The Dynamic Behavior Of A Thermal Energy Harvester". *Sensors and Actuators A: Physical* 236 (2015): 104-115.

## Chapter 3

# Harvester's architecture and materials improvements

Chapter 3.....	68
I. Introduction.....	70
II. Piezoelectric materials selection .....	70
1. Types of piezoelectric materials .....	70
1.1. Naturally piezoelectric crystals.....	70
1.2. Synthetic piezoelectric ceramics .....	71
1.3. Synthetic piezocrystals .....	71
1.4. Piezopolymers.....	72
1.5. Piezocomposites.....	72
1.6. Comparison of the piezoelectric materials .....	72
2. Impact of the piezoelectric materials properties on the output power .....	73
2.1. Elastic compliance $s_{11}$ .....	74
2.2. Piezoelectric strain constant $d_{31}$ and piezoelectric stress coefficient $g_{31}$ .....	74
2.3. Electromechanical coupling coefficient $k_{31}$ .....	75
2.4. Factor of merit FOM: .....	75
3. Comparison of piezoelectric materials properties.....	76
III. Device architectures improvements.....	77
1. Electrical power output calculation .....	77
2. Substrate material .....	78
3. Contact of the bimetal with the cold surface.....	80
4. Decreasing the device and bimetal dimensions .....	81
	68

5.	Positioning of the piezoelectric membrane .....	84
6.	Test of piezoelectric membrane from different manufactures .....	85
7.	Study of bimetals of higher thermal hysteresis and dimensions .....	88
8.	Improved device efficiency .....	94
IV.	Device lifetime and aging .....	95
1.	Bimetals lifetime .....	95
2.	Piezoelectric membranes lifetime .....	97
2.1.	Thermal degradation .....	97
2.2.	Mechanical degradation.....	98
V.	Conclusion .....	102
VI.	References.....	102

## I. Introduction

In the previous chapters, we explained the general working principle of the thermal energy harvester based on bimetallic strip heat engines and piezoelectric membranes. We also explained the thermal modeling and optimization of the generator in steady state conditions for a better thermal management and in dynamic mode for a higher output power generation through more efficient choice of thermally bistable bimetals. However, until now, no study has been realized to improve the device performances. This chapter will consequently deal with this issue.

First of all, piezoelectric materials types are reviewed, the pros and cons of each group of materials are exposed and the most adapted materials for our applications are pointed out. The piezoelectric materials properties are also independently studied and the way they are related to the piezoelectric output power explained. The goal is to have a methodology based on numerous piezoelectric materials properties to evaluate the effectiveness of each piezoelectric materials for energy harvesting purposes.

In the second part of this chapter, a benchmarking work on our thermal energy harvester will be presented. To do so, not only different piezoelectric membranes are tested experimentally and their efficiency evaluated but also experiments on different dimensions bimetals are realized. Moreover, based on the two key points of the harvester (piezoelectric membrane + bimetal), we tested new architectures with different piezoelectric membranes boundary conditions. The goal behind this work is to find the architectures that allows the highest amount of electrical power energy harvesting.

Finally, aging tests are realized on the generator to see if the different components of the device are sufficiently robust and stable over time.

## II. Piezoelectric materials selection

### 1. Types of piezoelectric materials

Since the discovery of the piezoelectric effect by the Curie brothers in 19<sup>th</sup> century [1], many piezoelectric materials have been developed and are now available. The first point we started our study with, is the choice of an adapted piezoelectric material to efficiently convert the bimetal kinetic energy into electrical energy. In this paragraph, a review of the different existing piezoelectric materials is proposed to finally point out the kind of piezoelectric material we will focus our work on.

Piezoelectric materials can be divided into 4 groups: piezocrystals, piezoceramics, piezopolymers and piezocomposites.

#### 1.1. Naturally piezoelectric crystals

The piezoelectric effect was first discovered and demonstrated in natural materials such as quartz, tourmaline and sodium potassium tartrate [2]. To exhibit a piezoelectric effect, the material structure must have no center of symmetry so that each time a tensile or compressive stress is applied to the crystal, the separation of positive and negative charges in each domain of the structure leads to the apparition of a net polarization at the crystal surface. These crystals have been widely used in the realization of electromechanical transducers. However, their low piezoelectric coupling coefficient, their high cost and fragility are the reasons why they are much less integrated in the current products for energy harvesting.

## 1.2. Synthetic piezoelectric ceramics

Besides these crystals, other piezoelectric materials have been discovered during the Second World War: the piezoelectric ceramics. Presently, piezoceramics are the most used piezoelectric materials. These are synthetic polycrystalline ferroelectric materials with a perovskite crystal structure. Their general formula is  $A^2+B^1+O^{2-}$  where A is a divalent metal ion such as barium or lead (Pb, Ba...) and B denotes a tetravalent metal ion like titanium or zirconium (Tr, Zr...). Barium titanate  $BaTiO_3$  [3] was the first piezoceramics to be discovered. Although it has higher performances than natural piezoelectric materials, it has a low Curie temperature ( $T_c = 120^\circ C$ ) and a relatively low piezoelectric coupling coefficient ( $k = 0.35$ ). Later, lead-based materials emerged with highest performances and exceeded those of barium titanate. Lead zirconate titanate is a metallic oxide based piezoelectric material developed by scientists at the Tokyo Institute of Technology around 1952 [4]. PZT ( $PbZr_{1-x}Ti_xO_3$ ) has a piezoelectric coupling coefficient around 0.7 and a high Curie temperature (up to  $400^\circ C$ ). It crystallizes in a perovskite structure and, it has been shown that for  $x \approx 0.5$ , the piezoelectric effect is maximized [5]. PZT is also easy to process so that molding in a wide variety of shapes and sizes is possible and it has an affordable cost which makes it the most commonly used piezo ceramic today.

There are different types of PZT ceramics. A simple classification is to consider soft and hard PZT ceramics. Soft ceramics as PZT 5H are used when high coupling coefficient and high charge sensitivity are required. They produce larger displacements and wider signal bandwidths than hard ceramics. However, they are more susceptible to depolarization or other deteriorations and their Curie temperature is below  $300^\circ C$ . Thus, these materials have a better piezoelectric response compared to hard ceramics and are used primarily in sensing applications, rather than in power applications like ultrasonic nondestructive testing applications or accurate inspections of automotive, structural or aerospace products.

Hard PZT ceramics are used for high power applications including the generation of ultrasonic waves or high-voltage energy in ultrasonic cleaners or sonar devices. PZT-4 belongs to hard PZT ceramics that have higher quality factors and so low mechanical losses under the demanding conditions. Their Curie temperature is above  $300^\circ C$  and they are more difficult to polarize or depolarize, explaining why hard ceramics present the advantage of being more stable. Table 1 sums up the main properties differences between soft and hard ceramics.

Material property	Soft PZT ceramic	Hard PZT ceramic
<b>Piezoelectric constant</b>	Larger	Small
<b>Permittivity</b>	High	Low
<b>Dielectric constants</b>	Large	Small
<b>Dielectric losses</b>	High	Low
<b>Electromechanical coupling factor</b>	Large	small
<b>Mechanical quality factor</b>	Low	High
<b>Coercive field</b>	Low	High
<b>Polarization/Depolarization</b>	Easy	difficult

*Table 1. Comparison of soft and hard ceramics properties [4].*

## 1.3. Synthetic piezocrystals

In the early 1980, new single crystal materials called PMN-PT have been synthesized. This family has the highest piezoelectric coefficients known to date. PMN-PT is particularly attractive because it has a coupling coefficient  $k_{33} \approx 0.9$ . It also has a factor of merit four times higher than

that of the PZT 5H due to the high values of its piezoelectric strain coefficient and piezoelectric voltage coefficient. However, PMN-PT's main drawbacks are its low Curie temperature that does not exceed  $T_c=120^\circ\text{C}$ , its high mechanical losses and its elevated cost. Researches are currently being done to overcome these drawbacks and to achieve better mechanical properties and thermal stability [6].

#### 1.4. Piezopolymers

These materials were first discovered in 1969 and were commercialized in the early 1980. PVDF (Polyvinylidene fluoride) is the most reported piezoelectric polymer and is very attractive for applications in the acoustic field. In fact, some of its properties are far lower than PZT's properties, more specifically if we look at its electromechanical coupling factor ( $k=0.2-0.3$ ) and its low breakdown voltage. Yet piezopolymers are very attractive because of their interesting mechanical properties and flexibility that make possible to have various material shapes and sizes and to realize films as thin as a few tens micrometers. Piezopolymers also benefit from a low acoustic impedance and low quality factors that make them good broadband receivers for underwater sonars and biomedical imaging applications [7].

#### 1.5. Piezocomposites

Piezoelectric composites are a combination of an active material such as piezoelectric ceramic or single crystal phase bound with a passive material such as a polymer matrix or epoxy. In these materials, it is important to define the dimensional connectivity that illustrates the number of dimensions through which a material is continuous. Connectivity of a piezoelectric composite is shown as a combination of two numbers such as 1-3, 2-2 or 0-3 where the first digit represents the active material and the second digit represents the passive material [8]. Piezocomposites are the materials of choice for acoustic devices and applications due to their low acoustic impedance. The advantage of mixing piezoelectric ceramics with polymers is to combine the good piezoelectric properties of the piezoelectric material with the mechanical flexibility of polymers. Piezocomposites also allow customization of materials properties through the choice of the constituent materials, their volume fraction and the disposition of the piezoelectric phase. The main drawbacks are the temperature constraints relative to the polymer phase that reduces the maximum operating temperature and the processing during the manufacture. Manufacturing is also more expensive than for piezoceramics as massive piezoceramics or crystal must be converted into composites [7].

#### 1.6. Comparison of the piezoelectric materials

Table 2 presents some materials of the aforementioned piezoelectric groups and compares all the important materials properties to find the adequate one for our application.

Type of material	Unit	PZT-4 hard ceramic	PZT-5H soft ceramic	PVDF polymer	PMN-PT single crystal
Coupling coefficient $k_{31}$		0.47	0.52	0.19	0.57
Coupling coefficient $k_{33}$		0.69	0.75	0.13	0.9
Strain coefficient $d_{33}$	pm.V <sup>-1</sup>	290	590	25	1400
Piezoelectric voltage constant $g_{33}$	mV.m.N <sup>-1</sup>	26	20	230	30
Mechanical quality factor $Q_m$		High	Medium	Low	Low
Electrical loss tangent $\tan\delta$		0.004	0.02	0.3	0.01
Relative permittivity at constant stress $\epsilon_{33}^T$		1270	3430	8.4	3950
Relative permittivity at constant strain $\epsilon_{33}^S$		640	1470	10-12	818
Young modulus $Y$	GPa	60	65	3	
Piezoelectric figure of merit FOM= $d_{33}.g_{33}$	pm.N <sup>-1</sup>	7.5	12	5.8	43
Curie temperature $T_c$	°C	Medium/High (≈350°C)	Medium (≈200°C)	Low (≈150°C)	Low (≈120°C)

*Table 2. Comparison of some piezoelectric materials properties [7,9].*

The calculation of the piezoelectric figure of merit and the comparison of the different materials parameters show that the most interesting material for our application is the soft ceramic PZT-5H. The single crystal PMN-PT has the highest performances but one should keep in mind its elevated cost and its low Curie temperature that are not compatible with our application. Our thermal energy harvester is bound to be a low cost solution and should function on hot source temperatures going from 50 and up to 200°C, thus the piezoelectric membrane temperature can reach 100°C for an ambient temperature of 25°C. Knowing that for a long term operating temperature should not exceed  $T_c/2$ , PZT-5H seems to be a good candidate. Generally, piezoelectric ceramics are the preferred choice for energy harvesting because they are physically strong, chemically inert and relatively inexpensive to manufacture.

## 2. Impact of the piezoelectric materials properties on the output power

From the previous part, soft and hard piezoelectric ceramic materials seem to be good candidates for energy harvesting purposes. However, it is important to point out the material parameters to consider in order to choose the most appropriate and the best material for our application. To do so, Daniels in [10] led a study on the impact of the piezoelectric material properties on the power output delivered by a piezoelectric plate poled in the thickness direction with an applied force at its both ends. The goal of this part is not to see the amount of power delivered by the plate but to see the impact of the different piezoelectric parameters on the output power. To find the optimal output power, the author used a finite-elements model to simulate the output power on different values of load resistances and kept only the optimal resistance that provides the highest power output from the piezoelectric generator. Details on the finite-elements model used for this study can be found in [11]. Different parameters can be considered to efficiently choose a piezoelectric material for energy harvesting purposes. Among them:

- $d$ : the piezoelectric strain constant
- $g$ : the piezoelectric stress constant
- the Factor of merit  $FOM=d \times g$

- the coupling coefficient  $k$
- the elastic compliance  $s$
- relative dielectric constant  $\epsilon$

The author in [10] studied the effect of each of these parameters to see how it is related to the piezoelectric output power.

### 2.1. Elastic compliance $s_{11}$

Figure 1 shows the electrical power as a function of the elastic compliance  $s_{11}$ . We observe that no trend appears on this plot and therefore no relation can be established between the elastic compliance and the amount of power output. Thus, the elastic compliance will not be taken into account for the choice of an efficient piezoelectric material for our energy harvester.

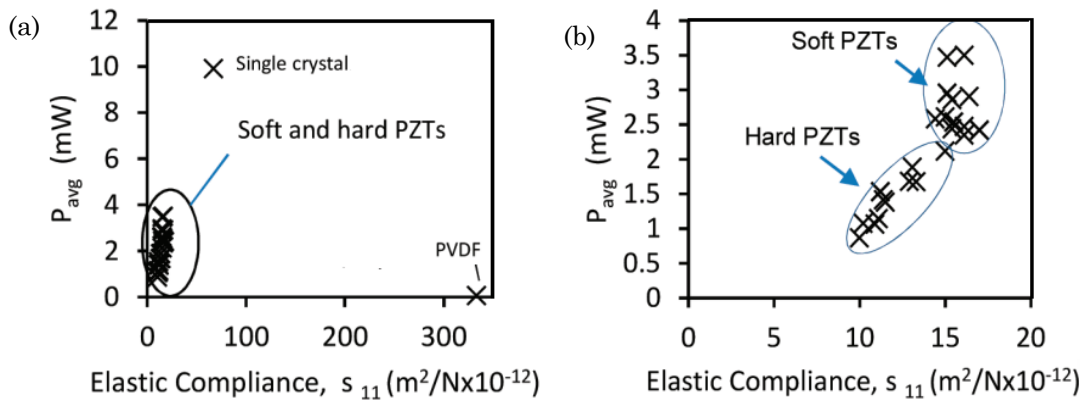


**Fig. 1.** Electrical power in function of elastic compliance a. for PZT ceramic, PVDF and single crystal materials, b. zoom on the PZT ceramics (from [10]).

### 2.2. Piezoelectric strain constant $d_{31}$ and piezoelectric stress coefficient $g_{31}$

Fig. 2.a shows the plot of the piezoelectric generator output power as a function of the piezoelectric materials strain constants and Fig. 2.b shows the output power with respect to the piezoelectric stress constant.

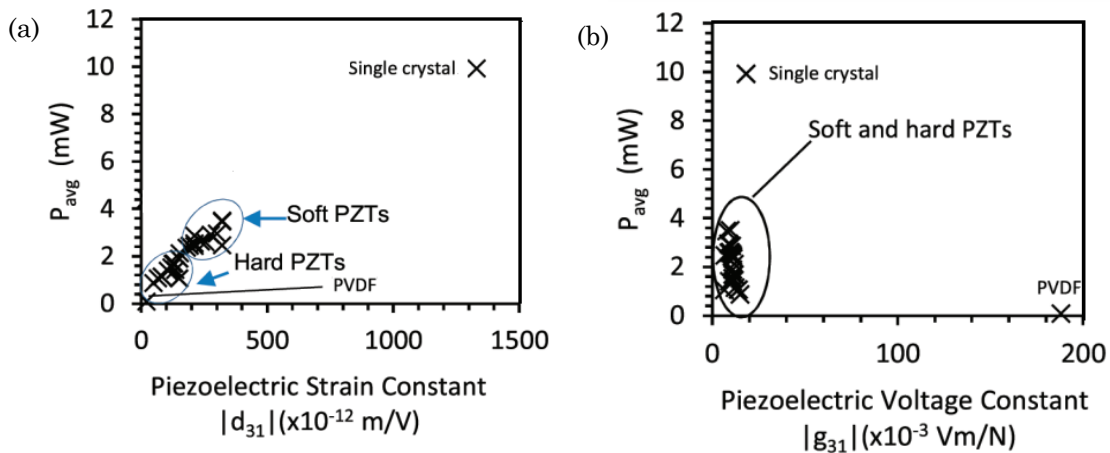


**Fig. 2.** Electrical power for PZT ceramics, PVDF and single crystal materials in function a. the piezoelectric strain constant  $d_{31}$ , b. the piezoelectric stress coefficient  $g_{31}$  (from [10]).

We observe that the higher  $d_{31}$  is, the higher the amount of electrical power is. Single crystal materials and soft PZT ceramics are the most powerful materials because of their higher  $d_{31}$ . This trend suggests that the piezoelectric strain constant should be considered as a parameter for piezoelectric materials choice. At the opposite, the piezoelectric stress coefficient shows no linearity with the output power. This suggests that  $g_{31}$  cannot be considered as a parameter for materials choice.

It is also shown in that paper that  $d_{31}$  is a more dominant parameter than  $\epsilon_{33}$  for higher electrical power output and that lower values of  $\epsilon_{33}$  lead to higher power. To demonstrate this results, the author selected several groups of materials with almost identical  $d_{31}$  but with different values of dielectric constants. The result was that materials with lower  $\epsilon_{33}$  allowed more power to be generated.

Up to now, the two most efficient parameters for materials choice are a high  $d_{31}$  coefficient value and if materials have the same  $d_{31}$ , one should choose the material with the lower  $\epsilon_{33}$ .

### 2.3. Electromechanical coupling coefficient $k_{31}$

Fig. 3 shows a plot of the power output as a function of the electromechanical coupling coefficients. This plot shows that higher  $k_{31}$  leads to higher electrical power. However, we observe that some materials have the same  $k_{31}$  but different values of electrical power. The author explains this difference by the fact that these materials have different values of  $d_{31}$  and the material with the highest strain coefficient creates more electrical charges.

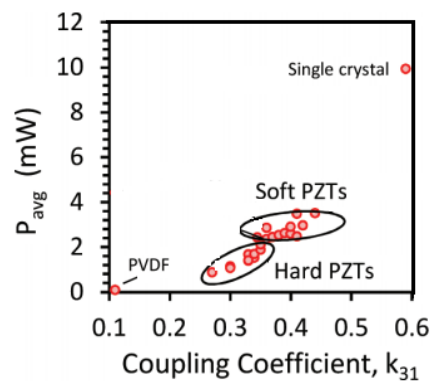


**Fig. 3.** Electrical power for PZT ceramics, PVDF and single crystals in function the coupling coefficient  $k_{31}$  (from [10]).

### 2.4. Factor of merit FOM:

Fig. 4 shows the evolution of the power output for soft and hard ceramic materials in function of these materials factor of merit. A linear relation is observed between the output power and the factor of merit. However, for materials 1 and 2 that have the same FOM, the electrical power is different. This explains that the FOM cannot be used a single parameter for materials choice but one should combine different parameters for a higher power output. What explains the difference between materials 1 and 2 is their respective values of  $d_{31}$  as material 2 has a higher piezoelectric strain constant than material 1.

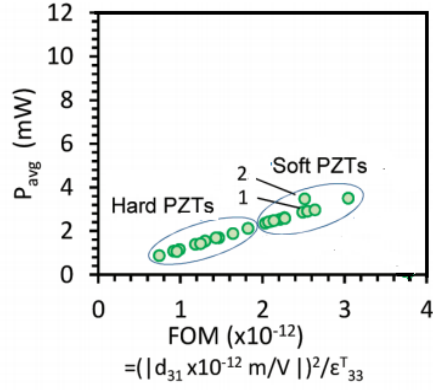


**Fig. 4.** Electrical power for PZT ceramics in function of the factor of merit (from [10]).

To sum up all the results presented above and extracted from Daniel’s study in [10], we can conclude that no single parameter can be considered for efficient piezoelectric material choice but one should combine the FOM with the  $d_{31}$  parameter for a best selection. First one should choose materials having the highest FOM. If two materials have similar FOM values, one should keep the materials having the highest piezoelectric strain coefficient. Again if materials have similar values of  $d_{31}$ , the relative dielectric constant should be considered and the material having the lowest  $\epsilon_{33}$  should be selected.

### 3. Comparison of piezoelectric materials properties

The aim of this paragraph is to present the benchmark realized to choose the best piezoelectric material for our energy harvester. To do so, we used the same methodology as the one presented previously in [10]. The goal of our device is to harvest wasted heat from a temperature range going from 50°C and up to 200°C. The piezoelectric material to be selected should not only satisfy the preceding conditions related to the FOM, the dielectric constant and the piezoelectric strain constant but should also have a high Curie temperature. Our piezoelectric materials supplier provided us with a list of soft and hard piezoelectric ceramics. We applied on these materials the same methodology as previously and compared all the parameters in Table 3. Soft PZT ceramics are the ones used for energy harvesting because their piezoelectric coefficient are more attractive however, for comparison purposes, we also took hard PZT ceramics into account in this study.

Material parameter	Properties	Unit	KP-PZT-4 4M11	KP-PZT-4D 4M13	KP-PZT-8 8M10	KP-PZT-5A 5M18
$k_{31}$			0,3	0,33	0,31	0,35
$ d_{31} $	constant	$10^{-12}C/N$	140	150	100	172
$\epsilon_{33}/\epsilon_0$	dielectric constant		1200	1400	1030	1800
$T_c$	curie temperature	°C	330	320	300	358
<b>FOM</b>		$10^{-24}$	16,3	16,1	9,71	16,4

KP-PZT-5B 5M20	KP-PZT-5B 5M23	KP-PZT-5B 5M25	KP-PZT-5T 5M27	KP-PZT-5T 5M27D	KP-PZT-5H 5H32	KP-PZT-5H 5H38	KP-PZT-5X 5H45
0,36	0,37	0,33	0,38	0,39	0,39	0,38	0,36
186	230	200	230	210	275	280	350
2000	2350	2500	2700	2750	3200	3800	4300
316	290	292	280	280	260	250	178
17,3	22,5	16	19,6	16,0	23,6	20,6	28,5

**Table 3:** Piezoelectric materials proprieties and calculation of the factor of merit FOM.

Two materials seems to be very interesting for our application: KP-PZT-5H 5H32 and the KP-PZT-5X 5H45. Both of them have high factors of merit, and high  $d_{31}$  coefficient. The main difference between them is their curie temperature. For the KP-PZT-5H 5H32, its Curie temperature is equal to 260°C whereas it is equal to 178°C for the KP-PZT-5X 5H45. To avoid the ceramic depolarization, we choose the KP-PZT-5H 5H32 ceramic as it fits better our needs. However, the KP-PZT-5X 5H45 could still be used for lower temperatures but no experiment have been done with it as our supplier no more produces it. For all the experiments presented in this manuscript, the PZT 5H32 has been selected.

### III. Device architectures improvements

#### 1. Electrical power output calculation

Before presenting the optimization steps of the piezoelectric and bimetal thermal energy harvester, it is important to present the methodology followed to compare all the fabricated devices after each improvement step. As previously seen, each thermal energy harvester based on our technology has an output electrical signal corresponding to a succession of voltage peaks for each bimetal's snap or snap-back with the piezoelectric membrane. Each of these peaks corresponds to a damped sinusoid whose equation is given in (1):

$$v(t) = v_0 \cos(\omega t) e^{-\frac{t}{\tau}} \quad (1)$$

Where  $\omega$  is the signal's pulsation and  $v_0$  the amplitude of the first peak. For this signal, we define the following quantities:

The logarithmic decay $\delta$	$\delta = \ln\left(\frac{v(t)}{v(t+T)}\right) = \frac{t}{\tau} = 2\pi\xi$
The amortization rate $\xi$	$\xi = \frac{\Pi}{Q}$
The mechanical quality factor	$Q = \frac{1}{2\xi}$

From these defined quantities, we can obtain the expression of the signal's mechanical quality factor given in equation (2):

$$Q = \frac{nT2\pi f}{\ln\left(\frac{v(t)}{v(t+nT)}\right)} \quad (2)$$

Where T is the bimetal snapping period, f the resonance frequency of the piezoelectric bimetal when the bimetal snaps and n the number of the snapping periods considered for the signal's quality factor calculation.

The signal's energy is then given by equation (3) where  $t_1$  and  $t_2$  correspond to the duration of the damped sinusoid.

$$E = \int_{t_1}^{t_2} |v(t)|^2 = \frac{v_0 Q (4Q^2 + 2)}{2\omega(4Q^2 + 1)} \quad (3)$$

However, this energy does not correspond to the electric energy available across the piezoelectric capacitor. To obtain it, one should take into account the capacitance of the piezoelectric ceramic.

The expression of the available electrical energy on the piezoelectric capacitor is given in equation (4):

$$E_p = C\omega \int_{t_1}^{t_2} |v(t)|^2 dt = \frac{v_0 Q (4Q^2 + 2)}{2\omega(4Q^2 + 1)} C\omega \quad (4)$$

Finally, to obtain the electrical output power of a generator,  $E_p$  should be divided by the bimetal's snapping period. Its expression is given in equation (5).

$$P_p = \frac{E_p}{\text{Bimetal snapping period}} \quad (5)$$

In this manuscript, each time the electrical power output or energy is given, it corresponds to the available energy or power across the piezoelectric capacitor which is different from the useful power and energy used to power a wireless sensor node. For our measurements, we can consider that the output signals and calculated powers across the piezoelectric capacitor were measured in open circuit as the probe's impedance was sufficiently high (10M $\Omega$ ) to be neglected and to allow the visualization of the electrical signals as if the device was in an open circuit configuration.

However, we can give an approximation of the maximum useful power and energy of each energy harvester, since if the impedance of the generator is well adapted with that of an external charge impedance, the piezoelectric voltage across the charge will be equal to half of that of the voltage across the piezoelectric voltage in open circuit configuration in the best case. Given that the power is proportional to the square of the voltage, the useful power of each device across an adapted charge is equal to the fourth of the total available output power in open circuit.

## 2. Substrate material

The first thermal energy harvesters developed by Puscasu during his thesis [12] were made of Teflon substrate. In fact, it was necessary to use a thermally insulator to protect the piezoelectric membrane from depolarization and to maintain a thermal gradient between the hot source and the cold surface of the energy harvester. Consequently, both the device substrate and the screws needed to clamp the piezoelectric membrane on the bimetal were made of PTFE. Fig. 5.a presents the top view of the device used to establish the first proof of concept of the coupled piezoelectric and bimetal thermal energy harvester and fig. 5.b presents its lateral view. In Fig. 5b, we observe some foam between the PTFE substrate and the piezoelectric membrane. It was initially used to obtain a thicker air cavity for the bimetal's snapping actions but also to fix the bimetal on the piezoelectric membrane so that it does not go out of the cavity when the device is maintained in a vertical position.

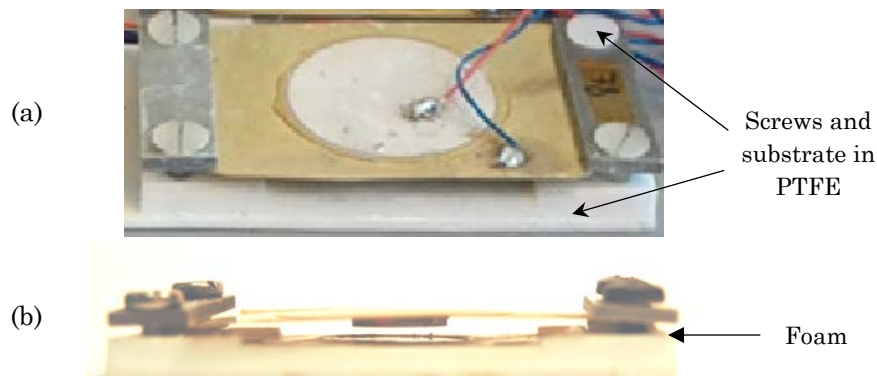


**Fig. 5.** (a). Top view and (b). Lateral view of the thermal energy harvester made of PTFE.

PolyTetraFluoroEthylene is commonly abbreviated PTFE. It offers high chemical resistance, low and high temperature capability, resistance to weathering, low friction and both electrical and thermal insulations [13]. However, its mechanical properties are low compared to other plastics. Table 4 presents thermal and mechanical properties of PTFE.

<b>Material property</b>	<b>Unit</b>	<b>Data</b>
<b>Thermal conductivity</b>	W/(K.m)	0.25
<b>Young modulus</b>	MPa	410 – 750
<b>Melting temperature</b>	°C	327
<b>Service temperature</b>	°C	-200 – 250
<b>Glass transition temperature</b>	°C	115

*Table 4. Thermal and mechanical properties of PTFE [14-15].*

The main drawback of using Teflon for our application is its low value of Young's modulus and its low glass transition temperature as our energy harvester is bound to work at a hot source's temperature reaching up to 200°C. Knowing that the PTFE substrate is in direct contact with the hot surface, this means that for temperatures ranging from 115°C to 200°C, the substrate will no more be hard and stiff, so the vibrations of the piezoelectric membrane after the bimetal snap will be damped, hence degrading the quality factor of the output electric signal. The same remark can be done for the screws in PTFE and for the foam which drastically damps the piezoelectric transducer's vibrations and reduces the efficiency of the generator. The other drawback of this material is that it provides no mechanical stability to the energy harvester: during the characterization of the piezoelectric membrane with an impedance meter, the resonance modes used to change at every frequency sweep even if the experimental conditions were kept exactly the same. This led us to conclude that the substrate material has to be changed. Keeping the device unchanged with a Teflon substrate did not allow the extraction of the membrane's quality factor and its piezoelectric coupling coefficient.

The first optimization step was to change the material of the substrate and to replace it by a material having better mechanical properties and thermal properties similar to PTFE. We thus replaced Teflon by another high temperature thermoplastic called PEEK for Poly (ether ether ketone). PEEK has the same thermal properties as PTFE as it is thermally stable for temperatures up to 250°C without a significant change of its physical properties. It has a thermal conductivity close to PTFE and its melting temperature is 340°C. However it overcomes the drawbacks of Teflon because of its high glass transition temperature around 143°C, but also due to its high elastic modulus (3,8GPa) which improves the clamp of the piezoelectric ceramic, hence reduces the mechanical energy losses. The thermal and mechanical properties of PEEK are summed up in table 5.

Material property	Unit	Data
Thermal conductivity	W/(K.m)	0.25
Young modulus	GPa	3.6
Melting temperature	°C	340
Service temperature	°C	-55 – 250
Glass transition temperature	°C	145

*Table 5. Thermal and mechanical properties of PTFE [15-16].*

Moreover, steel screws are used to clamp the oscillator to overcome the problems of weak tightening due to the screws made of PTFE. Finally foam is completely removed from the energy harvester, and air cavity is enlarged (as explained in Chapter 2) by increasing the thickness of the PEEK side parts.

Fig. 6 presents the new generator made of PEEK and thermally optimized in agreement with the specifications presented in the previous chapter.

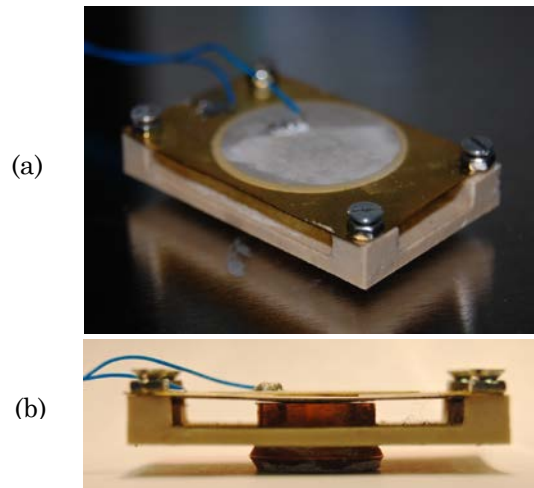


*Fig. 6. (a). Top view and (b). Lateral view of the thermal energy harvester made of PEEK and thermally optimized.*

### 3. Contact of the bimetal with the cold surface

Once the energy harvester was thermally optimized and the substrate material was changed, we measured the working range of each bimetal. The previous chapter explained that after the optimization of the generator's architecture, each bimetal can work over an extended temperature window of about 17°C. However, after designing a thermally optimized architecture, we experimentally observed that the generator was unable work over a range of few Kelvin degrees. We finally found that this issue was linked to the piece of cooper glued below the piezoelectric membrane whose initial role was to ensure a good contact between the bimetal at its upper position and the PZT membrane as shown in Fig. 7, but whose effect was an increase of the thermal resistance between the hot source and the bimetallic strip.

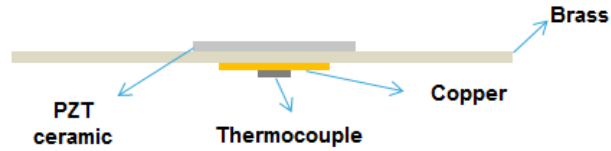


**Fig. 7.** Lateral view of the piezoelectric membrane.

To verify this hypothesis, a thermocouple was used to measure the temperature on this copper piece as shown in Fig. 7. First we tested 5 thin copper cylinders having a total height of 1.9mm and glued together using Loctite glue. Fig. 8 represents the temperature drop across the top of the harvester and the bottom of the copper pieces. A temperature drop around 12°C was observed across these copper cylinders which was an elevated temperature drop knowing that we chose copper for its very high thermal conductivity and its capability to evacuate the bimetal incident heat flux.

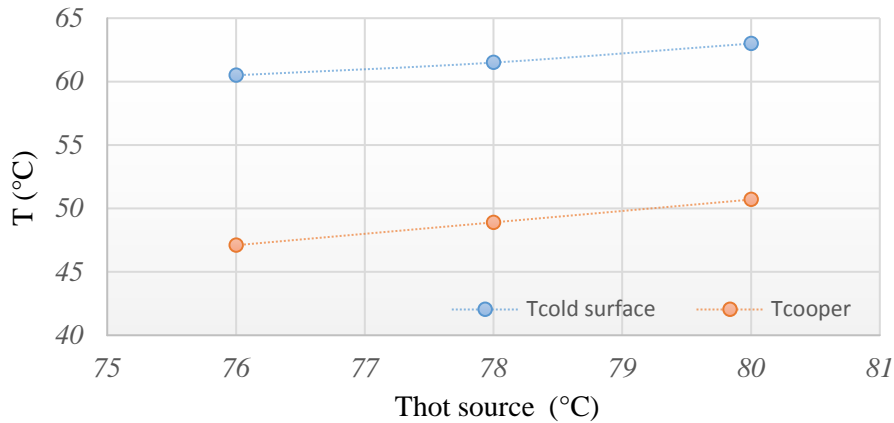


**Fig. 8.** Temperature drop across the glued copper cylinders and the cold surface.

To overcome this problem, we manufactured a copper cylinder whose height was equal to 1.9mm. We also used a thermally conductive adhesive (LOCTITE 384) that provides good heat dissipation. Then we performed the same experiment as in Fig. 8. This time, the temperature drop was equal to 2°C which is much more interesting for our device. When testing the new energy harvester with the optimized copper piece, the operation window was extended to more than 20K as shown in Chapter 2.

#### 4. Decreasing the device and bimetal dimensions

At the macro-scale the proof of concept of the thermal energy harvester was established by Puscasu in [12]. He also demonstrated in his work [17] that downscaling the device dimensions would allow an increase of the output power. This has led to further studies established by Trioux in [18] and Arnaud in [19] to show the feasibility of MEMS devices based on the same technology as at the macro scale. However, at the macro-scale, no generator's down-scaling was realized to check the validity of this scaling law. Consequently, we investigated this scaling and performances improvements by first scaling the energy harvester's dimensions by a factor 2.5. In his scaling law, Puscasu assumed that if the device's dimensions were scaled down by a factor k, then the electrical power generated by k coupled piezoelectric generators would be k times larger compared to a single component occupying the same surface and this, without using a heat sink

with fins. So following this law, if we scale the device dimensions by a factor 2.5, a single miniaturized module will produce the same amount of power as the initial harvester. To make a comparison, we ordered to Delta Concept bimetals snapping at 70°C and snapping back at 67°C at the dimensions 38x18x0.3mm<sup>3</sup> and 15x10x0.115mm<sup>3</sup>. The first difficulty encountered in this scaling strategy concerns the device thickness. Puscasu in his work specified that all the device dimensions should be scaled by the same factor  $k$ . But, as explained previously in chapter 3, the total thickness of the miniaturized harvester should not be scaled otherwise the thermal gradient across the harvester will be drastically reduced. So, to maintain the same thermal properties for the initial generator and the miniaturized generator, their height must be the same. Fig. 9 presents the two devices fabricated for this study.

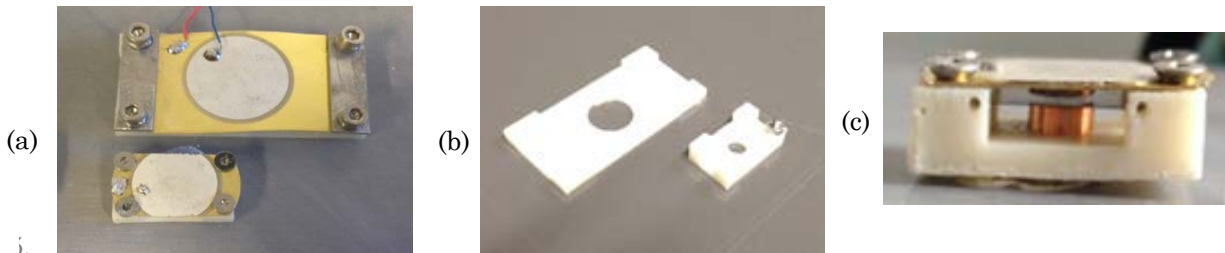


**Fig. 9.** (a) Top view of the two devices, (b) Top view of the substrates of the initial and the scaled devices, (c) Lateral view of the scaled harvester.

The miniaturized and the initial devices are tested under the same experimental conditions: in both cases, the bimetal's heating phase lasts the same time than its cooling phase. The output signals are shown in Fig. 10.a for the initial harvester and in Fig. 10.b for the scaled one. Table 6 sums up the evolution of the physical parameters of a scaled down harvester by a factor  $k$  according to [20].

Parameter	Evolution with the scaling by a factor $k$
Frequency	Increase $k^2$
Snapping and snapping back temperatures	Unchanged
Bimetal force	Decrease $k^2$
Piezoelectric capacitance	Decrease $k$
Piezoelectric voltage	Decrease $k$
Electrical power per surface	Increase $k$

**Table 6.** Evolution of the working parameters in the harvester in function of a scaling factor  $k$  according to [20].

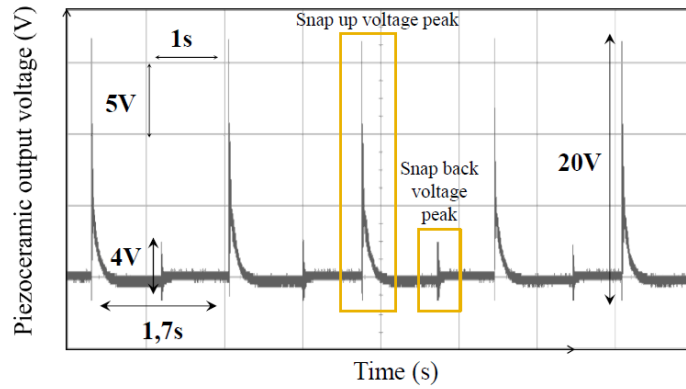


**Fig. 10.a.** Output electrical signal obtained with the initial harvester using a 67-70°C bimetal and a 10MΩ probe (at  $T_{hot} = 94^{\circ}\text{C}$ ).

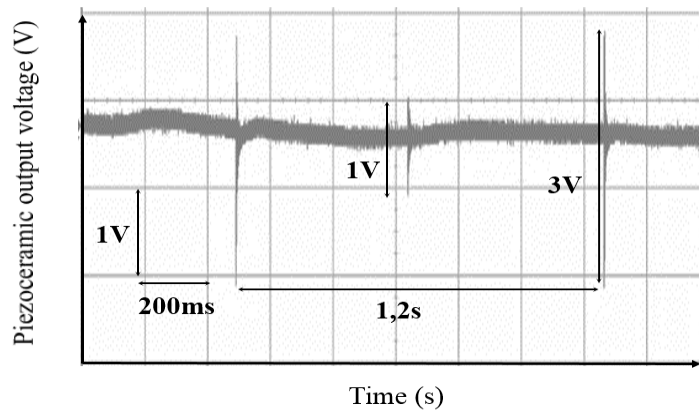


**Fig. 10.b.** Output electrical signal obtained with the scaled harvester using a 67-70°C bimetal and a 10MΩ probe (at  $T_{hot} = 96^{\circ}\text{C}$ ).

The capacitance of the initial piezoelectric membrane is 70nF and the capacitance of the small piezoelectric membrane is equal to 25nF. The comparison of the output signals of each of the harvesters shows that the scaling law is not satisfied. In fact, the working frequency for the downscaled generator was supposed to be 2.5 times higher than the switching frequency of the initial generator, due to the boosted thermal transfers. Here, the frequency is only 1.4 times higher. Moreover, the output piezoelectric voltage does not follow the expected trend: instead of being 2.5 times lower, it is more than 6.5 times lower when the bimetal snaps up and 4 times lower when the bimetal snaps down. Knowing that energy is proportional to the voltage square and to the capacitance, taking into account the output signals in Fig.10, the energy per bimetal snap is more than 100 times lower for the miniaturized and the power is more than 70 times lower for that harvester. In fact, for the initial energy harvester, the available electrical power is around  $32\mu\text{W}$  whereas for the scaled harvester by a factor 2.5, the available electrical power is equal to  $0.52\mu\text{W}$ . Following the model established by Puscasu, we should have had the same power for the scaled device and the non-scaled one. This study shows that the established law is not verified and other techniques should be investigated to increase the amount of output energy and power. Arnaud in his thesis [19] ended his work with this same conclusion concerning that scaling law. He stated that the miniaturization of energy harvesters can allow to reach the same level of power surface density as the energy harvesters at the macroscale in the best cases, under the condition that a heat sink be used to evacuate heat flowing through the energy harvester. He also explained that many issues will be encountered with miniaturized generators: first the reduction of output voltages of miniaturized piezoelectric transducers due to weaker impact of bimetallic strips will represent a major challenge for power management circuits, and the reduction of the generator's lifetime due to the increase of the cycling frequency.

## 5. Positioning of the piezoelectric membrane

The piezoelectric membrane realizing the electro-mechanical conversion step is positioned over the bimetal at the top of the device. Consequently, two different configurations are possible: it can either be clamped at one end of the peek substrate as shown in Fig.11 to be used as a cantilever or it can be clamped at its two ends as shown in Fig. 8.a. In our current energy harvester, only the second configuration has been tested and investigated. Hereafter the two other configurations are realized and tested to find out the most powerful one. The design of the thermal energy harvester with the simply clamped piezoelectric membrane is presented in Fig. 11.

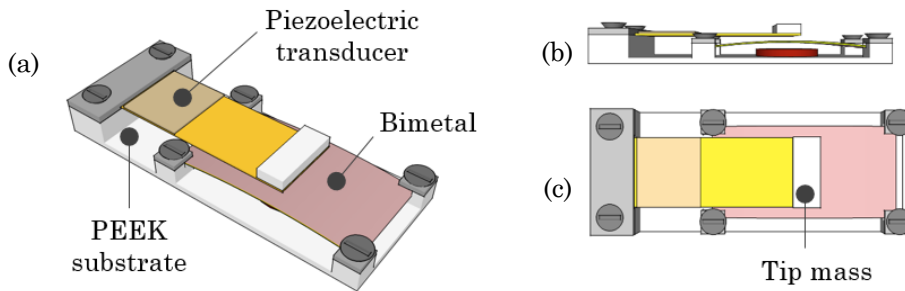


**Fig. 11.** (a). Thermal energy harvester with a simply clamped beam with a free end, (b). Lateral view of the device, (c). Top view of the device.

To extract the electrical power available across the piezoelectric ceramic capacitor, the output signal of the piezoelectric membrane was measured over the whole temperatures working range of the device. This enables to extract the optimal working temperature at which the output power reaches a maximum value. This procedure is repeated for each architecture to compare their performances.

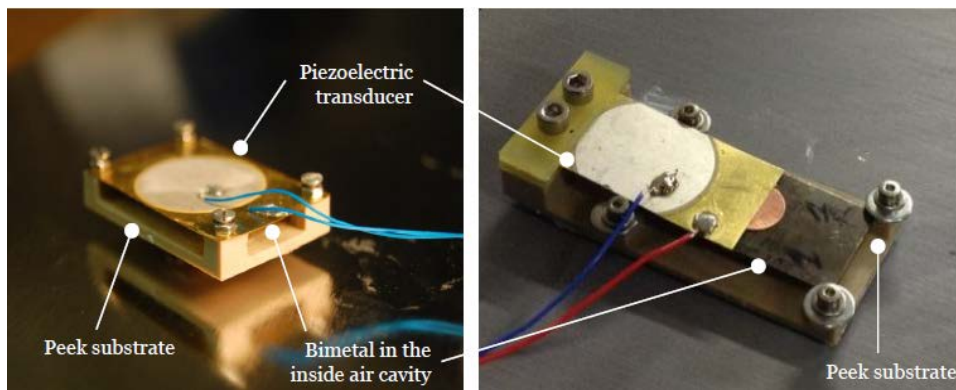


**Fig. 12.** Image of thermal energy harvester a. in a double clamped piezoelectric membrane configuration, b. with a cantilever piezo-beam with a free end.

The values of the electrical performances of the two devices are compared in Table 7. It shows that the double clamped piezoelectric membrane harvests more energy than the clamped-free membrane because the membrane is more stressed in the first harvester's configuration and the mechanical quality factor is higher. The mechanical kinetic energy delivered by the bimetal thus is converted into electrical energy more efficiently if the piezoelectric beam is clamped at its two ends. Arnaud also showed in his thesis [19] that the clamped-clamped piezoelectric transducers give the highest amounts of generated power when being hit by a bimetallic strip as the piezoelectric coupling is higher in such a configuration. For these devices, the Carnot efficiency can reach 0,01% of the Carnot efficiency.

Piezo-membrane state	Snapping frequency at thermal equilibrium (Hz)	Mechanical quality factor	Energy per snap ( $\mu\text{J}$ )	Electrical power (available on the piezoelectric capacitor) ( $\mu\text{W}$ )	Power volume density ( $\mu\text{W}/\text{cm}^3$ )
Simple clamp	0.28	18	54	15	1.49
Double clamp	0.28	32	115	32	4.7

**Table 7.** Performances comparison of the two designs in Fig. 12.

## 6. Test of piezoelectric membrane from different manufactures

Another key point of our system is the choice of the piezoelectric ceramic to convert the mechanical energy released by the switching bimetal into electricity. This point was studied in the first part of this chapter where all the piezoelectric ceramic materials from our supplier were benchmarked and the most interesting ones were kept for our tests. The reason we only considered the piezoelectric materials of our manufacturer is their very low cost given that the goal of our project is to generate low cost electric energy to power wireless sensor nodes. However, to see if it is possible to more efficiently harvest the mechanical energy delivered by the switching bimetal, we tested other piezoelectric membranes from other manufacturers. We used two different piezoelectric membranes for this work. The first one is fabricated by Piezosystem (Piezo System 5A4E) and it was chosen because it has a large capacitance value, the other piezoelectric membrane was fabricated by Mide engineering solutions (Piezo Vulture V21BL). We chose a piezoelectric membrane from Piezo Vulture because the brittle piezoelectric material is encapsulated between insulating materials creating a robust, hermetically sealed and electrically insulated transducer with easy connections ready to use in our device [21]. The general composition of the piezoelectric membranes from Mide is given in Fig. 14. At the opposite of the piezoelectric membrane from Kepo, both membranes are bimorph. The Vulture piezoelectric can only be clamped at one whereas the Piezosystem membrane can be used in two configuration. It can either be clamped at one end with the other free end or clamped at its both ends. Each Vulture's piezoelectric transducers contains two electrically-insulated piezoelectric wafers, which may independently be used or bridged to increase the output voltage (series configuration) or the output current (parallel configuration). We connected the cantilever in parallel mode to increase the output current. Fig. 13 presents the two piezoelectric membranes from Piezosystem and Mide.

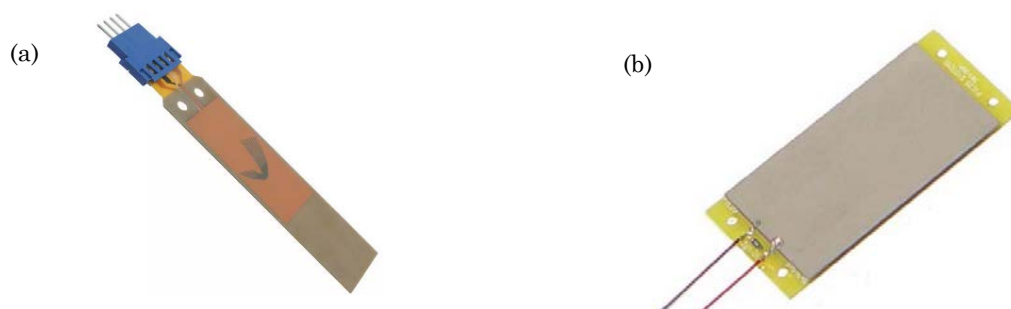


**Fig. 13.** (a). Vulture bimorph, (b). Piezosystem bimorph.

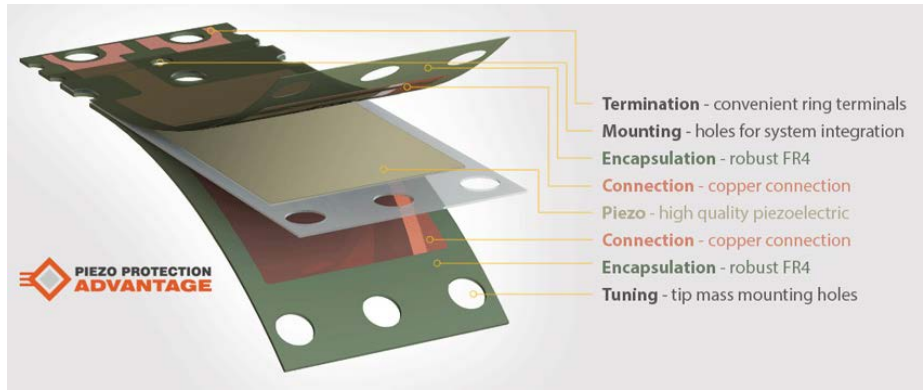


**Fig. 14.** Composition of the piezoelectric membranes from Mide Engineering solutions [21].

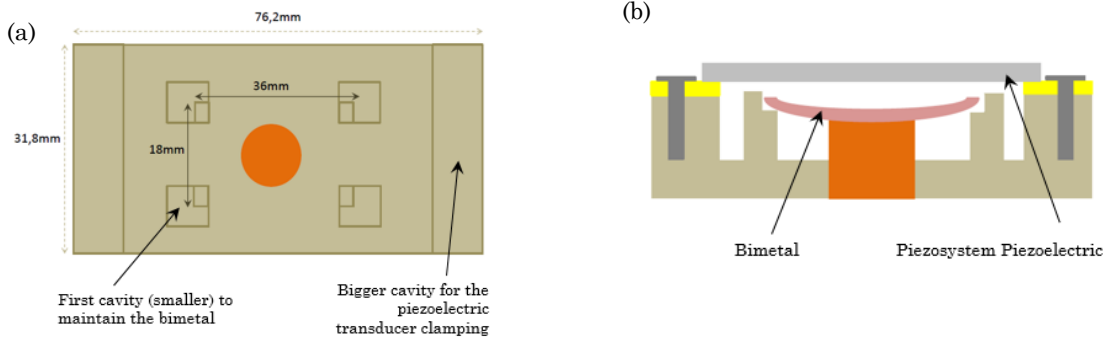
Based on the strategy developed by Daniels in [10] and used in the first part of this chapter to compare different piezoelectric materials, we established a comparison between the piezoelectric from Vulture, Piezosystem and Kepo in Table 7. Each of these materials shows interesting properties beside our needs. In fact, to harvest heat at high temperatures (40°C to 150°C), the piezoelectric materials must have a Curie temperature as high as possible. All the ceramics used in this study seem to be good candidates. Membrane 1 has good piezoelectric coefficients that ensure an efficient electro-mechanical transduction. However, membrane 2 and membrane 3 have other important advantages. Whereas Membrane 1 has a capacitance of 70nF and membrane 3 a capacitance of 52nF, membrane 2 has a larger capacitance (232nF). Its main drawback is its thickness as it is thicker than membrane 1 and 3. This is a disadvantage from a thermal point of view as the piezoelectric transducer also plays the role of a cold surface and a higher thermal capacitance implies a smaller snapping frequency of the bimetal. Concerning the membrane 3, it has a robust piezo packaging for use in harsh environments. Knowing that the energy harvester uses mechanical impacts to convert heat into electric energy, this piezoelectric generator seems to be the most appropriate one from a mechanical point of view as it cannot be cracked easily at the opposite of Kepo and Piezosystem ceramics.

Material parameter	Properties	Kepo PZT 5H Membrane 1	Piezo System 5A4E Membrane 2	Piezo Vulture V21BL Membrane 3
$K_{31}$	Coupling coefficient	0.39	0.35	0.36
$ d_{31} $	Piezo-coefficient (10 <sup>-12</sup> C/N)	275	190	190
$\epsilon_{33}/\epsilon_0$	dielectric constant	3200	1800	1700
$T_c$	curie temperature (°C)	260	350	350
<b>FOM</b>	Factor of merit (10 <sup>-24</sup> )	23.1	20.1	21.2
<b>Capacitance</b>	(nF)	70	232	52

**Table 8.** Comparison of piezoelectric materials properties.

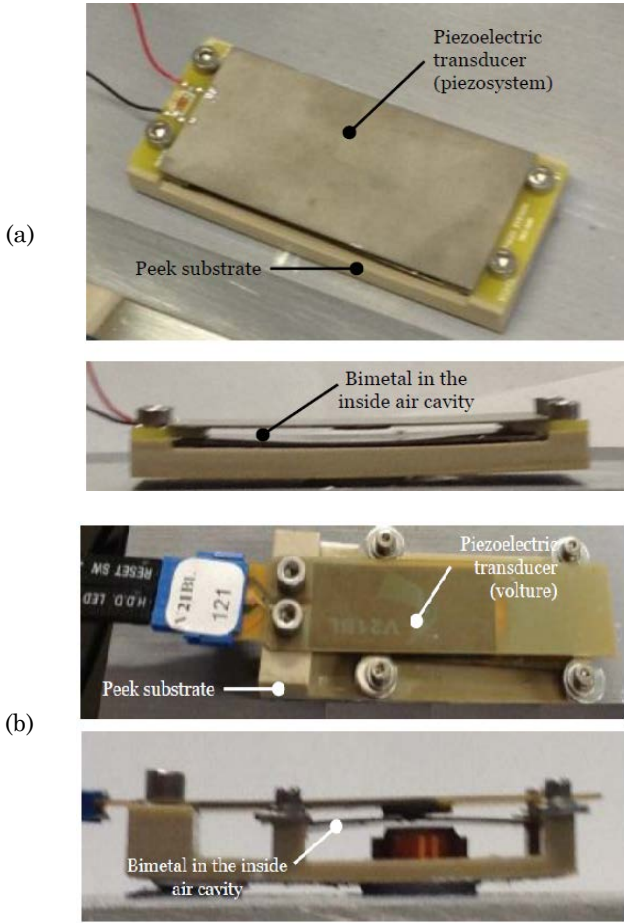
It appears from the comparison in Table 8 that membrane 1 is the one presenting the most interesting piezoelectric properties for energy harvesting applications. To complete this comparison, the three membranes are mounted on peek substrates with the same bimetal in the architecture cavity. The bimetal used for this experiment has a snap temperature of 92°C and a

snap-back temperature of 73°C. To test the piezoelectric bimorph from Volture, we used the same PEEK substrate as in Fig. 11 and Fig.12.b as that substrate was designed to be used as a piezoelectric cantilever. However, the dimensions of the piezoelectric membrane from Piezosystem are larger than those from the Kepo's piezoelectric membrane. This made us design a new PEEK architecture for Piezosystem's transducer. Fig. 15 presents this new design.



**Fig. 15.** (a). Top view of the peek substrate for Piezosystem piezoelectric and (b). Lateral view of the corresponding energy harvester.

Fig. 16 presents the realized devices with a top view and a lateral view of each.



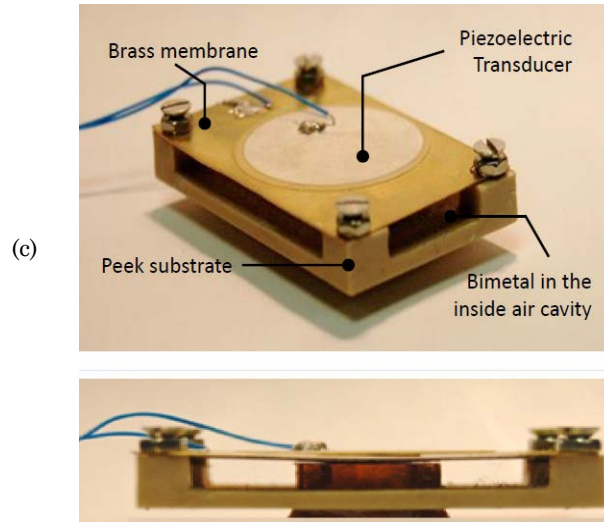


**Fig. 16.** (a). Energy harvester using a Piezosystem piezoelectric, (b). Energy harvester using a Vulture piezoelectric, (C). Energy harvester using a Kepo piezoelectric.

The experiments are realized using the same bimetal snapping at 92°C and snapping down at 73°C. A 10MΩ probe is used to visualize the electrical signal in open circuit and to estimate the electrical power available on the piezoelectric capacitor. The experimental results obtained are summed up in Table 9.

Piezo-membrane state	Snapping frequency at thermal equilibrium (Hz)	Mechanical quality factor	Energy per snap (μJ)	Electrical available power (μW)	Power volume density (μW/cm <sup>3</sup> )
Device A	0.05	40	260	13	0.89
Device B	0.03	26	128	3.9	0.39
Device C	0.06	21	178	11.2	1.64

**Table 9.** Comparison of the devices constructed using three different piezoelectric membranes from different manufacturers, experiments done using the same 73°C-92°C bimetal.

The first observation we can make is that the switching frequency of a 19K bimetal hysteresis is much lower than the frequency of a 3K bimetal. This is due to the fact that a bistable bimetal with a large thermal hysteresis needs a longer cooling time so that its temperature reaches the snap-back temperature. Devices A and C are the most powerful generators if we compare the piezoelectric transducers. However, from an industrial point of view, the first membrane is the most adapted one because of its low cost. So to sum up all the previous work, we can say that the best device configuration is the one using a double clamped piezoelectric membrane from Kepo manufacturer with a bimetal having a small thermal hysteresis. Arnaud demonstrated in his thesis that the system is more efficient by choosing bimetals having weak thermal hystereses.

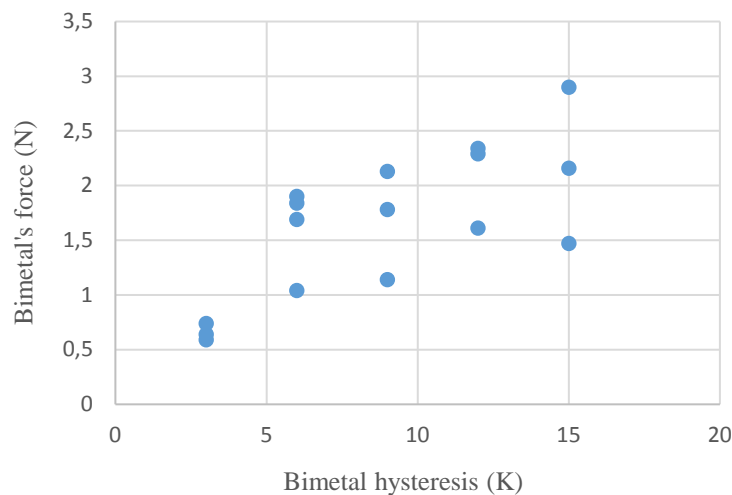
## 7. Study of bimetals of higher thermal hysteresis and dimensions

A bistable bimetallic strip heat engine is characterized by a thermal hysteresis with two specific temperatures: the snapping temperature and the snapping back one. To increase the electrical

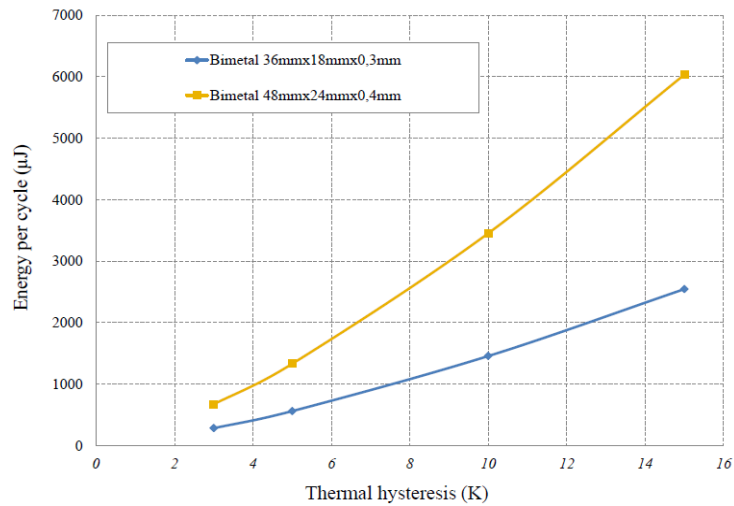
power delivered by the energy harvested studied here, tests with bimetals having large thermal hystereses and large dimensions are performed in order to find the combination of properties allowing to boost the generator's performances.

First of all, experiments on different bimetals having the dimensions  $36 \times 18 \times 0,3 \text{mm}^3$  were performed by means of a force sensor. The goal is to measure the force delivered by the bimetal when it snaps as a function of its thermal hysteresis. Experiments were carried out on bimetals having thermal hystereses ranging from 3K up to 15K. The results are shown in Fig. 17. In this graph, we observe that bimetals with a larger thermal hysteresis deliver higher amounts of kinetic energy. The same observation is reported in Refs [22-23] by Arnaud: he shows that the energy of a bimetal has a  $4/3$  exponential dependence on the thermal hysteresis. However, there is a main drawback in using highly thermal hysteresis bimetals, since the higher amounts of mechanical energy per snap do not balance for the decrease of the switching frequency of the bimetallic strips as it is reported in Ref. [24] and previously in this manuscript in Chapter 2.

To increase the output power without enlarging the thermal hysteresis, another solution is possible: increasing the bimetals' size. Using the model reported in Ref. [23], simulations are carried out to study the impact of the bimetal's size and dimensions on the available mechanical energy per snapping cycle. The results are shown in Fig. 18 where the cases of  $36 \times 18 \times 0,3 \text{mm}^3$  and  $48 \times 24 \times 0,4 \text{mm}^3$  bimetals are studied in function of different thermal hystereses (from 3K up to 15K). For every hot source temperature, we observe that bimetals of bigger dimensions produces higher amount of mechanical energy, since energy is a volumic data, i.e. directly proportional to the volume of the bimetallic strip.

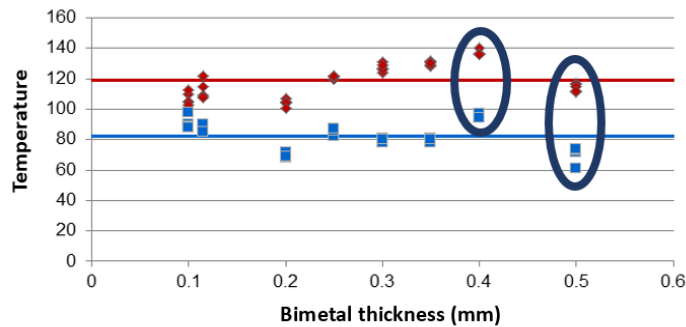


**Fig. 17.** Bimetal's force measured when snapping in function of their thermal hysteresis.



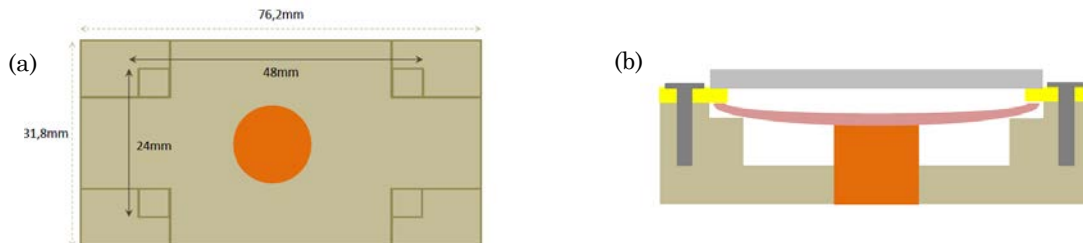
**Fig. 18.** Bimetals available mechanical energy per snapping cycle in function of their thermal hysteresis.

For our first experiments, we started testing some bigger bimetals that were at our disposal. Fig. 19 shows the various snap temperatures and snap-back temperatures of bimetals having various thicknesses. The first surrounded points correspond to bimetals having the dimensions  $48 \times 24 \times 0.4 \text{ mm}^3$  and the second group corresponds to bimetal having the dimensions  $62 \times 31 \times 0.5 \text{ mm}^3$ . For this experiment, we started with bimetals having the dimensions  $48 \times 24 \times 0.4 \text{ mm}^3$ . As shown in Fig. 19 these bimetals have thermal hysteresis of  $40^\circ\text{C}$ .



**Fig. 19.** Bimetals Snapping up and down temperatures in function of their thickness.

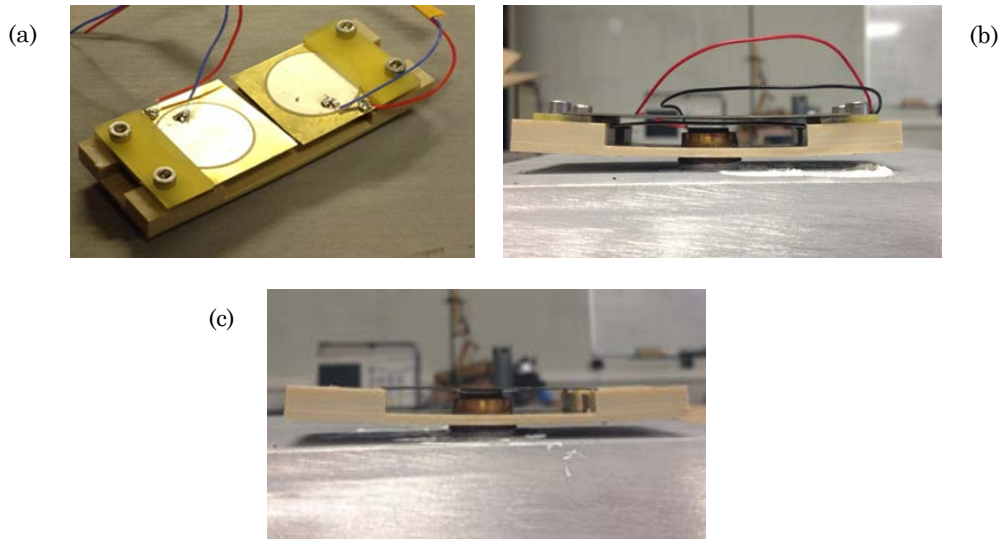
A new PEEK substrate was designed for these bimetals and was used with either Kepo's or Piezosystem's piezoelectric membranes. The new design is presented in Fig.20.



**Fig. 20.** (a) Top view of the PEEK substrate for a  $48 \times 24 \times 0.4 \text{ mm}^3$  bimetal, (b) cross sectional view of the mounted harvester with the bimetal and the Piezosystem piezoelectric.

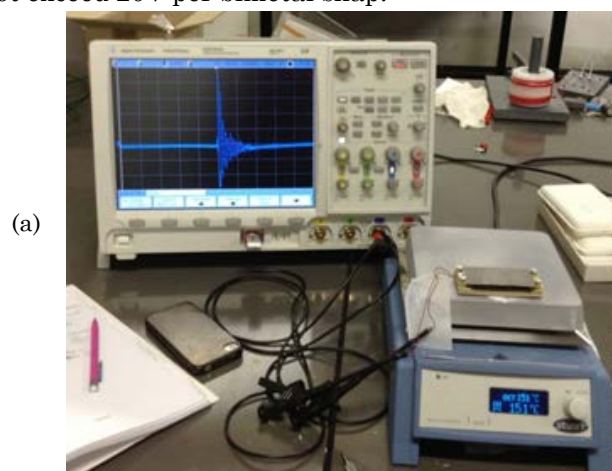
Experiments are first realized with Kepo's piezoelectric transducers (Fig.21.a). To do so, two piezoelectric cantilevers were clamped on both opposite edges of the architecture: as a consequence, the free cantilever's edges were left free to vibrate when they were hitted by the

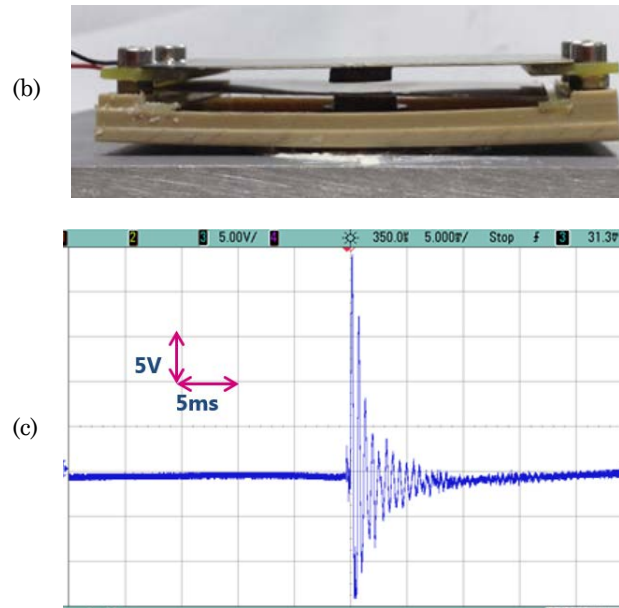
switching bimetallic strip. The used bimetal was bound to snap up at a temperature lower than 120°C, however, even at more than 150°C, no snap was observed. The same bimetal is then mounted in a generator using a piezoelectric transducer from Piezosystem (Fig.21.b) but no snapping occurs either. To check if the bimetal had a bistable behavior, it was directly put on a hot source at 160°C and, as shown in Fig. 21.c, the bimetal does not snap even if no stress was applied on it, meaning that it was not a bistable membrane. No further tests were then carried out with this group of bimetals, and we started testing bigger bimetals having the dimensions of 62x31x0.5mm<sup>3</sup>.



**Fig. 21.** (a) Tested harvester using Kepo piezoelectric and a 48x24x0.4mm<sup>3</sup> bimetal, (b) Tested harvester using Piezosystem piezoelectric and a 48x24x0.4mm<sup>3</sup> bimetal, (c) Test of the bimetal bistable behavior.

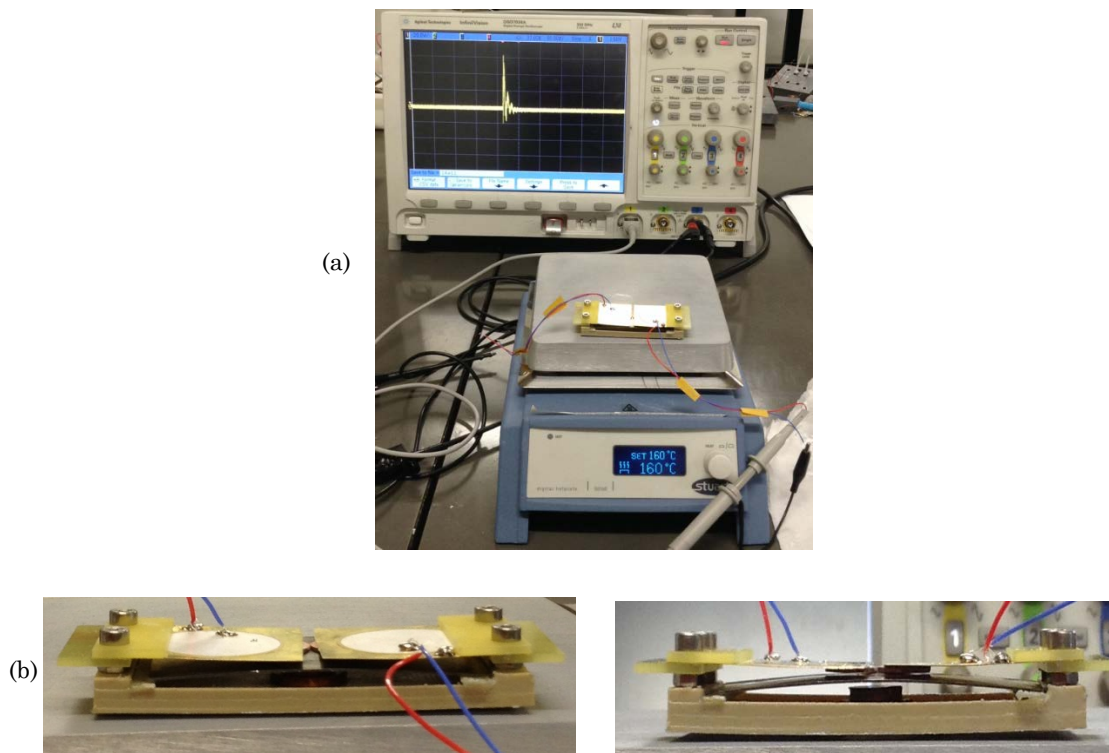
The same methodology was used here again with these bimetals. The tests are realized using piezoelectric from Piezosystem. The experimental setup showed in Fig. 22.a. Fig. 22.b shows a lateral view of the energy harvester and Fig. 22.c shows the output signal of the piezoelectric transducer when the bimetal snaps up. We observed that this bimetal allowed obtaining an output signal of 40V which was better than the commonly-used energy harvester whose output signal voltage did not exceed 20V per bimetal snap.





**Fig. 22.** (a) Tested harvester using Piezosystem piezoelectric and a  $62 \times 31 \times 0.5 \text{ mm}^3$  bimetal, (b) lateral view of the device with the bimetal in its lower position, (c) Output electrical signal of the harvester at  $T_{hot} = 151^\circ\text{C}$  using a  $10 \text{ M}\Omega$  probe.

The same experiment was realized using the same bimetal coupled with Kepo's piezoelectric membrane. Fig. 23.a shows the experimental setup, Fig. 23.b shows the generator with the two Kepo's piezoelectric membranes and Fig. 23.c presents the output signal of the device. It shows that the output voltage reached 80V per bimetal snap.



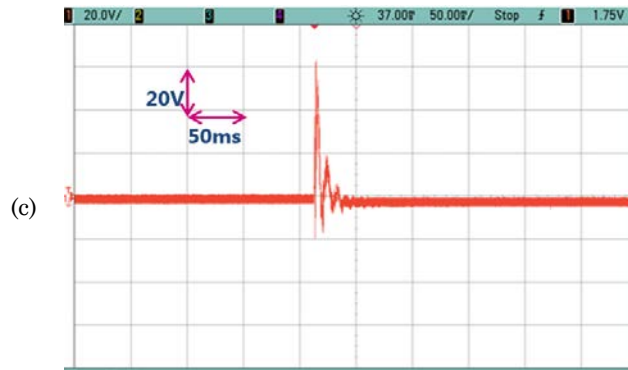


**Fig. 23.** (a) Tested harvester using Kepo membranes and a  $62 \times 31 \times 0.5 \text{ mm}^3$  bimetal, (b) lateral view of the device with the bimetal in its upper position, (c) Output electrical signal of the harvester at  $T_{hot} = 160^\circ\text{C}$  using a  $10 \text{ M}\Omega$  probe.

The main drawback of these bimetals with large thermal hysteresis and large dimensions is their inability to snap back. In fact, it would be very interesting to harvest the kinetic energy released by the bimetal when it snaps back but it is impossible for the bimetal to snap back even after a very long cooling time. This is due to their very large thermal hysteresis reaching  $60^\circ\text{C}$ . As a consequence it is impossible to balance the loss of electrical power due to the thermal hysteresis by the increased bimetal size.

The last experiment that can be realized to improve the device performance is to make the bimetal's hysteresis equal to  $3\text{K}$  but to increase its dimension. While all the previous tests were realized using bimetals at our disposal, we ordered new bimetals from Delta Concept. We specified the dimensions of  $62 \times 32 \text{ mm}^2$  and we preferred to keep the thickness of the bimetal unchanged and equal to  $0.3 \text{ mm}$  to keep the snapping frequency as high as possible. These bimetals had a snap temperature equal to  $81^\circ\text{C}$  and a hysteresis of  $4\text{K}$ . At  $25^\circ\text{C}$ , these bimetals had a very pronounced curvature but it becomes very small at higher temperature around the snapping temperature leading to very small displacement and kinetic energy release. Fig. 24 shows these five bimetals put on a hot plate at  $87^\circ\text{C}$  and we observed their very small curvature. Because of this behavior, these bimetals were not mounted into any harvester.



(c)



**Fig. 24.** (a) 4K hysteresis bimetals deposited on hot plate to check their bistability, (b) bimetals curvature at ambient temperature 25°C, (c) Bimetals curvature at their snapping temperature (87°C).

So to conclude this part, it can be said that the best configuration is the one of low thermal hysteresis bimetals having the dimensions of 36x18x0.3mm<sup>3</sup>. In fact, bimetals with larger thermal hysteresis deliver higher amounts of mechanical energy per snap but the electrical power is lower because of the lower switching frequency. In the same time, bigger bimetals are more difficult to process which does not make them be good candidates for our energy harvesters.

## 8. Improved device efficiency

In this part, the generator's overall efficiency and the efficiency of the different transduction steps composing the conversion chain are given. The overall conversion is given in Fig. 25. All the efficiencies are given for a hot source temperature equal to 90°C as it corresponds to the optimal working temperature of a bimetal having a hysteresis of 3K.

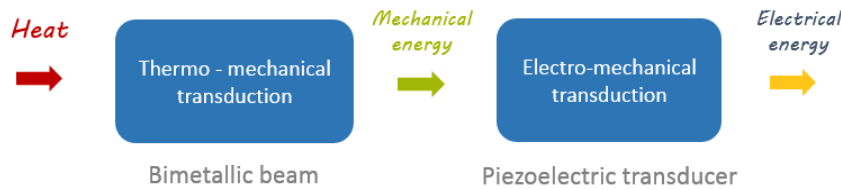


**Fig. 25.** Conversion steps of thermal energy into electrical energy.

First of all, we can define the absolute device efficiency that corresponds to the ratio between the harvester output electrical power and the incident thermal heat power. Given the thermal modeling developed in Chapter 3, we are able to estimate the input thermal power that is equal to 0.8W for the hot source's temperature equal to 90°C. As previously said, at the end of the conversion mechanism, 32μW of electrical power can potentially be harvested. This brings us to the calculation of the energy harvester absolute efficiency given in equation (5):

$$\eta_{abs} = \frac{\text{Output power}}{\text{incident heat flux}} = 4.10^{-5} = 4.10^{-3}\% \quad (5)$$

Then, we can estimate the Carnot efficiency of the energy harvester. The strength of Carnot's model is to give a simple expression of the maximal theoretical efficiency for every heat engines without making any assumption on the type of working medium. This efficiency is function of the external temperatures only. Its expression and value are given in equation (6) where  $T_C$  is the cold surface temperature and  $T_H$  is the hot source temperature. We consider the hot source at 90°C and ambient air at 25°C.

$$\eta_{carnot} = 1 - \frac{T_C}{T_H} = 0.09 = 9\% \quad (6)$$

Finally, we can define the device relative Carnot efficiency defined in equation (7).

$$\eta_{rel} = \frac{\eta_{abs}}{\eta_{carnot}} = 4.4 \cdot 10^{-4} = 4.4 \cdot 10^{-2} \% \quad (7)$$

Then, for each transduction step, we can define a transduction efficiency. To do so, it is important to estimate the amount of kinetic energy and power delivered by the bimetal when it snaps. We measured the bimetal's snap speed using a vibrometer. This allows us to estimate the bimetal's kinetic energy to 0.61mJ for a 3K-hysteresis bimetal. Given the cycling frequency, it corresponds to a mean mechanical power of 169 $\mu$ W. Given this value, we can calculate the thermo-mechanical efficiency of the transduction realized by the bimetal and also the electro-mechanical efficiency performed by the piezoelectric transducer. These efficiencies are respectively given in equations (8) and (9).

$$\eta_{ther-mech} = \frac{169\mu W}{0.8mW} = 2 \cdot 10^{-4} = 2 \cdot 10^{-2} \% \quad (8)$$

$$\eta_{elec-mech} = \frac{32\mu W}{169\mu W} = 19 \cdot 10^{-2} = 19 \% \quad (9)$$

As said previously in Chapter 1, thermoelectric energy harvesters have an efficiency of 6% in the best cases and the theoretical efficiency of these devices generally reaches 14% of the Carnot limit at a hot source at 30°C. Also, typical solar cells have an efficiency values in the range of 5% to 20% under standard conditions. In comparison with such energy harvesters, the coupled piezoelectric and bimetal thermal energy harvester has a low absolute efficiency of 4.10-3% leading to a relative Carnot efficiency of 4.4. 10-2 %. Despite these low values, it is interesting to develop this technology as in some use cases, neither thermoelectric generators nor solar cells can be used. Moreover, HEATec energy harvesters deliver enough power for WSN applications (Chapter 5).

#### IV. Device lifetime and aging

The thermal energy harvester is composed of two transducers realizing the two consecutive conversions of heat into mechanical energy and finally into electricity: the bistable bimetal and the piezoelectric membrane. For our application of energy harvesting, a lifetime of 10 years is aimed. Considering a bimetal that snaps at a frequency of 1Hz, this corresponds to 300 million cycles. However, in our case and until now, the bimetals generally snap at a frequency of 0.3Hz. This correspond to nearly 100 million cycles for a device lifetime of 10 years. To see whether if the bimetals and the piezoelectric materials are robust enough to withstand that cycling duration, aging tests are performed for each component. The bimetals tests are realized by Delta Concept.

##### 1. Bimetals lifetime

To cycle bimetals between a cold source and a hot source 100 million of time and to make sure that the experiment last a maximum of 1 year, it is necessary to make them operate at higher frequencies than 1Hz. To do so, the bimetals' manufacturer designed an experimental setup with two sources whose temperature is constantly monitored and where the cold source was colder than the bimetal snap-back temperature and the hot source temperature hotter than the bimetal's snap temperature. The temperature difference between the cold and the hot surface was around 100°C. The general working principle and components used for these aging tests are showed in Fig. 26.

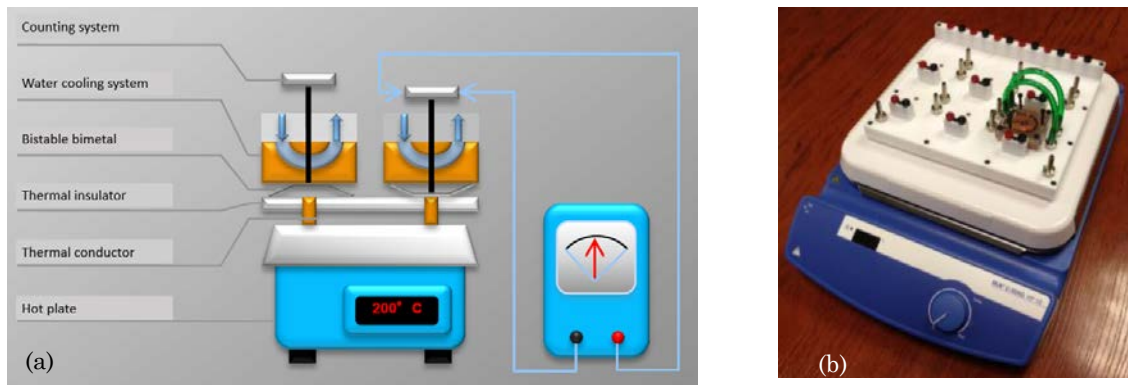


**Fig. 26.** (a) .Scheme of the bimetal's aging test and, (b). its realization.

The physical realization of this test bench showed that the bimetal maximal switching frequency is equal to 20Hz and it was very difficult to maintain this cycling frequency more than few minutes. Moreover, for this first experiment realized in ambient air, water condensation occurred over the bimetal's surface and disturbs the bimetal's operation. However, using this experiment, 10 million cycles were realized and no change in the bimetals' behavior was observed. To overcome these limitations, a new test bench was realized where the air was continuously dried and a climatic chamber was used. The first test bench was also very difficult to set and adjust (seven micrometer screws were necessary) so it was simplified and replaced by the setup in Fig. 27 where only two screws were necessary to set the experiment.

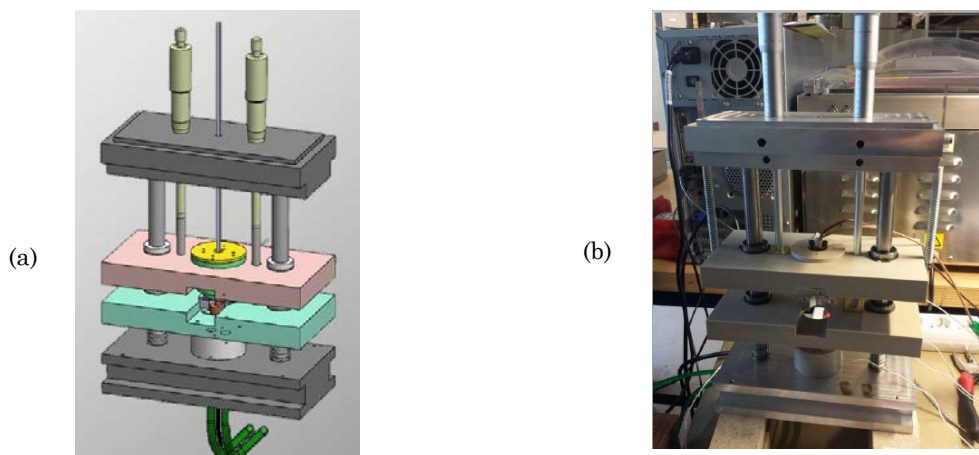


**Fig. 27.** (a). New Scheme of the bimetal's aging test and, (b). its realization.

The general experimental setup used for this experiment with a climatic chamber is presented in Fig. 28.

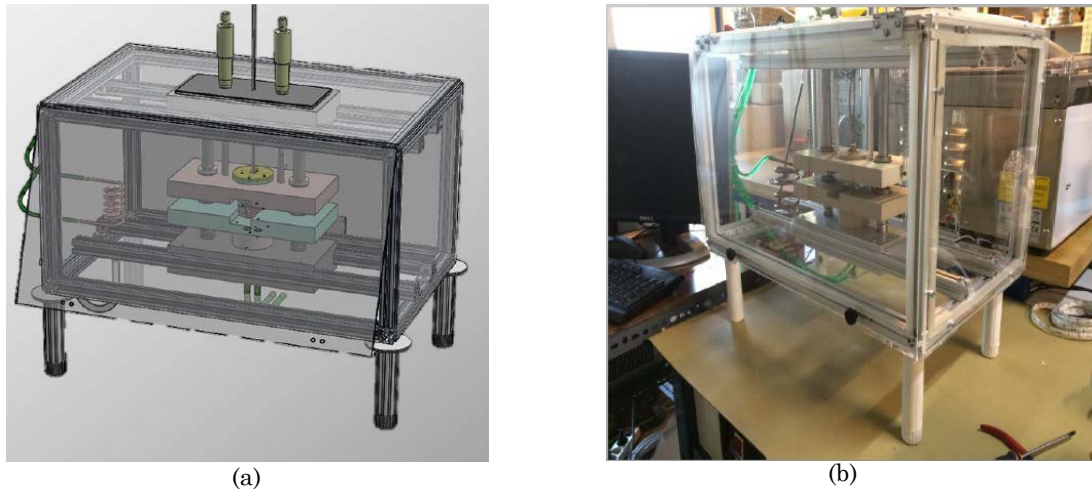


**Fig. 28.** (a). Scheme of the bimetal's aging test bench with a climatic chamber and, (b). its realization.

The first experiments using the setup in Fig. 28 showed that a frequency of 60Hz can be achieved in continuous operation. Each different part of the test bench was independently tested and the realization of the 90 million cycles will shortly get started at a frequency of 60Hz. All this work concerning the bimetal's aging tests is being realized by Delta concept.

## 2. Piezoelectric membranes lifetime

### 2.1. Thermal degradation

Aging tests were also realized on the piezoelectric membranes. In fact, as the piezoelectric ceramic deposited onto a brass substrate is brittle, it can be cracked or depolarized by mechanical fatigue or due to elevated temperatures. Because of the mechanical impact of the bimetal on the piezoelectric membrane and the elevated temperatures of the hot source reaching up to 200°C, the aging process can be an important drawback for the harvester's life time. To have a realistic test that could correspond at the same time to the thermal and mechanical constraints applied to the PZT buzzer, it should be better to simulate the mechanical impact of the bimetal at an elevated temperature of 100°C. But the realization of such experiment was not possible as we intended to simulate the impact of the bimetal using a steel beam fixed on a shaker that could not stand a temperature higher than 60°C. As a consequence we thought about realizing the thermal aging test independently of the mechanical one.

The characterization of the piezoelectric membrane at an elevated temperature have been realized by Puscasu during his thesis [12]. He used the inverse piezoelectric effect to make the piezoelectric membrane vibrate at 2 kHz in an oven at 110°C and measured regularly the values of the quality factor and the piezoelectric coupling coefficient. Fig. 29 presents the results of this experiment. 200 million cycles were realized at 110°C and at 25°C for a comparison purpose.

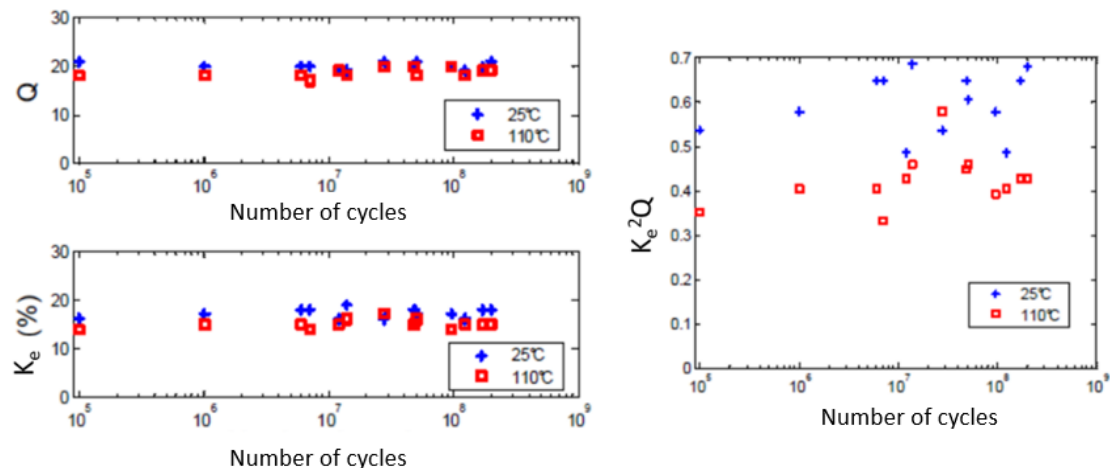


**Fig. 29.** Measurement of the quality factor and coupling coefficient of the piezoelectric membrane and calculation of  $k^2Q$  (experiment and measurements realized by PJ COTTINET).

From these measurements, we observe that both the quality factor and the coupling coefficient are a bit lower at 110°C than at 25°C. However, to see the evolution of the resonator efficiency, we should compare the  $k^2Q$  before and after the exposure to a high temperature. In fact, a resonator's figure of merit is defined in IEEE standards on Piezoelectricity [25] as follows:

$$\text{FOM} = \frac{k^2Q}{1-k^2} \quad (10)$$

The comparison of  $k^2Q$  at ambient air and at 110°C shows that its values is 30% lower at high temperatures meaning that the output power of the device decreases with the increase of the temperature. This thermal degradation is well known. Kim in [26] studied the temperature effects on output power of piezoelectric energy harvesters. A study of PZT materials performances is established in function of the temperature. It is shown that soft PZT materials generate more power than hard PZT ceramics at elevated temperature and for both material types, the coupling coefficient decreases significantly with temperature. For a soft PZT material studied in that paper, the coupling coefficient decreases of 30% when the temperature varies from 25°C to 110°C.

## 2.2. Mechanical degradation

The authors in [27] suggests that the mechanical degradation of piezoelectric materials can be much worse than the electrical ones. So, to simulate the bimetal's impact on the piezoelectric membrane, a steel beam is fixed on a shaker so that its end impacts the center of the piezoelectric membrane. Here again we intend to realize accelerated aging tests up to 100 million cycles. To do so, it was important to simulate exactly the bimetal's impact on the PZT beam. Consequently, a laser displacement sensor was used to measure the displacement of the center of the PZT beam to make it correspond to the displacement of the beam after a bimetal snap. The general experimental setup is showed in Fig. 30. It is composed of a laser sensor and its power supply, an oscilloscope to visualize the beam's displacement and its output voltage, a shaker with a steel beam and its power supply composed of a generator and a current amplifier and finally a sample holder on which the studied thermal energy harvester is fixed. The laser head reference is MTHI LTS-025-04 and it has a sensitivity of 0,5  $\mu\text{m}$  per mV. The piezoelectric membrane output voltage is visualized on the oscilloscope to be sure that the steel beam impacts correspond to the output voltage usually observed. Generally, an output voltage of 15V is measured after a bimetal snap which corresponds to a piezoelectric beam's displacement around 200 $\mu\text{m}$ . The shaker frequency was first fixed to 10Hz and both the voltage generator and the current amplifier were adjusted so

that the piezoelectric beam displacement and output voltage corresponded to the previously given values. In fact, in [28], the author studied the mechanical degradation of piezoelectric materials for energy harvesting applications and showed that even small difference in a piezoelectric membrane deflection can drastically affect the cycle life of piezoelectric beams so it is very important to simulate the same operating conditions for the piezoelectric ceramic.

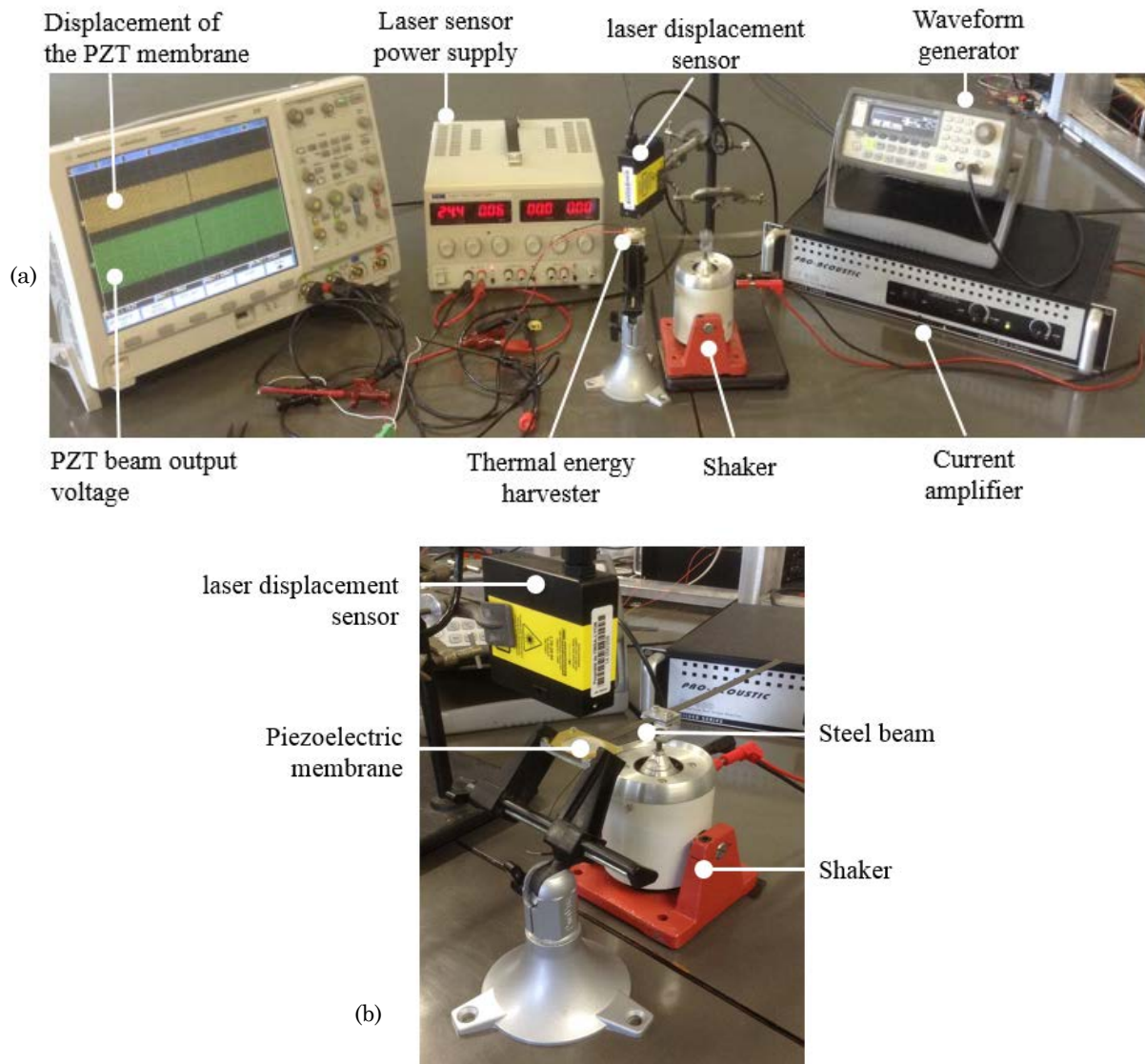


**Fig. 30.** (a). *Experimental setup for the piezoelectric membrane aging tests*, (b). *Image of the shaker with a steel beam impacting the piezoelectric membrane.*

The experiments were realized at ambient temperature. Fig. 31, 32 and 33 respectively represent the evolution of the piezoelectric coupling coefficient, of the quality factor and finally of the ceramic's factor-of-merit in function of the steel beam cycling representing the bimetal's impact on the piezoelectric ceramic. The experiment was supposed to last 100 million cycles but because of the evolution of the piezoelectric ceramic properties and also because the experimental setup is not adequate for such a continuous utilization, the aging tests were realized over 10 million cycles only. Over 10 million cycles, the coupling coefficient was lowered by a factor two. The quality factor that was initially equal to 25 was lower than one at the end of the aging test. This led to a factor of merit 115 times lower at the end of the ten million cycles. However, at the end of the experiment, the screws used to fix the piezoelectric membrane over the peek substrate were very

loose. These screws were tightened and the performances of the piezoelectric ceramic measured once again. After that step, the quality factor had a value of 21 instead of 25 at zero cycle and the coupling coefficient was equal to 0.19 instead of 0.26 before the aging tests. To be sure that the piezoelectric ceramic was still in a good state, the surface of the ceramic was observed under a microscope to see if some cracking occurred or not.

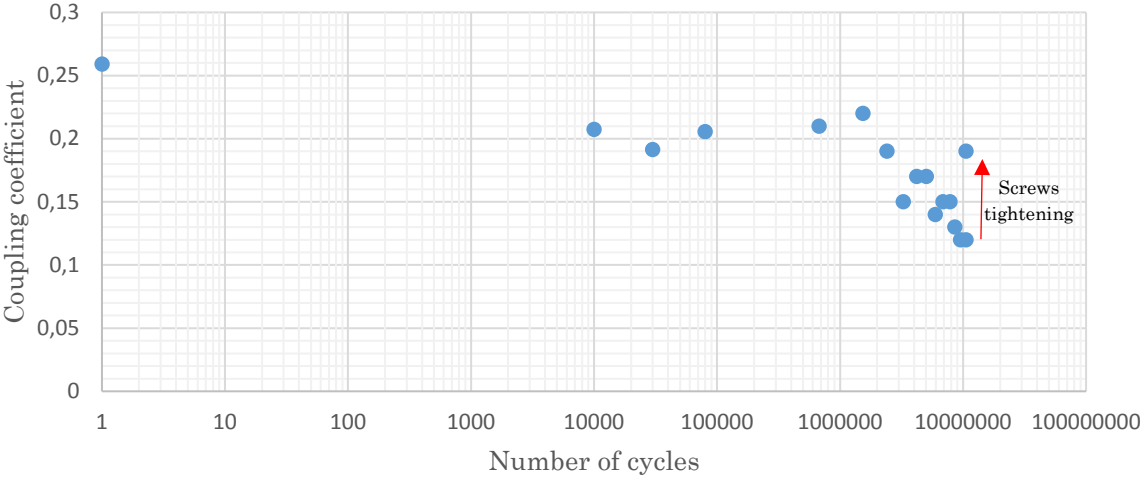


**Fig. 31.** Evolution of the piezoelectric ceramic coupling coefficient with the cycling.

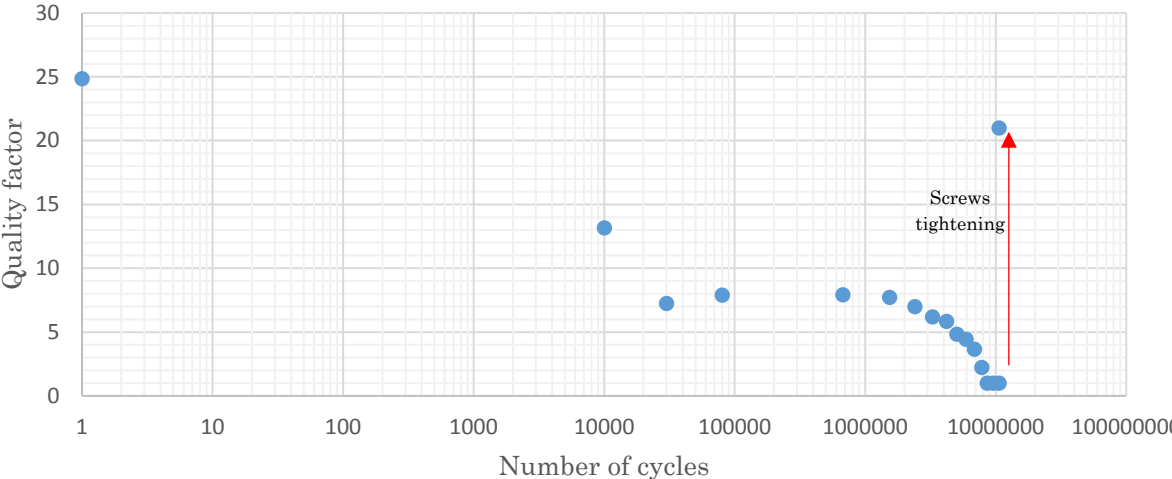


**Fig. 32.** Evolution of the piezoelectric ceramic quality factor with the cycling.



## V. Conclusion

In this chapter we established a complete benchmark of each device component. First of all, a review of the different piezoelectric materials used up to date was developed. A comparison of their performances and the effect of each piezoelectric parameter on the output power were showed. This allowed us to point out the most interesting material for our energy harvesting application.

In a second step, we studied the device architecture and improved each conversion step independently. We chose an adapted substrate for the device, improved the contact of the bimetal with the piezoelectric membrane and studied the best position and configuration of the piezoelectric beam over the bimetal as it could either be clamped at its both ends or used as a cantilever beam with a free end. We also tested different piezoelectric membranes from different manufacturers in order to improve the device's performances and to increase the amount of harvested power. However, the best configuration was the initial one: Kepo's membranes are the most affordable one and it delivers nearly the same amount of electrical power as the piezoelectric membranes from Piezosystem. Also, other experiments were realized to see if using bimetals with larger thermal hystereses and dimensions would allow to increase the generator's output power or not. Here again, the tests did not reveal any improvements and the best bimetal configuration is the one using bimetals having a hysteresis of 3°C with dimensions of 36mm x 18 mm x 0.3 mm. Finally, using the best device configuration, aging tests were realized on each key component of the system: the bimetals and the piezoelectric membranes. The bimetals manufacturers developed a test bench for an accelerated bimetal cycling. Up to now, 10 million cycles were realized and no change in the bimetals' properties was observed. Aging tests were also realized on piezoelectric membranes. To simulate the impact of the bimetal on the piezoelectric membrane, a steel beam was fixed on a shaker and more than ten million cycles were realized. However, at the end of this experiment, the piezoelectric membrane properties seemed to drastically decrease but the reason of such behavior was the screw's loosening due to the cycling. The piezoelectric membrane was tested after retightening all the four screws and this revealed that over the first ten million cycles, the coupling coefficient decreased of 27% and the quality factor decreased of 12%. These first tests are very promising.

## VI. References

- [1] Curie, Jacques and Curie, Pierre. "Development, via compression, of electric polarization in hemihedral crystals with inclined faces," *Bulletin de la Societe de Minerologie de France*, 3 1880): 90-93.
- [2] [www.morgantechnicalceramics.com/sites/default/files/documents/chapter2\\_1.pdf](http://www.morgantechnicalceramics.com/sites/default/files/documents/chapter2_1.pdf)
- [3] Haussonne, Jean-Marie. *Céramiques Pour L'électronique Et L'électrotechnique*. Lausanne: Presses polytechniques et universitaires romandes, 2002.
- [4] <https://www.americanpiezo.com/piezo-theory/pzt.html>.
- [5] Xu, Yuhuan. *Ferroelectric Materials and their Applications*. Netherlands, North – Holland Elsevier, 1991.
- [6] Shujun Zhang, and Thomas R Shrouf. "Relaxor-PT Single Crystals: Observations And Developments". *IEEE Transactions on Ultrasonics, Ferroelectrics and Frequency Control* 57.10 (2010): 2138-2146.

- [7] Cochran, S. "Piezoelectricity And Basic Configurations For Piezoelectric Ultrasonic Transducers". *Ultrasonic Transducers* (2012): 3-35.
- [8] Newnham, R.E., D.P. Skinner, and L.E. Cross. "Connectivity And Piezoelectric-Pyroelectric Composites". *Materials Research Bulletin* 13.5 (1978): 525-536.
- [9] Roundy, Shad, Paul Kenneth Wright, and Jan M Rabaey. *Energy Scavenging For Wireless Sensor Networks*. Boston: Kluwer Academic Publishers, 2004.
- [10] Daniels, Alice, Meiling Zhu, and Ashutosh Tiwari. "Evaluation of Piezoelectric Material Properties for a Higher Power Output from Energy Harvesters with Insight into Material Selection Using A Coupled Piezoelectric-Circuit-Finite Element Method". *IEEE Transactions on Ultrasonics, Ferroelectrics and Frequency Control* 60.12 (2013): 2626-2633.
- [11] Meiling Zhu, E. Worthington, and J. Njuguna. "Analyses Of Power Output Of Piezoelectric Energy-Harvesting Devices Directly Connected To A Load Resistor Using A Coupled Piezoelectric-Circuit Finite Element Method". *IEEE Transactions on Ultrasonics, Ferroelectrics and Frequency Control* 56.7 (2009): 1309-1317.
- [12] Puscasu Onoriu, "Dispositifs innovants pour la Récupération d'énergie thermique", PhD thesis, INSA de LYON, 2014.
- [13] [catalog.wshampshire.com/Asset/psg\\_teflon\\_ptfe.pdf](http://catalog.wshampshire.com/Asset/psg_teflon_ptfe.pdf)
- [14] [www.matbase.com](http://www.matbase.com)
- [15] Nicholson, John W. *The Chemistry of Polymers*. Cambridge: Royal Society of Chemistry, 2006.
- [16] [www.goodfellow.com/catalogue](http://www.goodfellow.com/catalogue)
- [17] Puscasu Onoriu et al, "An innovative heat harvesting technology (HEATec) for above Seebeck performance", in *Electron Devices Meeting (IEDM), 2012 IEEE international, 2012*, pp. 12–5.
- [18] Emilie Trioux "Piezoelectric micro-generators for energy harvesting applications. Micro and nanotechnologies/Microelectronics", Université Grenoble Alpes, 2015.
- [19] Arnaud Arthur, "Modeling and design of thermomechanical conversion systems for thermal energy harvesting applications", Université Grenoble Alpes, 2016.
- [20] Puscasu Onoriu et al, "A disruptive technology for thermal to electrical energy conversion," in *Thermal Investigations of ICs and Systems (THERMINIC), 18th International Workshop on, 2012*, pp. 1–3
- [21] <http://www.mide.com>
- [22] Arnaud, Arthur et al. "Reduced Model For The Comprehension Of The Operation Of A Thermo-Mechanical Energy Harvester". *2015 IEEE 13th International New Circuits and Systems Conference (NEWCAS)* (2015), pp: 1-4.
- [23] Arnaud, A et al. "Thermo-Mechanical Efficiency Of The Bimetallic Strip Heat Engine At The Macro-Scale And Micro-Scale". *J. Micromech. Microeng.* 25.10 (2015): 104003.

- [24] Boughaleb, J. et al. "Analysis Of The Thermal Impact Of A Bimetal On The Dynamic Behavior Of A Thermal Energy Harvester". *Sensors and Actuators A: Physical* 236 (2015): 104-115.
- [25] IEEE Standards on Piezoelectricity, Sponsored by the Standards Committee of the IEEE Ultrasonics, Ferroelectrics and Frequency Control Society, 1988.
- [26] Kim, Seon-Bae et al. "Temperature Effects on Output Power of Piezoelectric Vibration Energy Harvesters". *Microelectronics Journal* 42.8 (2011): 988-991.
- [27] Cain, M G et al. "Degradation of piezoelectric materials ". Tech. rep.NPL. (1999).
- [28] Pillatsch, P et al. "Degradation Of Piezoelectric Materials For Energy Harvesting Applications". *J. Phys.: Conf. Ser.* 557 (2014): 012129.

## Chapter 4

# Alternative piezoelectric and bimetal exploration for thermal and mechanical energy harvesting

Chapter 4 .....	104
I. Introduction .....	105
II. Energy harvesting using piezoelectric bimetals .....	105
1. Piezoelectric composite deposition on bimetals.....	105
1.1. Preparation and deposition of the piezoelectric paint on bimetals.....	106
1.2. Piezoelectric paint characterization.....	110
2. Piezoelectric thin films deposition on bimetals.....	113
2.1. Experimental procedure .....	113
2.2. Characterization of the piezoelectric bimetals.....	116
III. Thermal and mechanical energy harvesting.....	123
1. Available vibration sources .....	123
2. Dual energy harvester design rules.....	124
3. Numerical modeling.....	128
IV. Conclusion .....	130
V. References.....	131

## I. Introduction

In the thermal energy harvester studied in this thesis, the electro-mechanical conversion is insured by a piezoelectric ceramic. However, as seen in the previous part, only 19% of the mechanical energy delivered by the bimetal during its snap is converted into electrical energy. To extract more energy from the bimetallic strip and to increase the transduction efficiency, a new way to couple piezoelectric materials with bimetals is explored through direct deposition of piezoelectric layers on bimetals. Two different piezoelectric layers are realized and tested experimentally. First a composite piezoelectric layer with BaTiO<sub>3</sub> or PZT particles are deposited on thermally bistable bimetals in LGEF. Then different PZT thin films are synthesized and deposited on the bimetallic membrane's surface. Different piezoelectric layers thicknesses and substrate thicknesses are tested to find out the best configuration and the most powerful one. These two kinds of piezoelectric bimetals are tested and ways of future improvements are given. The first layers were realized in the laboratory LGEF using a technique developed by J.F Capsal and the bimetals were directly covered with the piezoelectric paint whereas the thin films are realized in the laboratory IETR. The characterization of both samples was realized at LGEF. Apart from working on piezoelectric bimetals and in order to harvest higher amounts of energy, we thought of harvesting at the same time thermal and mechanical energies. In fact, in many use cases, the two energies are simultaneously available. This can be achieved using piezoelectric materials for ambient vibrations energy harvesting. Thus, we designed a vibrations-based energy harvester coupled to a thermal energy harvester. This study is presented in the second part of this chapter.

## II. Energy harvesting using piezoelectric bimetals

### 1. Piezoelectric composite deposition on bimetals

PZT composites are a combination of ferroelectric ceramics and polymers in order to overcome disadvantages of ceramics and to meet desirable ceramic properties that cannot be attainable in a single phase material.

Before presenting the piezoelectric bimetals realized using a piezoelectric paint, it is important to show the advantages of piezoelectric composites in comparison with the piezoelectric ceramics and polymers. Table 1 shows the main characteristics of piezoelectric ceramics, table 2 shows those of piezoelectric polymers and Table 3 presents the characteristics of piezoelectric composites.

Piezoelectric ceramic	
Advantages	drawbacks
- A strong piezoelectric response	- Most piezoelectric ceramics are brittle and hard
- High signal to noise ratio	- Prefabricated piezoceramics do not fit surfaces with complex geometry and may crack
- Self-powering ability	- The host structure should be flat and smooth to ensure a robust adhesion
	- Heavy and rigid

*Table 1. Piezoelectric ceramics properties [1,2,3].*

Piezoelectric polymers	
Advantages	drawbacks
<ul style="list-style-type: none"> <li>- Toughness</li> <li>- Flexibility</li> <li>- Lightness</li> <li>- Ease of processing</li> </ul>	<ul style="list-style-type: none"> <li>- Low piezoelectric activity and low electromechanical coupling properties</li> <li>- The polymers are generally vulnerable to the severe environment</li> </ul>

**Table 2.** Piezoelectric polymers properties [1,2,4,5,6].

Piezoelectric composites	
Advantages	drawbacks
<ul style="list-style-type: none"> <li>- Unique combination of the high electromechanical properties of ferroelectric ceramics and the mechanical flexibility and formability of organic synthetic polymer</li> <li>- The piezoelectric paint is directly deposited onto structural surfaces and thus conforms to curved surfaces</li> <li>- Adheres well to the host structure</li> <li>- By choosing appropriate polymer material for the matrix phase the properties of piezoelectric paints can be tuned to optimum for a particular application</li> <li>- The ease of processing of the piezoelectric paint can be utilized to form complex sensor patterns</li> <li>- Being distributable which means large area coverage</li> </ul>	<ul style="list-style-type: none"> <li>- The physical properties are vague if no characterization is performed before use</li> <li>- The fabrication of PZT paint has not reached an industrial standard which implies that its properties vary with the composition and the conditions it is subject to</li> <li>- Low piezoelectricity compared with ceramic sensors because of which its popularity is limited and application range is narrowed</li> </ul>

**Table 3.** Piezoelectric composites properties [1,2,3].

### 1.1. Preparation and deposition of the piezoelectric paint on bimetals

Piezoelectric composites are composed of tiny piezoelectric particles in a polymer matrix. Usually, piezoelectric paint is used for vibration sensing applications [1,7] but in this part, we will study its capability for energy harvesting. Piezoelectric paint has numerous requirements [1]: it must be capable of being sprayed using portable equipment and should adhere to the host structure. The piezoelectric particles should consequently have a small size to allow a good paint sprayability (less than  $5\mu\text{m}$ ) and should have a low tendency to aggregate to be sprayed and to form an homogeneous film.

A piezoelectric paint should be composed of three different components [2]:

- Piezoelectric ceramic particles acting as a filler.
- A polymer binder that facilitates the suspension of the piezoelectric particles during the application and binds the filler together after curing.
- Some chemical additives in order to enhance the paint mixing, deposition and curing properties.

Two types of piezoelectric composites are studied here: some are made of PZT particles and the other are made of barium titanate ( $\text{BaTiO}_3$ ) particles. In this part we will only detail the realization of the barium titanate part, but the fabrication process is exactly the same for both series.

The paint was prepared using different components from Stoppani: 5g of polyurethane varnish with polyester based resin, 2,5g of hardener and 1,5g of diluent. We also added 17,5g of barium

titanate particles from Inframat Advanced Materials with an average particles size of 700nm. The piezoelectric mixture was homogenized using the ultrasonic processor Hielscher UP400S. Fig. 1 shows the used ultrasonic processor and the piezoelectric composite paint we finally obtained.



**Fig. 1.** (a). Different constituents needed for the preparation of the piezoelectric paint, (b). Ultrasonic processor Hielscher UP400S used for the paint homogenization.

After mixing and stirring the piezoelectric paint, we selected numerous bimetals to be covered with the piezoelectric paint. We chose bimetals having different hysteresis and snapping temperatures. Table 4 sums up all the bimetals used for this experiment. Before the paint deposition, the bistable bimetals are cleaned. The paint was then applied on the surface of the bimetals using a brush except on the hallmark that is normally in contact with the hot and cold surfaces of the harvester to avoid the piezoelectric composite layer cracking and the bimetals snapping frequency decrease. With this deposition technique, the mean value of the paint's thickness was approximately of  $50\mu\text{m}$  to  $60\mu\text{m}$ . Only one layer was deposited on each bimetal. The paint was then cured for six hours in an oven at  $60^\circ\text{C}$  before subsequent poling and electroding steps. Fig. 2 shows the bimetals before the deposition of the piezoelectric layer, after the coverage of their hallmark and finally after the paint was deposited on their surface.

Bimetal properties	Bimetal thickness	Thickness of the piezoelectric bimetal	Thickness of the deposited PZT layer
$\Delta T=3\text{K}$ , $T_s= 70^\circ\text{C}$	0,3mm	0,36mm	$60\mu\text{m}$
$\Delta T=9\text{K}$ , $T_s= 70^\circ\text{C}$	0,31mm	0,36mm	$50\mu\text{m}$
$\Delta T=15\text{K}$ , $T_s= 70^\circ\text{C}$	0,31mm	0,36mm	$50\mu\text{m}$
$\Delta T=3\text{K}$ , $T_s= 115^\circ\text{C}$	0,31mm	0,36mm	$50\mu\text{m}$
$\Delta T=3\text{K}$ , $T_s= 110^\circ\text{C}$	0,3mm	0,35mm	$50\mu\text{m}$

**Table 4.** Characteristics of the tested piezoelectric bimetals and their thicknesses before and after the piezoelectric layer deposition.

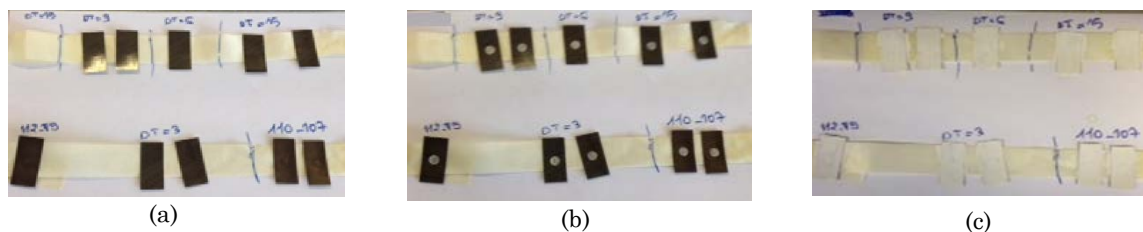


**Fig. 2.** (a). bimetals before the painting, (b). Bimetals with a mask on their hallmark, (c). Painted bimetals.

To polarize the samples to make them exhibit a piezoelectric effect, electroding should be performed. Knowing that bimetals are electrically conductive, we used the painted surface of the bimetal as a bottom electrode so that we only had to realize the top electrode by PVD gold deposition. However, before that, a mask should be put on the painted bimetal to avoid the sample's breakdown if the two electrodes come into contact each other. Fig. 3 shows the mask deposited on the bimetal's sides and all around the hallmark before the electroding step. The gold electrode is evaporated on the sample using a Cressington Sputter coater 208HR showed in Fig. 4.



**Fig. 3.** (a). mask on the hallmark of the bimetal, (b). Mask on the bimetal's hallmark and sides.



**Fig. 4.** (a). Cressington Sputter coater 208HR used for the PVD gold electrode deposition, (b,c). bimetals after the electroding step, (d) bimetal after the mask removal.

The next step for the preparation of the samples is the poling of the deposited layers on the bimetals to induce their piezoelectricity. The poling process switches the polar axis of crystallites

to the symmetry allowed directions nearest to that of the externally applied electric field. Usually, for the barium titanate particles used in this experiment, an external electric field varying from 4kV/mm to 6kV/mm should be applied to the samples at 90°C during 15min. For the thickness of the deposited layer of around 50µm, an external voltage around 250V is applied for 15 minutes on each sample at 80°C. The experimental setup used for the polarization is showed in Fig. 5. The oven's reference is Votsch VT7004 and the voltage generator is Spellman SL60.



**Fig. 5.** (a). Poling experimental setup, (b). Bimetal in the sample holder inside the oven.

Once the poling is over, the piezoelectric coefficient should be measured to check if the samples are now piezoelectric. To do so, a  $d_{33}$ -meter is used (YE273A  $d_{33}$ -meter) to measure paint's piezoelectric coefficient after the poling process. The experimental setup used for this measurement is showed in Fig. 6 and the values of  $d_{33}$  of each sample are showed in Table 5.



**Fig. 6.** Experimental setup used to measure  $d_{33}$  coefficient of each sample (in this picture the sample has not been poled yet).

Bimetal reference and snapping temperatures	Poling duration	Applied voltage	Oven temperature	Piezoelectric constant $d_{33}$
(O) 112-115°C	16min	248V	80°C	$10 \cdot 10^{-12} \text{C/N}$
(A) 110-107°C	15min	245V	80°C	$11,1 \cdot 10^{-12} \text{C/N}$
(B) 110-107°C	17min	250V	80°C	$12,4 \cdot 10^{-12} \text{C/N}$
(C) 67-70°C	18min	253V	80°C	$9,7 \cdot 10^{-12} \text{C/N}$
(D) 67-70°C	15min	248V	80°C	$10 \cdot 10^{-12} \text{C/N}$
(E) 61-70°C	15min	251V	80°C	$9,7 \cdot 10^{-12} \text{C/N}$
(F) 61-70°C	15min	263V	80°C	$11,5 \cdot 10^{-12} \text{C/N}$
(G) 55-70°C	16min	256V	80°C	$10,5 \cdot 10^{-12} \text{C/N}$
(H) 55-70°C	15min	252V	80°C	$12,5 \cdot 10^{-12} \text{C/N}$

**Table 5.** Poling experimental conditions of each bimetal and measurement of each piezoelectric bimetal  $d_{33}$ .

## 1.2. Piezoelectric paint characterization

The fabricated layers had a capacitance equal to 2,5nF. To test experimentally the different piezoelectric bimetal, it was necessary to fix some wires on each of the piezoelectric layer electrodes. We used a silver conductive epoxy from MG Chemicals to set the wires. Then the wired bimetals were set in an oven at 60°C for 15min necessary for the conductive epoxy drying process. At this step, the piezoelectric bimetals were ready for tests on a hot plate. To be able to observe the open circuit voltage of each piezoelectric bimetal during its heating and cooling phases, we used a voltage follower circuit (TL082IP) whose input impedance is equal to  $10^{12}$ ohms. Each bimetal was set in a peek substrate like those used previously in order to maintain the bimetal at its four ends. The experimental setup used for these tests is showed in Fig. 7.

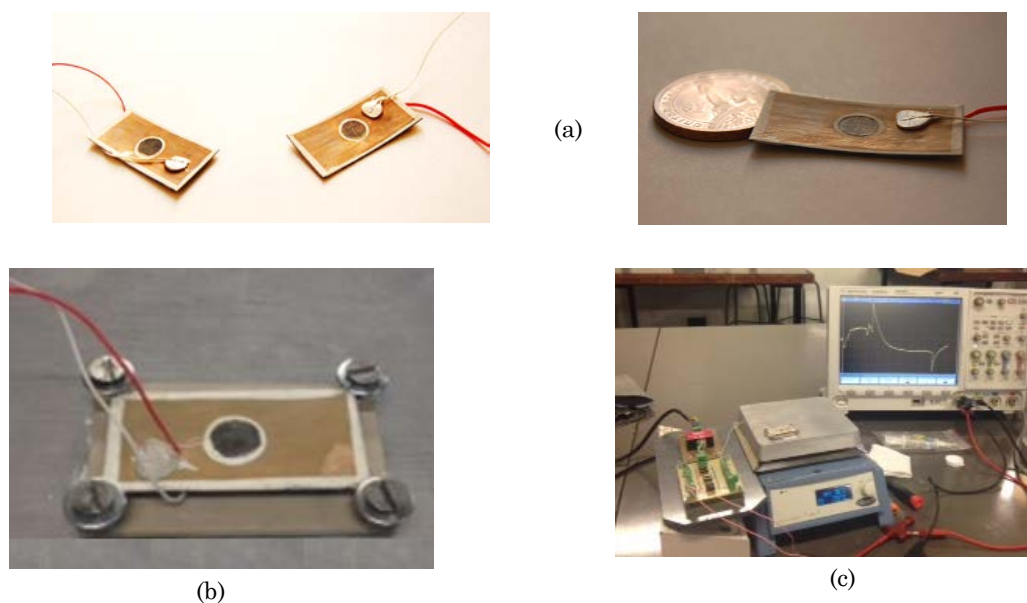


**Fig. 7.** (a). Piezoelectric bimetal after sticking the wires, (b). Piezoelectric bimetal in a peek substrate, (c). Experimental setup for the characterization of the piezoelectric bimetals.

The first observation we made during our tests is that the 3K hysteresis bimetal lost their bistability and no snapping is anymore observed even at temperatures much higher than their snapping temperatures. The reason of this behavior is that the deposition of a piezoelectric layer on a bimetal makes its hysteresis value decrease. For the bimetal with small hystereses, this led to their bistability loss. As explained by Arnaud in his thesis [24], the bistability of such a beam is related to the ratio between its curvature and its thickness, if the ratio between these two quantities does no more respect the bistability criterion, the beam becomes monostable. By adding a layer on a bimetal, its thickness increases and its curvature keeps the same which leads to the bistability loss.

Moreover, at the opposite of the usual energy harvesters presented previously where the snapped bimetal is cooled down by conduction when it comes in contact with the piezoelectric membrane acting as a cold surface, in the case of piezoelectric bimetal, the bimetal is cooled down by natural convection and no cold surface is put over the harvester. This is the reason why the 15K bimetal snaps up but never snaps down. The only samples we can study are the 9K hysteresis bimetal snapping up at 70°C and snapping back at 61°C. We also characterized other piezoelectric bimetal having a snap temperature equal to 42°C and a snap-back temperature equal to 35°C made using the same methodology as the first bimetal except that instead of using BaTiO<sub>3</sub> particles, a PZT powder is used. The characterization of these two series is exactly the same and the output signals of each bimetal is showed in Fig. 8. The comparison of the power delivered by each sample is represented in Fig. 8.c.

The first observation we can make is that the 9K hysteresis bimetal needs more time to snap down than the 7K bimetal and the snapping frequency are much lower than the usual thermal energy harvester. This can be explained by the heat evacuation occurring by natural convection in the case of piezoelectric bimetal. Moreover, we observe that the piezoelectric bimetal with PZT particles are much powerful than the ones with barium titanate powder. The reasons of such differences are first that PZT has a strongest piezoelectric response than BaTiO<sub>3</sub> (part II.1) but also the difference between the curie temperatures of each piezoelectric material. Whereas PZT has a curie temperature of 320°C, barium titanate has a much lower value of 120°C and the piezoelectric materials manufacturers only guarantee and ensure the piezoelectricity of their product until a temperature equal to half of the curie temperatures. In our case, because of the different snap temperatures of the bimetal, the ones with BaTiO<sub>3</sub> were tested at temperatures equal to 85°C at least and the other bimetal with PZT particles were tested at 60°C. This means that not only barium titanate has a lower response than PZT samples but also it may have been depolarized during the experiments.

Also, even for the piezoelectric bimetal with PZT particles, we can say that the level of power is much lower than the usually used harvesters as the available power is even lower than 1nW, whereas with piezoelectric membranes the amount of the available power is in the order of a few tens of micro watts. However, some improvements can be made to increase the harvested power. During the samples preparation, only one paint layer was deposited on each bimetal, we can think of increasing the number of deposited layers. Then, during the paint preparation, the piezoelectric particles only represented 25% of the total volume of the paint, we can easily double this amount without compromising the quality of the piezoelectric layer.

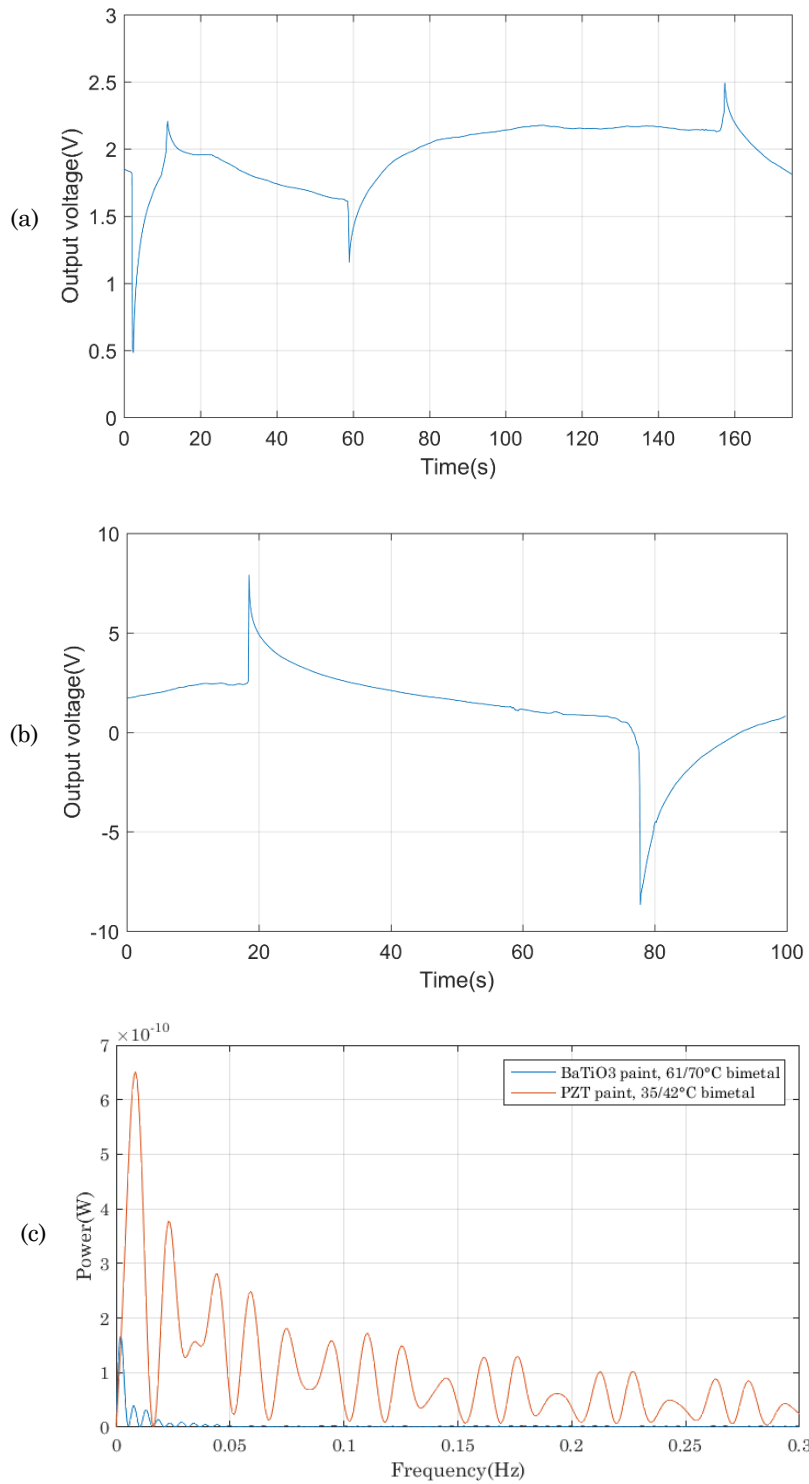


**Fig. 8.** (a). Output signal of a 61-70°C bimetal, (b). Output signal of a 35-42°C bimetal, (c). Comparison of the two samples output powers.

## 2. Piezoelectric thin films deposition on bimetals

### 2.1. Experimental procedure

Another way to directly harvest the mechanical energy delivered by the bimetals during their snap and snap back is to deposit PZT thin films on the bistable membrane's surface. Contrary to the previous part where the bimetal was covered with a piezoelectric composite, in the present paragraph thin PZT films were realized by multi-layer deposition technique. Several materials such as  $\text{Pb}(\text{Zr,Ti})\text{O}_3$  (PZT), ZnO or AlN can be used for piezoelectric thin films fabrication. Due to the superior piezoelectric properties of PZT, this material is the one used in this study. Thus, highly flexible lead zirconate titanate thin films are realized by a sol-gel process. It was shown that for bulk PZT materials, the maximum ferroelectric and piezoelectric properties are obtained at the morphotropic (MPB) phase boundary composition [8]. The MPB composition corresponds to the coexistence of rhombohedral and tetragonal phases of PZT. This composition is obtained for Zr/Ti ratio close to 53/47 [9]. Following these proportions, PZT thin films were fabricated at Nantes University by sol-gel process. This refers to a process in which solid particles dispersed in a liquid agglomerate together to form a continuous three dimensional network extending through the liquid and producing a gel which is then crystallized by heat treatment.

The PZT thin films were first deposited onto aluminum foils and then deposited onto the bimetals. Commercial aluminum foils present many advantages as ultralight weight ( $43\text{g.m}^{-2}$ ), flexibility and conformability, conduction, low pricing (less than  $0.1\text{\$.m}^{-2}$ ) and a low young's modulus ( $69\text{GPa}$ ). A team from IETR laboratory have fabricated and deposited the PZT thin films on our bimetals. To do so, they followed the same procedure as the one presented in [10-13]. Fig. 9 presents the deposition process of PZT thin films. The Zr/Ti ratio used for the solution preparation is of 57/43. Lead acetate ( $\text{Pb}(\text{CH}_3\text{CO}_2)_2 \cdot 3\text{H}_2\text{O}$ , Alfa Aesar), zirconium n-propoxide ( $\text{Zr}(\text{C}_3\text{H}_7\text{O})_4$ , Alfa Aesar, 70%) and titanium n-propoxyde ( $\text{Ti}(\text{C}_3\text{H}_7\text{O})_4$ , Adrich, 98%) are used as precursor materials. Acid acetic is used as a solvent. Ethylene glycerol ( $\text{C}_2\text{H}_6\text{O}_2$ , Fluka, 99,5%) is used to prevent cracks during the crystallization of the thin films. Lead acetate was first dissolved in a heated acid acetic. Zirconium and titanium were mixed together and then added to the lead acetate solution. Ethylene glycerol was finally added to the solution. The precursor solution was deposited onto different aluminum foils having different thicknesses by spin coating at  $6000\text{tr/min}$  during 20s to obtain a PZT film thickness of  $300\text{nm}$ . The coated layer was then introduced in a furnace at  $650^\circ\text{C}$  during 2 minutes to improve the crystallinity of the PZT films while keeping safe the aluminum foil. Depending of the targeted PZT thin film thickness, the same procedure is repeated for each  $300\text{nm}$  layer. The aluminum foils used for this experiment had thicknesses of  $15\mu\text{m}$  or  $30\mu\text{m}$  while the deposited PZT thin films have thicknesses of 2, 3 or  $4\mu\text{m}$ . For the electric measurement and poling, a  $150\text{nm}$  thick aluminum top electrode with an area of  $10\text{mm} \times 3\text{mm}$  have been sputtered. Once the PZT thin films were ready, they were glued on the bimetals using electric conductive epoxy.

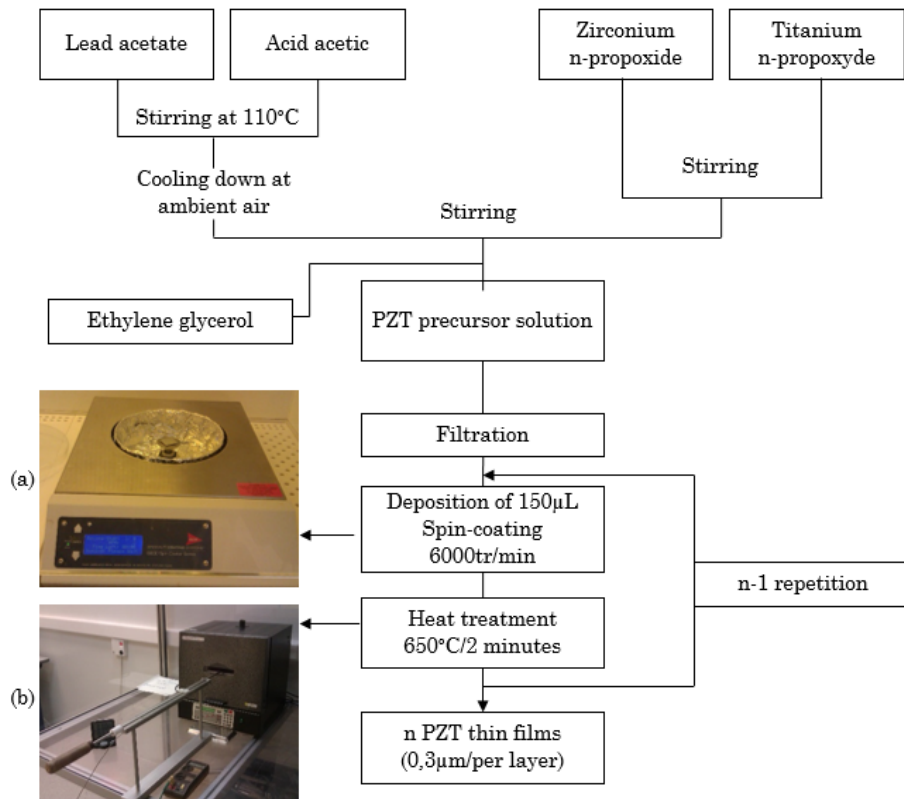


**Fig. 9.** Deposition process of the PZT thin films (a). Spin coating equipment, (b). Oven used for the thin films heat treatment.

To exhibit macroscopic piezoelectric properties, the samples must be poled. A sawyer-Tower circuit was employed for the poling and the investigation of the ferroelectric hysteresis cycle for each device. An electric field of 400kV/cm at 50Hz was applied to the samples. The measurement of the  $P(E)$  cycle allows obtaining the values of the coercive field corresponding to the electric field at zero poling field and the remnant polarization corresponding to the polarization of the ceramic at zero applied electric field. Fig. 10 shows the  $P(E)$  cycle of a ferroelectric material with  $P_r$  the remnant polarization and  $E_c$  the coercive field. Fig. 11 shows the hysteresis loop of a PZT thin film of  $4\mu\text{m}$  deposited onto an aluminum foil of  $30\mu\text{m}$  and then deposited onto a 6K hysteretic bimetal snapping at  $70^\circ\text{C}$  and snapping back at  $64^\circ\text{C}$ .

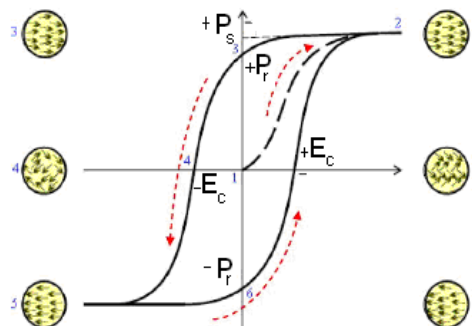


**Fig. 10.** Hysteresis loop ( $P(E)$ ) of a ferroelectric material.

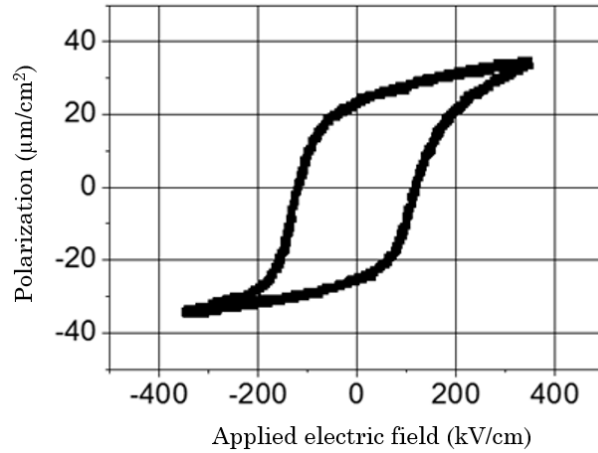


**Fig. 11.** Hysteresis loop ( $P(E)$ ) of a  $4\mu\text{m}$  PZT film deposited onto  $30\mu\text{m}$  aluminum foil.

The goal of this study is to investigate the electrical power delivered by a piezoelectric bimetal using PZT thin films and to study the impact of the aluminum and the PZT film thicknesses on the output power and also the number of PZT films deposited on each bimetal. As shown previously for the piezoelectric composites deposited onto bimetals, if the experiments are realized using low thermal hysteresis bimetals, these can lose their bistable behavior because of their increased thickness. To avoid this drawback, we used only higher hystereses than 3K. Consequently, two types of bimetals were sent to Nantes's university for the PZT films deposition: 8 bimetals of 6K hysteresis and 9 bimetals of 12K hysteresis. For some bimetals only one PZT layer was deposited and for the others 2 layers were used. In this last configuration, the two layers are poled in antiparallel configuration and are connected in a series configuration so as to reduce the equivalent capacitance and to increase the output piezoelectric voltage. Table 4 sums up all the devices realized and their characteristics in terms of thin film layers numbers and thicknesses, aluminum substrate thickness and finally bimetal's hysteresis.

	Al/PZT=	15/2 $\mu\text{m}$	15/3 $\mu\text{m}$	15/4 $\mu\text{m}$	30/2 $\mu\text{m}$	30/3 $\mu\text{m}$	30/2 $\mu\text{m}$
1 PZT layer per bimetal	Bimetal $\Delta T=6\text{K}$	X	X	X	X	X	X
	Bimetal $\Delta T=12\text{K}$	X	X		X	X	X
2 PZT layers per bimetal	Bimetal $\Delta T=6\text{K}$		X			X	
	Bimetal $\Delta T=12\text{K}$	X		X	X		X

**Table 4.** Properties of the PZT thin films deposited onto the bimetals at Nantes's university.

Fig. 12.a shows a top view of the fabricated PZT thin films on an aluminum foil with 4 deposited electrodes. Fig. 12.b shows a bimetal with one Al/PZT thin film and Fig. 12.c shows bimetals with one and two Al/PZT thin films.

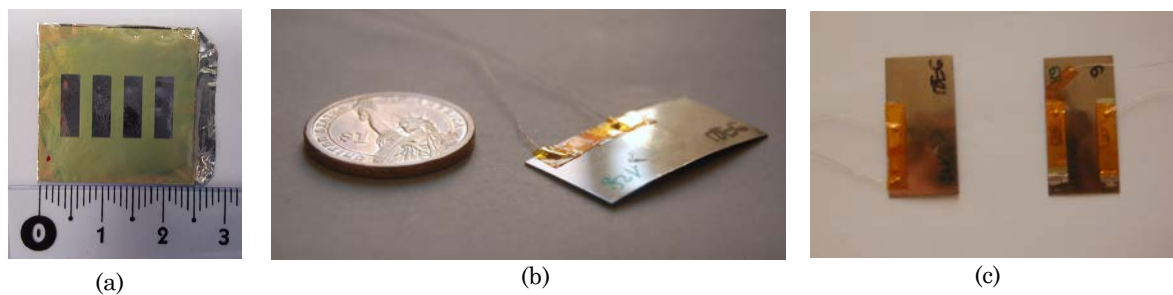


**Fig. 12.** (a). Top view of the realized PZT thin films, (b). Piezoelectric bimetal with one PZT thin film, (c). Piezoelectric bimetal with one and 2 PZT thin films.

## 2.2. Characterization of the piezoelectric bimetals

The capacitance value of each thin film, its dielectric losses, its remnant polarization and also its coercive field are measured at IETR previously to our tests at LGEF. The results are showed in Fig. 13 and Fig.14 for the bimetals having only one PZT layer. In the x-axis of these graphs, the references of each sample is given. The format of the reference is: bimetal hysteresis (K)/ Al foil thickness ( $\mu\text{m}$ )/ PZT film thickness ( $\mu\text{m}$ ). For example the reference 6/15/2 refers to the 6K hysteresis bimetal, with a deposited PZT thin film fabricated using a 15 $\mu\text{m}$  aluminum foil and a PZT film thickness of 2 $\mu\text{m}$ .

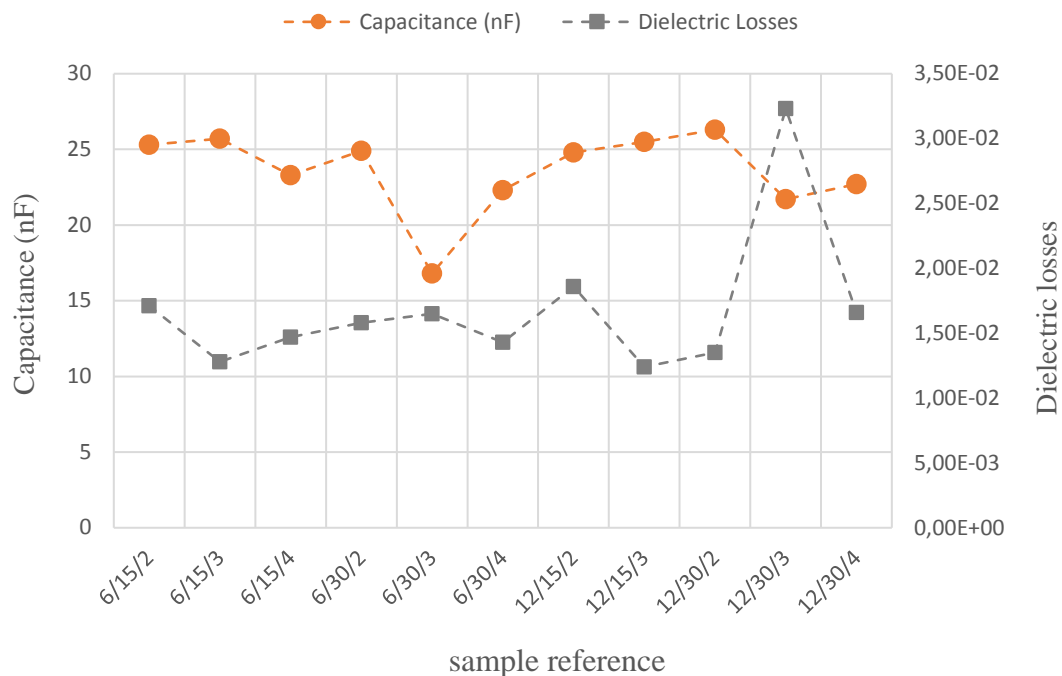


**Fig. 13.** Values of the capacitance and the dielectric losses of the fabricated samples.

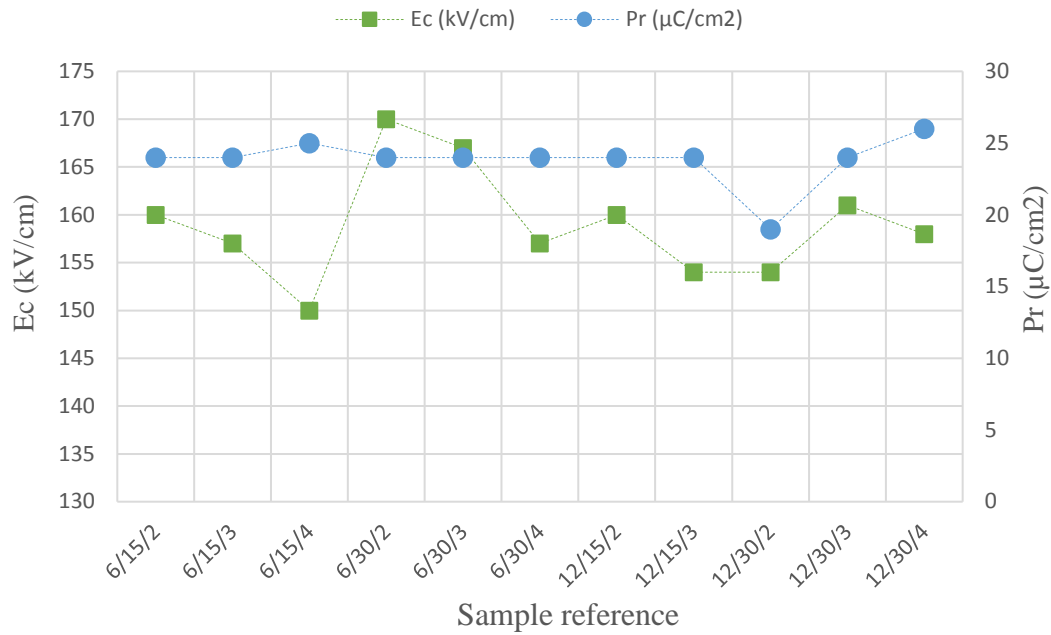


**Fig. 14.** Coercive field and remanent polarization of fabricated samples.

The fabricated PZT layers had a mean capacitance value equal to 25nF which is 10 times higher than that obtained with the PZT paint. This can be explained by the fact for the PZT paint, the PZT particles represent only 20% of the paint preparation volume. For the experimental tests of the piezoelectric bimetal, we followed exactly the same procedure as the one used for the piezoelectric paint. To observe the open circuit voltage of each piezoelectric bimetal during its heating and cooling phases, we use a voltage follower circuit (TL082IP) whose input impedance is equal to  $10^{12}$ ohms. Each bimetal was set in a peek substrate like those used previously in order to maintain the bimetal in its cavity. The same experimental setup as the one shown in Fig. 7 was used. Fig. 15 presents the signal delivered by the piezoelectric bimetal snapping up signal and Fig. 16 the snapping back one. These images were realized using a high resolution an synchronized camera whose reference is DS-CAM-600C from DEWESOFT.

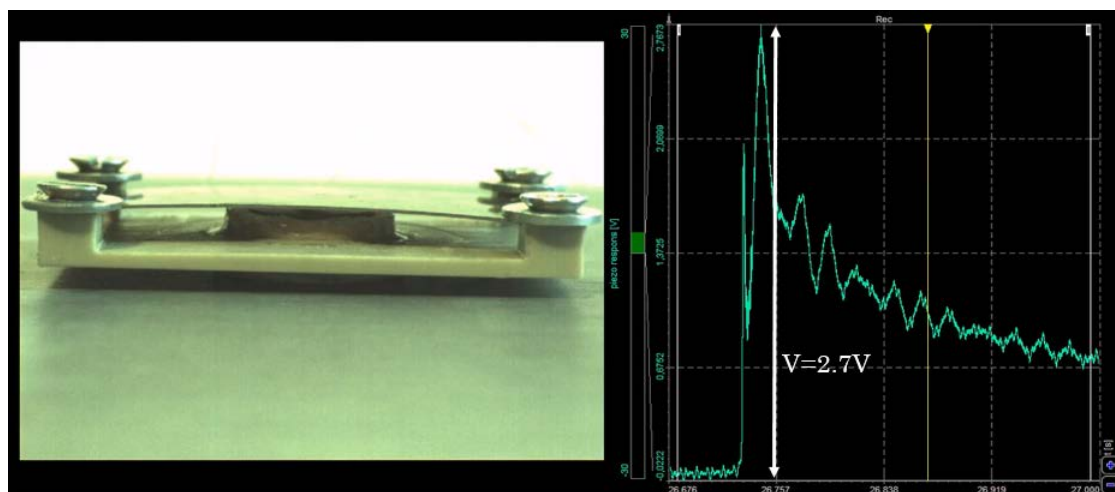


**Fig. 15.** Electrical signal of the piezoelectric bimetal during his snap- up (sample reference 6/30/4).

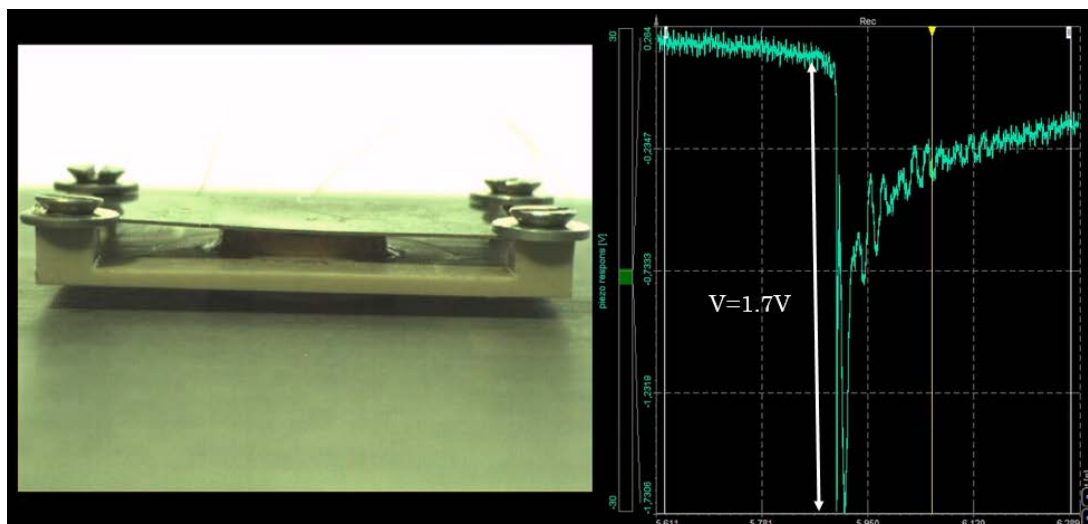


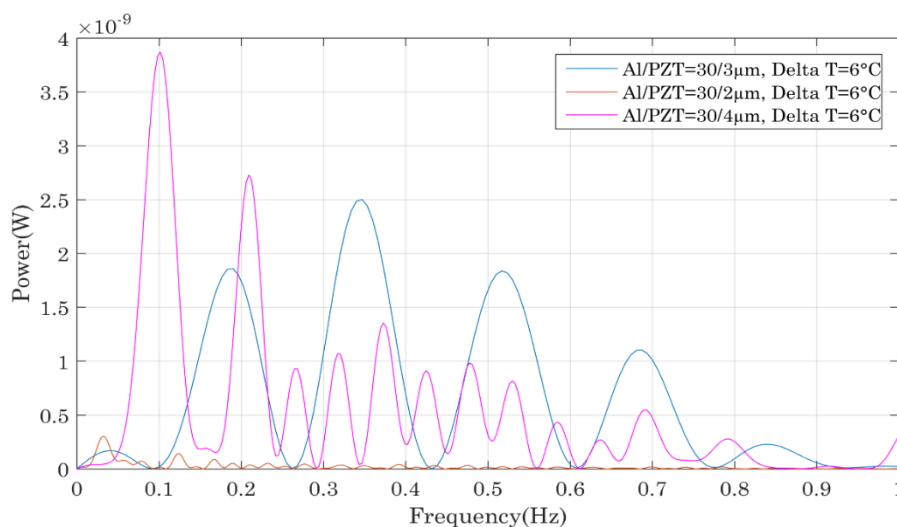
**Fig. 16.** Electrical signal of the piezoelectric bimetal during its snap-back (sample reference 6/30/4).

Some of the fabricated samples referred to in Table 4 are not characterized because the wires on the electrodes got removed and no electrical signal is obtained even after using a conductive silver paint to stick them again. It was the case for the samples 12/15/2 with one PZT thin film, and 12/30/2 with two PZT thin films.

The impact of the PZT and aluminum films thicknesses on the output power are studied hereafter. In both cases, the study is led in the case of one and two PZT layers per bimetal. Then, the devices with one and two layers are compared and the most powerful configuration is pointed out. The calculation of the power output in an open circuit configuration of each device is realized using the signal's FFT. Note that in this part, no comparison in function of the bimetal's hysteresis is established as this was the study developed in chapter 3.

#### Performances comparison of the bimetal with one PZT thin film each

Fig. 17 presents the FFT analysis of the piezoelectric bimetal's output signals. On each graph, the compared bimetal has the same hysteresis and the same Al layer thickness but the PZT thickness varies. In the three given graphs, we observe the same trend: the power increases when the PZT thickness increases, which is logical because a thicker PZT layer means more generated electrical charges and thus a higher amount of electrical power.



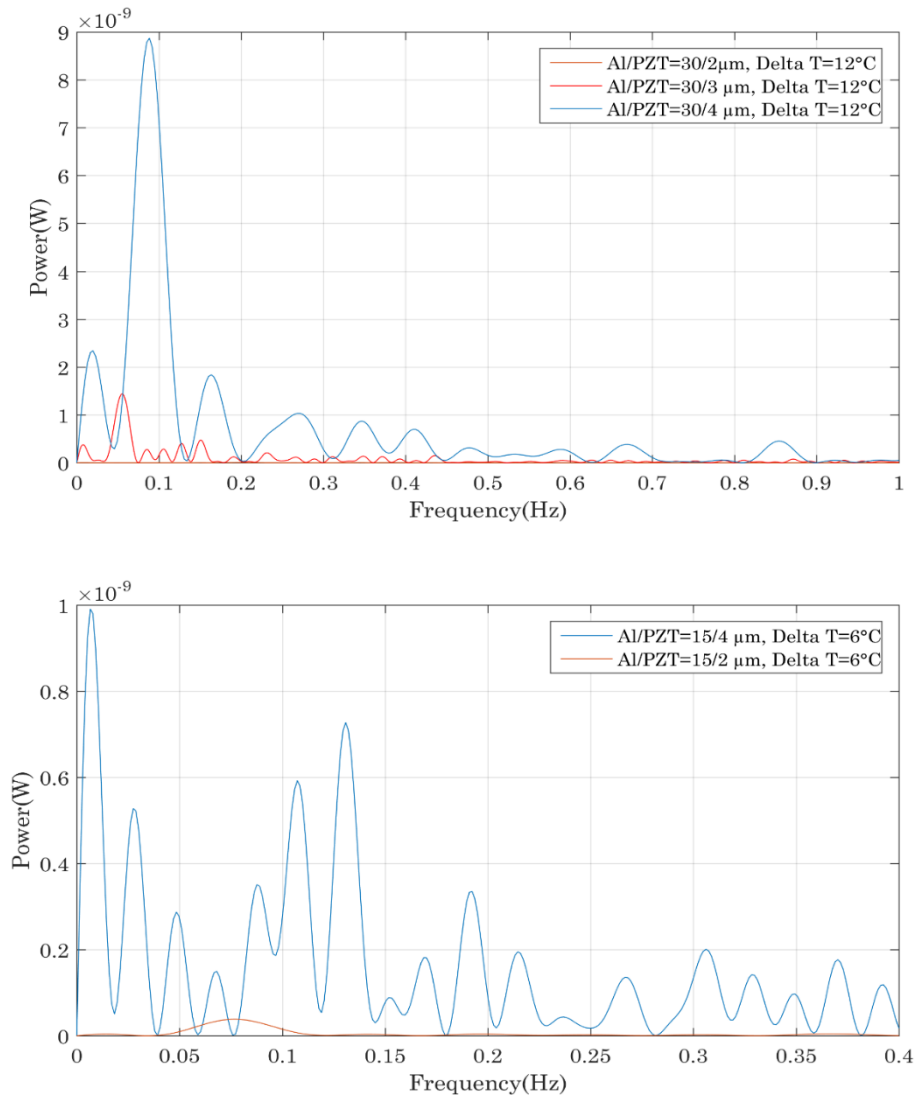


**Fig. 17.** Comparison of different piezoelectric bimetal performances in function of the PZT layer thickness.

Fig. 18 compares different piezoelectric bimetal output power as functions of the aluminum foil thickness. Here again the bimetal has the same thermal hysteresis and the same PZT film thickness but the aluminum foil thickness varies. The three comparisons show that thicker aluminum foils allow more power harvesting. The reason of such a trend is due to the position of the neutral axis across the beam: the stress distribution across the bimetal's thickness makes it more interesting to have a thicker aluminum foil as the PZT layers become located in a region of higher stress distribution which leads to higher electrical power.

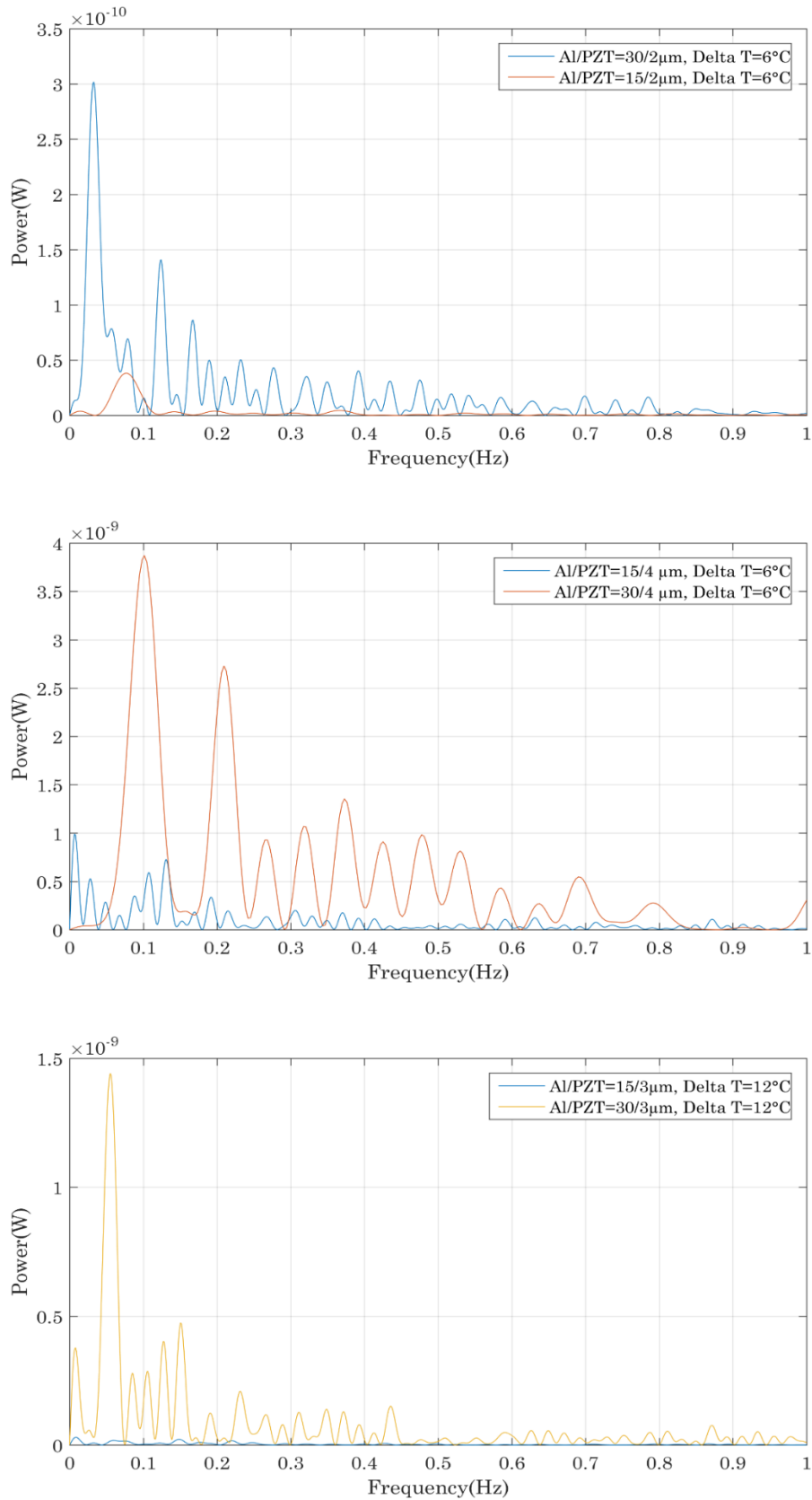
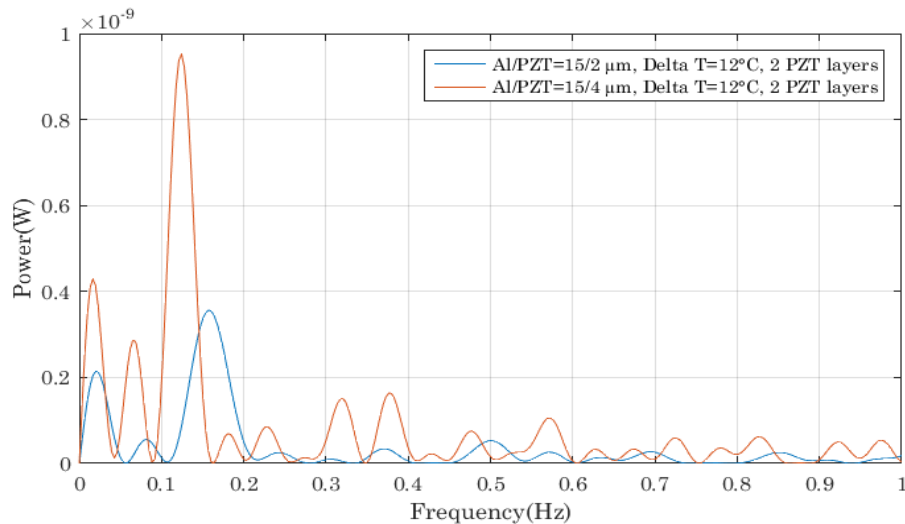


**Fig. 18.** Comparison of different piezoelectric bimetal performances in function of the Al layer thickness.

From this first comparison established for one PZT layer per bimetal, it seems that a thick PZT layer and a thick aluminum foil allow to harvest more power, since the best configuration is the one where the PZT layer is 4 $\mu\text{m}$  thick and the aluminum thickness equals to 30 $\mu\text{m}$ .

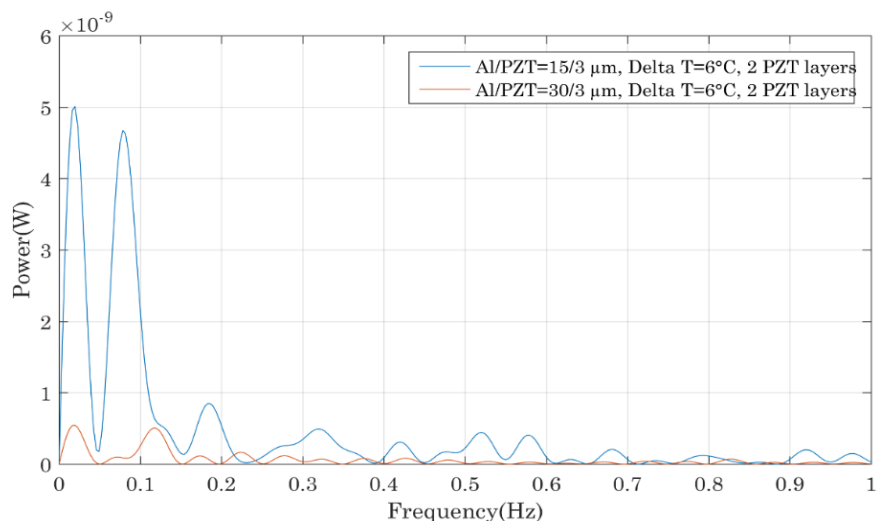
*Performances comparison of the bimetals with two PZT thin films each*

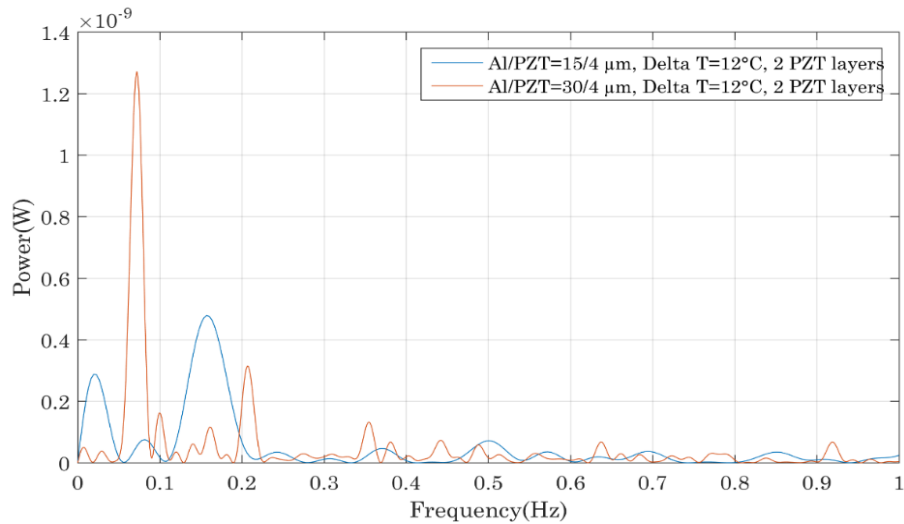
Let us see now if the previous observations are verified if two PZT layers are used on each bimetal. Fig. 19 compares different devices performances in function of the PZT thickness and here the same observation as previously is made, meaning that a higher PZT layer allows more charges to be generated and thus more power scavenging.



**Fig. 19.** Comparison of different piezoelectric bimetals performances in function of the PZT layer thickness.

Fig. 20 compares different bimetals having the same properties except the Aluminum thickness that varies. Contrary to the first comparison established previously when one PZT layer is deposited on each bimetal, here we do not observe any tendency so no conclusion can be given concerning the impact of the aluminum thickness on the output power if many layers are deposited on each bimetal.

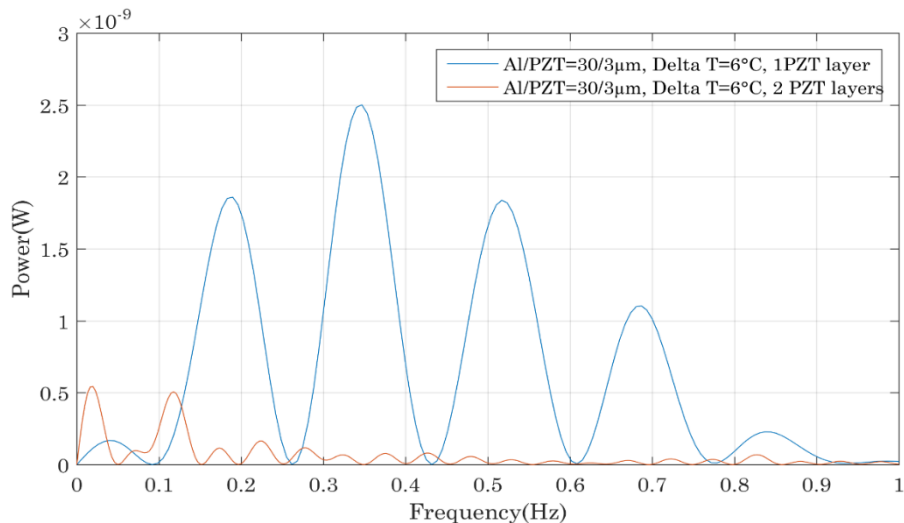




**Fig. 20.** Comparison of different piezoelectric bimetal performances in function of the Al layer thickness.

Performances comparison of bimetal with one and two PZT thin films

In this last part, we compare the performances of bimetal having the same properties and identical PZT layers except that one bimetal has one PZT layer deposited on it and the other has two. The two graphs of fig. 21 show that the bimetal with only one PZT layer are more powerful. This can seem to be counter-intuitive because more PZT is supposed to be generated. But the reason of such a behavior is related to the bimetal properties. Arnaud studied the bimetal modeling in his thesis and his work allows us to explain the observed trend [24]. In fact, for bi-stable bimetal having a certain hysteresis, one of the parameter that fixes the hysteresis value is the ratio between the thicknesses of the bimetal and its curvature. When additional layers are deposited onto the bimetal, its general thickness is increased and thus its hysteresis becomes lower [14]. A lower hysteresis bimetal delivers lower mechanical force when snapping and thus less electrical power is generated.



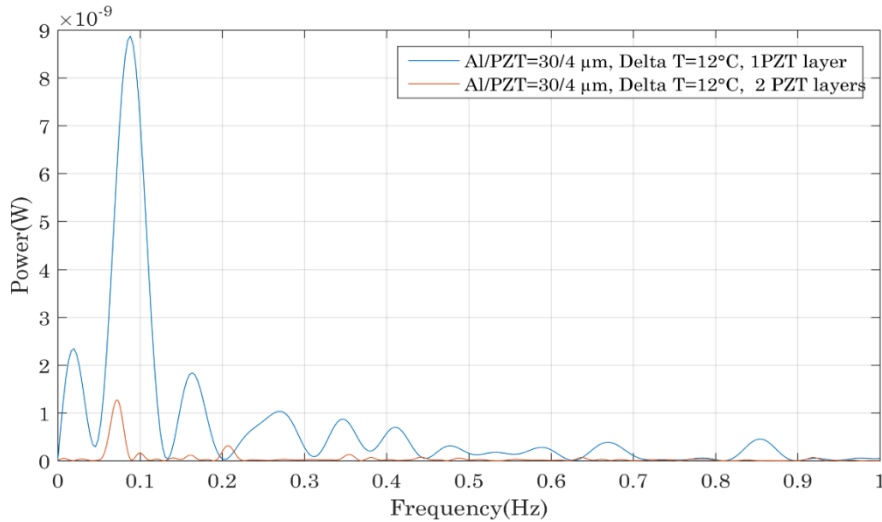


**Fig. 21.** Performance comparison of the piezoelectric bimetals with one and two PZT layers.

From all the comparisons established here, the most powerful bimetal was the one with one PZT film whose thickness equals  $4\mu\text{m}$  on an aluminum foil of  $30\mu\text{m}$  thick. This device generated an electrical power of  $9\text{nW}$ . So to conclude, PZT thin films allow harvesting electrical energies in the range of few nano-watts if thick Al foils PZT layers films are used. However, one should keep in mind that only thin PZT films can be deposited on each bimetal otherwise its thermal properties will be drastically changed: its thermal hysteresis can be lowered or even its bistability lost. For this reason, the best configuration is the one with only one PZT thin film per layer.

### III. Thermal and mechanical energy harvesting

To increase the level of generated power by our energy harvester, special interest is given to the ambient energies that may be exploited simultaneously as wasted heat. Vibrations offer the potential of occurring in many environments as commercial building, industrial environments, trains, automobiles, aircrafts.... Vibrations-to-electricity conversion also offers the potential for wireless sensor node to be self-sufficient in many environments due to the high power density reaching  $300\mu\text{W}/\text{cm}^3$  [15]. The goal of this part is to develop a dual energy harvester for thermal and vibrations energy harvesting in environments where both energies are available. We first start the study with a benchmark of the potential vibrations power sources and their characteristics. We then point out the most interesting and frequent frequencies and design for each frequency a dedicated piezoelectric cantilever. Numerical simulations using COMSOL Multiphysics were carried out and finally guidelines are given to extend the frequency operating range of each beam.

#### 1. Available vibration sources

Many studies were focused on the characterization of low-level vibrations to extract their characteristics and to estimate their capability for energy harvesting applications. Based on such studies, we intended to design a wide band vibrations energy harvester. The goal was to target the commonly occurring vibrations to maximize the potential applicability of the harvester. Our interest was more specifically in vibrations in office buildings, manufacturing environments or

home environment. In [15-16], vibrations from different sources were measured and characterized: the acceleration magnitude and the frequency at which that maximum occur are summed up in table 5.

Vibration source	Peak acceleration (m/s <sup>2</sup> )	Frequency of peak (Hz)
Kitchen blender	6.4	120
Clothes dryer	3.5	120
Door frame just after door closes	3	125
Microwave oven	2.25	120
Bread maker	1.03	120
Windows (size 0.6m x 1m) next to a busy street	0.7	100
Notebook computer while CD is being read	0.6	75
Refrigerator	0.1	240
Laptop (Lenovo)	0.01	90
Vacuum cleaner	0.158	100
Water heater (Panasonic)	0.006	100
Air cooler (at low speed)	0.032	100
Stand fan (Panasonic, at low speed)	0.6	100

**Table 5.** List of vibration sources with their maximum acceleration magnitude and frequency at peak acceleration.

It appears from this table that many ambient vibrations occur at 100Hz and 120Hz. Consequently, these frequencies are studied hereafter and two different piezoelectric beams will be designated to resonate at these frequencies. Moreover, depending on the continent, the frequency of the oscillations of alternating current (AC) in the electric power grid transmitted from a power plant to the end-user is either equal to 50Hz in Europe, Africa and Asia or 60Hz in America. Thus, we chose to target also the frequency of 50Hz in our application.

## 2. Dual energy harvester design rules

The dual energy harvester designed here has to harvest at the same time thermal and vibrational energy. To do so, the same PEEK substrate is used for both energies harvesting and the general energy harvester should constitute one module instead of two independent power generators. Generally, vibration energy harvesters are designed to work only at one particular frequency leading to a high quality factor resonance which means a limited bandwidth over which energy can be harvested [16]. Consequently, any difference between these two frequencies can result in a significant decrease in the harvested power. Thus, it is necessary to widen the bandwidth of such

generators. The review in [17] deals with the different strategies to follow in order to overcome the aforementioned limitation. One of the solutions is to employ an array of structures each with a different resonant frequency. This strategy has been studied by many researchers [18-19-20]. In [18], the author has realized a multifrequency energy harvester thanks to the different resonance frequencies of the several cantilevers. Its structure is shown in Fig. 22. It is made of three piezoelectric bimorph cantilevers with the same dimensions, equal to  $15\text{mm} \times 1.5\text{mm} \times 0.6\text{mm}$ , and different masses ( $m_1 = 1.4\text{g}$ ,  $m_2 = 0.7\text{g}$ ,  $m_3 = 0.6\text{g}$ ) at the free end. As a consequence, each cantilever has a different fundamental resonant frequency and exhibits a different voltage ( $V_1$ ,  $V_2$ ,  $V_3$ ) between its electrodes. The respective three fundamental resonant frequencies obtained are about  $f_1 = 113\text{Hz}$ ,  $f_2 = 183\text{Hz}$ , and  $f_3 = 281\text{Hz}$ .

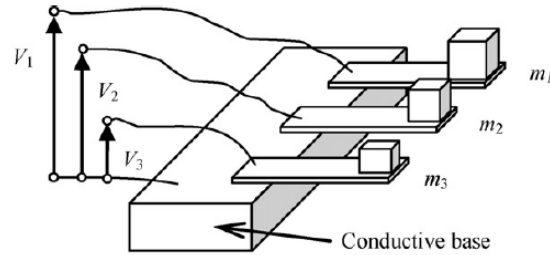


**Fig. 22.** Structure of a piezoelectric array energy harvester for wideband energy harvesting [18].

In [20], an array lead of zirconate titanate (PZT) thick-film cantilevers was designed and fabricated to demonstrate the possibility of harvesting vibration at different frequencies. Two configurations of multi-cantilever were fabricated. One having six cantilevers of constant width but different lengths (fig.23.a) and another having five cantilevers of constant length but different widths (fig.23.b). The experimental results showed different resonance frequencies between 220 Hz to 520 Hz. Fig. 23 shows the realized cantilevers arrays.

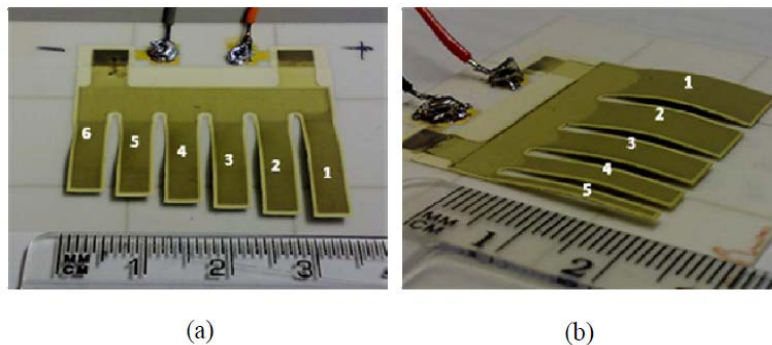


**Fig. 23.** An array of cantilever with (a) six fingers having different length and (b) an array of cantilever with five fingers having different width [20].

In this work, we use the same strategy to make each cantilever beam vibrate at one of the previously pointed out frequencies.

To make the cantilever beams vibrate at 50Hz, 100Hz and 120Hz, some design rules given in [17] are followed. That paper deals, among other things with the techniques for frequencies mechanical tuning. Changing the beam dimensions and moving the center of gravity of the proof mass are the solutions we finally selected. For his analysis, the author considered a cantilever beam with a tip mass at its end. The resonant frequency of such system is given by [21]:

$$f_r = \frac{1}{2\pi} \sqrt{\frac{Ywh^3}{4l^3(m + 0.24m_c)}} \quad (1)$$

Where  $Y$  is the young modulus of the cantilever beam,  $w$ ,  $h$  and  $l$  are the width, thickness and length of the cantilever respectively,  $m_c$  the mass of the cantilever and  $m$  the mass of the tip mass.

As the resonant frequency of the beam is inversely proportional to  $l^{3/2}$ , any change in the beam's length can modify its resonance frequency. The author considered  $l$  as the original length of the cantilever and  $l'=l+\Delta$  the modified length where  $\Delta$  is the difference between them. The author then simulated the evolution of the normalized resonant frequency  $\frac{f'_r}{f_r}$  in function of the variation in the cantilever length. Fig. 24 describes this evolution. It shows that a negative  $\frac{\Delta}{l}$  corresponding to a shorter cantilever beam has a higher resonance frequency than the initial beam. At the opposite, a longer beam leads to a lower resonance frequency.

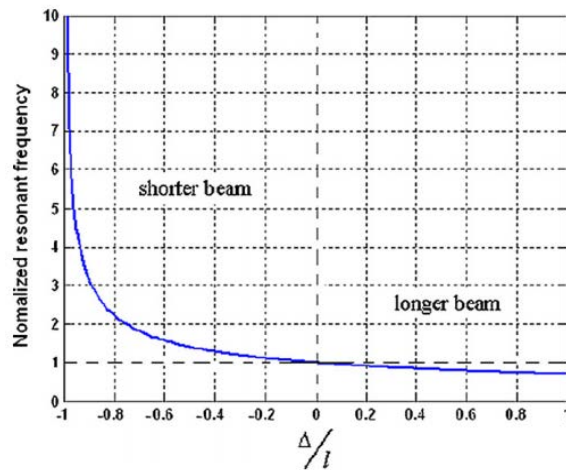


**Fig. 24.** Evolution of the normalized resonant frequency with a variation of the cantilever length (from [18]).

Until now, we have pointed out the most interesting frequencies for our application and how to make the cantilevers resonate at these frequencies. However, we also want each cantilever to be able to harvest energy over a large frequency range instead of using each beam at one specific frequency. Here again, the author in [18] also addressed this issue and proposed a study of the dependence of the resonant frequency on the position of the gravity center of the tip mass.

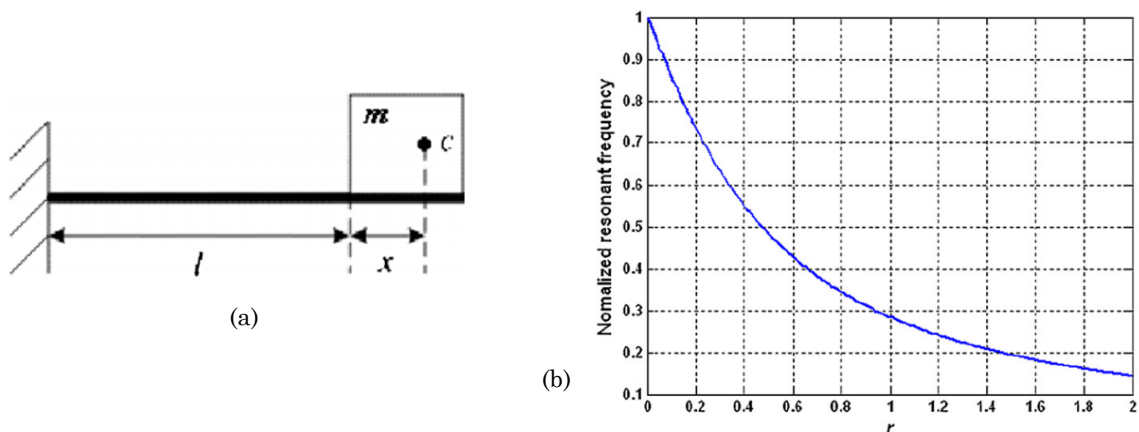


**Fig. 25.** Evolution of the normalized resonant frequency with a variation of the cantilever the mass center of gravity position (from [18]).

In the cross-section view of the cantilever beam with a mass at its free end in Fig. 25.a, the length of the cantilever without the mass is  $l$  and the proof mass on its free end is  $m$ . The center of

gravity of the proof mass is located at  $c$  and the distance between  $c$  and the end of the cantilever is  $x$ . In Fig. 25.b,  $r$  is equal to  $\frac{x}{l}$  and the graph represents the evolution of the normalized resonant frequency with a variation of the mass center of gravity position. It shows that the further the center of gravity of the proof mass is from the end of the cantilever, the lower the resonance frequency is. This principle was studied by Wu et al in [22] as they designed a piezoelectric energy harvester using a cantilever beam with a mass at its end but the mass is composed of two parts: a fixed mass attached to the cantilever beam and the other part is a movable screw. The center of gravity of the proof mass can consequently be adjusted by moving the position of the screw. The schematic representation of that system and its experimental realization are showed in Fig. 26.

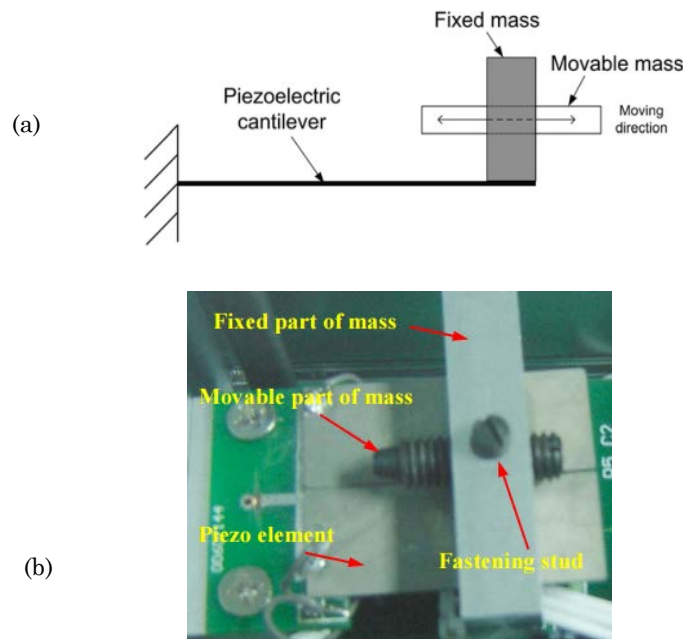


**Fig. 26.** (a). Schematic of the piezoelectric element with gravity center movable mass, (b). Picture of the piezoelectric cantilever prototype with gravity center movable mass (from [22-23]).

Using this experimental setup, the authors were able to study the frequency adjustment range depending on the extreme positions of the movable screw. The fixed mass has the dimensions 10 mm x 12 mm x 38 mm and the movable mass is an M6 screw of length of 30 mm. The resonant frequency of the device was tuned from 180Hz to 130Hz by moving the screw from one end to the other end. Fig. 27 shows the beam's resonance frequency adjustment.

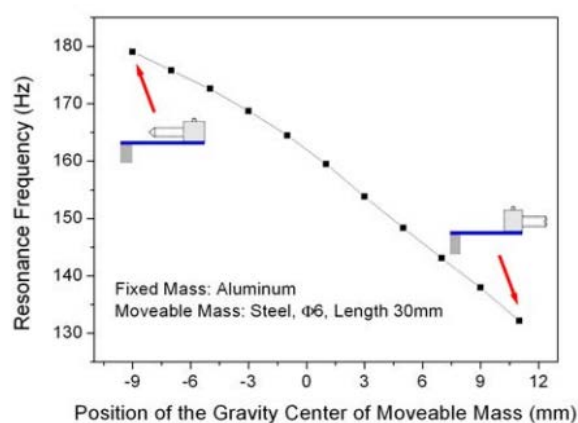


**Fig. 27.** Experimental result of frequency adjustment (from [21]).

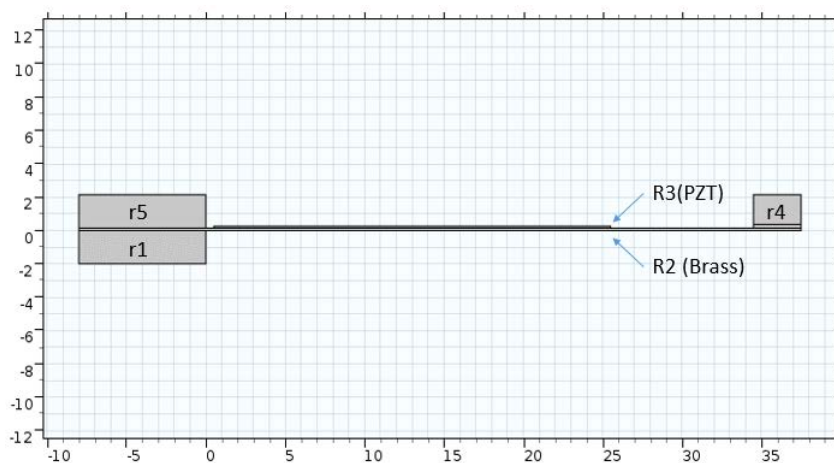
Based on all these papers and studies, we will design a broad-band vibrations energy harvester with three cantilever beams one for each targeted frequency. For each beam, its frequency operation window will be widened using a movable mass to move the tip mass center of gravity and thus the cantilever's beam resonance frequency. The design of the piezoelectric beams will be realized using a finite element modeling on Comsol.

### 3. Numerical modeling

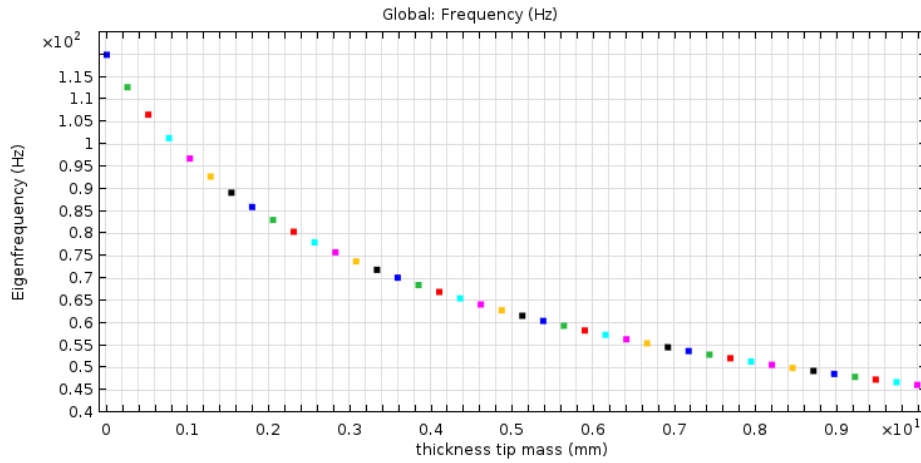
The three cantilever beams will be clamped at one end of the thermal energy harvester for both thermal and vibrations energy harvesting in environments where both energies are available. Because of the small size of our piezoelectric membranes (from stab), each cantilever is designed in a different piezoelectric membrane. However, given the width of our thermal energy harvester, the total width of the three cantilevers should not exceed 27mm.

Given the previous guidelines, we know that increasing the cantilever's beam length, width or tip mass leads to a decrease in the beam's resonance frequency. The first step we started our study with was to design the longest piezoelectric beam having a width of 8mm (to leave 1mm between each cantilever in the final device) on Comsol and to observe at which frequency it resonates. The device is modeled in a 2D configuration. The simulation of such a beam showed an eigenfrequency equal to 110Hz. To reach a resonance frequency equal to 120Hz, we chose to decrease the beam's width from 8mm to 7mm. The new resonance frequency was then equal to 120Hz.

The second step is to choose which technique will be used to reach the desired frequencies: decreasing the length will allow the beam's resonance frequency decrease and increasing the beam's width and tip mass will allow the resonance frequency decrease. However, knowing that the width of our dual energy harvester restricts the width of each beam, the fit parameter that is used here is the tip mass. Consequently, simulations are carried out using different tip masses having the same width (7mm) and length (3mm) but whose thicknesses varies from 0.01mm (equivalent to no tip mass) to 10mm. The designed piezoelectric cantilever is showed in Fig. 28 and the results of the simulation for the different mass thicknesses is represented in Fig. 29. In the scheme of the cantilever beam in Fig. 28, R1 and R5 represent the steel pieces used for the piezoelectric membrane clamping, R4 is the tip mass whose thickness is used to adjust the beam's resonance frequency with the ambient vibrations and finally R2 and R1 are respectively the brass and the piezoelectric ceramic constituting the piezoelectric membrane.

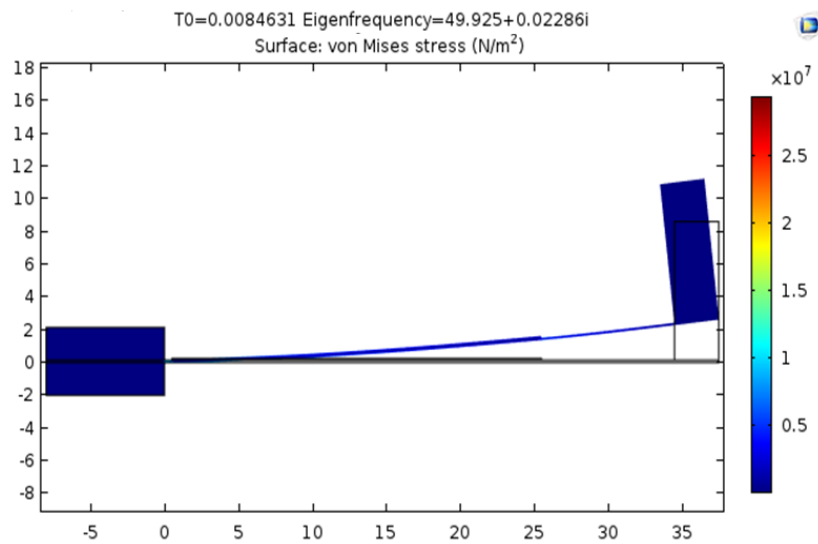


**Fig. 28.** View of the 2D piezoelectric cantilever beam for vibration energy harvesting.



**Fig. 29.** Evolution of the piezoelectric cantilever resonance frequency in function of the tip mass thickness.

Fig. 29 confirms the fact that the eigenfrequency increases when the tip mass thickness decreases. Given this graph, we selected the corresponding thicknesses giving respectively resonance frequencies equal to 120Hz, 100Hz and finally 50Hz. The results are shown in Fig. 30.



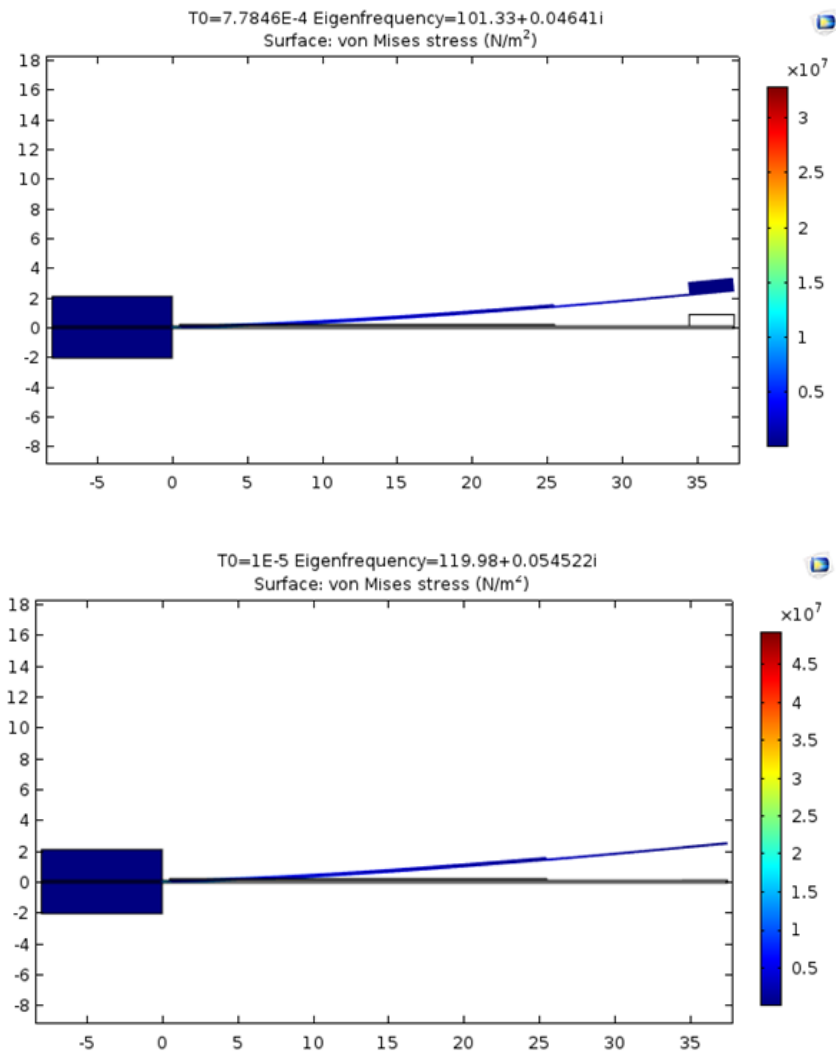


**Fig. 30.** Stress distribution for different piezoelectric beams having different tip masses (the tip mass thickness and the beam resonance frequency values are given in each case).

These simulated beams are currently being fabricated and experimental tests will be carried out on it to validate their resonance frequencies and lately to see the amount of power that may be harvested using such dual energy harvesters.

#### IV. Conclusion

In this chapter, we investigated new ways to harvested different kinds of wasted energies thanks to bimetal and piezoelectric membranes. First of all, we explored the direct deposition of piezoelectric materials on bistable bimetal. Two different techniques and materials were used for this experiment. On one hand, piezoelectric composites using barium titanate or PZT particles and a polymer matrix have been used and on the other hand, massive PZT thin films are fabricated and deposited onto bimetal. The bimetal with piezoelectric thin films showed better performances than the bimetal with piezoelectric composites, however, in both cases low amounts of electrical power are obtained reaching in the best case 10nW.

In the second part of this chapter, we developed a dual energy harvester to harvest both thermal energy and mechanical energy. Sources of wasted vibrations are very frequent in our

environment. The frequencies and acceleration of such vibrations are very different, so to point out the most interesting vibrations, we established a state of the art of the characteristics of ambient vibrations. This allowed us to concentrate our work on the frequencies 50Hz, 100Hz and 120Hz. Based on many previous studies concerning piezoelectric cantilever beams design, we gave the main guidelines to modify the piezoelectric beams to tune their eigenfrequency. A Finite Element Model of a cantilever beam was established in a 2D configuration and some geometrical parameters were changed using some sweeps on Comsol to find the right beams dimensions to reach frequencies of 50Hz, 100Hz and 120Hz. Moreover, a technique to widen the frequency operation window of each beam was given. Experimental tests on these structures are currently being done.

## V. References

- [1] Zhang, Y, "Piezoelectric Paint Sensor for Nondestructive Structural Condition Monitoring", SEM International Congress & Exposition on Experimental & Applied Mechanics, (2004).
- [2] Kang, L H, "Piezoelectric paint sensor for impact and vibration monitoring", 7th European Workshop on Structural Health Monitoring, (2014).
- [3] Yang, C and C-P Fritzen. "Piezoelectric Paint: Characterization For Further Applications". *Smart Mater. Struct.* 21.4 (2012): 045017.
- [4] White, J. R. et al. "Piezoelectric Paint: Ceramic-Polymer Composites For Vibration Sensors". *Journal of Materials Science* 39.9 (2004): 3105-3114.
- [5] Payo, Ismael and Jack Michael Hale. "Dynamic Characterization Of Piezoelectric Paint Sensors Under Biaxial Strain". *Sensors and Actuators A: Physical* 163.1 (2010): 150-158.
- [6] Capsal, Jean-Fabien et al. "Piezoelectric Sensing Coating For Real Time Impact Detection And Location On Aircraft Structures". *Smart Mater. Struct.* 21.5 (2012): 055021.
- [7] Klein, K A, "A Composite Piezoelectric Paints", IEEE 6th Int. Symp. on Appl. ferroelectrics, (1986): 285 -287.
- [8] Jaffe, Bernard, William R Cook, and Hans Ludwig Jaffe. *Piezoelectric Ceramics*. London: Academic Press, 1971.
- [9] Noheda, B. et al. "A Monoclinic Ferroelectric Phase In The Pb(Zr[Sub 1-X]Ti[Sub X])O[Sub 3] Solid Solution". *Appl. Phys. Lett.* 74.14 (1999): 2059.
- [10] Seveno, R et al. "Preparation Of Multi-Coating PZT Thick Films By Sol-Gel Method Onto Stainless Steel Substrates". *Journal of the European Ceramic Society* 20.12 (2000): 2025-2028.
- [11] Seveno, R. and D. Averty. "Ultra Light Tunable Capacitor Based On PZT Thin Film Deposited Onto Aluminium Foil". *J Sol-Gel Sci Technol* 68.2 (2013): 175-179.
- [12] Dufay, T. et al. "Transverse Piezoelectric Coefficient Measurement Of Flexible Lead Zirconate Titanate Thin Films". *J. Appl. Phys.* 117.20 (2015): 204101.

- [13] Seveno, R. et al. "Flexible PZT/Aluminium Thin Films Characterizations For Energy Harvesting At Very Low Frequencies (1 Hz)". *2015 Joint IEEE International Symposium on the Applications of Ferroelectric (ISAF), International Symposium on Integrated Functionalities (ISIF), and Piezoelectric Force Microscopy Workshop (PFM)* (2015): 94- 97.
- [14] Arnaud, A et al. "Thermo-Mechanical Efficiency Of The Bimetallic Strip Heat Engine At The Macro-Scale And Micro-Scale". *J. Micromech. Microeng.* 25.10 (2015): 104003.
- [15] Roundy, Shad, Paul Kenneth Wright, and Jan M Rabaey. *Energy Scavenging For Wireless Sensor Networks*. Boston: Kluwer Academic Publishers, 2004.
- [16] Beeby, S P, M J Tudor, and N M White. "Energy Harvesting Vibration Sources For Microsystems Applications". *Measurement Science and Technology* 17.12 (2006): R175-R195.
- [17] Zhu, Dibin, Michael J Tudor, and Stephen P Beeby. "Strategies For Increasing The Operating Frequency Range Of Vibration Energy Harvesters: A Review". *Measurement Science and Technology* 21.2 (2009): 02200.
- [18] Ferrari, Marco et al. "Piezoelectric Multifrequency Energy Converter For Power Harvesting In Autonomous Microsystems". *Sensors and Actuators A: Physical* 142.1 (2008): 329-335.
- [19] Qi, Shaofan et al. "Design Of A Multiresonant Beam For Broadband Piezoelectric Energy Harvesting". *Smart Mater. Struct.* 19.9 (2010): 094009.
- [20] Kok, Swee-Leong et al. "Multi-Frequency Energy Harvesting Using Thick- Film Piezoelectric Cantilever". International Conference on Electrical, Control and Computer Engineering, Malaysia, (2011).
- [21] Blevins, Robert D. *Formulas For Natural Frequency And Mode Shape*. New York: Van Nostrand Reinhold Co., 1979.
- [22] Wu, X et al, "A frequency adjustable vibration energy harvester", Proc. PowerMEMS (2008): 245-8.
- [23] Kaźmierski, Thomas J and Stephen Beeby. *Energy Harvesting Systems*. New York: Springer, 2011.
- [24] Arnaud Arthur, "Modeling and design of thermomechanical conversion systems for thermal energy harvesting applications", Université Grenoble Alpes, 2016.

## Chapter 5

# Device SPICE modelling *and* Power Management simulations for Wireless Sensor Node applications

Chapter 5 .....	133
I. Introduction .....	134
II. Device electromechanical modeling .....	134
1. General model of Kinetic energy harvesters .....	134
2. Modeling of piezoelectric energy harvesters .....	136
2.1. Mechanical modeling .....	136
2.2. Electrical modeling .....	138
3. SPICE modelling of the harvester .....	139
III. Power management.....	144
1. Review of the different power management technologies .....	144
1.1. Energy conversion steps .....	144
1.2. Power management circuits state of the art .....	144
2. Power management simulation.....	151
2.1. First modules using a rectifier and a storage capacitor .....	151
2.2. Power management results using discrete element PMC.....	153
2.3. Power management simulation using Integrated interface circuits .....	153
IV. Wireless sensor node demonstrations.....	154
V. Conclusion .....	161
VI. References.....	162

## I. Introduction

The thermal energy harvester studied in this thesis delivers small amounts of power in the range from few microwatts to one tenth of microwatts. As it will be shown later, this amount of power allows wireless sensor node to operate only in asynchronous mode. It is due to the increase of the consumption of synchronous operation mode consumptions which highlights the necessity of a dedicated power management circuit. Many techniques can be used to extract the piezoelectric charges out of a generator: passive circuits like diode bridges or voltages doublers are the most commonly used but not the most efficient for energy harvesting applications. Using some nonlinear techniques, it is possible to extract most of the charges out of the piezoelectric element which boosts its performances. This chapter thus deals with the whole integration process of our thermal energy harvester. To do so, in the first part of this chapter, an equivalent electrical model of our piezoelectric energy harvester is developed to model the harvester's output signal and to be able to simulate and compare different power management circuits. After that, a state-of-the-art of the existing nonlinear techniques and circuits used to extract energy is exposed followed by the exposition of the work of power management circuit simulations realized by CEA Leti. Finally, in the last part of this chapter, the different wireless sensor node demonstrations achieved thanks to our harvester and the standard passive power management circuit are exposed.

## II. Device electromechanical modeling

The piezoelectric membrane with the oscillating bimetallic shell can be assimilated to a vibration-based generator. In fact, each time the bimetal snaps up or down, it hits the piezoelectric membrane that vibrates at its resonance frequency. In the last decades, these vibration-based generators have known much interest and have been explored extensively.

In the first section of this part, the modeling of the general vibration-based kinetic energy harvesters is discussed. Then, the piezoelectric energy harvesting devices are presented and assessed, and finally a SPICE model of the coupled piezoelectric and bimetal energy harvester is presented.

### 1. General model of Kinetic energy harvesters

There mainly exists three types of vibration based generators: electrostatic, electromagnetic and piezoelectric generators. Whatever the type of electromechanical transduction used, a general model for the conversion of the kinetic energy of a vibrating mass into electrical power have been established first by Williams and Yates [1] and studied lately by many researchers [2-3]. It consists of a second order mass-spring-damper system (Fig. 1).

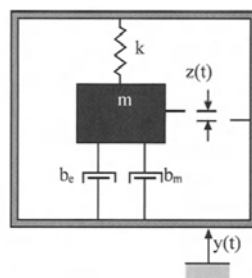


**Figure 1.** Schematic of a generic vibration-to-electricity converter [2].

In this schematic representation of a vibration based generator,  $z$  is the spring deflection,  $y$  the input displacement,  $m$  the vibrating mass,  $d_e$  the electrically induced damping coefficient,  $d_m$  the mechanical damping coefficient (due to friction, air resistance...) and  $k$  the spring constant. The movement of the mass can be used to deform a transducer, converting the mechanical energy into usable electrical energy. Due to electromechanical feedback, the transducer exerts a restoring force  $F_e$  on the seismic mass. This model has been widely studied by Shad Roundy in [2] as he established a mathematical model of such a generator taking into account its geometrical and physical parameters to estimate the amount of power that can be generated from a vibration source and so does Stephen Beeby [3]. Equation 1 describes this system.

$$m\ddot{y} = m\ddot{z} + d_m\dot{z} + kz + F_e \quad (1.a)$$

$$m\ddot{y} = m\ddot{z} + d\dot{z} + kz \quad (1.b)$$

Where  $m\ddot{y}$  represents the external force acting on the harvester and  $d$  the total damping of the system equal to the sum of the mechanical damping coefficient and the electrical one. Equation 1.a gives the forces balance of a general kinetic energy harvester and equation 1.b gives the force balance if the restoring force is considered as an electrical damping.

The expressions of the mechanical and electrical damping coefficients are given in equations 2 and 3 as functions of the dimensionless term  $\zeta$  for the damping.

$$\zeta_{meca} = \frac{d_m}{2m\omega} \quad (2)$$

$$\zeta_{elec} = \frac{d_e}{2m\omega} \quad (3)$$

Where  $\omega = \sqrt{\frac{k}{m}}$  denotes the natural frequency of the mechanical system.

Usually, the quality factor  $Q$  is used instead of the damping factor. These two quantities are related by:  $Q=1/(2\zeta)$ . Thus, the expression of the quality factor as a function the electrical and mechanical damping coefficients is given by equations 4 and 5.

$$Q_{meca} = \frac{m\omega}{d_m} \quad (4)$$

$$Q_{elec} = \frac{m\omega d_e}{d_e} \quad (5)$$

The total quality factor  $Q$  combining the mechanical and the electrical dampings can be expressed as:

$$\frac{1}{Q} = \frac{1}{Q_{meca}} + \frac{1}{Q_{elec}} \quad (6)$$

To extract the maximum output power, it is desirable to keep the mechanical damping as low as possible and in term of quality factor, it is desirable to achieve large values.

To be able to exploit such a model and to use it for the development of an interface circuit, an equivalent electrical circuit has to be implemented in a simulation software. The mechanical force and the mechanical velocity in the mechanical model are represented respectively by an electrical

voltage and an electric current [4]. Using this analogy, each term in equation 1 represents a voltage which leads to the electrical equivalent circuit in Fig. 2. In that circuit, the mass is represented by an inductor with the value  $m$ , the spring is modeled as a capacitor with the value  $1/k$ , the mechanical and electrical dampings are described by the resistors  $d_m$  and  $d_e$  [5].

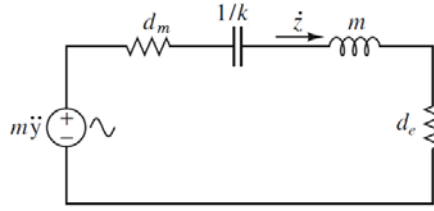


**Figure 2.** Equivalent circuit of the kinetic harvester [5].

## 2. Modeling of piezoelectric energy harvesters

### 2.1. Mechanical modeling

The harvester studied in this thesis is based on a piezoelectric conversion process, consequently we will show in this part the general electrical model of a piezoelectric energy harvester as previously developed by Thorsten in his thesis [5].

Let us consider a beam made of piezoelectric material used in 3-1 mode in order to harvest energy. If the structure is excited near its resonance frequency and undergoes little displacement for which the movement remains linear, then the piezoelectric structure can be modeled as a mass-piezo-spring-damper system. That model is inspired from Mason's representation to describe the piezoelectric oscillators [6]. The basic assumption that allows that modelling as a single degree of freedom system is that the transducer obeys to Euler Bernoulli beam mechanics [7-9] and that it operates near its first resonance frequency.

For a piezoelectric material operating in 31 mode, the constitutive equations are given below (eq.7 and eq.8):

$$\left\{ \begin{array}{l} S_1 = s_{11}^E \cdot T_1 + d_{31} \cdot E_3 \\ D_3 = d_{31} \cdot T_1 + \epsilon_{33}^T \cdot E_3 \end{array} \right. \quad (7)$$

$$\left. \begin{array}{l} S_1 = s_{11}^E \cdot T_1 + d_{31} \cdot E_3 \\ D_3 = d_{31} \cdot T_1 + \epsilon_{33}^T \cdot E_3 \end{array} \right\} \quad (8)$$

Where  $S$  is the mechanical strain,  $T$  the mechanical stress,  $D$  the electrical displacement (charge density),  $E$  is the electric field,  $s^E$  the compliance under a zero or constant electric field,  $\epsilon^T$  is the dielectric permittivity under a zero or constant stress and  $d_{31}$  the piezoelectric coefficient in 31 mode.

Let us consider that the piezoelectric layer used in the cantilever beam in Fig.3.b have the dimensions shown in Fig.3.a. In this cantilever configuration, a deflection of the beam in the 3 direction corresponds to an axial stress and strain in the 1 direction, thus creating an electric field parallel to the direction 3 given the 3-1 mode of piezoelectric couplings. This explains why the electrodes are deposited on the whole surface of the piezoelectric layer and why the metallic membrane can be used as the bottom electrode into a deflection of the piezoelectric layer in the 1 direction.

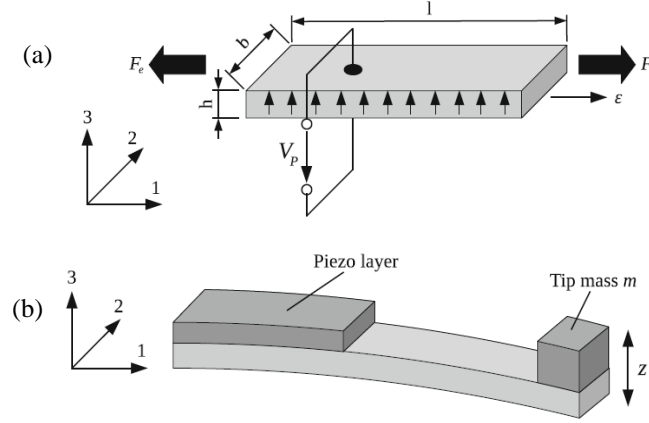


**Figure 3.** (a). Beam of piezoelectric material used in 31 mode, (b). cantilever structure converting the displacement  $z$  in the 3 direction into an elongation  $\varepsilon$  in the 1 direction [5].

The following relations in equation 9 are injected in equations 7 and 8.

$$E = -\frac{V_p}{h} \quad q = Dbl \quad T = \frac{F}{bh} \quad s = \frac{z}{l} \quad I = \frac{dq}{dt} \quad (9)$$

Where  $q$  denotes the generated charges,  $I$  the current flowing through the piezoelectric material and  $V_p$  the voltage across the piezoelectric capacitor.

Using these relations, equations 7 and 8 can be rewritten in terms of the macroscopic variables  $F$ ,  $z$ ,  $V$  and  $I$  instead of the local variables  $S$ ,  $E$ ,  $D$  and  $T$ :

$$\begin{cases} F = k_p \cdot z + \alpha \cdot V_p & (10) \\ I = \alpha \cdot \dot{z} - C_p \cdot \dot{V}_p & (11) \end{cases}$$

Where:

$$k_p = \frac{bh}{lS_{11}^E} \quad C_p = \left( \varepsilon_{33}^T - \frac{d_{31}^2}{S_{11}^E} \right) \frac{bh}{l} \quad \alpha = \frac{d_{31}b}{S_{11}^E} \quad (12)$$

$k_p$  represents the stiffness of the piezoelectric material,  $C_p$  the piezoelectric capacitance and finally  $\alpha$  the force factor.

Equation 10 shows that the force  $F$  is composed of the spring force  $k_p \cdot z$  that depends on the piezoelectric material stiffness and the coupling force  $\alpha \cdot V_p$  that depends on the voltage across the piezoelectric material. This force thus can be considered as the restoring force  $F_e$  acting on the tip mass.

Taking into account equations 10 and 11, equation 1.a describing the general model of a kinetic energy harvester can be rewritten as:

$$m\ddot{y} = m\ddot{z} + d\dot{z} + kz + \alpha \cdot V_p \quad (13)$$

In this equation, all the quantities correspond to the definitions previously given for the general model of a kinetic energy harvester, except  $k$  that denotes here the sum of the stiffness of the piezoelectric material and the mechanical structure acting as a frame so  $k = k_s + k_p$ .

The conversion of kinetic energy into electricity using a piezoelectric transducer can be modelled

using the equations 14 and 15:

$$\begin{cases} m\ddot{y} = m\ddot{z} + d\dot{z} + kz + \alpha.V_p & (14) \\ I = \alpha.\dot{z} - C_p.\dot{V}_p & (15) \end{cases}$$

To obtain the energy balance of the system, equation 14 is multiplied by the mass velocity  $\dot{z}(t)$  and integrated over time. Equation 16.a shows that energy balance:

$$\underbrace{\int m\dot{y}\dot{z}dt}_{Total} = \underbrace{\frac{1}{2}m\dot{z}^2}_{Kinetic} + \underbrace{\int d\dot{z}^2dt}_{Damping} + \underbrace{\frac{1}{2}kz^2}_{Elastic} + \underbrace{\int \alpha.V_p\dot{z}dt}_{Electrical} \quad (16.a)$$

This equation states that the total energy injected into the device is divided into kinetic energy, mechanical losses, elastic energy and finally electrical energy that can be harvested. Following the same procedure and applying it to equation 15, we obtain the electrical balance of the system showed below in equation 16.b:

$$\underbrace{\int \alpha.V_p\dot{z}dt}_{Total\ electric\ energy} = \underbrace{\frac{1}{2}C_pV_p^2}_{Stored\ on\ C_p} + \underbrace{\int V_p Idt}_{Absorbed\ by\ the\ electrical\ load} \quad (16.b)$$

This last equation shows that the electrical energy is separated into the energy absorbed by the electrical load and the energy stored on the piezoelectric capacitance.

## 2.2. Electrical modeling

Using the previous mechanical model of piezoelectric energy harvesters, an electrical representation of our generator is presented hereafter. As stated in [4], a mechanical force can be represented as an electrical voltage and a mechanical velocity can be represented by an electric current. Using this analogy, the mechanical velocity  $\dot{z}$  can be represented as an electric current  $I_m$ . Equations 14 and 15 can be rewritten as follows ( $\ddot{y}$  is replaced by  $a$  as it represents the input acceleration):

$$\begin{cases} ma = mI'_m + dI_m + k\int I_m dt + \alpha.V_p & (17) \\ I = \alpha.I_m - C_p.\dot{V}_p & (18) \end{cases}$$

Each term in equation 17 can be represented as an electrical voltage instead of a mechanical force. Consequently, the equivalent electrical circuit of a piezoelectric energy harvester is represented in Fig. 4 where equation 17 represents the mechanical domain of the circuit and equation 18 represents the electrical part of it [5, 10-12].

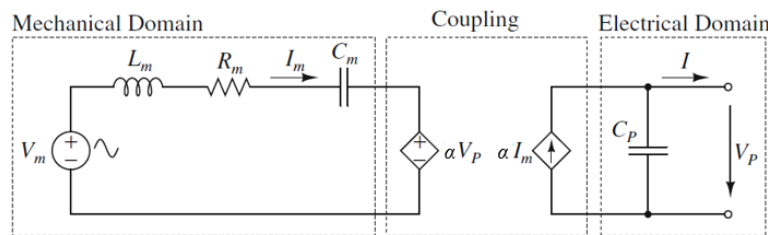


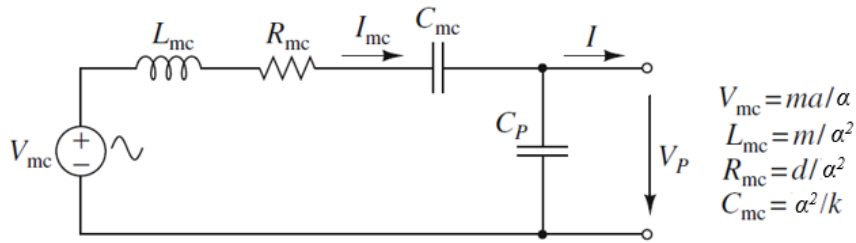
**Figure 4.** Equivalent electromechanical circuit of a piezoelectric energy harvester [5, 10-12].

To determine the various lumped parameters of this electrical representation, Kirchhoff Voltage Law (KVL) is applied to the circuit in fig. 4 in the mechanical domain and the coefficients of equation 17 are equated to those of the KVL equation (eq. 19):

$$V_m = L_m \dot{I}_m + R_m I_m + \frac{1}{C_m} \int I_m dt + \alpha V_p \quad (19)$$

As a result, the mass  $m$  is represented by an inductor  $L_m = m$ , the stiffness of the piezoelectric beam is represented by a capacitor whose capacitance is equal to  $C_m = \frac{1}{k}$ , the parasitic damping is modeled as a resistor whose value is  $R_m = d$  and finally the input excitation applied to the structure is represented as a voltage source  $V_m$ .

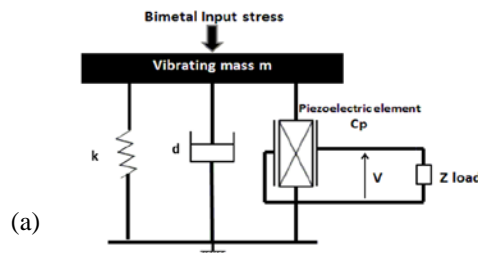
To simulate this circuit and have a simple electrical representation of a piezoelectric energy harvester, the mechanical branch in Fig. 4 is transposed into the electrical side using the transformer's ratio. This allows obtaining the electromechanical circuit in Fig. 5 with the formulas allowing the calculation of the mechanical branch parameters after the transposition.



**Figure 5.** Simplified electromechanical circuit of a piezoelectric energy harvester [5].

### 3. SPICE modelling of the harvester

Based on that electromechanical model of a piezoelectric energy harvesters, a SPICE representation of our thermal energy harvester is established. Our generator, excited near its resonance frequency and undergoing little displacements can be modelled, in the mechanical domain, as a vibrating mass  $m$  taking into account the effective beam mass associated with the deformation mode of the system, a spring  $k$  representing the stiffness of the device, a damper  $d$  and the capacitance of the piezoelectric ceramic  $C_p$  (Fig. 6.a). In the electrical representation (Fig. 6.b), the piezoelectric transducer is modelled as a transformer whose primary is the mechanical part of the system and whose secondary is its electrical part. The bimetal's input stress is modelled as a voltage source. In our modelling, the piezoelectric losses are supposed negligible [13], and the coupling factor between the mechanical and the electrical parts is the force factor  $\alpha$ .



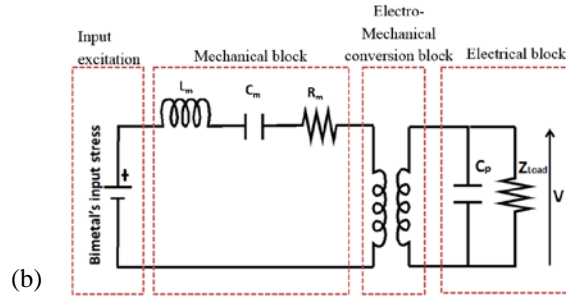


**Figure 6.** Equivalent Lumped Element Model of the piezoelectric system in the neighbourhood of resonance in (a) mechanical and, (b) electrical representations.

Tables 1 and 2 show respectively the parameters to extract experimentally and the calculation of the components of the electro-mechanical model of the piezoelectric transducer [14].

$f_r$	Short circuit resonance frequency
$f_a$	Open circuit resonance frequency
$\gamma$	Piezoelectric ceramic open circuit voltage to the beam displacement ratio
$C_0$	Clamped capacitance of the piezoelectric ceramic

**Table 1.** Measured parameters of the system

$$\alpha = \gamma C_0$$

$$k = 1/C_m = \alpha \gamma \frac{f_a^2}{f_r^2 - f_a^2}$$

$$L_m = \frac{k}{4\pi^2 f_a^2}$$

$$R_m = \frac{2\pi L_m f_r}{Q_m}$$

**Table 2.** Calculated parameters for the model

The first step before extracting the different parameters values is to find the resonance ( $f_r$ ) and antiresonances ( $f_a$ ) frequencies of the piezoelectric membrane. To do so, an impedance meter is used to measure the impedance module of the ceramic in function of the frequency. Figure 7 shows the evolution of the impedance module near a resonance frequency. Thanks to the measurement of the resonance and the antiresonances frequencies, the piezoelectric ceramic coupling coefficient  $k$  and quality factor  $Q$  can be deduced using equations 20 and 21:

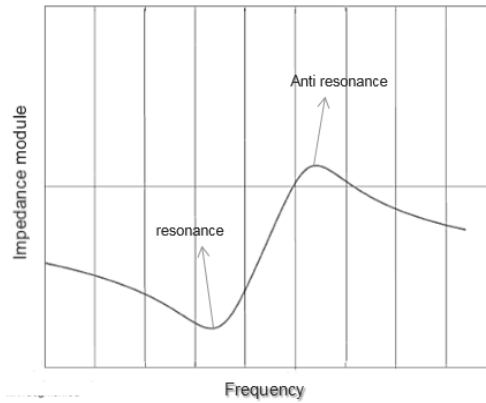


**Figure 7.** Evolution of the piezoelectric ceramic impedance module near a resonance frequency.

$$k^2 = 1 - \frac{fr^2}{fa^2} \quad (20)$$

$$Q = \frac{fa}{\Delta f} \quad (21)$$

where  $\Delta f = f_2 - f_1$ ,  $f_2$  and  $f_1$  defined as the frequency values where the magnitude of the electrical admittance is smaller by approximately -3dB when compared with the maximum at resonance.

As seen in table 2, before the calculation of the piezoelectric ceramic force factor, we should also measure the piezoelectric ceramic open-circuit voltage to the beam displacement ratio. To do so, the experimental setup in Fig. 8 is used. The piezoelectric ceramic is excited near its resonance frequency using a shaker and both its output voltage and displacement are measured using respectively an oscilloscope and a vibrometer.

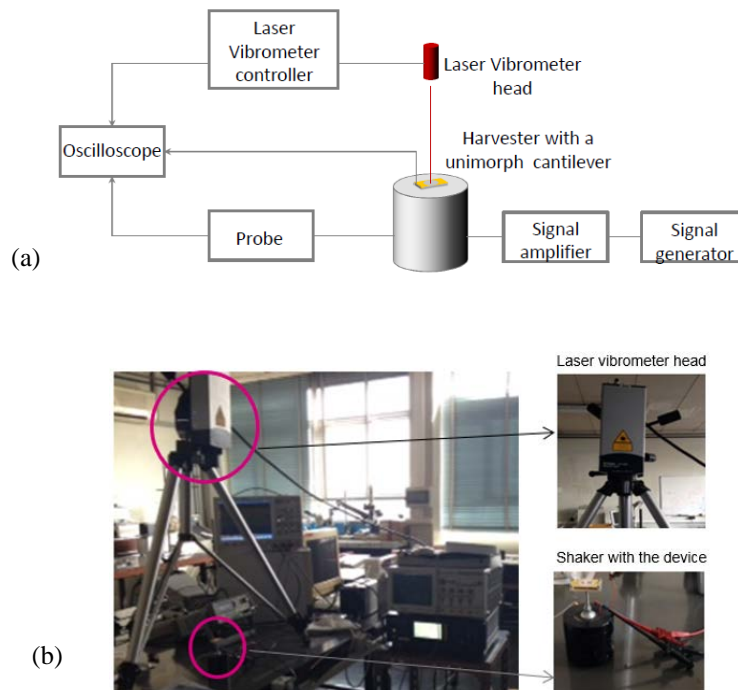


**Figure 8.** (a). Schematic of the experimental setup used to extract the force factor, (b). Experimental setup used to extract the piezoelectric force factor with the vibrometer and the shaker.

In our energy harvester, the source of the vibrations is the bimetal mechanical impacts when it snaps up and down. This type of energy harvesters have already been discussed by many scientists. Umeda [15-17] was the first to study an impact energy harvester through the energy generated by a steel ball on a piezoelectric membrane. The energy harvester studied in his paper [8] is shown in Fig. 9.

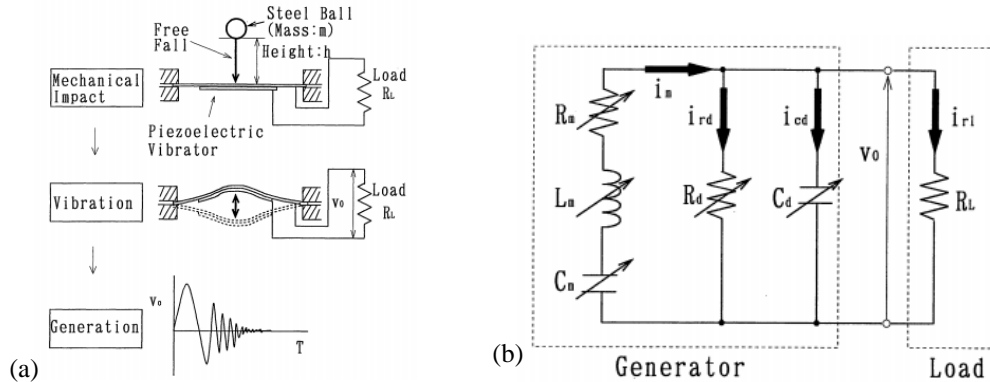


**Figure 9.** (a). Principle of electrical power generation, (b). Equivalent circuit of the generator [8].

In fig. 9.a, the author shows the working principle of his system. It consists of a steel mass impacting a piezoelectric membrane. At  $t=0$ , the steel ball impacts the membrane. After that the ball and the membrane vibrate together. At  $t=T_c$  near a half-cycle of the vibration, the system splits into two parts: the ball and the piezoelectric membrane that starts vibrating at its original frequency without the ball. To model its system in the two configurations, the author developed the model in Fig. 9.b where the values of  $R_m$ ,  $L_m$  and  $C_m$  denoting the equivalent resistance, equivalent inductance and equivalent capacitance at a resonance mode are different if the membrane vibrates alone or at the same time as the steel ball.

The same procedure is used in our case. The mechanical branch is first converted into the electrical part using the transformer's ratio. Then, assuming that the mechanical parameters are frequency dependent and that their values change significantly with the boundary conditions of the piezoelectric ceramic [18], two motional branches are employed to simulate the piezoelectric response when the bimetal snaps up and vibrates with the piezoelectric ceramic or when it snaps down allowing it to vibrate freely (Fig. 10). We show that a succession of electrical pulses models accurately the impact of the bimetal on the piezoelectric membrane. The duration of these pulses as well as their amplitude allows obtaining an electrical representation of these impacts whether it concerns a snap up or a snap down (Fig. 11.c). Finally, voltage controlled switches are used to establish the connection of the voltage sources to one of the two motional branches depending on the bimetal's state. The final SPICE model is shown in Fig. 10.

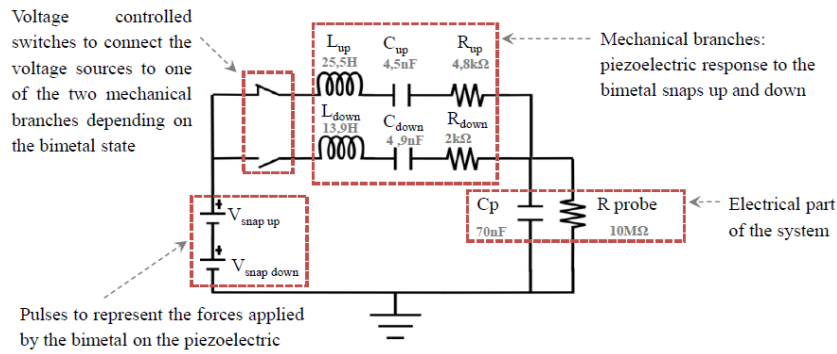


**Figure 10.** Equivalent SPICE model of the piezoelectric transducer taking into account the bimetal impacts.

Experimental measurements and simulations using this SPICE implementation are performed and the results of the voltage evolution across the piezoelectric capacitor, showing a good agreement, are exposed on Fig. 11 (a 10MΩ impedance probe is used for simulation and experiments). This comparison confirms the validity of this modelling. This work is published in [19-20].

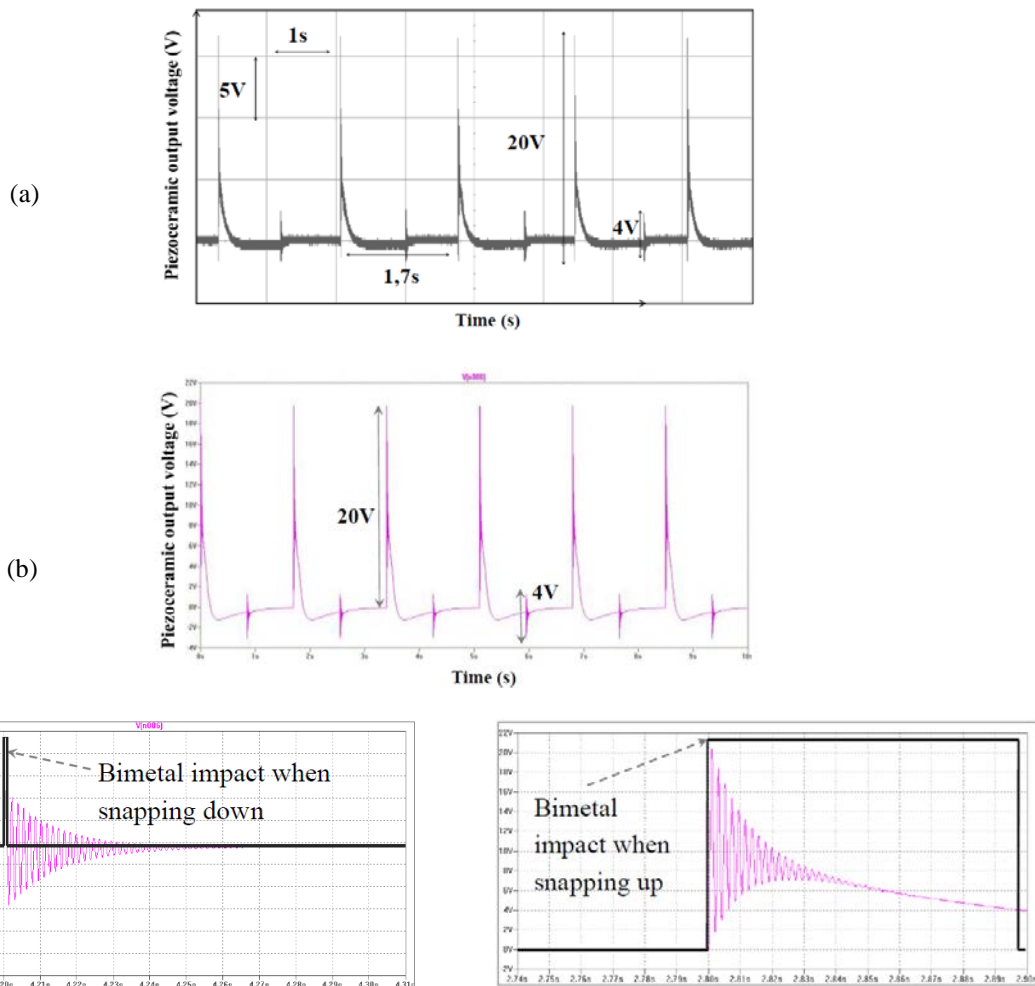


**Figure 11.** (a) Experimental piezoelectric signal measured with a 10MΩ probe, (b) SPICE simulation results of the piezoelectric ceramic output signal with a 10MΩ probe, and (c) bimetal impact modelling.

### III. Power management

#### 1. Review of the different power management technologies

##### 1.1. Energy conversion steps

The goal of energy harvesting systems is to power electrical devices and to replace batteries in very low power electronics such as wireless sensor networks and control systems. Generally, any electronic circuit requires a DC current to properly operate. For this reason, the alternative AC current delivered by piezoelectric generators should be converted into DC current. In this part, it is showed why interface circuits are essential for energy harvesting devices and applications.

Interface circuits are essential for energy harvesting applications for three main reasons: first of all, the interface circuit has to rectify the AC output signal of the piezoelectric energy harvester to convert it into DC current. Thus, the first stage of power management circuits is the rectifier. The second target of interface circuits is to optimize the output power which can be extracted from the energy harvesters. Finally, it is desirable that the interface circuit decouples the load from the harvester as for WSN applications, the load electronics needs to be powered periodically during short time intervals. The energy thus has to be stored in an intermediate buffer to allow the load circuit to take small amounts of energy out of the buffer whenever it is needed independently on the harvester's output power. Consequently, a general diagram of mechanical to electrical energy conversion through piezoelectric effect is depicted in Fig. 12.

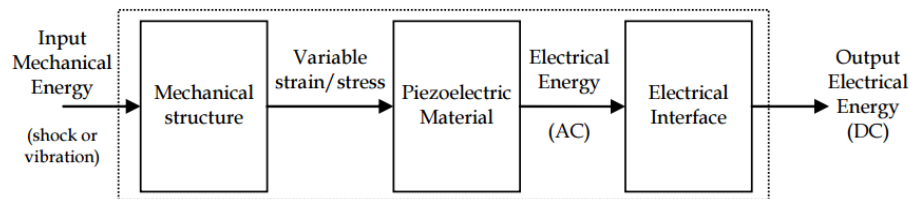


**Figure 12.** Energy conversion diagram of piezoelectric energy harvesting devices [2].

In this part, numerous power management circuits are investigated. Standard approaches using a resistor load for AC output signal as well as the standard circuits for DC output signals using a rectifier and a filtering capacitor, and finally different nonlinear processing techniques achieved by adding electrical switches to the piezoelectric elements are investigated.

##### 1.2. Power management circuits state of the art

There are many ways to extract power from piezoelectric energy harvesters. Diode rectifier is the simplest interface applicable to any generator with an alternating output. However, these last decades, many researchers have focused their work on nonlinear signal processing to increase the amount of extracted power in comparison with the standard techniques and decouple the load from the harvester. In this part, different power management circuits are investigated: their working principle are exposed and a comparison of their performances is established based on the numerous studies previously published on the subject.

###### i. AC standard device: resistive load

The resistive load is the simplest interface circuit that can be used for any harvesting device. In this case, a simple resistive load is directly connected to the piezoelectric element (Fig. 13). Thus, considering that the input excitation applied to the device is alternative, both the voltage and the current on the resistive load are alternative. The energy is then dissipated by joule effect in the

resistance. The resistive load is consequently inappropriate for energy harvesting applications but it is frequently used to characterize the piezoelectric devices.

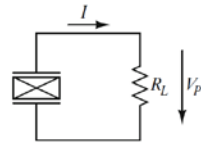


**Figure 13.** Piezoelectric harvester with resistor load [5].

ii. DC Standard device: rectifier and capacitor

As in the previous case, we consider a harmonic force  $F$  applied to the piezoelectric structure. The easiest way to rectify a piezoelectric device AC signal and to convert it into usable DC signal for common electronics supplying is to use a rectifier followed by a filtering capacitor. Hehn in [5] and Badel in [20] have studied such devices. The load is represented in Fig. 14 by a resistor in parallel with the capacitor.

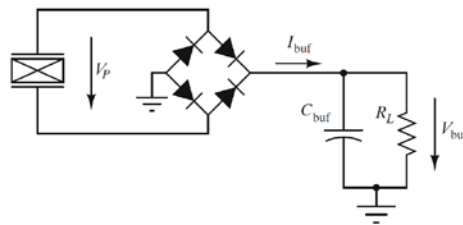


**Figure 14.** Piezoelectric harvester with a full wave rectifier with a buffer capacitor and a resistor load [5].

For such devices, the buffer capacitor  $C_{buf}$  is assumed to be very large so that the output voltage  $V_{buf}$  can be constant over several excitation periods. Typical waveform of the voltage across the piezoelectric element  $V_p$ , the current flowing into the buffer capacitor  $I_{buf}$  and the movement of the equivalent seismic mass of the harvester  $z$  are given below in Fig. 15. In this circuit, when the piezoelectric voltage  $V_p$  is lower than the rectified voltage  $V_{buf}$ , the rectifier is open circuited and the current through the buffer capacitor is null. Thus the displacement  $z$  and the harvester's voltage vary proportionally. However, when  $V_p$  reaches  $V_{buf}$ , the rectifier conducts and the voltage  $V_p$  is blocked at  $V_{buf}$ . The conduction is then cancelled again when the displacement starts decreasing and the whole cycle starts again.

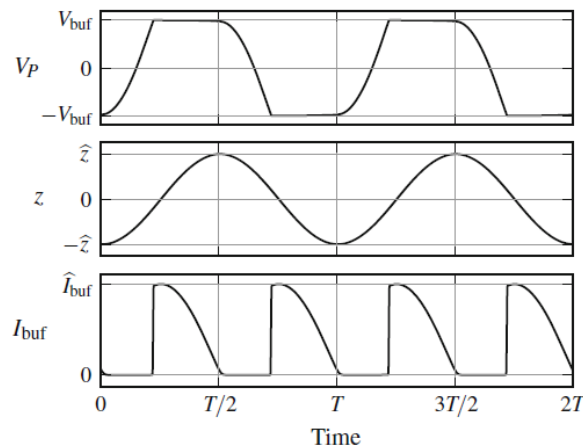


**Figure 15.** Typical waveforms of the piezoelectric output voltage  $V_p$ , of the movement of the mass  $z$  and the current flowing through the buffer capacitor  $I_{buf}$  (from [5]).

Such a circuit is a simple interface applicable to any power generator with an alternating output as it is composed of diodes that are passive elements needing no power supply. This solution of power management circuit is very advantageous when the harvested power is low.

iii. Nonlinear device: SSHI circuit

This nonlinear processing technique was first developed by Guyomar in [19-20]. It consists of a nonlinear processing achieved by an electrical switch device connected to the piezoelectric element. It increases the piezoelectric element output voltage resulting in a significant increase of the electrical power flow and it is called Synchronized Switch Harvesting on Inductor (SSHI). The effect of the switch is a quick inversion of the piezoelectric voltage obtained by electrical oscillation determined by the half-pseudo period of the resonant electric circuit composed of the piezoelectric capacitor and the inductance ( $t_i = \pi\sqrt{L_I C_0}$ ) where  $C_0$  is the value of the piezoelectric capacitance. The lower is the inductance  $L_I$  the lower will be the time  $t_i$  so this technique does not need a high inductance value. The effect of the switch and the inductance on the piezoelectric voltage is visualized in Fig. 16. Physical interpretation of this nonlinear treatment applied to the piezoelectric output voltage is that it creates piezoelectric forces that are opposed to the speed and the excitation force at resonant frequency.

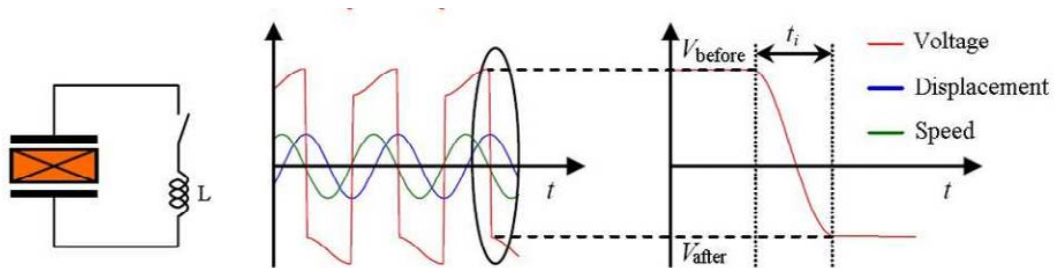


**Figure 16.** Effect of the nonlinear technique using an inductance and a switch on the piezoelectric output voltage [21].

The complete circuit used for energy harvesting applications is showed in Fig. 17.

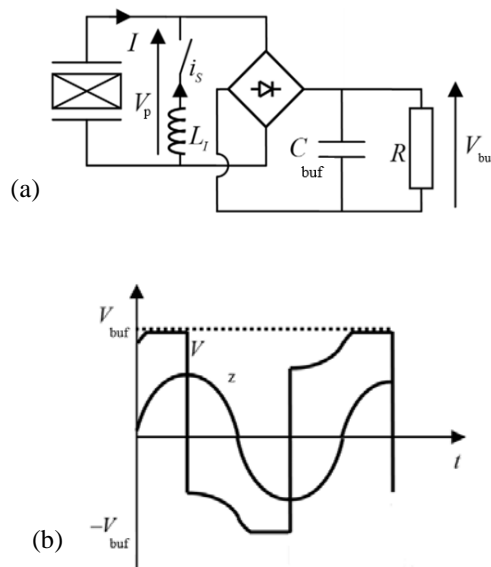


**Figure 17.** (a).SSHI Circuit with DC output voltage, (b). Typical voltage and displacement waveform for the nonlinear SSHI circuit [22].

The circuit is composed of a switch and an inductance  $L_I$  connected in series followed by a diode bridge and a filtering capacitor to obtain a DC output signal. The switch is almost always open except when a displacement extremum occurs. At that moment, the switch is closed and the capacitance of the piezoelectric element and the inductance  $L_I$  constitute an oscillator. This allows the inversion of the piezoelectric voltage through the switch and the inductance. Then, the piezoelectric voltage follows the same evolution as the displacement  $z$  until the DC voltage  $V_{buf}$  is reached again. At that moment, the diode bridge conducts and transfers electrical energy to the buffer capacitor.

This technique has demonstrated its interest for weakly coupled piezoelectric systems or for structures driven out of their resonance frequency as it was demonstrated that using SSHI circuit, a power gain of 400% is realized compared to the standard DC technique presented previously [22]. For structures driven at their resonance frequency, it is shown in [22] that for any power management technique, the harvested power tends to the same limit for an increasing electromechanical coupling and this limit is mainly affected by the mechanical losses occurring in the structure. However, the main drawback of this technique is the impedance matching that should be realized each time as the output power is also dependent of the load impedance value. Lefeuvre in [23] studied this SSHI technique and showed the evolution of the harvested power in function of the structure electromechanical coupling and also in function of the resistance load. The author used a vibrating structure composed of a 250mm long cantilever steel beam clamped at one end in a rigid structure and with six piezoelectric ceramic elements bonded on it. The cantilever vibrations are driven with an electromagnet that generates an alternative force on the beam. Fig. 18.b shows the evolution of the harvested power in function of the load resistor and the electromechanical coupling using SSHI technique and fig. 18.a the evolution of the harvested power in function of the load resistor and the electromechanical coupling using the standard DC technique exposed previously.

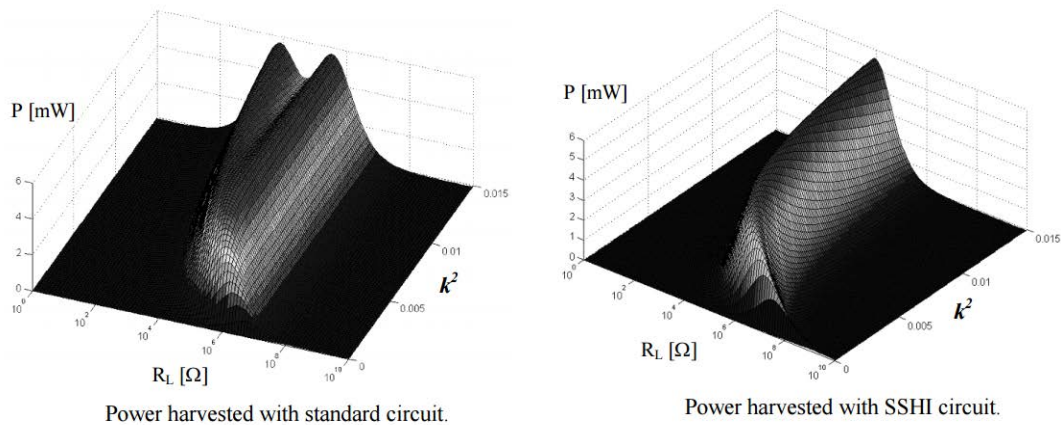


**Figure 18.** Comparison of the output power in function of the load resistor and the coupling coefficient for DC standard technique and SSHI technique [23].

These curves confirm the advantage of using SSHI technique compared to the standard technique in the case of weak coupling coefficient since the harvested power is much more important in that case. It also confirms that for strongly electromechanically coupled structures, the harvested power tends to the same limit for both cases.

Badel in [24] studied the piezoelectric energy harvesting in pulsed operation mode corresponding to the cases of harvesters excited by mechanical shocks and impacts. In these cases, the vibration

amplitude of the energy harvester decreases after each excitation shock. He showed that the amount of harvested power in such functioning mode increases by factors 2.5 to 5 in comparison to the standard technique.

iv. Nonlinear device: SECE circuit

Another nonlinear technique used to enhance the power extraction from piezoelectric energy harvesters is Synchronous Electric Charge Extraction called SECE. It has been developed by Lefeuvre in [27]. This technique consists in extracting promptly the electric energy converted by the piezoelectric element on each extremum of the mechanical displacement  $z$ . The SECE circuit consists of a rectifier, three switches  $S_1$ ,  $S_2$ ,  $S_3$  and an inductor  $L$ . Fig. 19 represents the electrical model of SECE circuit with a piezoelectric harvester and a resistor load.

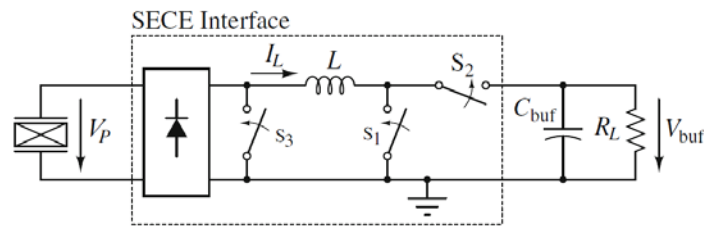


**Figure 19.** Piezoelectric interface with SECE interface and a resistor load [5].

The switches are used to store the energy drawn out of the piezoelectric capacitor in the inductance  $L$  before it is finally stored in the buffer capacitor  $C_{buf}$ . As it is the case for the SSHI technique, the SECE interface only operates during short time intervals compared to the excitation period in order to extract the power from the piezoelectric capacitor. These instants are triggered by the maxima and minima of the mass displacement and except from these moments, the SECE interface keeps the harvester in open circuit meaning that no current flows into the SECE interface. Fig. 20 shows the corresponding waveforms of the output voltage of the piezoelectric element, the mass displacement, the inductor current and finally the signals controlling the switches.

When the harvester voltage  $V_p$  reaches a maximum  $\widehat{V}_p$  meaning that the energy accumulated in the piezoelectric capacitance is also maximum, the stored energy is instantaneously transferred into the inductor  $L$  by closing the switch  $S_1$  until  $V_p$  reaches  $0V$ . At that moment,  $S_2$  and  $S_3$  are turned on and  $S_1$  is opened releasing the energy into the buffer capacitor. When the transfer is finished, the SECE interface is shut down and the whole cycle repeats when another maximum is detected.

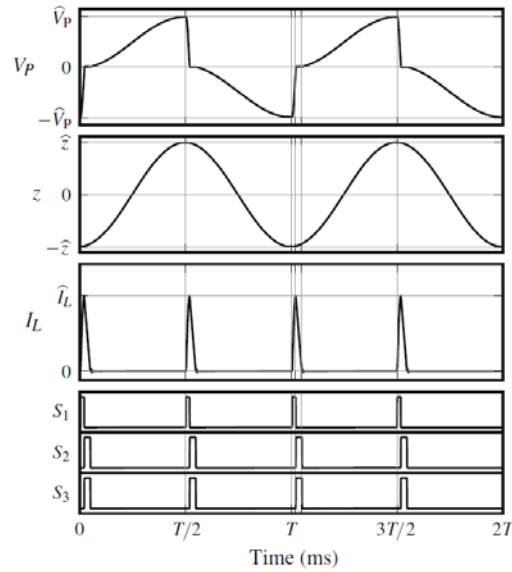


**Figure 20.** Corresponding waveforms of the output voltage of the piezoelectric element, the mass displacement, the inductor current and the signals controlling the switches (from [5]).

The main advantage of this technique is that it decouples the piezoelectric harvester from the load through the nonlinear switching. This makes the SECE technique more interesting than the SSHI technique or a diode rectifier because it is possible to set the device at an optimum operation point independently of the load. However, the amount of harvested power depends on two factors when SECE technique is used: the electromechanical coupling and the resonance frequency operation as the efficiency of the interface varies if the system is used at resonance or off resonance. Hehn in [5] compared different interface circuits and he differentiated the case of structures driven at resonance and off resonance. He showed that at resonance, the harvested power is increased of 124% in comparison with the rectifier capacitor load whereas for structures driven out of resonance, the harvested power is improved to 400% in comparison with the standard DC circuit. This is shown in fig. 21 where the author compares the amount of harvested power at resonance and off resonance in function of the resistance load value in three different cases: when the SECE circuit, a resistive load or a rectifier is used. These graphs are obtained using the Mide V22B piezoelectric harvester with additional 1g tip mass at an acceleration of  $10\text{m.s}^{-2}$  applied to the structure. The power in this graph is normalized by the absolute output power.

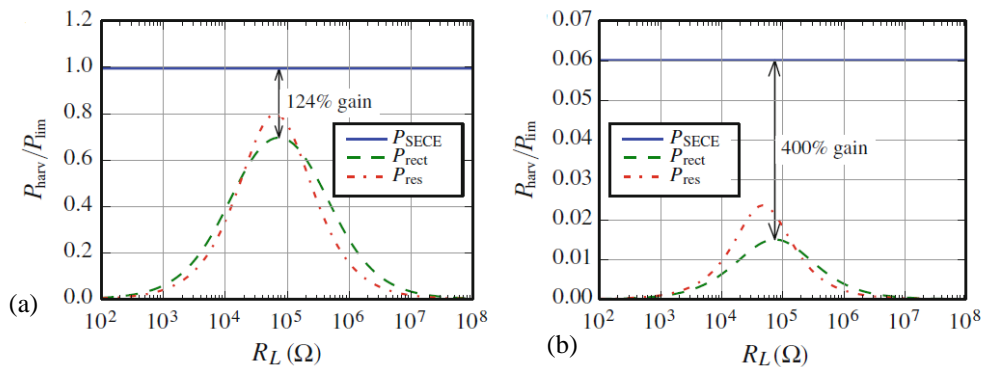


**Figure 21.** Normalized harvested power with resistive load, rectifier-capacitor load and SECE load (a). At resonance, (b). Off resonance (from [5]).

The same author in [5] also studied the effect of the harvested power in function of the electromechanical efficiency of the system. Fig. 22 represents a comparison of the harvested power

with a connected rectifier, resistor or SECE interface in function of the squared electromechanical coupling factor assuming a functioning at resonance. For that experiment, the same harvester as the one used for Fig. 21 is used.

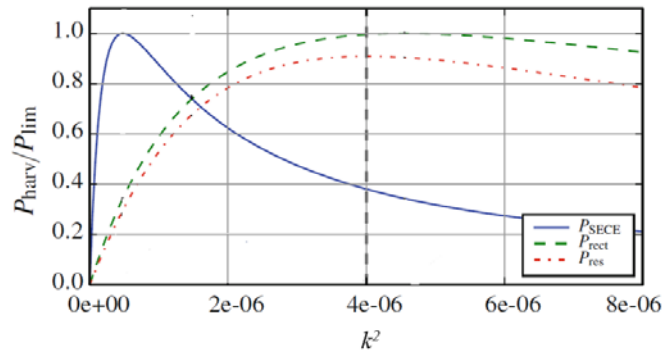


**Figure 22.** Comparison of the harvested power in function of the applied load (resistor, rectifier-capacitor or SECE interface) in function of the squared structure electromechanical coupling factor assuming operation at resonance and using a resistive load of 10kohm (from[5]).

This graph shows first that the optimum extracted power using a rectifier-capacitor load or an SECE interface tends to the same value. Then the author shows that each circuit interface has an optimal electromechanical coupling factor and that the optimal coupling coefficient of the SECE interface is much smaller than the two other circuits. The first effect can be explained by the fact that each interface circuit induces some damping in the beam's displacement. When the coupling is low, the electrical load has only little effect on the beam's displacement as the background coupling force is low compared to the external vibration amplitude. But above a certain coupling factor, the electrical load affects strongly the beam's displacement so that an increase in the coupling factor leads to a reduction in the extractable output power. Then, SECE interface damps very strongly the beam displacement by applying an important backward coupling force which explains why this interface increases the harvested power for piezoelectric harvesters with low electromechanical coupling factors whereas for harvesters with high coupling, the simple diode rectifier represents the better choice.

From the reported studies, we can say that it is impossible to make a general statement which interface circuit performs best. It depends on the operation frequency to know if the device operates at resonance or off resonance but also on the electromechanical coupling coefficient. However, SECE is more interesting than SSHI because no adaptation of the load is needed for optimal energy conversion. This is particularly interesting for broadband and random vibration energy harvesting. For high coupling coefficient, the diode bridge offers the best performances and SECE interface is desirable for weakly coupled structures.

#### v. Nonlinear device: PSCE circuit

Hehn during his thesis worked on energy harvesting interfaces [5, 24-26] and he developed a novel technique to reduce the circuit consumptions based on the SECE interface circuit. In fact, as explained by Lefevre in [27] SECE circuit has a consumption of 5.2mW for an average input power equal to 17.5mW. The losses in interfaces circuits are caused by conduction losses due to parasitic series resistances, losses caused by the switches drivers and finally the power consumption of the switch control circuit. This means that discrete type realization of SECE or SSHI circuits makes it mandatory to use piezoelectric energy harvesters with an output power of several milliwatts to get an acceptable efficiency and to outperform a simple diode bridge. In order not to cancel the benefit of a nonlinear interface, the power consumption of the interface has to be orders of magnitude

smaller than the transferred power [28]. This drawback is overcome using CMOS implementation that reduces the circuit power consumption. Hehn designed an improved circuit called PSCE for pulsed synchronous charge extraction in a 0.35 $\mu\text{m}$  CMOS process. This technique is based on SECE interface circuit and a small modification allows improving the circuit efficiency. In fact, SECE interface has three different functioning phases: during the first phase, no energy is transferred in the circuit until the displacement and the voltage across the piezoelectric element reach a maximum value. The energy transfer starts at the second phase and the energy on the piezoelectric capacitor is transferred to the inductance. Then during the last phase, the energy is transferred from the inductance to the buffer capacitor or a battery. For the PSCE circuit, the change happens during the second phase as when the piezoelectric voltage peak is detected, the energy is transferred simultaneously toward the inductance and the buffer capacitor at the same time. Using this technique, the same amount of energy is transferred during the transfer process but the current flowing through the inductance is smaller and causes thus less losses in the parasitic series resistances. The implementation of that integrated interface circuit allowed an efficiency improvement of 9% and the circuit consumption is estimated to 1.3 $\mu\text{W}$  [29]. The author showed that when the PEH is driven at resonance, the harvested power is increased of 123% compared to a rectifier and when the harvester is driven at off resonance, the extracted power gain is increased of 206%.

## 2. Power management simulation

To enhance the thermal energy harvester output power, different power management circuits are simulated and tested. The studies and results presented in this part are realized by the team of Sebastien Boisseau in CEA Leti who is involved in this project. To establish the power management simulations, the designers based their work on the harvester's SPICE modeling previously established in this thesis. In the next part, only the main results are presented and further information are available in the corresponding references.

### 2.1. First modules using a rectifier and a storage capacitor

The thermal energy harvesters developed here can be used in different configurations depending on the use cases and the amount of power required. In function of these parameters, a single module or a matrix of different modules can be used. The first issue we dealt with was the capability to connect the harvesters with each other if a matrix of energy harvesters is used. In fact, it is important to isolate devices from each other. Otherwise, the energy of each single module will be dissipated in the other modules acting as parasitic capacitances. This explains why the modules are electrically separated. Fig. 23 presents a 3x3 matrix modules with 9 energy harvesters made at CEA-Liten. Such a matrix can be used with the same bimetal for each single harvester in case the aimed application needs much more power than what is delivered by one single module or it can be used with a different snapping bimetal in each cell to cover a wide range of hot source functioning temperatures. Initially, a simple diode bridge followed by a storage capacitor is used for each cell. To have a compact single module or matrix, a Printed Circuit Board (PCB) is realized in polyimide with integrated diode bridges (BAS70BRW) and copper wires for the electrical connection.

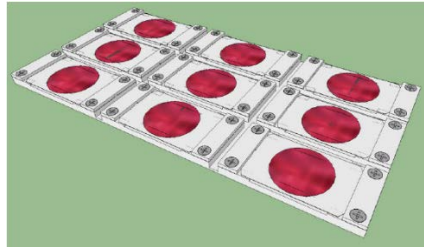


**Figure 23.** Matrix module with nine thermal energy harvesters.

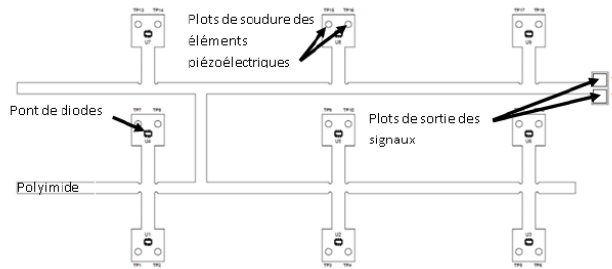


**Figure 24.** View of the realized PCB with the integrated diode bridges.

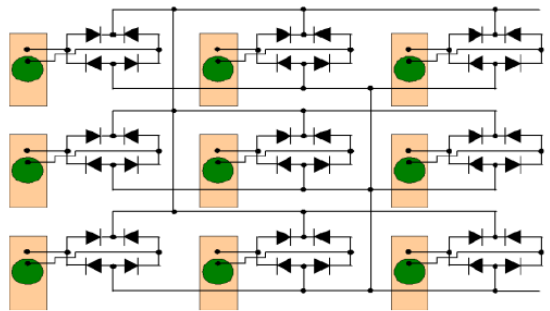


**Figure 25.** Matrix of nine thermal energy harvesters with a diode bridge for each module.



**Figure 26.** Realization of the matrix with the flexible PCB and deposition on a pipe.

For the wireless sensor node demonstrations presented in the last part of this chapter, the harvester output power is treated using this passive power management circuit through diode bridges and storage capacitors. In fact, the actions of integrating the thermal energy harvester for WSN applications and the developing of a power management interface are led simultaneously. Using this simple interface, an output power ranging from  $2\mu\text{W}$  up to  $5\mu\text{W}$  from each energy harvester are measured using different bimetals.

## 2.2. Power management results using discrete element PMC

In our project, various energy harvesters are realized based on different technologies: the thermal energy harvester presented in this thesis is one of them. Boisseau et al also developed a thermal energy harvester based on the electrostatic effect and on bistable bimetals in [30-31] and he designed a power management circuit interface based on SECE technique to enhance the harvested power. This circuit have been widely studied in [30-33]. It consists of a power management circuit with a flyback converter and it is based on the one developed by Lefeuvre in [25]. This circuit also integrates a self-startup architecture. The advantage of the self-start-up part is to be able to start an energy harvesting system and power management circuit (PMC) from scratch without any battery or initial energy. To do so, Boisseau in [32] combined the action of passive PMC and active PMC: as passive PMC based on a diode bridge and a capacitor needs no power supply to operate, the author uses the passive PMC to charge the empty buffer capacitor bound to supply the active PMC until it becomes charged enough to make the SECE circuit extract directly the energy from the thermal energy harvesters. Further details on this technique are given in [32]. Boisseau and his team have tested their discrete type power management circuit with the thermal energy harvester developed in this thesis and they came out to the conclusion that for low generated power ( $<20\text{-}30\mu\text{W}$ ), passive PMC are the most interesting one. Fig. 27 shows the evolution of the stored energy on a buffer capacitor using different active and passive power management techniques to extract energy from our thermal energy harvester. This confirms that in the case of discrete element circuits, the best way to extract energy is using passive power management circuits. As said previously, SECE technique cannot allow power extraction improvement for low power generators because of the losses occurring in the circuit and to the consumption of the circuit components that exceed the amount of generated power. To make active power management circuit improve power extraction from a generator, it should generate high amounts of power in the order of some mW and not  $\mu\text{W}$ .

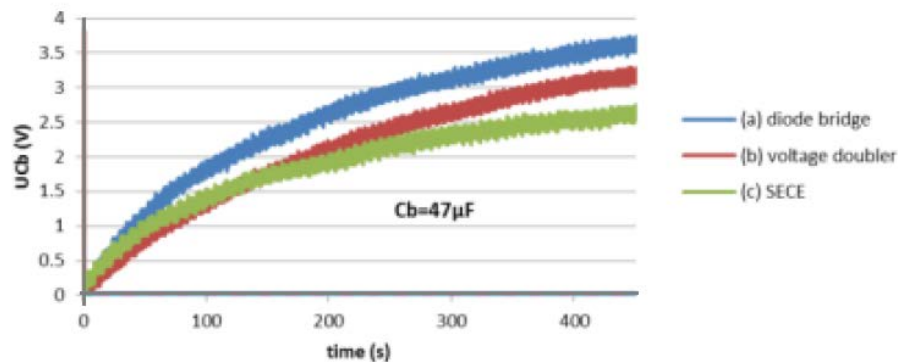


**Figure 27.** Comparison of active and passive PMC using discrete element circuits.

## 2.3. Power management simulation using Integrated interface circuits

To ensure an efficient extraction of electrical charges from the piezoelectric capacitor and to obtain higher amounts of harvester energies, it is compulsory to design an integrated interface circuit using CMOS technology. To do so, it was decided to realize the circuits using the technology CMOS HV (9,9V) M40 available at STMicroelectronics as in fact, the final purpose is to be able to fabricate theses circuits in STMicroelectronics fabrics and clean rooms.

The main drawback of diode bridges or voltage doubler is that once the diodes conduct, the piezoelectric capacitance is directly connected to the buffer capacitor. This limits the voltage increase across the piezoelectric capacitance and limits consequently the amount of harvested

power. To increase the extracted power from our thermal energy generators, the non-linear techniques presented previously are used. It allows synchronous charge extraction from the piezoelectric capacitance as energy is extracted once the piezoelectric capacitance reaches a maximum. Once this maximum is detected, the piezoelectric energy on the piezoelectric capacitance is transferred to the storage capacitor through an inductance or a transformer. At CEA Leti, two integrated interface circuits were simulated: a PSCE circuit using an inductive element for intermediate element storage and a SECE circuit using a transformer as an intermediate element storage. For these two interface circuits, the same controlling units are used. In fact, to detect a maximum voltage on the piezoelectric capacitor a peak detector is needed. Also, to detect a zero voltage on the piezoelectric capacitance once the piezoelectric charges are transferred from the piezoelectric capacitance toward the inductive intermediate storage element, and a zero current flowing through that element once its energy is completely transferred toward the storage capacitor, a zero crossing detector is needed. These circuit blocks are realized and simulations of both SECE circuit and PSCE circuit are done at LETI. These simulations are realized using the harvester's SPICE model in Fig. 10. Fig. 28 shows the output power harvested using different circuit interfaces: PSCE, SECE and finally a voltage doubler.

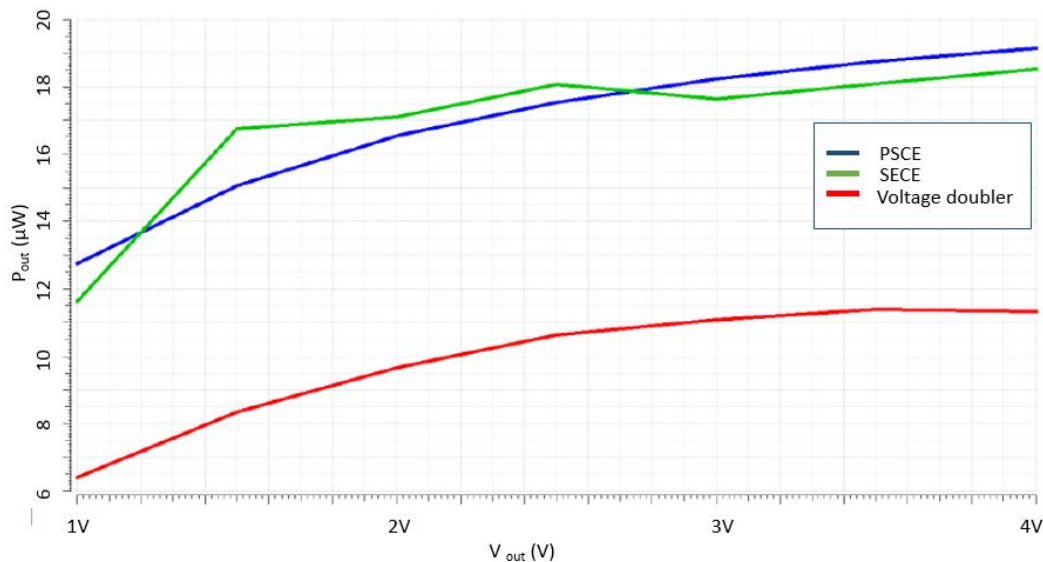


**Figure 28.** Comparison of the extracted power using different interface circuits (SECE, PSCE and voltage doubler) in function of the harvester's output voltage.

These results show that for a harvester's output voltage ranging from 1V to 4V, the harvested power using a voltage doubler ranges from 6.5 $\mu$ W to 11.5 $\mu$ W whereas it is two times higher using a synchronized and nonlinear techniques SECE and PSCE as it ranges from 11 $\mu$ W to 19 $\mu$ W for the same range of harvester's output voltages.

These first tests are very promising as a power gain of 100% is obtained. The next step of the study is the physical realization of these circuits to test them and to confirm the power gain obtained in the simulations.

#### IV. Wireless sensor node demonstrations

The main purpose behind the development of energy harvesters scavenging ambient energies is the development of wireless sensor nodes for applications linked to the Internet of Things. Such wireless devices enable parameters to be monitored in a way that would be too expensive and

impractical with conventional wired systems (a study estimated the cost of installing wiring to each sensor in a commercial building at \$200 [34]), allowing sensors to be embedded in complex machinery or in remote locations. These devices can continuously communicate their data, thus enabling data to be remotely monitored without the need to continuously revisit the deployment site.

For the first demonstrations exposed here and whose primary goal was to confirm the validity of WSN power supplied by our energy harvester, no specific power management circuitry similar to those exposed in the previous part of this chapter were used. In fact, the development of a dedicated power management circuit and the WSN demonstrations were simultaneously investigated. Instead of that, the energy harvester's alternative output signal is rectified and the energy is directly stored on a storage capacitor.

Thanks to the low power consumption of electronic circuits and the requirements of a single WSN node that can be as low as  $1\mu\text{W}$  in a sleep state [35], a demonstration of a ST-WSN (GreenNet) supplied by our thermal energy harvester in asynchronous mode (unidirectional data transmission) is realized. GreenNet is a wireless sensor network developed by STMicroelectronics and designed for ultra-low power operation, energy harvesting and secured IP-based communication. It aims at contributing to the emergence of the Internet of Things (IoT) that proposes the vision of rich interactions with the physical world through the interconnection of objects having advanced processing, communication, sensing and actuating capabilities [36]. This network is designed to operate in synchronous mode, however, in view of the power harvested by our thermal energy harvester in the range of few  $\mu\text{W}$ , the system is modified to operate in asynchronous mode. The GreenNet demonstration platform is supplied by ST GreenNet team and all the circuitry used for the demonstrations are simulated and implemented by CEA Leti.

As the harvester's AC output signal is not compatible with standard electronic circuits, a voltage doubler and a  $57\mu\text{F}$  storage capacitor are connected to the device, followed by a level detection circuit. The harvested energy is first stored in the capacitor until a threshold voltage value is reached and detected by a low power comparator. It is then released to supply the WSN. The GreenNet emission circuit transmits 64 bits of data with IEEE 8023.15.4 protocol toward the GreenNet reception module every 29s using two devices and every 15s using three cells. The GreenNet WSN emission module emits data at a frequency of 2.4GHz. Every data reception is illustrated by a switching led as shown In Fig. 29.b.  $110\mu\text{J}$  are needed for each data emission using this communication protocol in asynchronous mode. The microcontroller used in GreenNet WSN is the STM32. The architecture of this WSN is shown in Fig 29.a and the evolution of the storage capacitor voltage is shown in Fig 29.c. This experiment definitively validates the ability of these harvesters to power WSN.

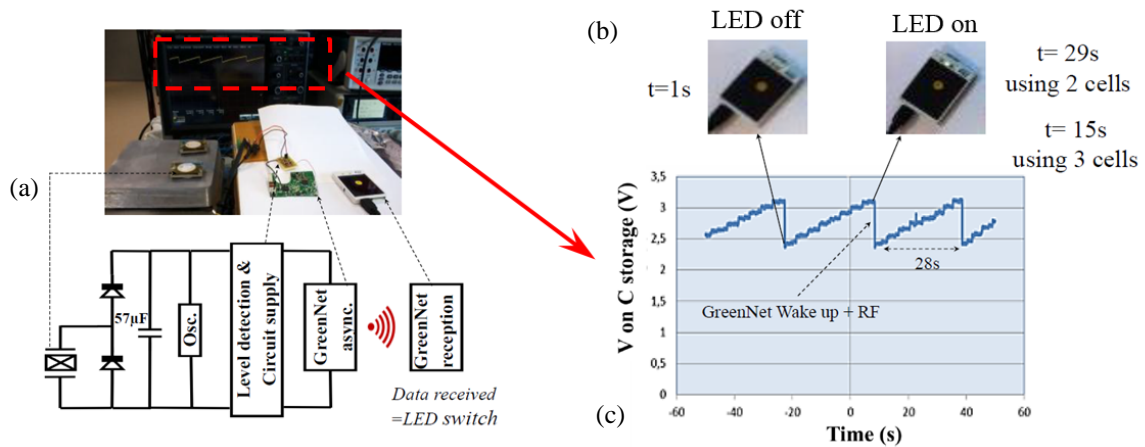


**Figure 29.** Test of a ST-WSN (GreenNet) in an asynchronous mode powered by the thermal energy harvesters and state of the reception node.

The level detection and power management circuit used for this demonstration is a Schmitt Trigger which is a comparator with a hysteresis used here for switching power supply. ST and CEA worked on developing a low power Schmitt trigger consuming 50nA instead of 500nA in literature and a patent have been deposited for this comparator. Such comparators are commonly used in energy harvesting applications and WSN demonstration; in our case, the circuit allows detecting the right moment when enough energy is stored on the buffer capacitor for the emission node to emit data toward the reception node. This circuit also allows the power consumption to cease as soon as the data is received. This enables to keep a minimal energy stored on the storage capacitor and to avoid the cold start that can last few minutes between each two data emission as shown in Fig. 30. That way, the cold start phase only occurs at the beginning of the demonstration and data is being emitted regularly after that. It also makes the system become auto-adaptive as the duration between two data emissions depends only on the amount of stored energy on the buffer capacitor. Using this comparator, the system has a consumption of 1 $\mu$ W only (the consumption of the control circuit is as low as 0.01 $\mu$ W). This first demonstration of a GreenNet WSN supply by our thermal energy harvester have been published at PowerMems Conference in 2014 [37].

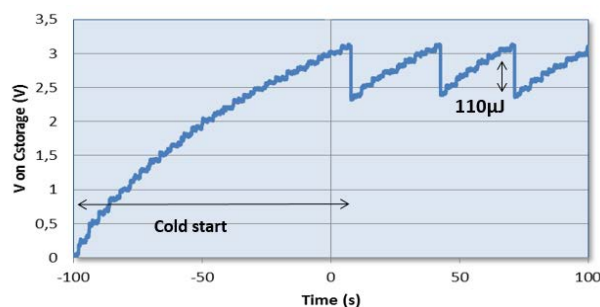


**Figure 30.** Cold start phase at the beginning of the WSN demonstration.

Using the same demonstration platform, the miniaturized thermal energy harvesters are tested too. As previously said in Chapter 3, scaling the devices down by a factor 2.5 did not lead to any performances improvements but at the opposite, the amount of harvested power decreased significantly. This is the reason why supplying the WSN by one single miniaturized thermal energy harvester leads to one data transmission each 4 minutes using one single module. The experimental setup used for this demonstration is showed in Fig. 31.

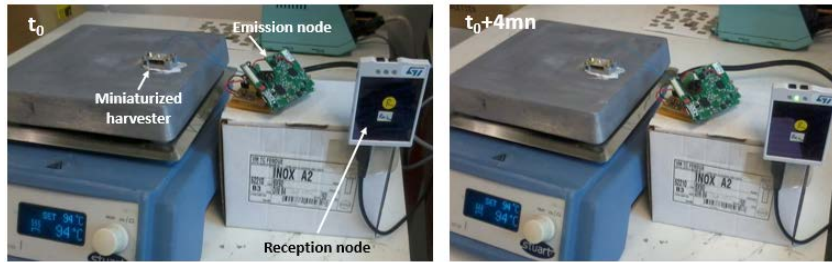


**Figure 31.** GreenNet WSN demonstration in asynchronous mode powered by a miniaturized energy harvester.

The GreenNet demonstration platform have also been modified by CEA Leti to send either the ambient temperature (using 110 $\mu$ J of stored energy) or the position of the emission node thanks to a magnetometer (consuming thus 700 $\mu$ J of energy). Each time the information is received by the GreenNet reception node, le led switches on. To receive data and visualize the temperature sensor and the magnetometer measurements on a computer, CEA-Leti developed a display program to visualize all the measurements (Fig. 32). Moreover, it were shown that this WSN allows data emission and reception for distances higher than 20m outdoors but indoors, this distance is decreased to 3m.

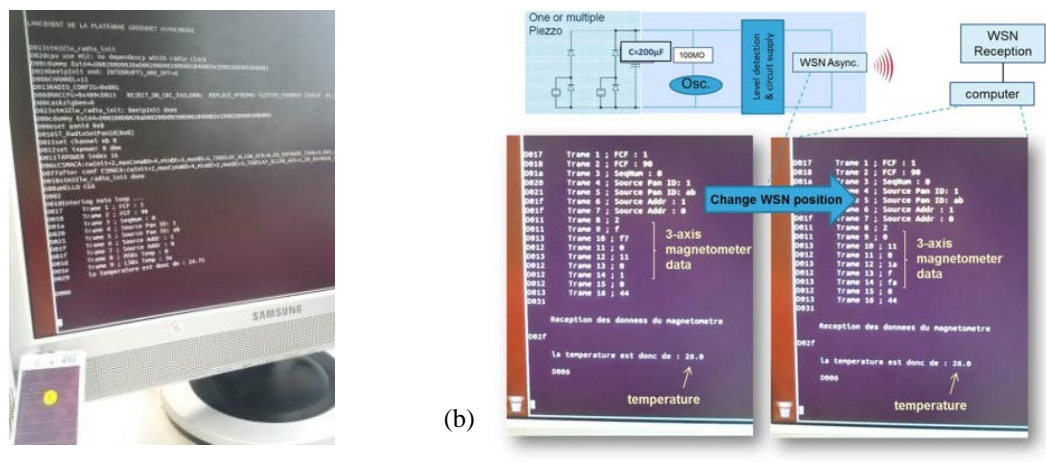


**Figure 32.** (a). Reception of the measured data by the emission node toward the reception one on a computer and (b). Validation of the sensors operations.

Once the first demonstration established using GreenNet WSN platform emitting data at 2,4GHz, ST in collaboration with CEA-Leti worked on various WSN platforms using various communication protocols in asynchronous mode. In fact, two more demonstrators are realized using the communication protocol 802.15.1 corresponding to Bluetooth Low Energy (BLE) for smartphone applications and the communication protocol 802.15.4 at 868MHz. BLE can allow data transmission at distances up to 30m on smartphones directly and the last communication protocol at 868MHz allows data transmission up to 100m indoor and up to 300m outdoor. This last type of communication protocol is very attractive for low data rate applications like for home security and automation and offers substantive benefits over the more powerful protocols as Wi-Fi, Bluetooth or ZigBee operating at 2,4GHz. Two more radios fabricated by ST and operating at 2.4GHz for BLE and at 868MHz are used. These radios are respectively the SPBLE and the Spirit 1. The two demonstration platforms were fabricated by CEA Leti. Each of these cards integrates: two power sources input terminals to connect one or two energy harvesters (the latest version not showed in this thesis integrate up to three inputs), voltage doublers and a storage capacitor, a level detection

circuit and circuit supply, a microcontroller STM32, different sensors (temperature, accelerometer and magnetometer all developed at STMicroelectronics) and finally a different radio for each node depending on the communication protocol. The corresponding electronic cards are shown in Fig. 33 and the general scheme of the demonstration platforms is shown in Fig. 34. Moreover, Leti have worked on the identification of each node when it sends data toward the reception node. Fig. 35 shows an example of this identification allowing the reception mode to recognize which emission node sends data.

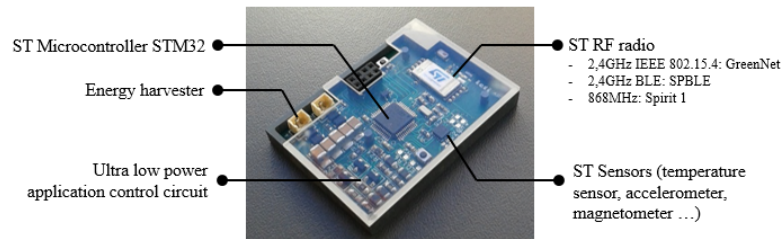


**Figure 33.** WSN emission module with different RF radio depending on the communication protocol.

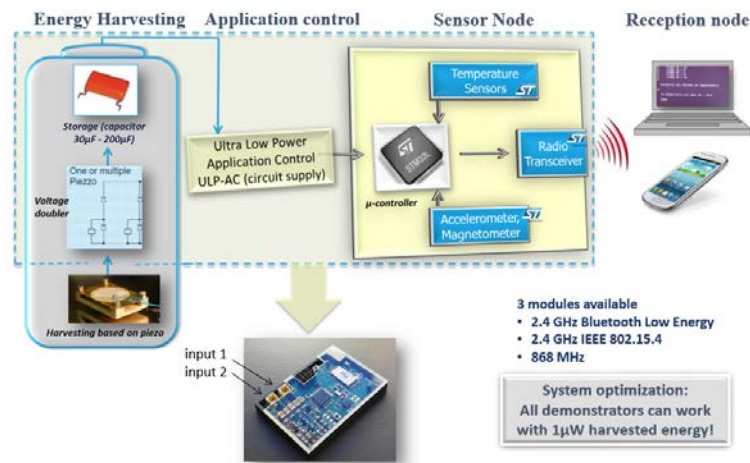


**Figure 34.** WSN Demonstration platform with reception of data on a smartphone or a computer depending on the communication protocol.

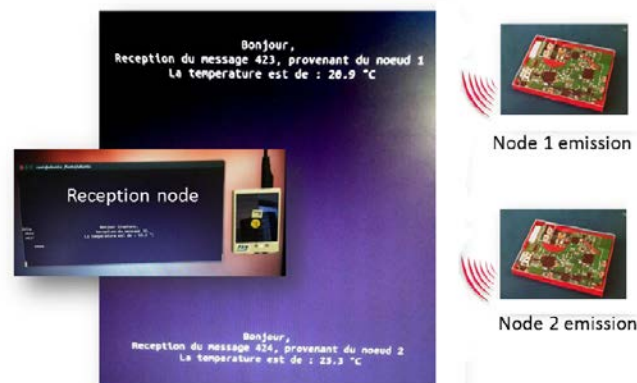


**Figure 35.** Identification of each emission node when data is received by the reception module.

The BLE WSN consumes  $600\mu\text{J}$  for each temperature measurement and RF data transmission toward the reception node. The 868MHz WSN consumes  $120\mu\text{J}$  for each temperature measurement and RF transmission and  $170\mu\text{J}$  for both acceleration and temperature measurement followed by

RF data transmission. Some ranging tests are realized to see if data can be measured outdoors and received indoors. To do so, experiments are realized using the BLE and the 868MHz. During the first experiment, both emission nodes with the sensors were put in a sewer pipe and the reception module was put inside a building as shown in Fig. 36.a. Then for the second test, the reception node was put outdoor and the emission nodes were installed in a pipe below the road. These ranging test showed that the transmission range of the 868MHz is more extended than that of BLE which is logical as the high frequencies (above GHz) are more subject to attenuation than low frequencies.

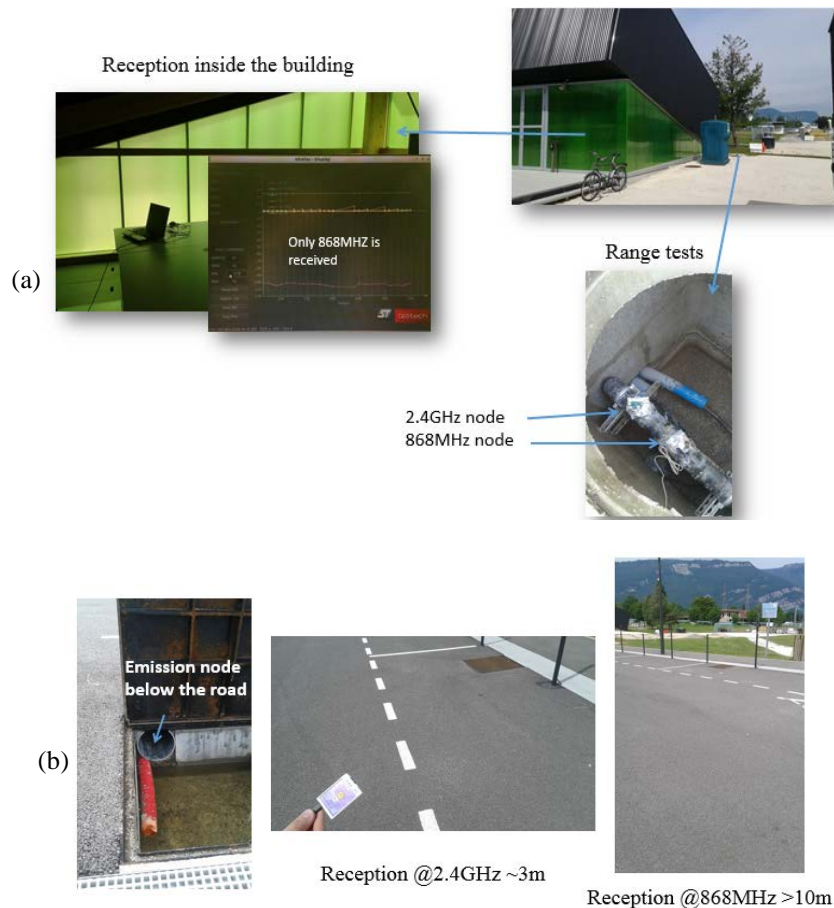


**Figure 36.** Ranging tests of the BLE WSN and the 868MHz WSN (a). With the reception node inside a building and the emission nodes in a sewer pipe, (b). With the reception node outdoor and the emission nodes inside a pipe below the road.

To obtain a fully autonomous WSN, a timer and a dedicated micro battery developed by STMicroelectronics Tours are integrated to the demonstrators. ST's EnFilm™ thin-film battery [39] is an extremely thin (220 μm), rechargeable solid-state battery with fast constant-voltage recharge and a lifetime of more than 10 years or 4000 cycles. The EFL700A39 is more specifically a rechargeable lithium battery intended to be used in a wide range of applications including: Internet of things, Sensors and networks, Smart card, Energy storage for energy harvesting devices.... It has a capacity of 0.7mAh, its operating temperature range extends from -20°C to 60°C, its operating voltage is from 3.0V to 4.2 V with a nominal voltage of 3.9V and it also has a low capacity loss as it losses only 20% of its capacity over 10 years. More information about this thin film battery can be found in [38].

The timer and the thin-film battery ensure the good functioning of the WSN in case the energy harvester stops working (which could happen if the hot source temperature becomes lower than the bimetal snapping temperature). The timer allows then a continuous data transmission thanks to

the battery and the interval between two consecutive RF emissions can be adjusted in function of the desired scenario:

- The harvester is working and the timer makes the WSN send the temperature every  $t_1 = 5\text{mn}$ . If there is a hot or ambient temperature shift that makes the energy harvester stop, this correspond to a critical event and the WSN becomes powered by the  $\mu$ -battery and can send the temperature every  $t_2 = 15\text{s}$  for example. ( $t_2$  can be equal to  $t_1$ )
- Harvester is working and the timer makes the WSN send the temperature every 5mn. If no heat source is available (heater stop during summer for example), the energy harvester stops, and the WSN becomes powered by the  $\mu$ -battery for minimum activity and can send the temperature every  $t_3 = 20\text{mn}$  for example ( $t_3$  should be lower than  $t_1$  if the harvester stops for a long time°).
- That way, the temperature (or acceleration...) is sent every  $t_1$  when the harvester works and at the same time it reloads  $\mu$ -battery with bonus energy; at the opposite, data is sent every  $t_2$  or  $t_3$  when harvesting stops and the circuit switches to the  $\mu$ -battery. For a temperature measurement and data emission every 16 minutes, the battery has enough charge for 500 days functioning.

During the last year of this project, other power sources and their compatibility with the WSN developed by CEA-Leti in collaboration with STMicroelectronics have been investigated in view of the low amount of harvested power using bimetallic strips and piezoelectric membranes. To do so, low cost (less than 2 euros for low cost WSN) solar cells and thermoelectric generators are tested for thermal energy harvesting. Fig. 37 shows an example of the corresponding energy harvesters.

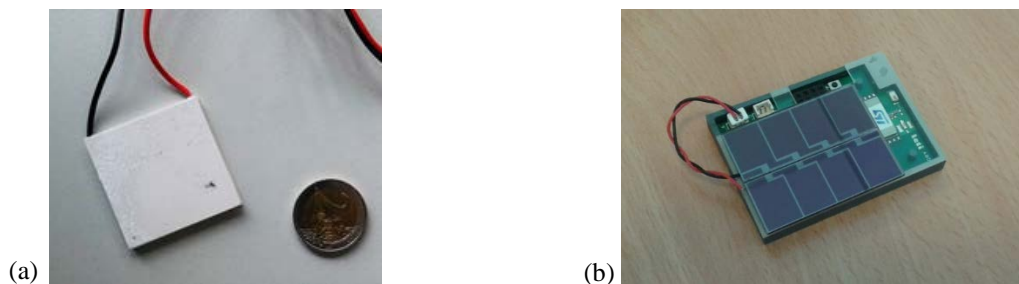


**Figure 36.** (a). Thermoelectric generator tested with ST WSN, (b). Solar cells deposited on the WSN emission module.

For example, using the solar cells, it is possible to make the WSN emit data toward smartphones every 5 seconds with indoor ambient light using BLE and every 3 to 4 minutes with low light (under a desk for example). These techniques allow more frequent measurements and data emission and explains why the bimetallic strip heat engines coupled with a piezoelectric membranes are not the most interesting solution for WSN applications. However, in some use cases where no light is available to use photovoltaic cells (darkness use cases) neither sufficient space to use a radiator over a thermoelectric energy harvester, the thermal energy harvester developed here is a good alternative. Contrary to photovoltaic cells, it functions independently of the environment's illumination and at the opposite of thermoelectric energy harvesters, the HEATec harvester is very thin and does not need any heat sink to function.

## V. Conclusion

In this chapter, we dealt with the integration part of the thermal energy harvester based on bimetallic strip heat engines and piezoelectric membranes. In fact, we started with the electromechanical modeling of our thermal energy harvester based on Mason model for piezoelectric energy harvesters. In function of the boundary conditions of the piezoelectric membrane, a general model of the system is presented taking into account the snapping behavior of the bistable bimetal. The proposed circuit is inspired from the equivalence between the mechanical quantities occurring in the harvester and the electrical ones and it allows simulating the output signal generated by the harvester when functioning.

This first step is followed by a benchmark of the existing circuits in the literature to process the harvester's output signal and extract the major part of it. To do so, we worked in collaboration with CEA Leti that compared SSHI, SECE and PSCE circuits. Each of those circuit has its advantages and may allow an improvement of the piezoelectric output power depending on these circuits implementation (discrete type or integrated circuit). Because SSHI technique does not make the output power to be independent of the load's impedance value, only SECE and PSCE technique are simulated and discrete element circuits have been realized. Using the discrete type circuit, no performance improvement have been observed because of the circuit components consumptions and to the losses occurring in the circuit. This made it compulsory to implement integrated circuits of these non-linear switching techniques. These last simulation results are very promising as a power gain of 100% is obtained. The next step is the physical realization of these circuits to test them and to confirm the power gain obtained in the simulations. This work is currently being realized at CEA Leti and STMicroelectronics.

The last part of this chapter is about the integration of the thermal energy harvester to realize WSN demonstrations. First of all, in view of the amount of power generated by thermal energy harvester, all the demonstrations are realized in asynchronous mode. The first demonstration is realized using a ST demonstration platform called GreenNet and operating using 802.15.4 communication protocol at 2.4GHz. Thanks to the collaboration of ST and CEA designer's teams, an ultra-low power application circuit is created and patented to make the WSN emission node detect when sufficient energy is stored on the buffer capacitor meaning that measurements can be realized by the sensors and the measured data transferred toward the reception node. That circuit consumption is as low as  $0.1\mu\text{W}$  and the entire WSN demonstration platform needs only  $1\mu\text{W}$  to operate. Numerous ST sensors have been implemented on the WSN as temperature sensor, accelerometer and a magnetometer. Apart from GreenNet demonstration, demonstrations using BLE and 868MHz communications protocols are also realized. In fact, this last kind of communication protocol are very attractive for low data rate applications like for home security and automation and it offers substantive benefits over the more powerful protocols as Wi-Fi, Bluetooth or ZigBee. Whereas the BLE WSN needs  $600\mu\text{J}$  to measure temperature and send data on a smartphone, GreenNet and 868MHz consume only  $120\mu\text{J}$  for that same task. However, because of its lower frequency, the node at 868MHz is the one having the most interesting range. To obtain a completely autonomous WSNs, a timer with a  $\mu$ battery are added in the system in order to use the battery's energy in case the thermal energy harvester stops functioning.

Finally, at the end of this chapter the compatibility of the developed WSN with other low cost energy harvesting techniques are tested like thermoelectric generators for thermal energy harvesting, photovoltaic cells for solar energy harvesting.... All these techniques are compatible with the developed WSN which makes it a good complement to the thermal energy harvesters developed in this thesis.

## VI. References

- [1] Williams, C.B. and R.B. Yates. "Analysis Of A Micro-Electric Generator For Microsystems". *Sensors and Actuators A: Physical* 52.1-3 (1996): 8-11.
- [2] Roundy, Shad, Paul Kenneth Wright, and Jan M Rabaey. *Energy Scavenging For Wireless Sensor Networks*. Boston: Kluwer Academic Publishers, 2004.
- [3] Kaźmierski, Thomas J and Stephen Beeby. *Energy Harvesting Systems*. New York: Springer, 2011.
- [4] Tilmans, Harrie A C. "Equivalent Circuit Representation Of Electromechanical Transducers: I. Lumped-Parameter Systems". *J. Micromech. Microeng.* 6.1 (1996): 157-176.
- [5] Hehn, Thorsten and Yiannos Manoli. *CMOS Circuits For Piezoelectric Energy Harvesters*. Dordrecht: Springer, 2014.
- [6] Mason, W. P. "An Electromechanical Representation Of A Piezoelectric Crystal Used As A Transducer\*". *Bell System Technical Journal* 14.4 (1935): 718-723.
- [7] Hibbeler, R. C. *Mechanics Of Materials*. Upper Saddle River, N.J.: Pearson Prentice Hall, 2005.
- [8] Rao, Singiresu S. *Vibration Of Continuous Systems*. Hoboken, N.J.: Wiley, 2007.
- [9] Phipps, Alex and Toshikazu Nishida. "System Modeling Of Piezoelectric Energy Harvesters". *IEEE Transactions on Power Electronics* 27.2 (2012): 790-802.
- [10] Renaud, M. et al. "Fabrication, Modelling And Characterization Of MEMS Piezoelectric Vibration Harvesters". *Sensors and Actuators A: Physical* 145-146 (2008): 380-386.
- [11] Renaud, Michael, Paolo Fiorini, and Chris van Hoof. "Optimization Of A Piezoelectric Unimorph For Shock And Impact Energy Harvesting". *Smart Mater. Struct.* 16.4 (2007): 1125-1135.
- [12] Renaud, Michael et al. "Harvesting Energy From The Motion Of Human Limbs: The Design And Analysis Of An Impact-Based Piezoelectric Generator". *Smart Mater. Struct.* 18.3 (2009): 035001.
- [13] Pinna, Luigi, Ravinder S. Dahiya, and Maurizio Valle. "SPICE Model For Piezoelectric Bender Generators". *2009 16th IEEE International Conference on Electronics, Circuits and Systems - (ICECS 2009)* (2009): 587-590.
- [14] Badel, Adrien. Thesis : "Récupération D'énergie Et Contrôle Vibratoire Par Éléments Piézoélectriques Suivant Une Approche Non Linéaire". Université de savoie, 2005.
- [15] Umeda, Mikio, Kentaro Nakamura, and Sadayuki Ueha. "Analysis Of The Transformation Of Mechanical Impact Energy To Electric Energy Using Piezoelectric Vibrator". *Jpn. J. Appl. Phys.* 35.Part 1, No. 5B (1996): 3267-3273.
- [16] Umeda, Mikio, Kentaro Nakamura, and Sadayuki Ueha. "Energy Storage Characteristics Of A Piezo-Generator Using Impact Induced Vibration". *Jpn. J. Appl. Phys.* 36.Part 1, No. 5B (1997): 3146-3151.

- [17] Umeda, Mikio, Yasuhiro Sakai, and Kentaro Nakamura. *IEEEJ Transactions on Sensors and Micromachines* 123.12 (2003): 534-540.
- [18] Priya, Shashank and D. J Inman. *Energy Harvesting Technologies*. New York: Springer, (2008) chapter 4 pp: 107-128.
- [19] Boughaleb, J et al. "SPICE Modelling Of A Coupled Piezoelectric-Bimetal Heat Engine For Autonomous Wireless Sensor Nodes (WSN) Power Supply". *J. Phys.: Conf. Ser.* 557 (2014): 012091.
- [20] Boughaleb, J. et al. "Coupling Of A Bimetallic Strip Heat Engine With A Piezoelectric Transducer For Thermal Energy Harvesting". *Molecular Crystals and Liquid Crystals* 628.1 (2016): 15-22.
- [21] Lefeuvre, Elie et al., "Piezoelectric material-based energy harvesting devices : advances of SSH optimization techniques (1999-2009)," in *Piezoelectric Ceramics*, E. Suaste-Gomez, Ed. InTech, (2010): 165–184.
- [22] Guyomar, D. et al. "Toward Energy Harvesting Using Active Materials And Conversion Improvement By Nonlinear Processing". *IEEE Transactions on Ultrasonics, Ferroelectrics and Frequency Control* 52.4 (2005): 584-595.
- [23] Lefeuvre, Elie et al. "High Performance Piezoelectric Vibration Energy Reclamation" SPIE Proceedings, (2004). Vol. 5390: 379-387.
- [24] Badel, A. "Efficiency Enhancement Of A Piezoelectric Energy Harvesting Device In Pulsed Operation By Synchronous Charge Inversion". *Journal of Intelligent Material Systems and Structures* 16.10 (2005): 889-901.
- [25] Lefeuvre, E. "Piezoelectric Energy Harvesting Device Optimization By Synchronous Electric Charge Extraction". *Journal of Intelligent Material Systems and Structures* 16.10 (2005): 865-876.
- [26] T. Hehn, Y. Manoli, "Highly Efficient CMOS Integrated Interface Circuit for High Voltage Piezoelectric Generators" In Proceedings of the International Workshop on Micro and Nanotechnology for Power Generation and Energy Conversion Applications (PowerMEMS), Washington DC, USA, 1–4 Dec 2009, pp. 431–434.
- [27] Hehn T et al. "A CMOS Integrated Interface for Piezoelectric Generators" Proc. PowerMEMS, Sendai, Japan, 9-12 November (2008): 457–460.
- [28] Hehn, Thorsten et al. "A Fully Autonomous Integrated Interface Circuit For Piezoelectric Harvesters". *IEEE J. Solid-State Circuits* 47.9 (2012): 2185-2198.
- [29] Hehn, T., F. Hagedorn, and Y. Manoli. "Highly Efficient Energy Extraction From Piezoelectric Generators". *Procedia Chemistry* 1.1 (2009): 1451-1454.
- [30] Arnaud, A et al. "Piezoelectric And Electrostatic Bimetal-Based Thermal Energy Harvesters". *J. Phys.: Conf. Ser.* 476 (2013): 012062.
- [31] Boisseau, S et al. "Semi-Flexible Bimetal-Based Thermal Energy Harvesters". *Smart Mater. Struct.* 22.2 (2013): 025021.
- [32] Boisseau, S et al. "Self-Starting Power Management Circuits For Piezoelectric And Electret-

- Based Electrostatic Mechanical Energy Harvesters". *J. Phys.: Conf. Ser.* 476 (2013): 012080.
- [33] Boisseau, S. et al. "Synchronous Electric Charge Extraction For Multiple Piezoelectric Energy Harvesters". *2015 IEEE 13th International New Circuits and Systems Conference (NEWCAS)* (2015).
- [34] Rabaey, J.M. et al. "Picoradio Supports Ad Hoc Ultra-Low Power Wireless Networking". *Computer* 33.7 (2000): 42-48.
- [35] Beeby, Stephen and Neil White. *Energy Harvesting For Autonomous Systems*. Norwood, Mass.: Artech House, 2010.
- [36] Varga, Liviu-Octavian et al. "Greenet: An Energy-Harvesting IP-Enabled Wireless Sensor Network". *IEEE Internet of Things Journal* 2.5 (2015): 412-426.
- [37] Boughaleb, J et al. "SPICE Modelling Of A Coupled Piezoelectric-Bimetal Heat Engine For Autonomous Wireless Sensor Nodes (WSN) Power Supply". *J. Phys.: Conf. Ser.* 557 (2014): 012091.
- [38] [http://www.st.com/content/st\\_com/en/products/power-management/battery-management-ics/enfilm-thin-film-batteries/efl700a39.html](http://www.st.com/content/st_com/en/products/power-management/battery-management-ics/enfilm-thin-film-batteries/efl700a39.html)

## General conclusion

The past years have known an increasing interest in energy harvesting technologies, especially because of the reduction in power consumption and in size of CMOS electronics. The main purpose of such a development is to give autonomy to Wireless Sensors Node (WSN) as the development of Wireless Sensor Networks have raised the problem of power supply. These networks can be used in numerous applications such as environmental or industrial control systems, health monitoring, and the Internet of Things (IoT) among other things. The ultimate objective is to develop networks comprised of hundreds of wireless nodes in order to replace long transmission distances with small-price and low-power wireless systems leading to the emergence of intelligent environments. In order that such devices be self-sufficient, researchers have developed a large number of energy harvesters to scavenge abundant environmental energy sources.

The work presented in this PhD manuscript is related to energy harvesting for WSN applications as it deals with the development and with the integration of a thermal energy harvester based on bimetallic strips heat engine and piezoelectric materials.

*Chapter 1* is an introduction on Wireless Sensor Networks. First of all, some applications of WSN are presented and the architecture and the power consumption of a typical autonomous smart sensor are exposed. Its consumption is comprised between 1 and 20 $\mu$ W. A review of the main energy harvesting technologies used to supply the WSN is also presented with a special focus on thermal energy harvesting. To do so, a thermoelectric generator from Micropelt is benchmarked and its performances are detailed in many configurations (with and without heat sink and with and without electronic board). The purpose of such a study was to find the properties a thermoelectric generator without any heat sink or board to be able to compare its thermal and electrical performances with the thermal energy harvester developed in the HEATec project. Finally, to end this first introductory chapter, the working principle of the coupled piezoelectric and bimetal energy harvester is exposed. This study revealed that Micropelt's thermoelectric energy harvesters when used with a radiator and mounted on a board can generate up to 12mW at 100°C and when the an ambient temperature is around 25°C. In the same experimental condition and without the heat sink, this value decreases to 0,8mW. From a thermal point of view, HEATec energy harvesters have a thermal gradient 1,5 times higher than that of Micropelt's module with no heat sink and no board. However, the electrical performances of HEATec and Micropelt energy harvesters could not be compared because the TEH could not have been characterized electrically once extracted from the board.

**Chapter 2** deals with the thermal study and optimization of the thermal energy harvester. In the first part of this chapter, the various steps of thermal analytical modeling in steady state conditions is presented and an equivalent circuit approach taking into account all the modes of heat transfer in the device is proposed. This thermal model made it possible to obtain an analytical value of the cold surface temperature in good agreement with the experimental measurements over a wide range of hot source temperatures. In this investigation, the analytical model based on the analogy between electricity and thermal transfers allowed further improvements based on the matching of thermal resistances. This model allowed to maintain a maximal temperature difference across the structure for any hot source's temperature and it gave us the main guidelines for an optimal design of the system. All these improvement steps were validated on an optimized energy harvester as the experimental measurements confirmed that the thermal gradient was improved by approximately a factor 2.

The heat transfer inside a matrix of many cells is also studied using the finite element model developed by ESI. Given the thermal optimization performed on one individual energy harvester, the temperature distribution remained very close to that of a single cell when matrix structures were considered. Moreover, predictions of the thermal behavior as a function of the downscaling of the energy harvester's dimensions are established, based on the thermal model of a thermally-matched energy harvester. Finally, in the case of a scaled-down device, ways of improvements were proposed to maintain good thermal properties.

In the second part of this chapter, a dynamic model describing the dynamic behavior of a bimetal inside the thermal energy harvester is presented. This model considers bimetal as switched capacitances oscillating between two equilibrium states depending on the evolution of their intrinsic temperature. Experimental data validated the analytical expressions of the performances obtained with this model. This approach was the key to extend the conditions of utilization of our energy harvesters and gave us the main guidelines to determine what kind of bimetal needed to be chosen as a function of their use.

**Chapter 3** presents a complete benchmark of each device component is presented. First of all, a review of various piezoelectric materials used in energy harvesting is developed. A comparison of their performances and the effect of each piezoelectric parameter on the output power is done. This allowed to point out the most interesting material for our harvesting application.

In a second step, we studied the device architecture and improved each conversion step independently. We chose an adapted substrate for the device, improved the contact of the bimetal with the piezoelectric membrane and studied the best position and configuration of the piezoelectric beam over the bimetal as it could either be clamped at its both ends or used as a cantilever beam with a free end. We also tested different piezoelectric membranes from different manufactures in order to improve the device performance and to increase the amount of harvested power. However, the best configuration was the initially-used one: Kepo's membranes were the most affordable transducers since it delivered nearly the same amount of electrical power as the Piezosystem's piezoelectric membranes but with a lower cost. Also, other experiments were realized to see either if using bimetal with larger thermal hysteresis and larger dimensions could allow to increase the generator's output power or not. Here again, the tests did not reveal any improvement and the best results were obtained with bimetal having a thermal hysteresis of 3°C and dimensions of 36mm x 18 mm x 0.3 mm.

Finally, using the best device configuration, aging tests were realized on each key component of the system: the bimetal and the piezoelectric membranes. For this purpose, the bimetal's manufacturer developed a tests bench to accelerate cycling of bimetal. Up to now, 10 million cycles were realized and no change in the bimetal's mechanical behavior was observed. Aging tests were also realized on the piezoelectric membrane. To simulate the impact of bimetal on its surface, a steel beam was fixed on a shaker and more than 10 million cycles were realized.

However, at the end of this experiment, the piezoelectric membrane properties seemed to drastically decrease but the reason of such a behavior was the progressive screw loosening during the cycling. The piezoelectric membrane was tested after having retightened the four screws and this revealed that the coupling coefficient decreased by 27% and the quality factor decreased by 12% after the first 10 million cycles. We could not do more tests because the experimental setup used here was not adequate for a continuous functioning. However, the first test were very revealing of the way the generator's performances will evolve in real use case.

**Chapter 4** deals with an investigation of new ways to harvest thermal and mechanical energies thanks to bimetals and piezoelectric membranes. First of all, the direct deposition of piezoelectric materials on the bistable bimetals was explored. Two different techniques and materials were used for this experiment. On one hand, piezoelectric composites using barium titanate or PZT particles and a polymer matrix were used and on the other hand, massive PZT thin films are fabricated and deposited onto bimetals. The bimetals with piezoelectric thin films showed better performances than the bimetals with piezoelectric composites, however, in both cases, low amounts of electrical power were obtained, reaching in the best case 10nW.

In the second part of this chapter, we developed a dual energy harvester enable to harvest thermal and mechanical energies harvesting the same time. Sources of wasted vibrations are very frequent in our environment. The frequencies and accelerations of such vibrations are very different and, to point out the most interesting vibrations, we established a state of the art of the characteristics of ambient vibrations. This allowed us to concentrate our work on the frequencies 50Hz, 100Hz and 120Hz. Based on many previous studies concerning piezoelectric cantilevers design, we gave the main guidelines to modify the piezoelectric beams in order to tune their eigen-frequency. A 2D Finite-Element Model of a cantilever was developed using Comsol software. Geometrical parameters were optimized find the beam's dimensions needed to reach frequencies of 50Hz, 100Hz and 120Hz. Moreover, a technique to widen the frequency operation window of each beam was given. Experimental tests on these structures are currently being done.

**Chapter 5** is about the integration of the HEATec thermal energy harvester. It begins with the electromechanical modeling of our thermal energy harvester based on Mason model for piezoelectric energy harvesters. In function of the boundary conditions of the piezoelectric membrane, a general model of the system is presented, taking into account the bistable behavior of the bimetal. The proposed circuit was inspired from the equivalence between the piezoelectric transducer's mechanical parameters and its electrical properties, and it allowed to simulate the output signal generated by the generator when the bimetal switches from a heat source to the other one.

A benchmark of the existing circuits in the literature to process the energy harvester's output signal and to extract the major part of it is then presented. To do so, we worked in collaboration with CEA Leti that compared SSHI, SECE and PSCE circuits. Each of those circuit has its advantages and may allow an improvement of the piezoelectric output power depending on the circuit's implementation (discrete type or integrated circuit). Because SSHI technique did not make the output power be independent of the load's impedance value, only SECE and PSCE technique were simulated and discrete element circuits are realized. Using the discrete type circuit, no performance improvement have been observed. This made it compulsory to implement integrated circuits of these non-linear switching techniques. These last simulation results were very promising as a power gain of 100% was obtained. The next step is the physical realization of these circuits to test them and to confirm the power gain obtained in the simulations. This work is currently being realized at CEA Leti.

Finally, the last part of this chapter is about the integration of the thermal energy harvester to realize WSN demonstrations. First of all, given the amount of power generated by thermal energy

harvester (few  $\mu\text{W}$ ), all the demonstrations were realized in asynchronous mode. The first demonstration was realized using an ST demonstration platform called GreenNet and operating using 802.15.4 communication protocol at 2.4GHz. Thanks to the collaboration of STMicroelectronics' and CEA's designer's teams, an ultra-low power application circuit was created and patented to make the WSN emission node detect when sufficient energy is stored on the buffer capacitor meaning that measurements can be realized by the sensors and the measured data transferred toward the reception node. The consumption of this circuit was as low as  $0.1\mu\text{W}$  and the entire WSN demonstration platform needed only  $1\mu\text{W}$  to operate. Numerous ST sensors were implemented on the WSN such as a temperature sensor, an accelerometer and a magnetometer. Demonstrations using BLE and 868MHz communications protocols were also realized. This last kind of communication protocol is very attractive for low data rate applications like for home security and automation and it offers substantive benefits over the more powerful protocols as Wi-Fi, Bluetooth or ZigBee. Whereas the BLE WSN needed  $600\mu\text{J}$  to measure the temperature and send data on a smartphone, GreenNet and 868MHz consume only  $120\mu\text{J}$  for that same task. However, because of its lower frequency, the node at 868MHz is the one having the most interesting range. To obtain a completely autonomous WSNs, a timer and a micro-battery were added in the system in order to use the battery's energy when the thermal energy harvester stops functioning.

After many optimization steps of the coupled piezoelectric and bimetallic strip heat engines, their output power was increased from  $1\mu\text{W}$  (generated by the first prototype developed by Puscasu) to  $30\mu\text{W}$  available on the piezoelectric capacitor, corresponding to  $5\mu\text{W}$  of usable power using a standard electronic circuit composed of a diode bridge and a storage capacitor. These measured efficiencies and power values are very small compared with the power generated by other low-cost energy harvesting technologies, like concurrent thermoelectric generators. For this reason, the compatibility of the developed WSN with other low cost energy harvesting techniques were tested like thermoelectric generators for thermal energy harvesting, photovoltaic cells for solar energy harvesting.... All these techniques are compatible with the WSN developed by CEA-Leti which makes them good alternatives to the thermal energy harvesters developed in this thesis. In fact, as these generators harvest more power, data emissions can be more frequent. This is particularly interesting for the use cases where data must be monitored with a period ranging from few seconds to one minute. For example, by using the solar cells, it is possible to make WSN emit data toward smartphones every five seconds with indoor ambient light using BLE and every 3 to 4 minutes with low light (under a desk for example). These techniques allow more frequent measurements and data emission and explain why the bimetallic strip heat engines coupled with a piezoelectric membranes are not the most interesting solution for WSN applications. However, in some use cases where neither no light is available to use photovoltaic cells (darkness use cases) nor sufficient space to use a radiator over a thermoelectric generator, the thermal energy harvester developed here represents a good alternative. Contrary to photovoltaic cells, it works independently of the environment's illumination and at the opposite of thermoelectric energy harvesters, the HEATec harvester is very thin and does not need any heat sink to function, if the cold source's temperature is not thermostated. As the limits of the HEATec energy harvester were reached, we can think of keeping it for WSN application for the use cases where other technologies do not function.



## FOLIO ADMINISTRATIF

### THESE DE L'UNIVERSITE DE LYON OPEREE AU SEIN DE L'INSA LYON

NOM : **BOUGHALEB**

DATE de SOUTENANCE : **09/11/2016**

Prénoms : **Jihane**

TITRE : **Développement et intégration d'un récupérateur d'énergie thermique à base de bilames thermiques et de matériaux piézoélectriques**

NATURE : **Doctorat**

Numéro d'ordre : 2016LYSE114

Ecole doctorale : **ELECTRONIQUE, ELECTROTECHNIQUE, AUTOMATIQUE (EEA)**

Spécialité : Génie Electrique

#### RESUME :

Le développement des systèmes de récupération d'énergie est liée à l'émergence des applications de type Internet des objets (IoT) plus spécifiquement à la prolifération des réseaux de capteurs autonomes qui doivent répondre aux besoins croissants de surveillance des données aussi bien dans l'industrie, les milieux urbains ou encore la domotique. Les progrès réalisés ces dernières années dans le domaine des technologies de l'information et de la communication ont permis de lever certains verrous technologiques au développement de ces réseaux de capteurs intelligents et autonomes, notamment grâce à l'amélioration des performances intrinsèques des composants microélectroniques (vitesse, consommation), la conception de circuits plus économes en énergie, ou bien la mise en place de standards de communications radio adaptés à ces contraintes énergétiques. Etant donné l'ubiquité des sources d'énergie, la fabrication de générateurs permettant d'alimenter directement ces capteurs et les rendre autonomes en énergie à partir de ces sources représente une alternative viable à l'utilisation de batteries pour prolonger la durée de vie de ces capteurs communicants. Diverses technologies de générateurs ont ainsi été proposées pour s'adapter aux différentes formes que peut prendre l'énergie, qu'elle soit d'origine thermique, mécanique ou solaire. Le présent travail est une contribution à l'élaboration d'un récupérateur d'énergie thermique à base de bilames thermiques et de matériaux piézoélectriques. Ce type de générateurs, proposé et développé au sein de STMicroelectronics à Crolles, se veut être une alternative fiable et bas cout à l'utilisation de matériaux thermoélectriques exploitant l'effet Seebeck pour générer de l'énergie électrique. Des preuves de concept de tels systèmes ont déjà été développées aussi bien à macro-échelle qu'à micro-échelle. Ce travail s'inscrit dans la continuité du développement d'un récupérateur d'énergie macroscopique reposant sur ce principe-là. L'objectif de cette thèse est dans un premier temps d'optimiser cette structure pour atteindre des niveaux de puissances plus élevés que la première preuve de concept puis dans un second temps, de réaliser son intégration afin d'effectuer des démonstrations de capteur autonome et confirmer la viabilité de la technologie développée pour de telles applications.

Une partie importante de ce manuscrit traite de l'optimisation thermique du récupérateur d'énergie aussi bien en mode statique que dynamique. Les travaux de modélisation thermique effectués ont permis d'accroître les performances thermiques du système et d'avoir une meilleure compréhension des échanges de chaleur dans la structure. Toujours dans une optique d'améliorer les performances et les puissances récupérées, différents matériaux piézoélectriques assurant la conversion mécano-electrique ont été comparés et testés pour trouver le matériau le plus adapté à notre application. Le même travail d'optimisation a été réalisé au niveau de la structure du système et différentes architectures ont été comparées et testées. La structure la plus efficace a été retenue et son intégration a été réalisée. Plusieurs démonstrations de fonctionnement de capteurs autonomes alimentés par le générateur optimisé ont été établies suivant différents protocoles de communications et avec différents capteurs (accéléromètre, capteur de température...). Par la suite et afin d'optimiser l'extraction de l'énergie du générateur grâce à un circuit de gestion de l'énergie, une modélisation SPICE du système s'inspirant du modèle électromécanique des générateurs piézoélectriques est proposé. Ce modèle permettant de simuler la tension en sortie du générateur a été utilisé ensuite par les designers de ST et du CEA pour mettre en place un circuit de gestion de l'énergie récupérée. D'autres moyens de récupérer l'énergie thermique grâce aux bilames thermiques et aux matériaux piézoélectriques ont été explorés par la suite. Dans un premier temps, des bilames piézoélectriques ont été réalisés en utilisant soit des composites piézoélectriques ou des couches minces piézoélectriques. Puis, un système capable de faire à la fois de la récupération d'énergie thermique et des vibrations ambiantes a été proposé grâce à des simulations en 2D de poutres piézoélectriques dont les fréquences de résonances correspondent aux fréquences des vibrations environnantes les plus fréquentes.

MOTS-CLÉS : Récupération d'énergie thermique, Bilame, Piézoélectricité, Nœuds de Capteurs autonomes.

Laboratoire (s) de recherche : **Laboratoire de Génie Electrique et de Ferroélectricité (LGEF)**

Directeur de thèse: Pr. Daniel Guyomar

Président de jury :

#### Composition du jury :

LIANG, Zhiyong	Rapporteur
GUIFFARD, Benoit	Rapporteur
ROUVIERE, Emmanuelle	Examinatrice
KANDA, Masae	Examinatrice
GUYOMAR, Daniel	Directeur de thèse
COTTINET, Pierre-Jean	Co-directeur de thèse
SKOTNICKI, Thomas	Invité
MONFRAY, Stéphane	Invité
QUENARD, Sébastien	Invité